

NUMERICAL MODELLING OF SPILLWAYS AND ENERGY DISSIPATORS USING THE SMOOTHED PARTICLE HYDRODYNAMICS METHOD

ANDREIA MANUELA BORGES MOREIRA

Doctoral Program in Civil Engineering
Hydraulics, Water Resources and Environment

Supervisor: Prof. Dr. Francisco Taveira Pinto

Co-supervisor: Dr. Damien Violeau

2021

ABSTRACT

In recent years, dam safety has drawn increasing attention from experts and the public in general. This is mostly because minor to significant incidents still happen in the twentieth-first century, of such, the Oroville dam spillway in California is probably the most remarkable and recent one. Functional problems in dams are as diverse as spillway chute overtopping, spillway failure (e.g. due to cavitation or uplift resulting from high velocity discharges over open offset joints), or spillway gate failure. Current solutions for some of these problems include raising the dam crest (to increase flood storage), the modification of the existing spillway or even the construction of a new one (to increase discharge capacity). Such adaptations require the completion of complex studies to support an ultimate decision. The development of expedite methodologies to find solutions of optimum and safer performance in time, is then a present priority.

For years, laboratory studies were the only available tool to assess flow behaviour in spillways and energy dissipators (apart from prototype measurements and visual inspection). More recently, Computational Fluid Dynamics has opened a new way to the design of hydraulic structures. Meshfree methods present many advantages in the simulation of flows involving large deformations and fragmentations in the free-surface, such as those encountered in spillways and energy dissipators, because the computational domain is represented by a set of discrete free-moving particles. Despite the capabilities of these methods, they are far less used in comparison with grid-based methods, such as the Finite Volume Method (FVM). Smoothed Particle Hydrodynamics (SPH) is a meshfree method that is becoming widely used for research applications of free-surface flows. However, its application to large-scale dam spillways by design engineers is still hampered by the lack of confidence in this method, owed to the significant lack of quantitative validation for such complex studies. The growing use of this technique as a tool for design and assessment of the mentioned hydraulic structures, presupposes a systematization of this knowledge in the research context.

Efforts in this research concentrated on the exploitation of the SPH method capabilities to predict the flow features in spillways and energy dissipators, using physical model experiments of real and distinct case studies. To do so, the Crestuma and the Caniçada dam case studies were used. A third case study aimed at evaluating the hydrodynamic load produced by jets commonly found in dam spillways was also addressed. The completion of these studies resulted in the most in-depth validation of an SPH-based code to model real spillway flows, to date. It allowed to evaluate the hydraulic phenomena that the current state-of-knowledge of the method can well or badly reproduce aiding to direct the future research needs in terms of new numerical formulations. Comparison between SPH and mesh-based results was also done, showing that SPH can be equally well-succeed in the prediction of, e.g., pressures and flow velocities. In the end a set of practical recommendations for the application of SPH to model spillway flows is given, based on the empirical knowledge attained with the completion of the numerical modelling work. It is aimed at encouraging and simplifying the use of SPH to model spillway flows by the industry, as a complement of what can currently be done with mesh-based methods.

KEYWORDS: Dam spillways; free-surface flow; mesh-free methods; numerical simulation; spillway flows; SPH.

RESUMO

A segurança de barragens tem sido alvo, nos últimos anos, de maior atenção por parte dos especialistas e do público em geral. Tal deve-se sobretudo ao facto de que incidentes pequenos a significativos ainda acontecem no século XXI, dos quais o caso da barragem de Oroville na Califórnia é provavelmente o mais marcante e recente. Os problemas funcionais em barragens podem ser tão diversos como o galgamento do descarregador, a sua falha (por exemplo, devido a problemas de cavitação ou à danificação da soleira descarregadora por ação de um escoamento de alta velocidade sobre juntas de dilatação), ou a falha de comportas. As soluções atuais para alguns desses problemas incluem a elevação da crista da barragem (de forma a aumentar a capacidade de armazenamento), a modificação do descarregador existente ou até a construção de um novo, complementar. Tais adaptações exigem a execução de estudos complexos para apoiar uma decisão final. O desenvolvimento de metodologias rápidas para encontrar soluções de desempenho otimizado e mais seguro em tempo útil é, portanto, uma prioridade presente.

Durante anos, os estudos em modelo físico reduzido foram a única ferramenta disponível para avaliar o escoamento em descarregadores de barragens (além de medições em protótipo e da inspeção visual). Mais recentemente, a Dinâmica de Fluidos Computacional trouxe uma nova maneira de projetar estruturas hidráulicas. Os métodos numéricos sem malha apresentam muitas vantagens na simulação de escoamentos envolvendo grandes deformações e fragmentações da superfície livre, características normalmente presentes em escoamentos em descarregadores de barragens, pois o domínio computacional é representado por um conjunto de partículas que se movem livremente. Apesar das reconhecidas capacidades desses métodos, eles são muito menos usados em comparação com métodos cujo cálculo é baseado numa malha, como o Método dos Volume Finitos (FVM). O método da Hidrodinâmica Suavizada de Partículas (SPH) é um método sem malha que está a ser amplamente utilizado no âmbito da investigação de escoamentos de superfície livre. No entanto, a sua aplicação a descarregadores de barragens à escala real ainda é limitada pela falta de confiança neste método, devido à significativa falta de validação quantitativa para estudos desta complexidade. A crescente utilização destas técnicas como ferramenta de dimensionamento e verificação das referidas estruturas hidráulicas, pressupõe uma sistematização deste conhecimento em contexto de investigação.

A presente investigação concentrou-se na exploração das capacidades do método SPH para prever as características do escoamento em descarregadores e dissipadores de energia de barragens, usando casos de estudo reais e distintos. Para tal, foram utilizados modelos físicos dos casos de estudos das barragens de Crestuma e da Caniçada. Um terceiro caso de estudo teve como objetivo a avaliação da carga hidrodinâmica produzida por jatos comumente encontrados em barragens. A conclusão destes estudos resultou na validação mais profunda de um código baseado no método SPH, para modelar escoamentos em descarregadores de barragens, até o momento. Permitiu avaliar os fenómenos hidráulicos que o atual estado de conhecimento do método permite reproduzir melhor ou pior, ajudando a direcionar as necessidades futuras de investigação em termos de novas formulações numéricas. Foi também realizada uma comparação entre os resultados obtidos com o método SPH e um método numérico de malha, mostrando que o SPH permite prever, igualmente, com significativo sucesso, por exemplo, pressões e velocidades de escoamento. No final, é fornecido um conjunto de recomendações práticas para a aplicação do SPH na modelação de escoamentos em barragens, com base no conhecimento empírico obtido. Este visa incentivar e simplificar o uso do SPH na modelação de escoamentos em descarregadores de barragens pela indústria, como um complemento do que pode atualmente ser feito com os métodos numéricos de malha.

PALAVRAS-CHAVE: Descarregadores de cheias; escoamento de superfície livre; métodos sem malha; modelação numérica; escoamento em descarregadores; SPH.

O binómio de Newton é tão belo como a Vénus de Milo.

O que há é pouca gente para dar por isso.

(Álvaro de Campos)

ACKNOWLEDGEMENTS

I would like to express my deepest gratitude and appreciation to those who have contributed to the realization of this Ph.D. thesis.

I would like to thank my supervisor Professor Francisco Taveira Pinto for suggesting me studying such an interesting topic and for all the practical and intellectual guidance throughout my research.

I also want to express my gratitude to my co-supervisor Doctor Damien Violeau for providing me the opportunity of spending some time at the Saint Venant Hydraulics Laboratory, in France, and for all of his precious comments and insights to this research.

Another big thank you goes to Doctor Agnès Leroy for her guidance. I have incorporated various of her interesting suggestions during the setup of the numerical models, without which my task would have been harder. To have worked with her was a challenging and enriching experience, which I appreciated.

Another word of gratitude is due to Doctor Pedro Manso for his collaboration on the topic of high velocity jets, and to have kindly received me in the Laboratory of Hydraulic Constructions, at EPFL.

Appreciation is extended to all other faculty members and staff in the Hydraulics, Water Resources and Environment Division. In particular, I would like to thank my friends Sandra and Juliana who I shared not only the office but most specially the ups and downs of carrying out an individual research work. Another “thank you” goes to Sr. Miguel who helped me many times to carry my computer to have it fixed and to my colleague Luís Brandão for his clarifications with respect to the physical and numerical modelling of the Caniçada’s complementary spillway.

A special thank you is reserved to those whom I love the most, my family, in particular my mother, Tiago and our beloved sons Lucas and Simão.

Lastly, the completion of this study would not be possible without the scholarship by the *Fundação Portuguesa para a Ciência e a Tecnologia* through the grant reference SFRH/BD/102192/2014, which support is here gratefully acknowledged.



NOMENCLATURE

Abbreviations

ALE	Arbitrary Lagrangian-Eulerian-based
ASCE	American Society of Civil Engineers
ASDSO	Association of State Dam Safety Officials
CAD	Computer-Aided Design
CAE	Computer-Aided Engineering
CEDEX	<i>Centro de Estudios y Experimentación de Obras Públicas</i>
CFD	Computational Fluid Dynamics
CFL	Courant–Friedrichs–Lewy
CPU	Central Processing Unit
CUDA	Compute Unified Device Architecture
DEC	Department of Civil Engineering
DNS	Direct Numerical Simulation
EDF	<i>Electricité de France</i>
EDP	<i>Eletricidade de Portugal</i>
EPFL	<i>École Polytechnique Fédérale de Lausanne</i>
ERCOFTAC	European Research Community on Flow Turbulence and Combustion
FEM	Finite Element Method
FEMA	Federal Emergency Management Agency
FEUP	Faculty of Engineering of the University of Porto
FVM	Finite Volume Method
GPU	Graphics Processing Unit
HPC	High-Performance Computing
ICOLD	International Commission on Large Dams
IFT	Independent Forensic Team
IPCC	Intergovernmental Panel on Climate Change
IRENA	International Renewable Energy Agency
ISPH	Incompressible Smoothed Particle Hydrodynamics
LCH	Laboratory of Hydraulic Constructions
LDA	Laser-Doppler Anemometer
LNEC	National Laboratory of Civil Engineering

LS	Level Set
LES	Large Eddy Simulation
MPI	Message Passing Interface
RANS	Reynolds-Averaged Navier–Stokes
R&D	Research and Development
REN	National Energy Network
RMS	Root Mean Square
RSM	Reynolds-Stress Model
SHRHA	Hydraulics, Water Resources and Environment Division
SPH	Smoothed Particle Hydrodynamics
SPHERIC	Smoothed Particle Hydrodynamics Research and Engineering International Community
SVE	Saint-Venant Equations
ODE	Ordinary Differential Equations
PDE	Partial Differential Equations
PNBEPH	National Program of Hydropower Plants with High Hydroelectric Potential
PNCOLD	Portuguese National Committee on Large dams
NSE	Navier–Stokes Equations
USACE	United States Army Corps of Engineers
USA	United States of America
USAW	Unified Semi-Analytical Wall Boundary Conditions
USBR	United States Bureau of Reclamation
USCOLD	United States Committee on Large Dams
VoF	Volume of Fluid
WCSPH	Weakly Compressible Smoothed Particle Hydrodynamics
WES	Waterways Experiment Station

Greek symbols

β_A	Free diffusion length (m)
γ	Boundary renormalization parameter (-)
γ_w	Water's specific weight (N/m ³)
κ	Von Kármán constant
δt	Time step (s)

ϵ	Energy dissipation rate (m^2/s^3)
σ	Standard deviation (or RMS) of a data sample
$\boldsymbol{\sigma}$	Stress tensor ($\text{kg}/\text{m}\cdot\text{s}^2$)
σ_k	Constant of the $k - \epsilon$ turbulence model
σ_ϵ	Constant of the $k - \epsilon$ turbulence model
$\boldsymbol{\tau}$	Shear-stress vector ($\text{kg}/\text{m}\cdot\text{s}^2$)
ρ	Density (kg/m^3)
ρ_0	Reference density (kg/m^3)
μ	Dynamic molecular viscosity ($\text{Pa}\cdot\text{s}$)
ν	Kinematic molecular viscosity (m^2/s)
ν_T	Kinematic eddy viscosity (m^2/s)
ξ	Polytropic index (-)
Π	Artificial viscosity (m^2/s)
ϕ	Correction coefficient for the kinetic energy
Ω	Computational domain

Roman symbols

c_0	Speed of sound (m/s)
C_a	Cavitation index
C_p	Mean dynamic pressure coefficient
$C_{p'}$	Turbulent pressure fluctuation coefficient
$C_{\epsilon 1}$	Constant of the $k - \epsilon$ turbulence model
$C_{\epsilon 2}$	Constant of the $k - \epsilon$ turbulence model
C_μ	Constant of the $k - \epsilon$ turbulence model
D	Nozzle diameter (m)
D_i	Jet's diameter at issuance (m)
D_j	Jet's diameter at impact with the pool water (m)
d_p	Particle's diameter in SPH
Fr	Froude number
g	Gravity acceleration (m/s^2)
H	Water depth (m)
H_{des}	Design hydraulic head (m)
h	Smoothing length (m)

Y	Pool water depth (m)
y^+	Dimensionless distance to a wall in turbulent regime
k	Turbulent kinetic energy (m^2/s^2)
L	Length of jet travel in the air (m)
L_c	Jet's length of core decay (m)
l	Length scale (m)
m	Mass (kg)
P	Mean pressure (Pa)
$P_{stagnation}$	Mean pressure at the stagnation point (Pa)
P_{vapor}	Vapor pressure (Pa)
P_a	Production of turbulent kinetic energy (m^2/s^3)
p	Pressure (Pa)
Q	Flow rate (m^3/s)
Q_d	Design flow rate (m^3/s)
R	Nozzle radius (m)
Re	Reynolds number
\mathbf{r}	Position vector (m)
\mathbf{s}	Strain-rate tensor (s^{-1})
t	Time (s)
U	Velocity (m/s)
U_0	Jet's exit velocity (m/s)
u_*	Friction velocity (m/s)
\mathbf{u}	Velocity vector (m/s)
V	Volume (m^3)
W	Kernel function (m^3)

CONTENTS

CONTENTS.....	XIII
LIST OF FIGURES.....	XVII
LIST OF TABLES	XXV
1. INTRODUCTION	1
1.1. Context and aim of the work	1
1.2. Thesis outline	3
2. GENERAL BACKGROUND TO THE TOPIC.....	5
2.1. Hydropower dams around the world.....	5
2.2. Dam Spillways	9
2.2.1. Hydraulic schemes	9
2.2.2. Energy dissipators	14
2.2.3. Characteristics of spillway flows	17
2.2.4. Dam failures and incidents	22
2.3. Numerical modelling	26
2.3.1. Introduction	26
2.3.2. Mesh-based methods	27
2.3.3. Meshfree methods.....	28
2.3.4. Governing equations for fluid dynamics	29
2.3.5. Turbulence modelling	31
2.3.6. Conclusions	33
3. SMOOTHED PARTICLE HYDRODYNAMICS.....	35
3.1. Introduction.....	35
3.2. SPH formulation	37
3.3. Density correction in SPH	41
3.4. Boundary conditions in SPH.....	43

3.5.	Turbulence modelling in SPH	46
3.6.	Multiphase modelling in SPH	48
3.7.	Parallelization through GPU computing	50
3.8.	SPH modelling of free-surface and spillway flows	52
3.8.1.	Schematic geometries	53
3.8.2.	Industrial case studies	55
3.9.	Conclusions	63
4.	DEVELOPMENT OF SPH APPLICATIONS	65
4.1.	Introduction	65
4.2.	GPUSPH	66
4.2.1.	The GPUSPH project	66
4.2.2.	Running GPUSPH	66
4.3.	Overgate discharge – case study I	69
4.3.1.	Introduction	69
4.3.2.	Laboratory experiments	70
4.3.3.	SPH model set-up	72
4.2.3.	Analysis of results	75
4.3.4.	Conclusions	82
4.4.	Chute flow – case study II	84
4.4.1.	Introduction	84
4.4.2.	Laboratory experiments	86
4.4.3.	SPH model set-up	89
4.4.4.	Analysis of results	91
4.4.5.	GPUSPH vs. mesh-based model results	110
4.4.6.	Conclusions	114
4.5.	High-velocity jet – case study III	115
4.5.1.	Introduction	115
4.5.2.	Previous studies	116
4.5.3.	SPH model set-up	119
4.5.1.	Results and discussion	125
4.5.2.	Conclusions	135
4.6.	Conclusion	136
5.	PRACTICAL RECOMMENDATIONS	137
5.1.	Introduction	137

5.2. Problem statement	137
5.3. Design and meshing	140
5.4. Hardware related issues	143
5.5. Spillway3D case example	144
5.6. Conclusions	148
6. CONCLUSIONS AND FUTURE DEVELOPMENTS	149
6.1. Summary	149
6.2. Future developments	150
REFERENCES	153
APPENDIX A	173
APPENDIX B	177
APPENDIX C	185

LIST OF FIGURES

CHAPTER 2 - GENERAL BACKGROUND TO THE TOPIC

Fig. 1. Typical “low head” hydropower plant with storage (picture from Dolf, 2012, adapted from Hydropower News and Information - http://www.alternative-energy-news.info/technology/hydro/).	5
Fig. 2 - Distribution of sources in electricity production, in Portugal, in 2016 and 2017 (REN, 2017). ...	8
Fig. 3 - Theoretical and harnessed potential in Portugal and other European countries (Mendes, 2017).	8
Fig. 4 - Downstream view of the 40m-high Wagendrift dam, Estcourt, South Africa, 1963 (photo credit: Neil Overy).....	11
Fig. 5 - Overflow spillway of Picote dam, located at Miranda do Douro, Portugal, 1958 (web 3 Nov 2016 www.ordemengenharios.pt).	11
Fig. 6 - Chute spillway of the Vermiosa dam on the right hillside, Guarda, Portugal, 1999 (web 3 Nov 2016 www.mota-engil.pt).....	11
Fig. 7 - Shaft spillway intake of the Chaffey dam, located at New South Wales, Australia, 1979, (photo credit: Brad Sherman).	12
Fig. 8 - Outlet of the Cahora-Bassa dam, located in Mozambique, 1974, (web 11 Dez 2018 https://macauhub.com.mo).....	13
Fig. 9 – Stepped spillway of the Hinze dam, South East Queensland, Australia 1976, (copyright ©Hubert Chanson 2014).	13
Fig. 10 - Drop structure in a prismatic rectangular channel and related flow types (adapted from Visser and Hager, 1998).	16
Fig. 11 - Free-surface aeration in the spillway of Hartbeespoort Dam, North West Province, South Africa, 1923 (web 3 Nov 2016 www.ewiza.co.za).	18
Fig. 12 - Cross-waves’ characteristics in nappe flows without hydraulic jump (adapted from Chanson and Toombes, 1997).	19
Fig. 13 – Cross-waves over the spillway of Gardiner dam, Saskatchewan, Canada, 1967 (copyright © Neil A Rawlyk).	19
Fig. 14 - Roll waves in the spillway of the Llyn Brianne Rock-fill Dam, Wales, United Kingdom (copyright © Geoffrey Davies).....	20
Fig. 15 - Cavitation damage in the Nagarjuna Sagar Dam, India, 1967 (from Giridhar <i>et al.</i> , 2014)....	21
Fig. 16 - Association of State Dam Safety Officials (ASDSO) incident Database - dam failure incidents’ (from 2010 to 2015) causes (web 12 Dec 2018 www.damsafety.org).	24
Fig. 17 – Evolution of the Oroville spillway failure in chronological order from (a) to (d). Photographs from Williamson (2017).	24
Fig. 18 – Flooded area after the Saddle Dam D dam collapse, in Laos (web 12 Dec 2018 www.aljazeera.com).	26
Fig. 19 – Evolution of the number of high hazard dams in need of remediation in the USA (web 13 Dec 2018 www.fema.gov).....	26

Fig. 20 - Near-Wall treatment approaches (from ANSYS, 2006).....	33
Fig. 21 - Design changes and costs all over the project when numerical simulation is used at the design stage (up-front simulation process) and when it does not (conventional process) (web 8 Jan 2019, www.midasoftware.com).....	34
CHAPTER 3 - SMOOTHED PARTICLE HYDRODYNAMICS	
Fig. 22 - Timeline of some SPH developments (BC – boundary conditions; OB – open boundaries)..	42
Fig. 23 - Generic SPH boundary treatments for rigid walls as particle approaches the boundary $\partial\Omega_b$. The grey shaded area is the solid boundary, the blue particles are fluid particles and the red particles are boundary particles (adapted from Violeau and Rogers, 2016).....	44
Fig. 24 - Sketch of the continuous medium discretisation with the USAW boundary conditions technique. Vertex particles, e , in green and segments, s , which have a surface, S_s , and an inward normal, \mathbf{n}_s (from Ferrand <i>et al.</i> , 2013).....	45
Fig. 25 - Sketch of the process of particles creation with vertex particles e in green, free fluid particles in blue and segments s at an inflow boundary (adapted from Ferrand <i>et al.</i> , 2017).....	46
Fig. 26 - CPU and GPU performance evolution (adapted from https://michaelgalloy.com).....	51
Fig. 27 - Speedups of GPU against CPU simulating 1 million particles (Domínguez, 2014).....	51
Fig. 28 - Runtimes for different CPU and GPU implementations as a function of the number of particles, N (adapted from Domínguez, 2014).....	52
Fig. 29 - Time history of pressure at the toe of a square obstacle (Kleefsman <i>et al.</i> , 2005 experiments' configuration) according to WCSPH, ISPH, VoF and experiments (from Lee <i>et al.</i> , 2009, a fictitious particles approach was used for the boundary conditions treatment).....	54
Fig. 30 - Comparison of the evolution of the pressure force applied on the left-side of the wedge between VoF, ISPH-USAW and WCSPH-USAW (from Leroy, 2014; $t+= tgH$).....	55
Fig. 31 - Spillway of Goulours dam from the physical model (left) and the numerical model (right) (from Lee <i>et al.</i> , 2009).	55
Fig. 32 - Physical model testing on the left and computed flow field on the right (from Saunders <i>et al.</i> , 2014).	57
Fig. 33 - Percentage difference in simulated reservoir water depth for different SPH resolutions at a discharge rate of 35.86 L/s (from Saunders <i>et al.</i> , 2014).....	58
Fig. 34 - Dissipation basin of the Villar del Rey dam: numerical model (a) and (c), the physical model (b) and prototype (d) (from López, 2013).	60
Fig. 35 – SPH vs. prototype pressure records for the Villar del Rey dam (adapted from López <i>et al.</i> , 2010a).	60
Fig. 36 - SPH model of the Alarcón dam. Plot according to particles velocity magnitude (blue – 0 m/s to red – 20 m/s) (from Rebollo <i>et al.</i> , 2010).	61
Fig. 37 - Calanda dam spillway study: (a) Physical and SPH model of the morning glory spillway (López, 2013); (b) comparison between experimental and SPH discharge rating curves for the morning glory labyrinth spillway solutions (López, 2013); and (c) physical and SPH models of the labyrinth spillway solution (adapted from López <i>et al.</i> , 2015).....	62

Fig. 38 – Nagore dam study: numerical model on the left and comparison between experimental and computed discharges on the right (from López <i>et al.</i> , 2016).....	62
Fig. 39 - Work flow.	68

CHAPTER 4 - DEVELOPMENT OF SPH APPLICATIONS

Fig. 40 – Exemplification sketch of the <i>testTriangle</i> algorithm. The triangular mesh represents the generated mesh used for the boundary particles positioning; the blue particles represent the boundary particles; and the red particles represent the fluid particles, initially placed on a cartesian grid.	69
Fig. 41 - Overhead view of Crestuma dam (© IPTM, F. Piqueiro /Foto Engenho).	69
Fig. 42 – Crestuma dam: (a) profile along the dam axis on top; (b) cut view (along the flow direction); and (c) gates’ definition (from PNCOLD, 1992 and LNEC, 1985).....	71
Fig. 43 - Crestuma dam physical model – plant view (Lopes <i>et al.</i> , 2006).	72
Fig. 44 - Location of the measured profiles (adapted from Lopes <i>et al.</i> , 2006).	72
Fig. 45 - Experimental facility by Lopes (2005): (a) upper gate; (b) physical mode in the water channel; (c) measuring equipment (LDA); and (d) physical model testing for an over gate discharge of 11.5 L/s/m . All photographs from Lopes (2005).	73
Fig. 46 - Numerical model’s geometry for the simulation of the over gate flow in the Crestuma dam..	74
Fig. 47 - Flow visualization within the first 6 s of simulation. SPH particles coloured by their flow velocity in m/s.	76
Fig. 48 - Number of fluid particles in the computational domain over the simulation time and corresponding percentage variation.	77
Fig. 49 - Particle leakage issue near/in the downstream open boundary.	77
Fig. 50 - Simulated velocity field in the Crestuma dam (in m/s).....	77
Fig. 51 - Crestuma dam simulation with GPUSPH. Computed turbulent kinetic energy, k (in m^2/s^2): side view at half channel width (on the left) and top view (on the right).	78
Fig. 52 - Details of the flow upstream of the gates for an overgate discharge from Lopes (2005) on the left and from the SPH model on the right.	78
Fig. 53 - Computed vs. experimental free-surfaces profile. The experimental free-surface profile was digitized from Fig. 7.3 of Lopes (2005) work.	80
Fig. 54 – Comparison between the computed trajectory and that obtained with Eq. (38)	80
Fig. 55 - Computed (black line) vs. experimental (red circles) velocity profiles in sections: (a) P-1; (b) P0; and (c) P1. The experimental data was obtained through digitalization of Fig. 7.4 from Lopes (2005) work.	80
Fig. 56 - Computed (black line) vs. experimental (red circles) velocity profiles in sections: (a) P2; (b) P3; and (c) P4. Experimental data was obtained through digitalization of Fig. 7.4 from Lopes (2005) work.	81
Fig. 57 - Computed (black line) vs. experimental (red circles) velocity profiles in sections: (a) P5; (b) P6; and (c) P7. Experimental data was obtained through digitalization of Fig. 7.4 from Lopes (2005) work.	81

Fig. 58 - Computed (black line) vs. experimental (red circles) velocity profiles in sections: (a) P10; and (b) P15. Experimental data was obtained through digitalization of Fig. 7.4 from Lopes (2005) work...	81
Fig. 59 - Computed vs. experimental U_{max} , U_{mean} , H and h' . The dashed lines represent the bounds for a relative error of 15%. The experimental data was obtained from Table B.1 of Lopes (2005) work.	82
Fig. 60 - U_{max} , U_{mean} , H and h' errors' statistical distribution.....	82
Fig. 61 – Model scheme of an under-gate discharge simulation using a periodic boundary condition. 11 million SPH particles.	83
Fig. 62 - Caniçada dam (downstream view).....	84
Fig. 63 – New spillway of the Caniçada dam: (a) schematic location with respect to the dam body (from Brandão, 2015); (b) downstream view of the new spillway's outlet; (c) up and downstream view of the new spillway' s intake; and (d) upstream view of reservoir and new spillway's intake. Photographs of the engineering works obtained from https://afaplan.com/projeto	85
Fig. 64 - Downstream view of the physical model (Brandão, 2015).....	87
Fig. 65 - Measurement points and sections location.....	88
Fig. 66 - Numerical model's geometry: (a) upstream reservoir; (b) spillway's intake; (c) ski jump structure; and (d) general view.....	90
Fig. 67 - Caniçada dam: (a) numerical velocity flow field (in m/s), obtained with GPUSPH (GPUSPH), for the flow rate 890 m ³ /s; (b) physical model being tested.	92
Fig. 68 - Computed vs. experimental free-surface elevation, at the spillways' intake, on the right guiding wall (on the left) and on the left guiding wall (on the right), for the design flow rate, Q_{des} . The thick black line schematizes the ogee crest profile.	92
Fig. 69 - Computed vs. experimental free-surface elevation, at the spillways' intake, on the right side of the pier (on the left) and on the left side of the pier (on the right), for the design flow rate, Q_{des} . The thick black line schematizes the ogee crest.	93
Fig. 70 - Flow pattern in the approach channel for the design flow rate.	93
Fig. 71 - Free-surface shape in sections 1 and 2: flow rate 896 m ³ /s - red line; flow rate of 690 m ³ /s - green line; and flow rate of 527m ³ /s – blue line.	94
Fig. 72 - Free-surface shape in sections 3 and 4: flow rate 896 m ³ /s - red line; flow rate of 690 m ³ /s - green line; and flow rate of 527 m ³ /s – blue line.	94
Fig. 73 - Free-surface shape in sections 5 and 6: flow rate 896 m ³ /s - red line; flow rate of 690 m ³ /s - green line; and flow rate of 527 m ³ /s – blue line.	94
Fig. 74 – Free-surface shape in sections 7 and 8: flow rate 896 m ³ /s - red line; flow rate of 690 m ³ /s - green line; and flow rate of 527 m ³ /s – blue line.	95
Fig. 75 – Free-surface shape in sections 9 and 10: flow rate of 896 m ³ /s - red line; flow rate of 690 m ³ /s - green line; and flow rate of 527 m ³ /s – blue line.	95
Fig. 76 - Graphic comparison of the free surface for sections 1 and 2 for the flow rate of 896 m ³ /s: Experimental results - blue line; GPUSPH results - red line.	96
Fig. 77 - Graphic comparison of the free-surface for sections 3 and 4 for the flow rate of 896 m ³ /s: Experimental results - blue line; GPUSPH results - red line.	96

Fig. 78 - Graphic comparison of the free-surface for sections 5 and 6 for the flow rate of 896 m ³ /s: Experimental results - blue line; GPUSPH results - red line.	96
Fig. 79 - Graphic comparison of the free-surface for sections 7 and 8 for the flow rate of 896 m ³ /s: Experimental results - blue line; GPUSPH results - red line.	97
Fig. 80 - Graphic comparison of the free surface for sections 9 and 10 for the flow rate of 896 m ³ /s: Experimental results - blue line; GPUSPH results - red line.	97
Fig. 81 – Numerical cross-waves development in the complementary spillway of the Caniçada dam. Fluid particles coloured by their elevation with respect to the channel bottom, Z , for the design flow rate, Q_{des} (on the left – blue, 5 m, to red, 9m), and the flow rate of 896 m ³ /s, Q_1 (on the left – blue, 2 m, to red, 3.5 m).	98
Fig. 82 - Computed pressure history at P2 (above) and at P3 (below) for the flow rate of 690 m ³ /s....	98
Fig. 83 - Experimental vs. computed pressures, on the spillway bottom, for the flow rate of 2026 m ³ /s, Q_{des}	101
Fig. 84 - Experimental vs. computed pressures, on the spillway walls, for the flow rate of 2026 m ³ /s, Q_{des}	101
Fig. 85 - Experimental vs. computed pressures, on the spillway bottom, for the flow rate of 896 m ³ /s, Q_1	101
Fig. 86 - Experimental vs. computed pressures, on the spillway walls, for the flow rate of 896 m ³ /s, Q_1	102
Fig. 87 - Experimental vs. computed pressures, on the spillway bottom, for the flow rate of 690 m ³ /s, Q_2	102
Fig. 88 - Experimental vs. computed pressures, on the spillway walls, for the flow rate of 690 m ³ /s, Q_2	102
Fig. 89 - Experimental vs. computed pressures, on the spillway bottom, for the flow rate of 527 m ³ /s, Q_3	103
Fig. 90 - Experimental vs. computed pressures, on the spillway walls, for the flow rate of 527 m ³ /s, Q_3	103
Fig. 91 – Fluid particles coloured by their renormalization factor value r, γ , for the flow rate of 890 m ³ /s, Q_1 . (bottom to top view).	103
Fig. 92 - Evolution of the velocity magnitude over time, at sections V1, V2, V3 and V5 for the flow rate of 896 m ³ /s, Q_1	104
Fig. 93 – Normalized upper (above) and lower (below) SPH jet trajectories and corresponding fit to Eq. (41). Comparison with Eq. (41) fitted to the normalized experimental results by Schmocker (2006) and Balestra (2012).	107
Fig. 94 - Comparison between the geometrical take-off angle, α , and the virtual take-off angle α_j obtained for the SPH results (right and left jets, for the design flow rate, Q_{des}). Comparison with the results envelope for the experimental data by Schmocker (2006) and Balestra (2012).	107
Fig. 95 - Jets' configuration for the design flow rate, Q_{des} : horizontal component of velocity, U_x , on the right (blue, 0 m/s, to red, 32 m/s) and vertical component of velocity, U_z , on the left (blue, -20 m/s, to red, 10 m/s).	108

Fig. 96 - Jets' configuration for the flow rate of 896 m ³ /s, Q1: horizontal component of velocity, U_x , on the right (blue, 0 m/s, to red, 32 m/s) and vertical component of velocity, U_z , on the left (blue, -20 m/s, to red, 10 m/s).	108
Fig. 97 - Jets' configuration for the flow rate of 690 m ³ /s, Q2: horizontal component of velocity, U_x , on the right (blue, 0 m/s, to red, 32 m/s) and vertical component of velocity, U_z , on the left (blue, -20 m/s, to red, 10 m/s).	108
Fig. 98 - Jets' configuration for the flow rate of 527 m ³ /s, Q3: horizontal component of velocity, U_x , on the right (blue, 0 m/s, to red, 32 m/s) and vertical component of velocity, U_z , on the left (blue, -20 m/s, to red, 10 m/s).	109
Fig. 99 - Graphic water depths comparison for sections 1, 2, 3, 4, 5, 7, 8 and 9, for the flow rate of 890 m ³ /s, Q1. Blue line: experimental results; red line: GPUSPH results; and black line: FLOW-3D results.	111
Fig. 100 – Illustration of a particle leakage problem in the upstream reservoir.	112
Fig. 101 – Dispersion of results comparison for the bottom channel pressures: (a) GPUSPH vs. experimental results; and (b) Mesh based model (Brandão, 2015) vs. experimental results. The dashed lines represent the bounds for a variation of 2×10^4 Pa.	113
Fig. 102 - Dispersion of results comparison for the wall channel pressures: (a) GPUSPH vs. experimental results; and (b) FLOW-3D (Brandão, 2015) vs. experimental results. The dashed lines represent the bounds for a variation of 2×10^4 Pa.	113
Fig. 103 - Dispersion of results comparison for the flow velocity, in sections V1 to V6, for the flow rates Q_{des} and Q1, for both numerical models. The dashed lines represent the bounds for a relative error of 15%.	114
Fig. 104 - Dispersion of results comparison for the jets' length, for the flow rates Q_{des} , Q1, Q2, and Q3, for both numerical models. The dashed lines represent the bounds for a relative error of 15%.	114
Fig. 105 – (a) Caniçada dam impinging jets (Image from www.meteopt.com , forum (https://www.meteopt.com/forum/topico/seguimento-rios-e-albufeiras-2014.7457/pagina-2)). (b) Bottom outlet jet of the Baixo Sabor dam, Portugal, 2016 (image from https://akisabor.blogspot.com/2014/04/descarga-de-fundo.html)	116
Fig. 106 – Ongoing experiment and side view of the facility assembled at the LCH-EPFL (Bollaert, 2002): 1) cylindrical jet outlet, 2) reinforced plastic cylindrical basin, 3) pre-stressed two-plate steel structure, 4) PC-DAQ and pressure sensors, 5) restitution system, 6) thin steel sheeting pre-stressed between steel structure (defining the form of artificial 1D and 2D joints), 7) pre-stressed steel bars.	118
Fig. 107 - Schematic plot of the three major flow regimes of a vertical plunging jet.	119
Fig. 108 - Flow conditions inside the 0.072 m diameter nozzle, for different particle resolutions: $Ddp=7.7$ on the left, $Ddp=17.2$ in the middle and $Ddp=34.1$ on the right. Plot according to particles' velocity (in m/s).....	120
Fig. 109 - Relative error in the mean exit velocity, U , vs. estimated number of fluid particles in the simulation.	121
Fig. 110 - Comparison between experimental and computed velocity profiles obtained along the nozzle diameter, at the exit section. Experimental profiles were obtained from pressure measurements.	122
Fig. 111 - Evolution of the computed mean pressure at 0.025 m from the stagnation point and corresponding percentage variation, in a 15-s simulation (with $Y/D = 4.2$), sampled at 40 Hz.....	123
Fig. 112 - Evolution of the computed maximum pressures at 0.025, 0.050, 0.075, 0.095, 0.150 and 0.200 m from the stagnation point, in a 15-s simulation (with $Y/D = 4.2$), sampled at 40 Hz.....	124

Fig. 113 – Flow evolution throughout the simulation: shallow pool, $Y/D = 2.8$, on the left and deep pool, $Y/D = 9.3$, on the right. Fluid particles coloured by their velocity magnitude in m/s.....	125
Fig. 114 - Free-surface shape (at a radial plane) for the tested hydrodynamic conditions: (a) $Y/D = 2.8$; (b) $Y/D = 4.2$; (c) $Y/D = 5.6$; (d) $Y/D = 6.9$; (e) $Y/D = 8.3$; and (f) $Y/D = 9.3$. The red particles represent the fluid particles identified as free-surface particles (zero pressure).....	126
Fig. 115 - Free-surface shape in the plunge pool at the end of the simulations: (a) $Y/D = 2.8$; (b) $Y/D = 5.6$; and (c) $Y/D = 8.3$. Plot coloured according to the z-coordinate of the fluid particles	126
Fig. 116 - Velocity field (m/s) for core jet impact conditions ($Y/D = 2.8$, top image) and developed jet impact conditions ($Y/D = 5.6$, bottom image). Black thick lines added in post-processing for clarification of main flow features.	127
Fig. 117 - Fluid particles coloured by their turbulent kinetic energy, k , (m^2/s^2) for different ratios of plunge pool water depth Y to jet diameter D : (a) $Y/D = 2.8$; (b) $Y/D = 4.2$; (c) $Y/D = 5.6$; (d) $Y/D = 6.9$; (e) $Y/D = 8.3$; and (f) $Y/D = 9.3$	128
Fig. 118 - Centreline velocity decay of the tested jets for different Y/D ratios: (a) $Y/D = 2.8$; (b) $Y/D = 5.6$; and (c) $Y/D = 8.3$. The shaded region represents the minimum and maximum bounds either sides of the average profile.....	129
Fig. 119 - Pressure signal in the time domain, computed by SPH under the jet's centreline, at the plunge pool bottom, for $Y/D = 2.8$	130
Fig. 120 - Computed vs. experimental minimum, mean and maximum pressures at 0.025 m from the stagnation point, for various pool depths ratios Y/D , sampled at 40 Hz during a 10-s run. Comparison with experimental minimum, mean and maximum pressures by Manso (2006), sampled at 1 kHz during a 3-min run, for the same hydrodynamic conditions ($U = 29.5$ m/s).	131
Fig. 121 - Computed vs. experimental non-dimensional mean dynamic pressure coefficients, C_p , at 0.025 m from the stagnation point, for various Y/D_j ratios. Comparison with Manso (2006)'s results for equivalent hydrodynamic conditions ($U = 29.5$ m/s) and Ervine <i>et al.</i> (1997)'s best fit of data obtained for circular plunging water jets, sampled at 100-230 Hz during 2-min runs ($U < 25$ m/s).....	132
Fig. 122 - Computed non-dimensional fluctuating dynamic pressure coefficient C_p' at 0.025 m from the stagnation point, for various Y/D_j ratios.. Comparison with the experimental values by Manso (2006), Ervine <i>et al.</i> (1997)'s best fit of data and Bollaert (2002)'s results envelope obtained from circular plunging water jets sampled at 1 kHz during ~1-min runs ($U < 30$ m/s).	133
Fig. 123 - Computed absolute mean pressures (a) and maximum pressures (b) along the plunge pool's radial direction for $Y/D = 2.8$ m. Comparison with the experimental data by Manso (2006) for the equivalent hydrodynamic conditions.	134
Fig. 124 - Experimental vs. computed non-dimensional pressures along the plunge pool's radial direction for $Y/D = 2.8$ m.....	135

CHAPTER 5 - PRACTICAL RECOMMENDATIONS

Fig. 125 - Design and meshing of the Crestuma dam model (a) Geometry model showing the two piers cut (by the gates) in order to get a correct mesh connectivity, without overlapped faces; (b) boundary particles plotted according to its renormalization factor values.....	142
Fig. 126 – Model's geometry and dimensions.....	145
Fig. 127 - GPUSPH directory tree. For simplicity not all of the folders and files in the GPUSPH directory are represented.	146

Fig. 128 - Schematic 3-D flow over an ogee spillway. Shape of the free-surface and velocity field obtained with GPUSPH within the first 5 s of simulation..... 147

LIST OF TABLES

CHAPTER 2 - GENERAL BACKGROUND TO THE TOPIC

Table 1. Evolution of the total installed hydropower capacity (in MW) in European Union countries from 2008 to 2017 (IRENA, 2018).....	7
Table 2. Examples of international dam disasters causing loss of life (Williamson, 2017).....	23
Table 3. Timeline of the Oroville incident events.	25
Table 4 – Literature search on the ASCE publication database for “CFD” on the Journal of Hydraulic Engineering till the end of 2018.....	27
Table 5 - Some typical meshfree methods in chronological order (refer to Liu and Liu, 2003).	29
Table 6 - Main elements of a CFD code and corresponding features.	31
Table 7 – Common turbulence models.	32

CHAPTER 3 - SMOOTHED PARTICLE HYDRODYNAMICS

Table 8 - Summary of some SPH models’ setup characteristics and quantitative validations carried out.	63
------------------------------------------------------------------------------------------------------------	----

CHAPTER 4 - DEVELOPMENT OF SPH APPLICATIONS

Table 9 – Resume of some of the case studies’ characteristics.....	66
Table 10 – Main characteristics of the Nvidia GPU processors used in the present work.	68
Table 11 – Crestuma dam characteristics.....	70
Table 12 - Main flow characteristics applied in the experiments (in model dimensions).	72
Table 13 - Caniçada dam characteristics.....	86
Table 14. Hydrodynamic conditions tested and respective gate openings.....	87
Table 15 – GPUSPH simulations’ characteristics.	89
Table 16 – Computed pressures for the measuring points in the channel bottom.	99
Table 17 - Computed pressures for the measuring points in the lateral channel walls.	100
Table 18 – Comparison of the velocity magnitude, U , at sections V1, V3, V5 and V6 for the design flow rate, Q_{des}	104
Table 19 – Comparison of the velocity magnitude in sections V1 to V6 for the flow rate of $896 \text{ m}^3/\text{s}$, Q_1	105
Table 20 – Computed vs. experimental jets’ length.	109
Table 21 - GPUSPH vs. FLOW-3D models’ characteristics.	110
Table 22 - Characteristics of some experimental studies on jets.....	117

Table 23 - Numerical simulations characteristics 124

CHAPTER 5 - PRACTICAL RECOMMENDATIONS

Table 24 - Summary of some flow characteristics in common spillway schemes^a. 138

INTRODUCTION

1.1. CONTEXT AND AIM OF THE WORK

Dams control the flow of fresh water to improve and simplify one's lives in many ways, but they also pose an inherent and inevitable threat to the environment and public safety, because, when dams (or even its spillway structure) fail, they often do it catastrophically, due to the large amount of potential energy involved. Since the construction of the first dams, incidents due to unpredictable environmental conditions, poor engineering, or improper management have occurred. Given the diversity of existing variables, recognizing the reason behind dam incidents is a challenging task. The International Commission on Large Dams (ICOLD) has reported statistics of dam failures (ICOLD, 1995) and the United States Committee on Large Dams (USCOLD) has made a survey of incidents, including failures and accidents, to dams in the United States (USCOLD, 1988). Many researchers also conducted analyses of dam failures using statistical methods (e.g., Howard, 1982; Von Thu, 1985 and Foster *et al.*, 2000). The many records documenting case histories of dam incidents have led to improved guidance and technical understanding, and ultimately to safer and optimised dams. By understanding how incidents arise, hazards' vulnerability can be reduced and ultimately countermeasures can be rapidly implemented in sudden or unexpected incidents. ICOLD (1995) found evidence that the percentage of dam failures fell significantly, with less than 0.5% of failures occurring of the 12 138 large dams built between 1951 and 1986. However, that was still 59 failures around the world.

In recent years, dam safety has drawn increasing attention from experts and the public in general. This is mostly because minor to significant incidents still happen in the twentieth-first century, of such, the Oroville dam spillway is probably the most remarkable recent one¹. It has brought renewed attention not only to potential failure modes associated with both concrete and unlined spillways at dams (but also to their current state of conservation, which may lead to operational malfunctions. Although the safety of a dam is evaluated thoroughly, spillways often receive less attention than other features. This fact is even more remarkable for complementary spillways, for which the safety guidelines are far less rigid. Climate change, ageing dams and deterioration are as well long-term concerns for improving dam safety. As a result, there is a growing need to raise awareness regarding safety issues associated with developing conditions that could result in a spillway failure or malfunction during a flood.

Advances witnessed in the monitoring equipment technology allow engineers to monitor the performance of dams and spillways under construction and in service with better reliability and accuracy. However, the majority of dams around the world are old and have little monitoring

¹ This and other spillway incidents (and frequent incident causes) are addressed posteriorly in section "2.2.4. Dam failures and incidents"

INTRODUCTION

instrumentation, unless specific problems have occurred before. Engineering simulation is a powerful tool that can be used upon dam safety. It is one of the strongest growing fields in the engineering practice and it has become central in industrial design and analysis process over the last decades. The hydraulics engineering area has naturally evolved into an adaptation to this computational revolution, which resulted in the creation of the Computational Fluid Dynamics (CFD) branch of Fluid Mechanics. Its current state-of-knowledge is reaching its full promise as a general tool for engineering design and simulation. With the growing need for fresh water supply, hydropower, flood mitigation, industry and agriculture, dams will continue to be built and raised in height and given the advantages of CFD models (e.g. versatility, low-costs and time-saving) it is anticipated that these will have a role on the future development of the hydropower sector.

Engineering simulation has been applied to study the behaviour of various components of hydropower plants, e.g., turbines (Souari and Hassairi, 2013), the effect of surge tanks (Riasi *et al.*, 2010) or spillways (Moreira and Taveira-Pinto, 2017a, 2017b). Hydropower CFD developers keep evolving CFD models' capabilities for a range of applications, including spillway design, namely for confirmation of spillway discharges estimates, pressures verification, assessment flow features around obstacles such as piers, refinement of the powerhouse intake design, among others. To keep developing the links between CFD tools and dam hydraulics engineering, further research is needed. In this thesis, attention is turned to spillways and energy dissipators, as components of a hydropower plant. The development of expedite methodologies to seek solutions of optimum and safer spillway performance in time, was identified as a priority for future research, as explained above. Functional problems in dams are as diverse as: spillway chute overtopping; potential for spillway failure (e.g. due to cavitation resulting from high velocity discharges over open offset joints and/or negative pressures); spillway gate failure; and foundation failure from scour erosion. Current solutions for some of these problems include raising the dam crest (to increase flood storage), the modification of the existing spillway or even the construction of a new complementary one (to increase discharge capacity). Such adaptations require the completion of complex studies to support an ultimate decision. Engineering simulation will be routinely used in the future, as computational power can only increase from then on and CFD codes are becoming more efficient and realistic.

Most of the research done so far on the use of CFD models to assess spillway and energy dissipators performance or design employed mesh-based models. These have demonstrated to produce accurate results with regard to the most common issues in spillway design and safety assessment. Less attention has been given to meshfree methods, nevertheless they are particularly suited to model turbulent flows with significant free-surface distortions and fragmentations, such as those encountered in spillways. These flow characteristics may difficult the performance of the traditional mesh-based numerical methods. The Smoothed Particle Hydrodynamics method (SPH) is a meshfree, Lagrangian method, that has witnessed relevant developments in the last decade with respect to its application to simulate free-surface flows, yet, the lack of consistent theory (e.g. with relation to boundary conditions implementation and density correction) and quantitative validation on large-scale applications, along with high computational times, still hamper its application by the industry and water companies.

This thesis summarizes the motivation, challenges and results of the author's research contribution to the exploitation of the SPH method capabilities to predict the flow features in spillways and energy dissipators. The maturity of the current state-of-knowledge of this method, together with the advent of the Compute Unified Device Architecture (CUDA) programming language from Nvidia in 2007 (simple C++ language can be used to access the mathematical power of the massively parallel cards), make it an interesting matter of research within the scope of large-scale spillway applications. Most of the studies performed within this engineering matter refer to quite simplified hydraulic systems or, when a

rather complex hydraulic system was analysed, there was poor quantitative validation. In this research, real dam spillways were selected as case studies to develop SPH models. These correspond to two dams located in the North of Portugal, specifically the Crestuma and the Caniçada dams. The distinct characteristics of the hydraulic schemes allowed to analyse the SPH performance upon different flow features such as those existents in hydraulic jumps and chute flows. The diffusion and hydrodynamic loading produced by impinging jets on a flat bottom (a common energy dissipation method in dams) was also investigated through the development of a third SPH model, which is based on the experimental setup by Manso (2006). The numerical models were developed within the framework of the SPH free-access code GPUSPH, having been established a fruitful collaboration with the GPUSPH code developers.

The research motivation is based on the belief that overcoming the lack of quantitative validation and evaluate the hydraulic phenomena that the current state-of-knowledge of the method can well/badly reproduce are key to contribute to the continuous verification and validation of the SPH codes, as well as direct the future research needs in terms of new numerical formulations. Indeed, the knowledge exchange between code developers and the hydraulic engineers (potential users), is essential as the former may be aware of the industry needs, and the latter may, in turn, be taught about the possibilities and limitations of the method. The present work is a contribution to that knowledge. It will not cover all of the open issues but rather focus on a main objective with implications for practice, which relates to challenging applications and good practices for the integration of well-validated SPH codes into design methodologies. From this point of view, a final objective of summing up a set of recommendations for the application of SPH models in the engineering matter of dam spillways was completed.

1.2. THESIS OUTLINE

This thesis summarizes the author's research work on the development of SPH applications in dam spillway systems and energy dissipators, carried out at the Hydraulics, Water Resources and Environment Division (SHRHA) of the Department of Civil Engineering (DEC) of the Faculty of Engineering of the University of Porto (FEUP). The main text of the thesis is divided into six chapters. These are relatively self-contained and can be read independently. Each chapter covers the following aspects:

Chapter 1 constitutes the present chapter, which introduces the topic under investigation, showing its relevance to the state-of-the-art knowledge and to practice. It explains the author's motivation laying on the choice of the research theme, the methodology to achieve the scientific objective, and the structure of the contents.

Chapter 2 introduces the general background to the topic. The chapter's content is divided into three sections which are intended to provide the basic knowledge about the research theme. The first section draws the big picture in the hydropower sector as it is the major driving force behind the construction and upgrade of spillways and energy dissipators. The second section gives a brief overview of the different types of dam spillways and energy dissipators schemes, the characteristics of spillway flows, and the most common spillway failure modes and incidents that occurred world-wide. The third section provides background knowledge on numerical simulation, namely the characteristics of mesh-based and meshfree numerical methods and the governing equations that describe the fluid dynamics.

Chapter 3 is a literature review concerning the SPH method and it is structured in nine sections, being the first and the ninth an introduction and a conclusion, accordingly. Section 2 presents the fundamentals of the SPH method, namely the integral representation and particle approximation and its

INTRODUCTION

implementation on the Navier-Stokes equations. Sections 3 to 7 are devoted to a brief review of the most recent techniques for density correction, boundary conditions implementation, turbulence and multiphase modelling and parallel computing in SPH. In the eighth section, a literature review of the most relevant works performed with SPH in the field of free-surface and spillway flows is presented.

Chapter 4 describes the development of the SPH model applications and the results' analysis for the targeted case studies. It is structured in 6 sections being the first and the sixth an introduction and a conclusion, accordingly. Sections 2 to 5 describe the GPUSPH code employed and the process of the numerical models' development and validation, separately for each of the three case studies addressed, which are the Crestuma dam, the Caniçada dam and the plunge pool, respectively.

Chapter 5 consists of a set of practical recommendations for the application of SPH models to simulate the flow behaviour in spillways and energy dissipators. It summarises the empirical knowledge accomplished with the completion of the numerical modelling described in the previous chapter. It also presents a spillway case example included in GPUSPH for potential users.

Chapter 6 gives a general overview of the most important conclusions derived from the research carried out and points out possible future developments.

GENERAL BACKGROUND TO THE TOPIC

2.1. HYDROPOWER DAMS AROUND THE WORLD

Hydropower is the most widely used type of renewable energy source, being a mature and cost-competitive technology. Because the source of hydroelectric power is water, hydropower plants are usually located on a water course, falling into one of the following four categories: run-of-the-river power plants, storage power plants, pumped storage power plants and, still less conventionally, power plants for exploiting marine energy. Run-of-the-river power plants are the most common category world-wide. These use the flow energy in a river and are normally used to cover the base-load power (the minimum level of demand on an electrical grid over 24h). Storage power plants store the water in a reservoir and feed it via pipelines into a lower-lying power plant (Fig. 1). Such hydropower plants can operate independently of the natural water inflow and are particularly suited to balance fluctuations in regional and national electricity generation and consumption. They are used both to cover the electrical base and peak-loads. A pumped storage power plant uses two reservoirs to store water, with the greatest possible height difference between them. During off-peak periods, e.g., at night or when there is a large amount of solar or wind energy in the electrical grid, water is pumped from the lower to the upper reservoir.

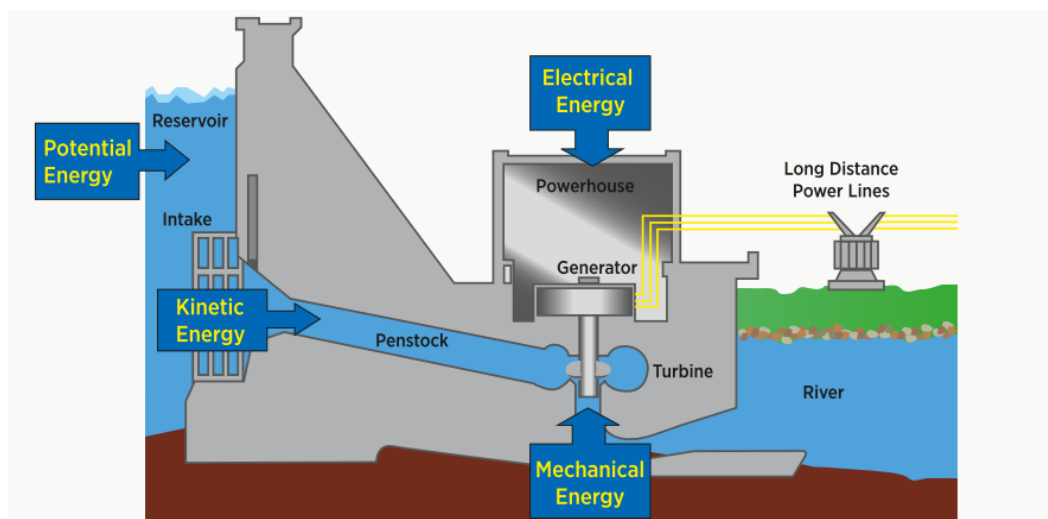


Fig. 1. Typical "low head" hydropower plant with storage (picture from Dolf, 2012, adapted from Hydropower News and Information - <http://www.alternative-energy-news.info/technology/hydro/>).

There, it exists once again available water for electricity generation at peak-load times. The kinetic energy of waves, tidal range and tidal flow can also be used to generate electricity. One advantage of using marine energy is the uniform energy supply and the ensuing balancing effect on the renewable energy mix.

Owing to the characteristics described, hydropower is the most flexible source of power generation available, as it can respond to demand fluctuations in minutes, delivering base-load power and, when a reservoir is present, storing electricity over weeks, months, seasons or even years (Brown *et al.*, 2011 and IPCC, 2011). Despite promising developments in other energy storage technologies, hydropower is still the only technology offering economically viable large-scale storage (Dolf, 2012). This capability of stabilising fluctuations between demand and supply is a feature that will be even more valuable in the future, as more extreme weather-related events are expected.

According to Dolf (2012), more than 25 countries in the world depend on hydropower for 90 % of their electricity supply, and 12 countries are 100 % reliant on hydropower. Hydropower produces the bulk of electricity in 65 countries and plays role in more than 150 countries. According to IRENA (2018), in 2017 the global installed hydropower capacity reached approximately 1270 GW (58% of the global installed capacity of all forms of renewable energy). The top countries for hydropower capacity are China, Brazil, the United States, Canada, the Russian Federation, India and Norway, which together accounted for about 60% of global installed capacity at the end of 2017. Europe represents a 17% share of the global installed capacity and Africa remains the region with the lowest ratio of deployment-to-potential, where the opportunities for growth are very large (corresponding to a 2.8% share).

In March 2007, the European Union leaders signed a proposal designed to cut greenhouse gas emissions by 20% (compared with 1990 levels). To achieve this, the member countries must increase their share of energy production through renewable sources like hydro, wave, solar, wind and biomass to approximately 50%, in 2020. This mandate translates to significant growth in development of new capacity and in upgrading of existing dams throughout Europe. National authorities are making efforts in this direction, which has been reflecting on the installed hydropower capacity on European Union member countries (Table 1).

DNV GL (2015) presents a macroeconomic evaluation of the hydropower sector in Europe, which stresses the role of hydropower in Europe's economy in several ways, pointing out some figures, such as:

- The total value creation of hydropower in Europe is approximately 38 billion of euros (2015 data), which may grow to 75 to 90 billion of euros by 2030. The hydropower sector makes then an important contribution to the European economy, which is similar to the gross domestic product of Slovenia;
- Presently, European hydropower generation and manufacturing companies invest an average of 8 to 12 billion of euros per year. Projected investments in the European hydropower sector may reach up to 180 billion of euros by 2030 but may be lower due to deteriorating conditions of the hydropower schemes, by virtue of their longevity, which exceeds that of any other type of energy generation; and
- Directly and indirectly, European hydropower ensures more than 100 000 jobs, which is comparable to the European aluminium industry.

Even if figures preview that the hydropower sector will continue to thrive in the future, it is anticipated that scientific research will play a part on its development in the followings decades. That is because new concerns are arising. On the topic of the day are the increasingly strict environmental constraints.

GENERAL BACKGROUND TO THE TOPIC

Table 1. Evolution of the total installed hydropower capacity (in MW) in European Union countries from 2008 to 2017 (IRENA, 2018).

Country	2008	2017
Austria	12263	14125
Belgium	1418	1425
Bulgaria	2984	3224
Czech Republic	2176	2262
Denmark	9	9
Estonia	5	6
Finland	3122	3285
France	25120	25520
Germany	10805	11307
Greece	3170	3394
Hungary	51	57
Ireland	526	529
Italy	21276	22393
Latvia	1536	1565
Lithuania	875	877
Luxembourg	1134	1330
The Netherlands	37	37
Poland	2335	2382
Portugal	5058	7221
Romania	6362	6754
Slovakia	2548	2487
Slovenia	1027	1338
Spain	18450	20034
Sweden	16437	16493
United Kingdom	4364	4611

Even if hydropower energy production is clean (it produces no greenhouse gases, toxic waste and particulate matter), it can affect the environment, namely fish. Still, the potential damage of global climate change, enhanced by the fossil fuels consumption, drastically outweighs the local consequences of hydropower. In the future, governments will further dedicate to address environmental issues, before considering the development of the new hydroelectric power plants. In fact, fish-friendly dams are being implemented incrementally to avoid damage to local fisheries (e.g. the Rock Island hydropower plant, located in the USA, had its five Kaplan turbines rehabilitated in 2006 giving special attention to the fish-friendliness of their design). In addition, hydropower projects are capital intensive and an expensive luxury many countries in the developing world cannot afford. Innovations in technology and extensive investigation (e.g. through experiments and computational simulations) before their implementation should make projects in the future more cost-friendly, allowing the exploitation of this renewable energy source in locations such as Africa. The rehabilitation and repair of the existing range of dams built nearly

GENERAL BACKGROUND TO THE TOPIC

a century ago equally poses new challenges to engineering whose response should be rapid and cost-performant.

In Portugal, the current installed hydropower capacity is about 7 GW, which corresponds to about 43 + 110 hydropower plants (large-scale and medium-to-small scale, accordingly) (Costa, 2016). In 2016 and 2017, the electricity production derived from hydropower plants in Portugal was approximately 28% and 10%, respectively (Fig. 2). The hydropower potential exploited in 2016 was approximately 67% of the total theoretical potential, which considering environmental constraints can be reduced to 60%. This percentage is still far from that achieved by many other European countries (Fig. 3). Nowadays, the investments made in hydropower in Portugal are narrow, almost ten times lower than those made in the 80s (Cardoso *et al.*, 2013).

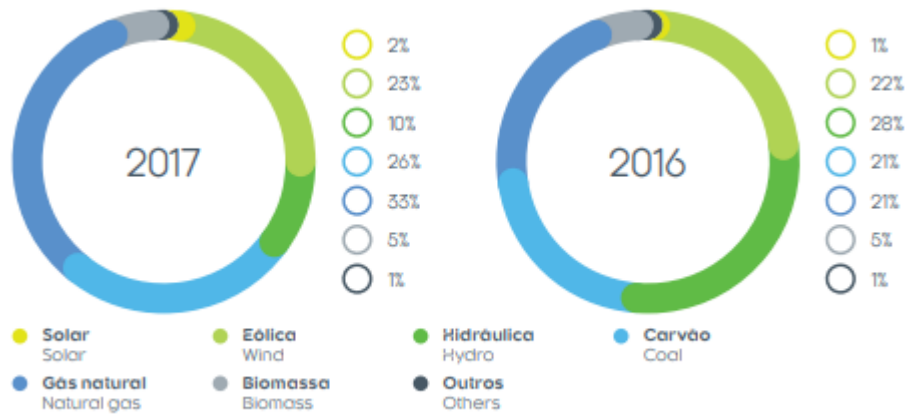


Fig. 2 - Distribution of sources in electricity production, in Portugal, in 2016 and 2017 (REN, 2017).

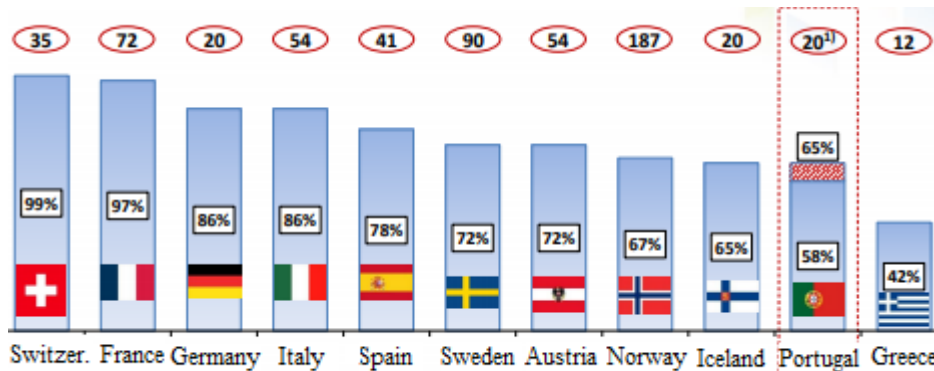


Fig. 3 - Theoretical and harnessed potential in Portugal and other European countries (Mendes, 2017).

To improve and develop the hydropower system in Portugal, the National Program of Hydropower Plants with High Hydroelectric Potential (PNBEPH) was created in 2007 and the new dams were constructed such as the Baixo Sabor or the Ribeiradio-Ermida dams. Climate risk and growing shares of variable renewable power are driving further adaptation in the hydropower industry. Modernisation, retrofits and expansion of existing facilities continued in many markets to improve efficiency, flexibility and system resilience (REN21, 2016). Engineers should be prepared to answer these new challenges, making use of the cutting-edge computational tools available today.

2.2. DAM SPILLWAYS

2.2.1. HYDRAULIC SCHEMES

A dam is as a large structure built across a valley to store water in the upstream area. The reservoir created by a dam not only dampens floods but also provides water for activities such as irrigation, human consumption, industrial use and electricity production. Over than forty-two thousand large dams have been built worldwide, and hundreds of thousands of smaller ones, which have made possible a rational use of a certain amount of river water – the most important water resource for human life and activity (Tanchev, 2005).

Because of this, considerable attention has been given towards theoretical research relating to dams over the past decades. ICOLD divided dams into two main groups based on the construction characteristics (e.g. the construction materials and the design solutions), which are embankment dams and concrete dams. The first are built with clay and/or rock and resist the water pressure by their weight. If the material is not inherently water tight, they are covered with an impervious material or have a watertight core. The latter can be: gravity dams, when they resist against water pressure by their weight; buttress dams, when the water load is transmitted to triangular buttresses parallel to the direction of river flow; arch dams, when the dam transmits most of the water load into the valley sides or large concrete thrust blocks; and multiple arch dams, when there is a number of small arches bearing on buttresses. Gravity dams are the most widespread type of concrete dams, accounting for two thirds of the total (Wrachien and Mambretti, 2009).

Spillways are structures used for controlled release of water stored upstream of a dam into a downstream area, typically the river that was dammed. Their design seeks to provide a safe and adequate release of water, at the lowest combined cost of the spillway and dam. Although a spillway is designed for specific conditions, that is, the design flow rate, Q_{des} and the design hydraulic head, H_{des} , it must operate safely and efficiently for a range of operating flow conditions (from $0.1 Q_{des}$ to Q_{des}) and for emergency situations (i.e. $Q > Q_{des}$) (Chanson, 1999). Flood waters can be discharged beneath the dam (e.g. culvert, bottom outlet), through the dam (e.g. rockfill dam) or above the dam (i.e. overflow spillway) (Chanson, 1999). Where large reservoir storage is provided, or where large outlet or diversion capacity is available, the spillway will be utilized infrequently. In contrast, when the storage capacity is almost null, the spillway is in almost continuous operation. A good performance of the spillway is achieved when the crest design maximizes the discharge capacity of the spillway, the chute passes the flood waters safely and the energy dissipator allows dissipation of the kinetic energy to a level compatible with the stability of the river foundation downstream.

Spillway flows can be classified as controlled or uncontrolled (Ghosh, 1999; Khatsuria, 2005). A controlled spillway is provided with gates which can be raised or lowered to regulate the mass flow rate. This solution allows nearly the full height of the dam to be used for water storage, and flood waters can be released as required by opening one or more gates. In contrast, an uncontrolled spillway does not have gates. When the water level rises above the crest of the spillway it begins to be released from the reservoir. In such case, the rate of discharge is controlled only by the water depth in the reservoir.

The storage volume in the reservoir, above the spillway crest, can only be used for the temporary storage of floodwater, it cannot be used as water supply storage because it is normally empty. Free overflow spillway crests offer some advantages over gated control structures, by virtue of their simplicity, freedom from operating mechanism, and independence from operating personnel (Jansen, 1988). The United States Army Corps of Engineers (USACE) procedure for selection of controlled or uncontrolled spillway crests includes determination of the time of concentration for the basin runoff to reach the reservoir. If it is less than 12h, a controlled crest is required. If it is between 12 and 24h, preference

should be given to the uncontrolled crest. Spillways can also be classified according to their most prominent feature (Ghosh, 1999; Jansen, 1988; Jordaan and Bell, 2009; Khatsuria, 2005), either as it pertains to the control, to the discharge channel, or to some other component. The most common types of spillway are the following:

- Free overfall Spillway;
- Overflow Spillway;
- Tunnel (conduit) spillway;
- Shaft spillway;
- Siphon spillway;
- Bottom outlets (middle to low elevation); and
- Stepped spillway.

In a free overfall spillway, the water freely drops down from the crest of the dam. A vertical sharp-crested weir, characterized by a thin sharp-edged crest, is an example of this spillway type. The use of free overfall spillways requires for a riverbed of high-quality rock, which can withstand the erosive power of the falling water. Normally, a stilling basin made of concrete is built to assure the integrity of the riverbed through the operation time of the dam, and not infrequently, riverbanks are protected as well against erosion. Fig. 4 shows the free overfall waters of the multi-arch Wagendrift dam located in South Africa, completed in 1963.

The overflow type spillway has a crest shaped in form of an ogee. It typically includes three sections: a crest, a chute and an energy dissipator at the downstream end. It can be located over the dam body (frontal spillway), or along a dam abutment (side channel spillway). The crest shape of the overflow spillway is designed according to the shape of the lower nappe of a free overfall spillway, conveying the discharge flood.

Several ogee crest profiles were developed, of which the following are examples: Creager (1917) profile; Scimemi (1930) profile (also called WES profile); Hager (1991); and Montes (1992). The most usual profiles are the Creager profile and the WES profile (Chanson, 1999). The Creager design is a mathematical extension of the original data of Bazin in 1886-88 (Creager, 1917). The WES-standard ogee shape is based upon detailed observations of the lower nape of sharp-crested weir flows (Scimemi, 1930). The behaviour of water discharging over ogee spillways has been extensively investigated by USACE-WES (1952) since the early 1950s. A manual by USACE (1995) is available for engineers to design a spillway profile for given design flood conditions. Fig. 5 and Fig. 6 show the frontal and side channel overflow spillways of the Picote and Vermiosa dams, accordingly, both located in Portugal.

Where a closed channel is used to convey the discharge of a dam, the spillway is often called a tunnel or conduit spillway. Most forms of control structures, including overflow crests, can be used with tunnel spillways. These spillways are advantageous for dam sites in narrow gorges with steep abutments or at sites where there is danger to open channels from rockslides from the hills or even snow (Khatsuria, 2005).

The shaft type spillway was developed in the 1930s and has proved to be especially economical, provided the diversion tunnel can be used as a tailrace (Vischer and Hager, 1998). These uncontrolled spillway devices are also called morning glory or bell-mouth spillways.

GENERAL BACKGROUND TO THE TOPIC



Fig. 4 - Downstream view of the 40m-high Wagendrift dam, Estcourt, South Africa, 1963 (photo credit: Neil Overy).

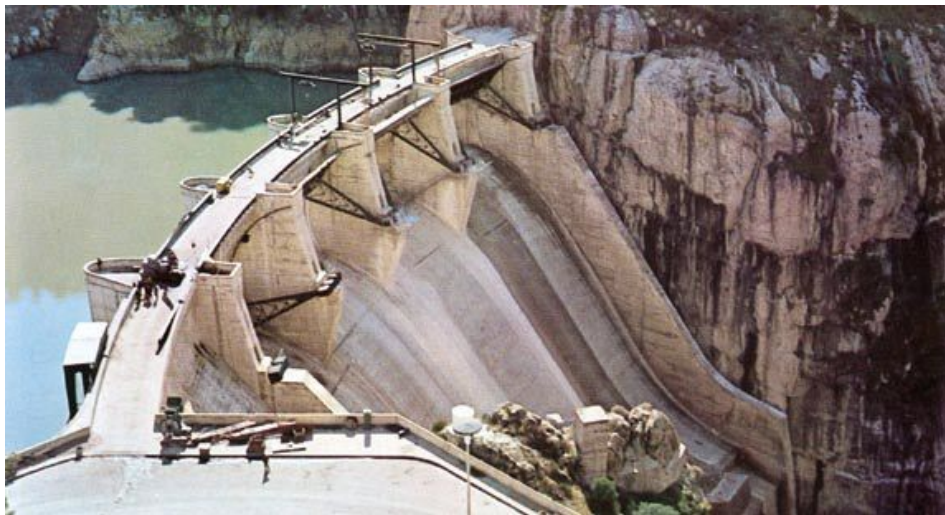


Fig. 5 - Overflow spillway of Picote dam, located at Miranda do Douro, Portugal, 1958 (web 3 Nov 2016 www.ordemengenharios.pt).



Fig. 6 - Chute spillway of the Vermiosa dam on the right hillside, Guarda, Portugal, 1999 (web 3 Nov 2016 www.mota-engil.pt).

GENERAL BACKGROUND TO THE TOPIC

The structure consists of an intake, a vertical shaft with a 90 degrees bend, and the almost horizontal spillway tunnel. For flood safety, only free surface flow occurs in the entire structure. The aeration of a shaft is an important concept in the design of this overflow structure in order to inhibit possible vibrations, cavitation and air backflow. The Chaffey dam, located near Tamworth, New South Wales in Australia is a classic example of this spillway type (Fig. 7).

Siphon spillway structures fall within the series of spillway structures with automatic action and they operate as uncontrolled structures (Tanchev, 2005). A siphon spillway is a closed conduit system, with the shape of an inverted U, positioned so that the bend of the upper passage way is at normal reservoir storage level. Owing to the high-head under which it operates, there is a danger of occurrence of cavitation. As a result, a short aeration pipe as an air vent should be included. Both Head (1975) and Irvine and Oliver (1980) have provided detailed design guidelines on this spillway type.

In bottom outlets the intake of the structure is constructed at a middle to low level. These might work either pressurized or free flowing over some parts of the system, depending on the position of outflow against the tailwater level, and type and location of the control structure (gates).



Fig. 7 - Shaft spillway intake of the Chaffey dam, located at New South Wales, Australia, 1979, (photo credit: Brad Sherman).

The objective is to enhance jets dissipation in the air before it strikes the river bed. To do so, multiple jets can be used, and energy dissipation can be increased by their collision. The number, size and elevation of bottom outlets are governed by the discharge, the operating head and the conditions to be obtained downstream (Khatsuria, 2005). In the Cahora-Bassa dam eight bottom outlets were provided at the same elevation (Fig. 8).

Stepped spillways have steps on the spillway chute to assist in the dissipation of the kinetic energy of the descending water (Fig. 9). Their advantages include ease of construction and reduction of the stilling basin dimensions. Optimization of stepped spillways design involve the definition of the steps' height and width or the number of steps. Design guidelines have been presented, among others, by Chanson (2002), Gonzalez and Chanson (2007), and Felder and Chanson (2016).

GENERAL BACKGROUND TO THE TOPIC



Fig. 8 - Outlet of the Cahora-Bassa dam, located in Mozambique, 1974, (web 11 Dez 2018 <https://macaclub.com.mo>).



Fig. 9 – Stepped spillway of the Hinze dam, South East Queensland, Australia 1976, (copyright ©Hubert Chanson 2014).

2.2.2. ENERGY DISSIPATORS

Water flowing over a spillway has a very high kinetic energy because of the conversion of the potential energy into kinetic energy. An energy dissipator is any device designed to protect downstream areas from erosion by reducing the velocity of the flow to an acceptable limit (Panwar and Tiwari, 2014). Dissipation of energy is mainly owned to internal friction and turbulence, jet diffusion or impact of the high velocity flow with a mass of water. The magnitude of energy dissipated at high dams with large spillway discharges is enormous. Energy dissipation of flood discharges is an essential issue that must be carefully assessed during the design stage of a dam. It is achieved usually by: a standard stilling basin downstream of a steep spillway in which a hydraulic jump is created to dissipate a large amount of flow energy and to convert the flow from supercritical to subcritical conditions; a high velocity water jet taking off from a flip bucket and impinging into a downstream plunge pool or; a plunging jet pool in which the spillway flow impinges and the kinetic energy is dissipated in turbulent recirculation (Chanson, 1999). The factors that govern the choice for the type of dissipator are: hydraulic considerations, topography, geology, type of dam, layout of other associated structures, economic comparison, frequency of usage and environmental considerations (Nigam *et al.*, 2015).

The stilling basin is the most common type of energy dissipator (Bessaih and Rezak, 2002). In a stilling basin, most of the energy is dissipated by means of a hydraulic jump, sometimes assisted by appurtenances, such as, steps, baffles or blocks (refer to Fig. 9), which aid in the stabilization of the jump, decreasing its length and increasing the energy dissipation. Several standardized designs of stilling basins were developed in the 1950s and 1960s, by USBR, USACE and the Saint Anthony Falls Hydraulic Laboratory. Particularly, the USBR systematically tested ten different types of stilling basins (USBR, 1958). These basins were tested in models and prototypes over a considerable range of operating flow conditions. According to Chanson (1999), in practice, the following types are highly recommended:

- The USBR Type II basin for large structures and $Fr > 4.5$ (being Fr the Froude number);
- The USBR Type III basin and the Saint Anthony Falls basin, for small structures; and
- The USBR Type IV basin, for oscillating jump flow conditions.

FEMA (2010) compiles a detailed description of the characteristics and recommended field of application of each standardized stilling basin. In practice, design engineers must ensure that a stilling basin can operate safely for a wide range of flow conditions. Damage to the basin and riverbed occurs several times due to (Chanson, 1999): short and/or shallow apron for an optimum hydraulic jump location (i.e. on the basin); poor shape and/or construction of the blocks; flow conditions larger than design flow conditions; unusual overflow during construction periods; and seepage underneath the apron, inadequate drainage and uplift pressure build-up.

Over the past decades, considerable research has been carried out on the hydraulic performance of this type of energy dissipators, in particular, on the effect of baffle blocks on the enhancement of energy dissipation and shortening of the hydraulic jump. Reducing the length of the jump reduces the size and the cost of the stilling basin. Performance of baffle walls and blocks in free hydraulic jumps has been studied by numerous researchers (e.g., Basco and Adams, 1971 and Rajaratnam and Murahari, 1971). As stated by Peterka (1978), changing the shape of the front face of the blocks can induce eddies which will cause additional energy dissipation. Eloubaidy *et al.* (1999) has shown that curved blocks can provide 33% increase in additional kinetic energy dissipation, however, no results regarding the length of the jump were reported. Hager (1996) investigated the performance of counter-current type stilling basin. This device induces additional shear layers considerably decreasing the length of the jump. Bessaih and Rezak (2002), investigated the effect of baffle blocks with a sloping vertical face on the

length of the hydraulic jump. Their study showed that baffle blocks with sloping face are more effective in reducing the length of the jump than a block with a vertical face or a roughened bed, because of the strong vortices generated.

Wu and Rajaratnam (1995) studied submerged flows with baffle walls and observed that the flow could be classified into two regimes. For low submergences, the incoming stream, after impacting the baffle wall, was deflected towards the water surface and a region of circulating flow was established. This type of flow is called the deflected surface jet regime. When the tailwater depth was larger than a certain threshold, the incoming jet was first deflected away from the bed and then impinged on the bed further downstream. This flow regime is called the reattaching wall jet. Tiwari (2013) examined the energy dissipation by varying the gap of baffle wall in the stilling basin to protect the downstream structures from scouring. Experiments were carried out for different Froude numbers, keeping the baffle wall at the same location, and changing the gap underneath the wall, above the basin. The referred gap demonstrated to have impact on the scouring pattern.

Habibzadeh *et al.* (2011) conducted a preliminary study of the flow properties of submerged jumps with baffle blocks. A general theoretical equation for the drag force on the blocks was derived. The energy dissipation in submerged jumps with blocks was also compared with free jumps. The energy dissipation efficiency, defined as the ratio of the dissipated energy to the initial energy of the supercritical flow in the submerged jump to that in the free jump, was found to be a function of the submergence factor with the maximum efficiency being slightly larger than in the corresponding free jump. However, their experiments included only one block shape and location. Habibzadeh *et al.* (2012) investigated the global features and hydraulic behaviour of this flow over a wide range of Froude numbers, submergence factors, and block shapes and locations. Both flow regimes (the deflected surface jet and the reattaching wall jet) were observed, being the first more efficient in dissipating energy. From this study, empirical equations were derived for predicting the critical values of the submergence factor at which each flow regime forms.

Flip buckets are widely used because they allow the control of large quantities of excess hydraulic energy, in a technically sound and hydraulically safe way (Khatsuria, 2005; Novak *et al.*, 2006). Using a flip bucket is recommended when the flow velocity is larger than about 15-20 m/s (Vischer and Hager, 1995; and Vischer and Hager, 1998), because the deflection of the flow downstream allows transferring the high amount of energy to a position where the impact, turbulence and subsequent erosion will not put at risk the dam or appurtenant structures. In comparison to a stilling basin, the flip bucket is a more economical alternative. Regarding the energy dissipation process of this system, a small amount of energy is dissipated by friction through the bucket, other portion is dissipated during the jet's trajectory in the air (which results in intense spray), and the major portion of energy dissipation is due to the impact of the jet with the downstream plunge pool. As a result, the use of a flip bucket should be considered only where bed scour caused by the impact of the water jet cannot endanger the dam or cause unacceptable environmental damage (Omidvarinia and Jahromi, 2011). The Picote dam, located in Portugal (refer to Fig. 5), is an example of this type of energy dissipator, also known as ski jump.

Considerable research has been carried out on flip buckets as energy dissipator systems. Rhone and Peterka (1959) studied and improved design of flip buckets implemented by the USBR (Peterka, 1983). Pressures on buckets were computed and observed by Balloffet (1961), using a potential flow model. Yamini and Kavianpour (2011) presented the dynamic pressure distribution over the simple circular flip bucket. Kerman-Nejad *et al.* (2011) also investigated the dynamic pressures due to the impact of a ski jump out of a flip bucket downstream of a chute spillway model. Their results showed that the dynamic pressure is highly sensitive to horizontal and vertical distances from the impact location as well as to the impact angle. Steiner *et al.* (2008) performed a laboratory study to investigate the hydraulic performance

of a triangular-shaped (rather than the conventional circular-shaped) bucket placed at the take-off of ski jumps. A significant effect of the approach flow Froude number, the relative bucket height, and the deflector angle was found. A comparison with previous results for the circular shaped bucket geometry indicated a favourable behaviour of the novel bucket design. Schmocker *et al.* (2008) studied the trajectory and aeration characteristics of ski jump jets both for pure water and pre-aerated approach flow conditions. The air concentration profile was measured at different locations downstream from the ski jump and results demonstrated the significant effect of the approach flow Froude number, the approach flow depth, and of pre-aeration on the jet's disintegration.

Drop structures are used when the tailwater required for a stilling basin is not available or the downstream formation consists of rock where the potential for erosion is negligible. In this case, energy dissipation occurs from the impact of a nearly vertical water nappe with a water pool. Since impact forces are significant, the designer must thoroughly investigate any localized flow conditions that can compromise the security or the performance at end of the chute. This investigation must be done considering the effect of several seasons of operation (FEMA, 2010). The basic flow types occurring in a prismatic drop structure depend on the approach water depth and the tailwater depth measured from the drop elevation and are (Visher and Hager, 1998) (Fig. 10): (i) free falling jet and supercritical tailwater; (ii) hydraulic jump if tailwater depth is smaller than drop height; (iii) plunging jet flow; and (iv) undulating surface jet flow.

Several types of basins were developed using a drop structure, such as those by Rand in 1955, the Inlet Drop Spillway by Blaisdell and Donnely in 1954, and the Straight Drop Spillway Stilling Basin by Donnelly and Blaisdell in 1965. A review of these types of basins is provided by Visher and Hager (1995).

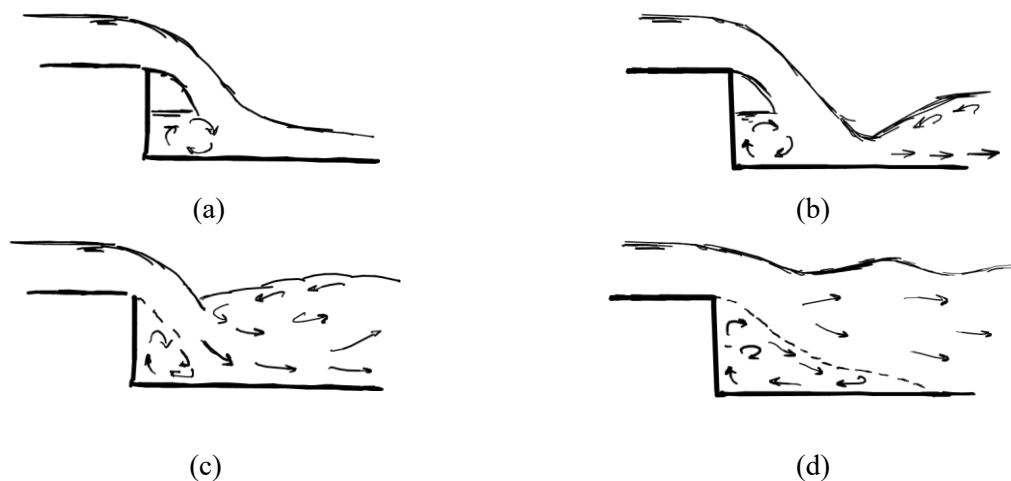


Fig. 10 - Drop structure in a prismatic rectangular channel and related flow types (adapted from Visher and Hager, 1998).

A typical engineering concern is the definition of the dynamic pressures generated at the impact in the pool bottom. Dynamic pressures have been studied by e.g. Cola (1966), Hartung and Häusler (1973), Melo (2001) and Bollaert (2002). Dissipating water energy by jet diffusion in a water pool and impact with the river bottom brings concerns related to rock scour. Yuditskii (1963) presented the first method to assess rock scour based on hydrodynamic pressures and rock characteristics. At the present stage-of-knowledge, at least two physically based engineering models for prediction of scour in rock as a function of time are available for practice: the one by Yuditskii (1963) and the one by Bollaert (2004). These models relate hydrodynamic pressures in rock joints with the resistance of these joints against cracking. The development of the jet in the air has been discussed by, amongst others, Ervine and Falvey (1987).

Manso (2006) conducted an experimental investigation on the influence of pool geometry in the diffusion of plunging jets and in pool aeration, providing new insight on the interaction between jet diffusion and pool geometry.

The prediction of the scour depth generated by a ski jump jet was also object of study of investigators, which proposed empirical formulae based on laboratory and prototype observations (Schoklitsch, 1935; Veronese, 1937; Damle *et al.*, 1966; Wu, 1973; Martins, 1975; Taraimovich, 1978; Incyth, 1982; Mason, 1984). Alias *et al.* (2008) investigated the impact of the take-off angle of bucket type energy dissipator on the scour hole. Experimental results showed that the take-off angle of 45° is the optimum angle which gives minimum longitudinal area of the scour hole. Also, validation of selected equations for predicting maximum scour depth at downstream of the bucket type energy dissipator showed that the equation proposed by Schoklitsch gave minimum error (33%).

2.2.3. CHARACTERISTICS OF SPILLWAY FLOWS

The design and assessment of hydroelectric facilities involves the understanding of the very complex behaviour of moving water. To accomplish this, engineers must develop a thorough understanding of the complexities of fluid flow phenomena, which are often two or three dimensional in nature (Teklemariam *et al.*, 2002). Spillway flows are essentially rapidly varying flows with pronounced curvature streamlines (Bhajantri *et al.*, 2006). They are generally aerated (two-phase flow) and, given their high kinetic energy, flow instabilities may develop due to their interaction with geometric elements (eg. piers, channel contractions and offset joints).

The ogee or overflow spillway is the most common type of spillway (Katsuria, 2005). Once the water flows past the crest, the fluid is accelerated by gravity along the chute, and two processes simultaneously occur: formation and gradual thickening of the turbulent boundary layer along the profile and gradual increase in the velocity and decrease in the depth of the main flow (Bhajantri *et al.*, 2006). When the outer edge of the boundary layer reaches the free-surface, the flow becomes fully-developed - this is called the inception point. Here, self-aeration of the flow begins to occur, raising the bulk of the flow which is a design parameter that determines the height of the sidewalls. The presence of air within the boundary layer may reduce the shear stress between the flow layers and hence the flow resistance (Chanson, 1994). The air entrainment can be clearly identified by the “white water” appearance of the free-surface flow, as shown in Fig. 11 for the spillway of Hartbeespoort Dam, located in South Africa.

As the air entrainment develops, bubbles penetrate the water towards the chute bottom along the flow direction, until a two-phase flow fully develops and becomes uniform (Wei *et al.*, 2016). Wood (1991) and Chanson (1997) presented comprehensive studies of free-surface aeration on smooth chutes, whereas Chanson (1995) reviewed the effects of free-surface aeration on stepped channels. A large amount of data on the fully developed uniform region is available for predicting the air-water flow properties of supercritical chute flows (Straub and Anderson, 1958; Wood, 1991; Deng *et al.*, 2002 and 2003 – cited in Wei *et al.*, 2016). Wood (1983) and Hager (1991) investigated the relationship between the air concentration and the hydraulic conditions, including the flow discharge and channel slope in uniform flows. Basic equations for the uniform aerated region were developed based on turbulent diffusion theory (Chanson 1993).

Contractions along spillway chutes are provided whenever the reduction of the channel width is necessary. This may be due to geological, topographical, economical or hydraulic considerations. Since the flow along a spillway chute is supercritical, any deviation in the streamlines creates oblique standing waves (also designated as shockwaves) that can propagate downstream unless a properly designed

contraction is provided to minimize this effect. The prediction of the location of oblique standing waves and the sequent elevation of the water surface is necessary to design the required wall height to prevent overtopping. Studies relating to the design of high-velocity flow in channel contractions and expansions have been reported by Ippen and Dawson (1951). Later, Ippen and Harleman (1956) conducted experiments to verify the hydrodynamic theory for oblique hydraulic jumps and expansion waves over a range of Froude numbers. Various researchers (e.g., Terzidis and Strelkoff, 1970; Herbich and Walsh, 1972; Ellis and Pender, 1982; Hager, 1989; Gharangik and Chaudhry, 1991; Hager *et al.*, 1994; Reinauer and Hager, 1998) have carried out investigations of supercritical flow in channels in the presence of abrupt wall deflections, sudden expansions, channel junctions, and in spillway contractions.



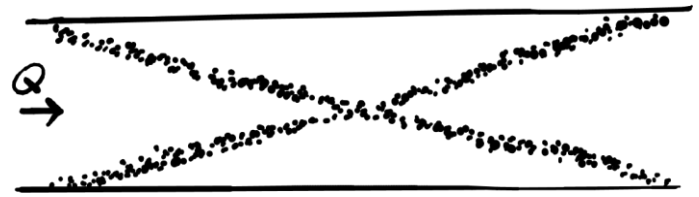
Fig. 11 - Free-surface aeration in the spillway of Hartbeespoort Dam, North West Province, South Africa, 1923 (web 3 Nov 2016 www.ewiza.co.za).

Chanson and Toombes (1997) observed several types of cross-waves (also called shockwaves) intersections at stepped spillways, Fig. 12. At low flow rates, the traditional cross-wave intersection was observed (Fig. 12a), for which the cross-waves intersect in absence of free-surface aeration; downstream of the first few steps the free-surface was characterised by turbulent wavelets and aeration (Fig. 12b); on the upstream steps, for large flow rates, a merging cross-wave intersection was observed (Chanson, 2002). Woolbright (2008), Hunt (2008) and Hunt *et al.* (2008) evaluated physical models of converging stepped spillways. Study findings showed that a taller wall height is required to contain the increased flow depth created by the cross-wave at the wall convergence.

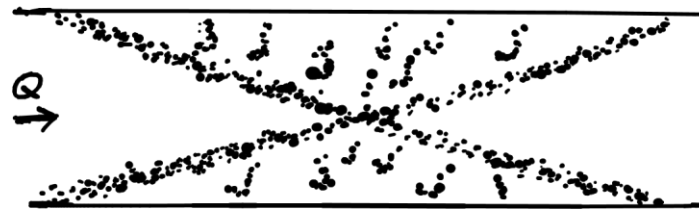
Hunt (2008) provides generalized design guidelines to determine the minimum training wall heights for converging stepped spillways with vertical training walls, with convergences ranging between 0 and 70°. Woolbright (2008) provides generalized design guidelines for converging stepped spillways with sloped training walls, with convergences ranging from 18–45°. Both model studies used relatively flat spillway slopes of 3:1. As stated by Reisi *et al.* (2015), to date there has been no generalized guideline for convergent spillways. In this regard, further investigation of the flow behaviour and the hydraulic characteristics through these spillways is needed. Fig. 13 shows the occurrence of shockwaves over the spillway of Gardiner dam, located in Canada, one of the largest embankment dams in the world.

Roll waves are surface waves developing in steep chutes, predominantly at low flows, and caused by shear instabilities, hence impossible in absence of boundary friction (Chanson, 2002), Fig. 14. When roll-wave trains occur, the water depth periodically increases, and the water may exceed the side wall

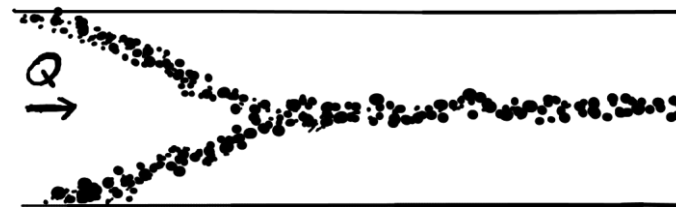
and overflow. Because of this, the prediction of occurrence of roll waves is of importance while designing the side walls of a chute.



(a) Crossover



(b) Crossover with high turbulence



(c) Merging

Fig. 12 - Cross-waves' characteristics in nappe flows without hydraulic jump (adapted from Chanson and Toombes, 1997).



Fig. 13 – Cross-waves over the spillway of Gardiner dam, Saskatchewan, Canada, 1967 (copyright © Neil A Rawlyk).



Fig. 14 - Roll waves in the spillway of the Llyn Brianne Rock-fill Dam, Wales, United Kingdom (copyright © Geoffrey Davies).

Roll waves create unstable and turbulent behaviour in channels and also change the behaviour of water entering the energy dissipation structures (Aghebatie and Hosseini, 2016). Since the pioneer work by Cornish (1934), which described the detail roll-wave phenomenon, most researches in this field have been analytical. Within the shallow-water approximation, the Saint-Venant Equations (SVE), either in their hyperbolic or diffusive formulation, represent the main framework for the theoretical studies of roll-waves in turbulent flows (Campomaggiore *et al.*, 2016). A few studies are documented regarding the occurrence of roll waves in spillways (e.g. Bazargan and Aghebatie, 2015; and Aghebatie and Hosseini, 2016).

As previously stated, spillway discharges sometimes exceed the design flow discharge, Q_{des} . In such situation, the spillway structure will be subjected to negative pressures, that depending on their extend, may induce damage on the spillway surface. The occurrence of the cavitation phenomenon, due to the development of high negative pressures (below the water's vapor pressure), is a common and very complex process on spillways that threatens the stability of the structure. Cavitation occurs in the low-pressure zone created by the deflection of the flow away from the boundary (flow separation), when cavities collapse up against the concrete surface, cavitation attacks the sand-cement component and loosens the aggregate, which is then pulled out by the flow (May and Deamer, 1989).

The cavitation phenomenon in hydraulic structures is a function of the flow velocity, flow pressure, duration of operation, boundary roughness and alignment, strength of the materials from which the boundary is constructed and the amount of dissolved air in water (Falvey, 1990). Cavitation risk is usually characterized by the cavitation index, C_a , given by,

$$C_a = \frac{p - P_{vapor}}{\frac{1}{2}\rho U^2} \quad (1)$$

where p and P_{vapor} are the pressure and vapor pressure respectively, ρ is the density of water and U is the velocity of the fluid. The smaller the value of C_a , the higher the risk of cavitation. A value of C_a of around 0.2 is sometimes considered (Falvey, 1990) when assessing the critical velocity on smooth concrete surfaces, to cavitation damage.

The spillway of the Nagarjuna Sagar Dam across in India is an example of a documented case of cavitation damage, Fig. 15. The spillway was eroded during flood events in 2009, due to cavitation. On further investigation of the problem, it was found that there was a large deviation of the existing profile of the spillway from the design profile, which led to the development of negative pressures in such a magnitude that could create the problem (Giridhar *et al.*, 2014).



Fig. 15 - Cavitation damage in the Nagarjuna Sagar Dam, India, 1967 (from Giridhar *et al.*, 2014).

Peterka (1953) is an early reference reporting some experimental investigations on cavitation damage in hydraulic structures and the effect of aeration. He concluded that about 6-8% air was needed to stop damage in a concrete surface having a 28-day compressive strength of approximately 17 MPa. Nie (2001) examined the effect of surface roughness on the cavitation damage, concluding that a rough surface reduces the pressure drop and the possibility of cavitation downstream of the roughness. Dong and Su (2006) presented a study on the cavitation control by means of aeration and concluded that aeration remarkably increases the pressure in the cavitation region.

Bordbar *et al.* (2010) investigated the cavitation risk in stepped morning glory spillways, with focus on the effects of the flow regime changes on spillway, step dimensions and number of steps. They concluded that the more is the number of steps in morning glory spillways, the less is the cavitation risk.

Chute aeration has been considered the most efficient technical measure to counter cavitation damage. Other means, including the treatment of chute concrete, the use of smooth shuttering formwork or the application of steel fibers were less effective, in addition to increased cost (Pan and Shao, 1984). The natural presence of air in high-velocity flows may prevent or reduce the damage caused by cavitation, but it is often insufficient. Aerators (devices to prevent cavitation damage) have been extensively investigated in terms of global air entrainment coefficient (e.g. Koschitzky 1987; Chanson 1988 and Rutschmann, 1988) as well as streamwise air transport and air detrainment (e.g. Kramer, 2004 and Pfister, 2008).

2.2.4. DAM FAILURES AND INCIDENTS

The reliable performance of dams and their appurtenant structures depends on the complex interaction between a large number of natural, engineered, and human factors. Despite, dams have been designed for extreme loads (e.g., the largest flood that might occur during some service life), incidents and failures seldom derive from loads resulting from uncommon combinations of mishaps difficult or impossible to identify during design. Failure of a spillway has potentially serious consequences, which can include loss of reservoir storage, downstream damage and eventual loss of life. Although the safety of a dam is evaluated thoroughly, spillways often receive less attention than other features, especially when they are complementary spillways. As a result, there is a growing need to raise awareness among dam owners regarding safety issues associated with developing conditions that could result in a spillway failure during a flood. Possible conditions that can lead to a spillway failure during a spill event are:

- Existing structural damage;
- Flows that exceed spillway capacity;
- Cavitation damage;
- Foundation erosion related to seepage or groundwater;
- Improper gate operation and mechanical gate failures.

Most structural damage is normally observable during a site inspection, unless the damaged areas are inaccessible or require special inspection. The inspector should seriously consider the possibility that observed structural damage can affect the performance of the spillway.

Despite the spillway design capacity is known, the original dam design may have been based on limited hydrologic data. Updated hydrology assessments can show that predictable flood discharges can exceed the spillway design capacity, which may lead to overtopping the dam and poor performance of the spillway chute (especially in areas of rapidly varying flow, including changes in slope or cross section) or stilling basin. With this purpose, it is important to evaluate flow depths and velocities in spillway chutes, stilling basin capacity, and (if applicable) sweep out conditions that occur when the tailwater is not sufficient to develop a hydraulic jump (resulting in high-velocity flows in the downstream river channel). Flows passing over offsets in spillway liners can induce either high uplift pressures that can lift concrete slabs or flows into the crack that can erode foundation materials. Even if there are no open joints or cracks in the chute concrete, foundation erosion can be caused by reservoir seepage, flowing groundwater, or seepage from local precipitation.

Hundreds of dam failures have occurred around the world throughout the history. There are a number of databases and reports detailing dam incidents and failures providing important references of information, namely ICOLD (1984), ICOLD (1995), and Environment Agency (2008). Table 2 summarizes some of them.

Across the world, the number of dams categorised as high hazard dams (which means that a failure or mis-operation is expected to result in loss of life and may also cause significant economic losses) is increasing, because engineering plans and risk management strategies are not keeping pace with the deteriorating infrastructure or escalating extreme weather events. The majority of the operating dams were built on hydro-climatic data now made obsolete by climate change. Extreme weather events are striking high hazard infrastructure more often, with devastating results. In the United States of America (USA), from January 2005 through June 2013, state dam safety programs reported 173 dam failures and 587 incidents² - episodes that, without intervention, would likely have resulted in dam failure.

² Statistics from <https://damsafety.org/dam-failures>

GENERAL BACKGROUND TO THE TOPIC

Table 2. Examples of international dam disasters causing loss of life (Williamson, 2017).

Dam	Dam type	Country	Height (m)	Reservoir volume (10 ⁶ m ³)	Date built	Failure		No. of Deaths
						Date	Type	
Vega de Tera	CMB	Spain	34	7.8	1957	1959	SF	144
Malpasset	CA	France	66	22	1954	1959	FF	421
Vajont	CA	Italy	265	150	1960	1963	L	2600
Baldwin Hills	Emb	USA	71	1.1	1951	1963	IE	5
Frias	Emb	Argentina	15	0.2	1940	1970	OF	>42
Teton	Emb	USA	93	356	1975	1976	IE	14
Machhu II	Emb	India	26	100	1972	1979	OF	2000
Bagauda	Emb	Nigeria	20	0.7	1970	1988	OF	50
Belci	Emb	Romania	18	13	1962	1991	OF	25
Gouhou	Emb	China	71	3	1989	1993	IE	400
Zeizoun	Emb	Syria	42	71	1996	2002	OF	20
Shakidor	Emb	Pakistan	-	--	2003	2005	OF	>135
Situ Gintung	Emb	Indonesia	16	2	1933	2009	IE	100

Dam type: CA = concrete arch, CMB = concrete and masonry buttress, Emb = embankment, RCC = roller compacted concrete. Type of failure: IE = internal erosion, FF = foundation failure, OF = overtopping during flood, SF = structural failure on first filling, L = landslide into the reservoir causing overtopping.

For instance, after Hurricane Harvey in September 2017, the US Army Corps of Engineers released water from Houston’s Addicks and Barker dams - two of the most high-risk dams in the USA - inundating several thousand buildings with controlled releases to avoid destroying most of the city. In Puerto Rico, Hurricane Maria in October 2017 cracked the Guajataca Dam, while downpours began to erode its spillway. The town of Isabela was flooded and hundreds of people in the surrounding towns were forced to evacuate. Most of the dam failure incidents registered in the USA between 2010 and 2015 were caused by extreme weather events (Fig. 16).

The Oroville dam incident, occurred in February 2017, is one of the most recent and remarkable incidents (Fig. 17). This embankment dam, located on the Feather River, California, is the tallest dam in the USA (235 m high) and serves mainly for water supply, hydroelectricity generation and flood control. The hydraulic scheme was designed with four routes for water to pass, namely:

- Through the hydro-electric generators;
- Through a river outlet (also known as the bypass valve);
- Through the main (service) spillway which is used to control the height of the reservoir (by means of eight radial gates); and

GENERAL BACKGROUND TO THE TOPIC

- Over the top of an emergency spillway, consisting of a concrete weir beside the main spillway and the adjacent earthen slope of the abutment. Once the lake reaches an elevation 6 m below the height of the main dam structure, water flows, uncontrolled, over the weir and down the earthen slope until it reaches the river below.

The Oroville crisis started after a series of storms occurred in early to mid-January, which lead to the use of the main spillway. The Independent Forensic Team (IFT) believes that the service spillway chute failure most likely initiated by the uplift and removal of a section of the slab in the chute on the 7th of February (see Table 3 for a resumed chronological order of events).

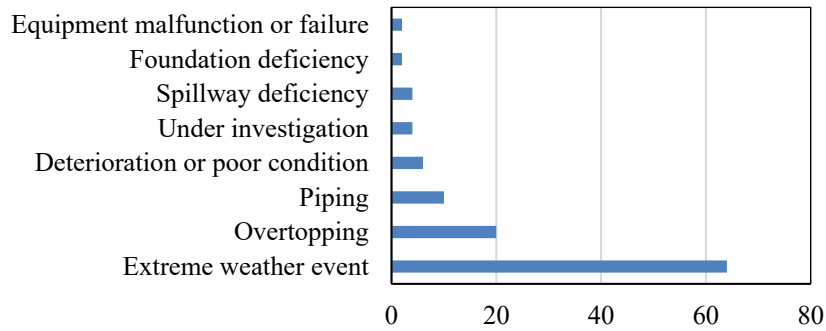


Fig. 16 - Association of State Dam Safety Officials (ASDSO) incident Database - dam failure incidents' (from 2010 to 2015) causes (web 12 Dec 2018 www.damsafety.org).



Fig. 17 – Evolution of the Oroville spillway failure in chronological order from (a) to (d). Photographs from Williamson (2017).

GENERAL BACKGROUND TO THE TOPIC

Once the initial section of the chute slab was removed, the underlying moderately to highly weathered rock and soil-like material beneath the slab in this location was directly exposed to high-velocity spillway flow. The high-velocity flow rapidly eroded the foundation materials at this location, removed additional chute slab sections in both upstream and downstream directions, and quickly created the erosion hole. The excessive uplift pressure that likely removed the slab section was mainly due to high-velocity spillway flow injecting water into slab surface features, such as open joints, unsealed cracks, spalled concrete at either a joint or drain location in either a new or previously repaired area, or some combination of these features. If there is a lesson that must be learned from this incident, it is that even when a critical structure like Oroville Dam seems to operate up to standard, one small flaw can emerge at any time and result in a severe failure due to the sheer scale of the facilities and the conditions they are expected to consistently work under (Koskinas *et al.*, 2019).

Another very recent dam failure, with reported life loss, is that occurred on the 23rd of July 2018 in the Saddle Dam D dam, in Laos (Fig. 18). A dam-break followed by a massive flood wave propagation resulted in various submerged villages, killing 40 people.

According to ICOLD, more than 59000 dams have reservoirs big enough to flood entire communities. In the United States, the number of high-hazard potential dams in 2016 was almost 15500, and the number of those in need of immediate remediation keeps growing (Fig. 19). In addition to life and property, the failure of a dam threatens energy security. In some developing countries, such as Brazil, dams generate more than three quarters of the country’s electricity. For instance, the Itaipu Dam, between Brazil and Paraguay, generates enough electricity each year to power the entire world for two days. To ensure the statistic for dam failures continues to fall and to prevent further serious dam incidents excellent standards of dam safety management are vital.

Table 3. Timeline of the Oroville incident events.

Early to mid-January	Series of storms; main spillway gates opened
7 th February	Flows increase; spillway damage discovered; flows stopped (Fig. 17a)
8 th to 10 th February	Reservoir continues to fill
11 th to 12 th February	Emergency spillway overflows – the hillside began eroding uphill, threatening to collapse the concrete lip, causing the top 10 m of the reservoir to empty
12 th February	Main spillway gates opened again to reduce flows over the emergency spillway and evacuation started
13 th February	Eroded hillside was filled with concrete and rocks
13 th to 26 th February	Main spillway flows continue erosion (Fig. 17c)
27 th February	With the reservoir lowered, flows stopped down the main spillway to allow assessment of damage (Fig. 17d)
28 th February	Works start to clear the debris at the base of the main spillway



Fig. 18 – Flooded area after the Saddle Dam D dam collapse, in Laos (web 12 Dec 2018 www.aljazeera.com).

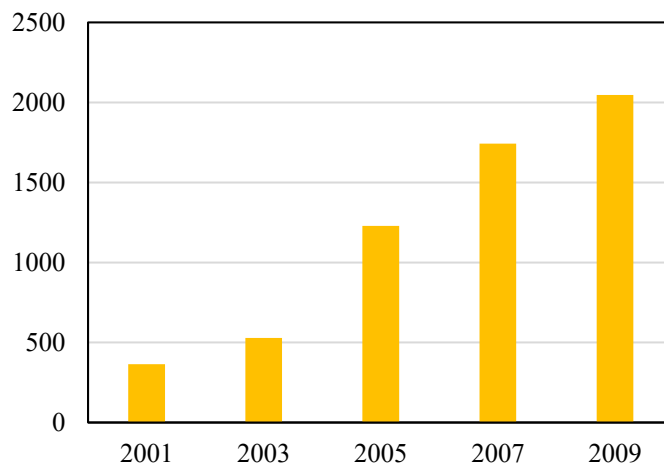


Fig. 19 – Evolution of the number of high hazard dams in need of remediation in the USA (web 13 Dec 2018 www.fema.gov).

Identification of dams in need of repair and execution of dam safety studies is urgent. Long-term concerns for improving dam safety include climate change, ageing dams and deterioration.

2.3. NUMERICAL MODELLING

2.3.1. INTRODUCTION

Over the last decades, the development of computer-based simulation of fluid flows has been noteworthy. This has a twofold justification: first, the availability of affordable high-performance computing hardware (along with the introduction of user-friendly interfaces of commercial packages); and second, the several advantages of Computational Fluid Dynamics (CFD) over experimental-based approaches to fluid systems design. A literature search of numerical modelling of spillways revealed that it began as an investigative tool at research institutions (Savage and Johnson, 2001), and it was gradually being accepted by the dam engineering community. It was in the early 1980s that commercial CFD codes came into the open market to stay. The use of commercial CFD software started to become accepted by major companies around the world and it is now recognized to be a part of the Computer-

Aided Engineering (CAE) spectrum of tools used extensively in many industries. A keyword search for “CFD” in the American Society of Civil Engineers (ASCE) database revealed that the number of publications related to this technology in the Journal of Hydraulic Engineering increased rapidly since the early 2000s (Table 4).

The use of computational tools in engineering practice gives rise to a new way of working, which is intermediate between purely theoretical and experimental. The main advantages achieved are: (i) improved quality and safety of the final design; (ii) reduced design time, achieved through fewer design iterations; and (iii) reduced costs. Numerical simulation can provide tests for theories, insights to complex physics and assist in the interpretation and even discovery of new phenomena.

Mesh-based methods are still the class of CFD models mostly used for industrial applications, as they have gathered greater research efforts. Flow-3D, ANSYS Fluent and OpenFOAM are examples of available, well-tested CFD codes for free-surface flows. More recently, researchers’ interests are also towards meshfree methods, of which the open-source codes (based on the SPH method) DualSPHysics and GPUSPH are examples. The characteristics of each numerical models’ class (mesh-based and meshfree) are presented in sections 2.3.2 and 2.3.3, respectively. Despite the differences among the afore mentioned CFD codes, they share a general procedure, being the Navier–Stokes equations (NSE) the fundamental basis³. The NSE are presented henceforward in section “2.3.4. Governing equations for fluid dynamics”, in their Lagrangian form.

Table 4 - Literature search on the ASCE publication database for “CFD” on the Journal of Hydraulic Engineering till the end of 2018.

Time period	Number of journal papers containing the “CFD” term in the title
1985-1989	0
1990-1994	4
1995-1999	18
2000-2004	44
2005-2009	57
2010-2014	80
2015-2018	86

2.3.2. MESH-BASED METHODS

Mesh-based numerical methods, such as the Finite Element Method (FEM) and the Finite Volume Method (FVM), have been widely applied in CFD problems and are still dominant in numerical

³ It should be noted that, despite CFD models are generally associated with the NSE in the literature, free-surface flows are also treated using the SVE.

simulations. Despite their great success, grid-based numerical methods suffer from some inherent difficulties in many aspects, which limit their application to many problems, especially those dealing with large deformations and complex geometries. Generally, two approaches can be used - the Lagrangian description and the Eulerian description. In the Lagrangian description the grid is fixed to the material so that the mesh is deformed with the material. A buoyant probe is an example of a Lagrangian measuring device. The particle properties, such as density, velocity and pressure are time dependent. In the Eulerian description, the grid or mesh is fixed in the space, but not to the material, which moves across the grid cells. In this approach, the flow properties are recorded in space, as time varies. It means that the flow properties at a specified location depend on time. A probe fixed in space is an example of an Eulerian measuring device.

Lagrangian methods have many advantages (e.g. easier implementation) and are well suited to solve Computational Solid Mechanics problems, where deformation is not as large as in CFD problems. In applications where large deformations are expected to occur, such as in turbulent free-surface flows, the high distortion of the mesh affects the accuracy of the formulation and hence the solution obtained. Mesh rezoning or re-meshing the problem's domain can help to overcome this issue, yet it may introduce additional inaccuracy into the solution.

On the other turn, the Eulerian grid can tackle large deformations in the object because the mesh is not attached to it. Eulerian methods are therefore dominant in CFD, and particularly in dam-related flows modelling (e.g. Ho *et al.*, 2001; Bhajantri *et al.*, 2006; Kim *et al.*, 2010; Kumcu, 2016). However, there are many disadvantages as well, of which the treatment of complicated geometries is an example. The Arbitrary Lagrangian-Eulerian-based (ALE) approach can alleviate many of the drawbacks that the traditional Lagrangian-based and Eulerian-based finite element simulations have (Benson, 2013).

2.3.3. MESHFREE METHODS

Meshless methods can be traced back to 1977 when Lucy (1977) and Gingold and Monaghan (1977) proposed a smooth particle hydrodynamics (SPH) method that was used for modelling astrophysical phenomena. Since then, the use of meshfree methods has experienced an exponential growth during the last decade. These methods (refer to Table 5), whose main idea is to substitute the grid by a set of arbitrarily distributed nodes, are expected to be more versatile than the conventional grid-based methods, especially when treating problems dealing with large deformations, complex geometries and deformable boundaries. Moreover, the process of grid generation itself is not always straightforward in terms of computational time and mathematical complexity. In a particle meshfree method, each particle possesses a set of field variables such as mass, velocity, energy and position.

The evolution of the system is determined by the conservation laws for mass, momentum and energy. The procedure of meshfree methods consists of four basic steps:

- Domain representation;
- Function approximation;
- Formation of system equations; and
- Solving the global equations.

A number of meshfree methods have been proposed in the last years. These methods share some common features but are different in the methods of approximation. The present research focusses on the SPH method, a Lagrangian particle method, which fundamentals are described in chapter 3.

GENERAL BACKGROUND TO THE TOPIC

Table 5 - Some typical meshfree methods in chronological order (refer to Liu and Liu, 2003).

Methods	Methods of approximation
Particle-in-cell (PIC)	
Smoothed particle hydrodynamics (SPH)	Integral representation
Finite point method	Finite difference representation
Diffuse element method (DEM)	Moving least square (MLS) approximation Galerkin method
Element free Galerkin (EFG) method	MLS approximation Galerkin method
Reproduced kernel particle method (RKPM)	Integral representation Galerkin method
Moving particle semi-implicit (MPS)	Integral representation
HP-cloud method	MLS approximation, Partition of unity
Free mesh method	Galerkin method
Meshless local Petrov-Galerkin (MLPG) method	MLS approximation Petrov-Galerkin method
Point interpolation method (PIM)	Point interpolation, (Radial and Polynomial basis), Galerkin method, Petrov-Galerkin method
Meshfree weak-strong form (MWS)	MLS, PIM, radial PIM (RPIM), Collocation plus Petrov-Galerkin

2.3.4. GOVERNING EQUATIONS FOR FLUID DYNAMICS

The governing equations of fluid dynamics, namely the NSE, represent mathematical statements of the conservation laws of physics, which are (Versteeg and Malalasekera, 1995): *(i)* the mass of the fluid is conserved; *(ii)* the rate of change of momentum equals the sum of the forces on a fluid particle (Newton's second law); and *(iii)* the rate of change of energy is equal to the sum of the rate of heat addition to the rate of work done on a fluid particle (first law of thermodynamics). As previously stated, there are two approaches for describing the governing equations - the Eulerian description and the Lagrangian description.

Here, the NSE in the Lagrangian form are presented (as this is the one used in the SPH model). These consist of the following set of equations,

$$\left\{ \begin{array}{l} \frac{D\rho}{Dt} = -\rho \frac{\partial u^\beta}{\partial x^\beta} \\ \frac{Du^\alpha}{Dt} = \frac{1}{\rho} \frac{\partial \sigma^{\alpha\beta}}{\partial x^\beta} + F \\ \frac{De}{Dt} = \frac{\sigma^{\alpha\beta}}{\rho} \frac{\partial u^\beta}{\partial x^\beta} \end{array} \right. \quad (2)$$

where the Greek superscripts α and β are used to denote the coordinate directions, the summation in the equation is taken over repeated indices, and the total time derivatives are taken in the moving Lagrangian

frame. σ is the total stress tensor, constituted by the isotropic pressure, p , the identity tensor δ and the shear-stress vector, τ . F refers to the external forces.

$$\sigma^{\alpha\beta} = -p\delta^{\alpha\beta} + \tau^{\alpha\beta} \quad (3)$$

For Newtonian fluids, the shear stress should be proportional to the strain-rate tensor denoted by s through the dynamic molecular viscosity, μ

$$\tau^{\alpha\beta} = \mu s^{\alpha\beta} \quad (4)$$

where

$$s^{\alpha\beta} = \frac{\partial u^\beta}{\partial x^\alpha} + \frac{\partial u^\alpha}{\partial x^\beta} - \frac{2}{3}(\nabla \cdot \mathbf{u})\delta^{\alpha\beta} \quad (5)$$

Separating the isotropic pressure and the viscous stress, the energy equation can be rewritten as

$$\frac{De}{Dt} = \frac{p}{\rho} \frac{\partial u^\beta}{\partial x^\beta} + \frac{\mu}{2\rho} s^{\alpha\beta} s^{\alpha\beta} \quad (6)$$

Eq. (2) is a set of Partial Differential Equations (PDE) that along with proper boundary and initial conditions can describe the problem under investigation. Since these PDE are not analytically solvable so far (except for simple cases), domain discretization shall be carried out. It refers to the representation of a continuum problem domain by a finite number of components, which form the computational frame for the numerical approximation. It can be a grid (quantities are evaluated at nodes) or even a set of particles (quantities are evaluated at each particle).

Numerical discretization provides means to change the PDE in continuous forms into discrete representations, so that, the original physical equations are changed into a set of Ordinary Differential Equations (ODE), which can be solved (after time-discretization), using the existing numerical routines. The ODEs are solved to obtain numerical values for field functions (e.g., density, pressure, velocity) at discrete points in space and/or time. Lastly, the domain decomposition and numerical algorithms are translated into a computer in some programming language(s), which will constitute the CFD code.

To provide users easy access to the solving power of commercial CDF packages, they are normally structured into three main elements: (i) a pre-processor; (ii) a solver; and (iii) a post-processor (Table 6).

Table 6 - Main elements of a CFD code and corresponding features.

Pre-processor	Solver	Post-processor
Geometry		
Domain discretization: e.g. cell nodes, particles	Numerical discretization: e.g. FEM, FVM, SPH	2D and 3D surface plots Particle tracking
Material properties	Solution of algebraic equations	Vector plots
Boundary and initial conditions		View manipulation
Turbulence model		

2.3.5. TURBULENCE MODELLING

The velocity field of turbulent flows is three-dimensional, time dependent and has a random and irregular feature. The main difference between visualizations of laminar and turbulent flows is the appearance of eddying motions or vortices of a wide range of length scales in turbulent flows. Many of the incompressible flow problems to which CFD has been applied (e.g. floods and coastal flows) are turbulent. The vortices can have different sizes, from the largest size to the smallest, being the later dissipated by viscous processes (Tennekes and Lumley, 1972). Turbulence modelling is a key issue in most CFD simulations. The NSE are not closed and there is a need to use turbulence modelling to resolve the Reynold’s stress and close the equation set. The three main approaches used to do this are:

- Direct Numerical Simulation (DNS);
- Large Eddy Simulation (LES); and
- Reynolds-Averaged Navier-Stokes (RANS).

The DNS solves the NSE by resolving all the scales of motion. This is only possible with a very fine grid to resolve even the smallest eddies. This procedure is very extensive and computationally demanding, yet it gives the best accuracy. Furthermore, only fluid flows with small Reynolds numbers can be considered, because the grid has to be finer with increasing Reynolds number, Re , because eddy scales become finer.

The main idea behind LES is to reduce the computational cost by reducing the range of time and length scales that are being solved for, via a low-pass filtering of the NSE. Such a low-pass filtering effectively removes small-scale information from the numerical solution. As only the larger eddies are simulated, the mesh can be coarser, the simulation costs are lower, and the modelling complexity increases in respect to DNS.

RANS approach represents a statistical view of turbulence. The NSE are time-averaged and therefore only steady equations for the mean values have to be solved. The RANS equations only differ from the NSE in the Reynolds-stress term which inserts six more unknowns. Because of the averaging process a closure problem occurs. This can be solved using two approaches: the first (and most commonly used) is the use of an isotropic value for the turbulent viscosity value which is called an Eddy Viscosity Model; the other is to solve using the Reynolds Stress Model (RSM) for the 6 separate Reynolds stresses, which results in an anisotropic solution. The limitation with Eddy Viscosity models is the use of an isotropic value which may not be realistic and hence can increase the diffusion of the result. As expected, solving for the 6 Reynolds stresses and dissipation will be more accurate, but requires complex closure models and will increase the run time considerably. The RANS models are the most commonly used models due to their low cost in terms of computational power and run times. The disadvantage of RANS is the

difficulty in finding a universal model, because the fluctuations are strongly influenced by the geometry. Table 7 summarizes some of the most common turbulence models.

The presence of walls in turbulent flows increases the production of turbulence due to shearing effects. Modelling near-wall turbulence is crucial in order to correctly reproduce the flows, since the no-slip condition leads to large values of the velocity gradient at the walls. Traditionally, there are two approaches to modelling the near-wall region: the wall function approach and the near-wall model approach (Fig. 20). The wall y^+ is a non-dimensional value that computes the distance to a wall mesh in the turbulent regime and it reads,

$$y^+ = \frac{yu_*}{\nu} \quad (7)$$

Being y the wall normal coordinate and u_* a friction velocity.

Table 7 – Common turbulence models.

	Based on (time-averaged) Reynolds equations:
Classical RANS models	1. Zero equation model - mixing length model
	2. Two-equation model: $k - \epsilon$ and $k - \omega$ models
	3. RSM models
	4. Algebraic stress models
Large eddy simulation	Based on space-filtered equations

The observation of the turbulent flow between two horizontal parallel plane walls (this configuration is called the plane Poiseuille channel) led to a sub-division of the near-wall region into three areas (Viollet *et al.*, 2002):

- The viscous sub-layer where velocity profiles are assumed to be laminar and viscous stress dominates the wall shear: $0 < y^+ < 8$;
- The buffer layer where both viscous and turbulent shear dominates: $5 < y^+ < 30$; and
- The inertial sub-layer or log-law region which corresponds to the region where turbulent shear predominates: $30 < y^+ < 0.2 e^+$.

where e^+ is the dimensionless half-height of the channel, defined by $e^+ = e u_*/\nu$, with e being the half-height.

To directly simulate the near-wall turbulence a very fine mesh is required⁴ along with a modified turbulence model (low-Reynolds-number turbulence model) which is computationally expensive, especially for flows with high-Reynolds numbers. This led to the development of wall functions, based on semi-empirical formulae, which allow reproducing near-wall effects with a coarser discretisation. This corresponds to high-Reynolds-number turbulence models and requires the computational points

⁴ The closest computational points to the wall must be located within the viscous sub-layer.

closest to the wall to be located in the inertial layer. In Eulerian models, this can be done by designing the mesh so that the first calculation point is located in the logarithmic zone.

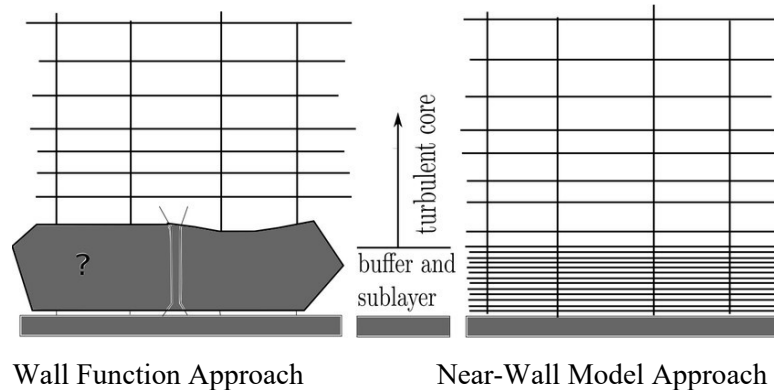


Fig. 20 - Near-Wall treatment approaches (from ANSYS, 2006).

2.3.6. CONCLUSIONS

The use of CFD models in hydraulic engineering have been changing the paradigm that physical models are the ultimate tool to assess flow dynamics. Throughout the last decades mesh-based CFD codes ruled the most advanced studies and proved to be accurate enough to support the process of decision-making. However, the laborious task of mesh generation and improvement, along with other limitations of mesh-based models such as the simulation specific problems (e.g., those having large free-surface deformations and complex geometries) or the free-surface computation which implies the resolution of additional equations (e.g. using the VoF method), have triggered the search for a new concept of numerical modelling which does not require the employment of a mesh. Despite the great success that standard mesh-based numerical methods have achieved these drawbacks impair their computational efficiency and limit their wider applications. That is why the search for ever better numerical methods continues.

As engineers find and solve problems at the design stage, costs can be reduced, and the overall business become more competitive (Fig. 21). In the past two decades, meshfree methods have emerged into a new class of computational methods with considerable success. In addition, a significant amount of progress has been made in addressing the major shortcomings that were present in these methods at the early stages of their development. The advantages of meshfree methods in the simulation of some sort of fluid problems are well recognized. They provide, above all, freedom to simulate reality with none to minor simplifications. On the duality between meshfree and mesh-based methods, it is important to consider some aspects:

- All meshless methods are not suitable for every kind of problems. Meshfree methods are useful when one need to have mesh independence or where problems are constrained due to mesh, e.g., fracture or large deformation problems;
- When dealing with meshfree methods, one is working with the more recent numerical methods;
- Because mesh-based methods have been largely exploited, when dealing with, e.g., the FVM, little new can be added.

GENERAL BACKGROUND TO THE TOPIC

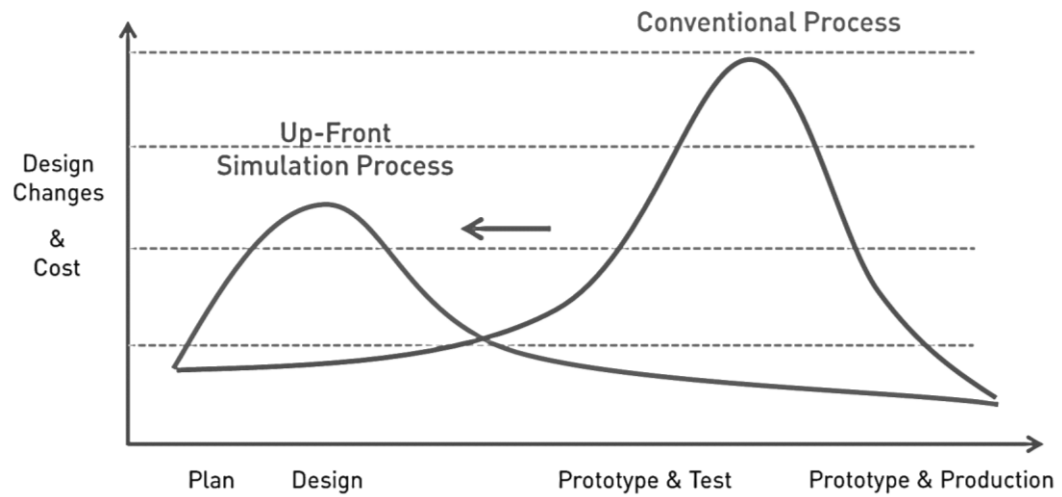


Fig. 21 - Design changes and costs all over the project when numerical simulation is used at the design stage (up-front simulation process) and when it does not (conventional process) (web 8 Jan 2019, www.midasoft.com).

SMOOTHED PARTICLE HYDRODYNAMICS

3.1. INTRODUCTION

The SPH method is a meshfree, Lagrangian particle method for modelling fluid flows, firstly developed and applied by Lucy (1977) and Gingold and Monaghan (1977) to solve astrophysical problems. Despite its early appearance, the SPH method did not attract the interest of researchers in other fields than Astrophysics and Elasticity/Fracturing until the beginning of the 1990s (Gomez-Gesteira *et al.*, 2010). It is only in the mid-90s that Monaghan (1994) made a first attempt of using SPH to model free-surface flows. After this first successful attempt, the community of SPH modellers have grown significantly, proposing new ideas and improvements. Since SPH was originally formulated for compressible flows, its application to incompressible flows (e.g. simulating the flow around hydraulic structures) is a more challenging task, and the subject of more debate (Ghadampour *et al.*, 2015). Currently, there are two main approaches for modelling incompressible flows in SPH – the weakly-compressible SPH (referred as WCSPH) and the incompressible SPH (referred as ISPH). In WCSPH computations, the fluid pressure is related to particle density using a stiff equation of state or a Riemann solver, whilst in ISPH computations, a Poisson equation is solved to determine the pressure in an approach based upon the orthogonal decomposition method, frequently used in grid-based methods. In Monaghan's first attempt of using SPH to model free-surface flows, the state equation was used to determine fluid pressure, which is much faster than solving an equation such as the Poisson's equation. Generally, there are two main approaches for imposing incompressibility in SPH: divergence-free velocity and density invariant methods. The source term in the Poisson equation is responsible for the difference in these two methods, which description is available in Ghadampour *et al.* (2015).

In 2005, the SPHERIC (Smoothed Particle Hydrodynamics European Research Community) community was founded, with the objective of bringing together SPH researchers and users, pushing the development of the model and engaging (among others) with water, energy and environmental hydraulics companies (Violeau and Rogers 2016). In recent years, some of the main research centers and universities have developed their own codes for modelling turbulent free-surface flows, some of which have become an inherent part of the numerical arsenal of industrial research and academic institutions. The Electricité de France (EDF) group has successfully used their code to study both incompressible flows (Issa *et al.*, 2005; Lee *et al.*, 2008) and turbulent free-surface flows (Violeau and Issa, 2007). The SPHysics group, has mainly focused its research on the wave propagation and interaction with coastal structures, both in 2D (Gomez-Gesteira *et al.*, 2005; Dalrymple and Rogers, 2006) and 3D (Crespo *et al.*, 2007; Crespo *et al.*, 2008). Other authors have focused their interest on the study of sloshing problems (Souto-Iglesias *et al.*, 2006), flows in Pelton turbines (Marongiu *et al.*, 2007), or near shore processes (Landrini *et al.*, 2007). According to Violeau and Rogers (2016), there are several reasons explaining this success: (i) the growing needs of industry and research for appropriate

tools for complex hydrodynamics; (ii) recent advances in SPH theory that resolved a number of problems with this method; and (iii) the emergence of general-purpose Graphic Processing Units (GPUs) that make it possible to use SPH codes to study complex 3D flows at real-life scales, while keeping the computational times manageable.

The SPH method, being a Lagrangian meshless method, has several advantages (Cleary *et al.*, 2007; Liu and Liu, 2003), which are worth underlining:

- Free-surfaces are handled easily and naturally. The fluid particles move to new locations and the shape of the free-surface is indicated by the free-surface particles⁵. There is no need for any form of explicit surface tracking method such as the Volume of Fluid (VoF) method which is generally applied in mesh-based methods. Complex topological changes in the free-surface can be easily tracked in situations where VoF and other surface tracking methods struggle or fail completely;
- As it is a Lagrangian method, it does not have the non-linear convective term in the momentum equation (as happens in Eulerian methods). Therefore, the code is conceptually simpler and should be faster as no computational effort is necessary for dealing with the convective terms. Moreover, numerical diffusion is avoided, contrary to mesh-based methods where it is a consequence of the space-time discretisation of convection. This feature also makes this method especially suited for simulating momentum-dominated flows;
- SPH is a fully transient method and so it is suitable for environmental flows that are not steady state;
- SPH can easily include complex additional physics (e.g., solidification, sediment transport, freezing). This arises partially from the flexibility of the continuum modelling, partially from the fact that each element of fluid or solid has a specific identity, that stays with the material over time (thereby considerably simplifying the tracking of history dependent quantities), and also from the ability to impose specific rule bases on the particles that can change the way in which the PDEs and other governing equations are used;
- Very complex geometries can be handled relatively easily, eliminating the need to create complex volume meshes, in which to solve the fluid flow, as needed for mesh-based methods. This is particularly important for large scale transient free-surface flows, where the volumes of space that would need to be meshed would be significantly larger than the volume of the fluid of interest; and
- With the continuing improvements and modifications, the accuracy, stability and adaptivity of the SPH method have reached an acceptable level for practical engineering applications.

Despite all the advantages that SPH method offer to model free-surface flows, as in any other method there are also some drawbacks, which still hamper its use in industrial applications, such as (Violeau and Rogers, 2016):

- Large computational time, particularly in 3D simulations;
- Difficulties in prescribing wall boundary conditions, and even greater problems at open (inflow/outflow) boundaries;
- Lack of consistent theory in relation to the mathematical foundation of the method (e.g. convergence, stability);

⁵ Through the implementation of a free-surface detection technique to distinguish the fluid particles that belong to the free-surface from those which do not (e.g. Marrone *et al.*, 2010).

- Inaccuracy of pressures' prediction, at least for the original WCSPH variant;
- Difficulties in dealing with variable space resolution for (nearly) incompressible flows.

The SPHERIC community is carrying out systematic research devoted to overcoming these drawbacks. Recently, SPHERIC researchers identified the five SPH grand challenges for the next years, that must be tackled to bring the method to maturity, which are (Violeau and Rogers, 2016): *(i)* convergence, consistency and stability; *(ii)* boundary conditions; *(iii)* adaptivity; *(iv)* coupling to other models; and *(v)* applicability to industry. Violeau and Rogers (2016) are keen in the identification of future challenges developments and long-term aims for the SPH model. The following are cited, as they relate to the objectives of the present research, which can be generally fitted within the fifth SPH grand challenge:

- “Integration of well-validated SPH codes into the design methodologies should be promoted to hydraulic, water, energy, and environmental companies (...) this necessitates a dialogue with industrial companies to identify their needs at the same time as educating potential users of possibilities and limitations of the method”;
- “New applications help developers to identify the shortcomings of the method, but also highlight new opportunities for its development”;
- “SPH should become part of the overall CFD landscape for hydraulic, water, energy and environmental companies and government agencies, used appropriately and with experience-based insight”;
- “main efforts should be directed primarily at addressing the issues that prevent industry investing in and using the method”.

3.2. SPH FORMULATION

The main features of the classical SPH formulation are described in this section, based on Monaghan (1982), Monaghan (1992), Liu and Liu (2003), and Monaghan (2005). Alternative formulations can be found in Vila (1999), Ferrari *et al.* (2009), Molteni *et al.* (2007), Colagrossi and Landrini (2003). Some numerical aspects of SPH for dynamic fluid flows, namely, density smoothing techniques and numerical stability, are briefly addressed as well.

The SPH essential formulation lays on the idea of discretizing the media into material points (referred to as particles) carrying individual quantities, e.g. mass (m), density (ρ) volume (V), dynamic viscosity (μ) and velocity vector (\mathbf{u}). These particles evolve according to governing equations which are written in terms of fluxes between particles. Hereafter, particles are denoted by subscripts a and b , being b any particle in the neighborhood of particle a . Interpolation is based on the particle position \mathbf{r}_a , using a weighting function or kernel W .

For the sake of clarity, the SPH formulation is often divided into two steps: the first step is the integral representation or the kernel approximation of field functions and the second is the particle approximation. The SPH formulation starts with the integral representation of a field function using the Dirac delta function $\delta(\mathbf{r}_a - \mathbf{r})$. Let f be an arbitrary scalar field defined on the computational domain, Ω . The value of f at position \mathbf{r}_a is given by

$$f(\mathbf{r}_a) = \int_{\Omega} f(\mathbf{r})\delta(\mathbf{r}_a - \mathbf{r}_b)d\mathbf{r} \quad (8)$$

The Delta Dirac function lacks properties as continuity and differentiability and so, for practical reasons, the Dirac distribution is approached through an interpolation kernel, denoted as $W(\mathbf{r}_a - \mathbf{r}_b, h)$, where

h is the smoothing length⁶ or smoothing scale, which is a measure of the kernel's support size. The smoothing length, h , is an important parameter in the SPH method - if h is too small, there may be not enough particles in the support domain to exert forces on a given particle, which results in low accuracy; on the other hand, if h is too large, all details of the particle or local properties may be smoothed out and the accuracy suffers too. There is a range of SPH kernels in the literature, e.g. Cubic spline, quintic spline, Wendland C^2 , Wendland C^4 , among others (refer to e.g. Monaghan, 1992, Liu, 2003, Liu and Liu, 2003 and Monaghan, 2005). In the framework of this thesis, the continuous SPH interpolation is performed with the following Wendland C^2 kernel (Wendland, 1995):

$$W(q, h) = \begin{cases} \frac{\alpha_w}{h^3} \left(1 - \frac{q}{2}\right)^4 (1 + 2q) & \text{if } 0 \leq q \leq 2 \\ 0 & \text{if } q > 2 \end{cases} \quad (9)$$

With $\alpha_w = \frac{21}{16\pi}$ in three dimensions and $q = \frac{r}{h}$, being r the radial distance.

The value of f at \mathbf{r}_a can be estimated through a continuous interpolation that involves its values at surrounding points. This reads

$$f(\mathbf{r}_a) = \int_{\Omega} f(\mathbf{r}_b) W(\mathbf{r}_a - \mathbf{r}_b, h) d\mathbf{r} \quad (10)$$

The number of neighbouring particles contributing to the estimation of Eq (10) is typically 30 in 2D simulations and 250 in 3D simulations. Therefore, it can be concluded that the method can be computationally expensive to simulate large-scale 3D applications. GPUs make it now possible to run simulations with millions of particles with runtimes of the order of hours rather than months (Violeau and Rogers, 2016). Each GPU has numerous streaming processors, which mathematical power can be used for computer simulations that are not data-intensive, through the Compute Unified Device Architecture (CUDA) programming language from Nvidia, firstly introduced in 2007.

The approximation for the spatial derivative $\nabla \cdot f(\mathbf{r}_a)$ is obtained by substituting $f(\mathbf{r}_a)$ with $\nabla \cdot f(\mathbf{r}_a)$ in Eq. (10), which gives

$$\nabla \cdot f(\mathbf{r}_a) = \int_{\Omega} [\nabla \cdot f(\mathbf{r}_b)] W(\mathbf{r}_a - \mathbf{r}_b, h) d\mathbf{r} \quad (11)$$

Developing equation (11) and applying the divergence theorem it appears

$$\nabla f(\mathbf{r}_a) = \int_S f(\mathbf{r}) W(\mathbf{r}_a - \mathbf{r}_b) \cdot \vec{\mathbf{n}} ds - \int_{\Omega} f(\mathbf{r}) \cdot \nabla W(\mathbf{r}_a - \mathbf{r}_b, h) d\mathbf{r} \quad (12)$$

Where $\vec{\mathbf{n}}$ is the unit vector normal to the surface S .

When the support domain of the smoothing function W is located within the problem domain, the surface integral on the right-hand side of Eq. (12) is zero. Otherwise W is truncated by the boundary and this parcel is no longer zero. Under such circumstances, modifications should be made to remedy the

⁶ Dehnen and Aly (2012) pointed out that h should be replaced by the kernel standard deviation.

boundary effects, so that a wall boundary condition treatment is required. Some of the existing approaches are addressed in section “3.4. Boundary conditions in SPH”.

Since the entire system is not continuous but represented by a finite number of particles, the continuous integral representations are converted to discretized forms of summation over all the particles in the support domain. This constitutes the second key step of SPH, known as particle approximation. The particle approximation of a function at particle a can be written as

$$f(\mathbf{r}_a) = \sum_b V_b f_b W_{ab} \quad (13)$$

Where $f_b = f(\mathbf{r}_b)$ and $W_{ab} = w(\mathbf{r}_{ab}) = W(\mathbf{r}_a - \mathbf{r}_b)$.

The particle approximation for the spatial derivative of the function at particle a is

$$\nabla \cdot f(\mathbf{r}_a) = - \sum_b V_b f_b \cdot \nabla W_{ab} \quad (14)$$

The particle approximation introduces the mass and density (as these relate to V as $V = m/\rho$) of the particle into the equations. This is probably one of the major reasons for the SPH method being popular for dynamic fluid flow problems, in which density is a key field variable. The density of a particle is a weighted average of those of all particles in its support domain, which gives

$$\rho_a = \sum_b m_b W_{ab} \quad (15)$$

The density approximation is very important in SPH method because density determines the particles' distribution and the smoothing length evolution. There are two approaches to evolve density in the conventional SPH method: the summation density and the continuity. The former was presented previously in Eq. (15). The continuity approach, which approximates the density according to the continuity equation using the concepts of SPH approximations plus some transformations, is written, using the Einstein summation, as

$$\frac{D\rho_a}{Dt} = \sum_b m_b \mathbf{u}_{ab}^\beta \frac{\partial W_{ab}}{\partial x_a^\beta} \quad (16)$$

Where $\mathbf{u}_{ab} = \mathbf{u}_a - \mathbf{u}_b$. The derivation of SPH formulations for particle approximation of momentum and energy can be written as

$$\frac{D\mathbf{u}_a^\alpha}{Dt} = - \sum_b m_b \left(\frac{\sigma_a^{\alpha\beta}}{\rho_a^2} + \frac{\sigma_b^{\alpha\beta}}{\rho_b^2} \right) \frac{\partial W_{ab}}{\partial x_a^\beta} + F_a \quad (17)$$

$$\frac{De_i}{Dt} = \frac{1}{2} \sum_b m_b \left(\frac{p_a}{\rho_a^2} + \frac{p_b}{\rho_b^2} \right) \mathbf{u}_{ab}^\beta \frac{\partial W_{ab}}{\partial x_a^\beta} + \frac{\mu_a}{2\rho_a} \mathbf{s}_a^{\alpha\beta} \mathbf{s}_a^{\alpha\beta} \quad (18)$$

Where F_a represents the external forces acting on particle a , e the internal energy, $\sigma^{\alpha\beta}$ the stress tensor, $s^{\alpha\beta}$ the strain-rate tensor and u^β the velocity component.

Equations (16), (17) and (18) are a set of commonly used SPH equations for the NSE. It should be noted that by using different numerical tricks, it is possible to get other different forms of SPH equations for the same PDEs. The pressure, p , is then evaluated from a state equation, Riemann solver or Poisson equation, as stated above.

A common way of writing the pressure gradient in SPH consists of inserting the density into the gradient operator in the continuous formalism

$$\frac{1}{\rho} \nabla p = \nabla \frac{p}{\rho} + \frac{p}{\rho^2} \nabla \rho \quad (19)$$

Then, approximating the right-hand-side of Eq. (19), with the basic form of the gradient of a function at a particle a , yields a SPH form of the pressure force experienced by a particle a

$$\left(-\frac{1}{\rho} \nabla p \right)_a \approx -\sum_b m_b \left(\frac{p_a}{\rho_a^2} + \frac{p_b}{\rho_b^2} \right) \nabla_a W_{ab} \quad (20)$$

In the traditional SPH solvers (WCSPH), the pressure is obtained from the Tait equation of state (Tait, 1888), as suggested by Monaghan (1994), which links the pressure, p , to the density, ρ , by

$$p = \frac{\rho_0 c_0^2}{\xi} \left[\left(\frac{\rho}{\rho_0} \right)^\xi - 1 \right] \quad (21)$$

Where c_0 is the numerical speed of sound, ρ_0 the reference density and ξ the polytropic index ($\xi = 7$, for water, Monaghan 1994). The value of the numerical speed of sound, c_0 , is set so that the density variations are kept in the interval $\pm 1\%$. For confined flows c_0 is usually taken as $c_0 = 10 u_{max}$, where u_{max} is the maximum velocity of the flow. For free-surface flows, c_0 is taken as $c_0 = 10 \max(u_{max}, \sqrt{gH})$, where H is a reference water depth.

Such as all numerical models, SPH suffers from numerical instabilities if the time step is not carefully controlled. Thus, restrictions on the time-step size must be enforced (Violeau and Leroy, 2014). Due to the complexity of the theoretical stability analysis in SPH, empirical conditions on the time-step size are usually applied, inspired from the mesh-based methods (Morris *et al.*, 1997). The first one is the Courant-Friedrichs-Levy (CFL) condition, which ensures that the time-step remains lower than the maximal convection time on the smoothing length h , during the simulation. Moreover, a condition relative to the viscous forces must be enforced. The time-step can then set through the following relation (Leroy, 2014)

$$\delta t = \min \left(C_{CFL} \frac{h}{c_0}, C_{visq} \frac{h^2}{\nu} \right) \quad (22)$$

The coefficient $C_{CFL} = 0.3$ and $C_{visq} = 0.125$ were determined based on numerical studies (refer to, e.g., Morris *et al.*, 1997). The condition relative to the viscous forces may be dominant in the case where

dense granular flows are simulated, e.g. landslides, and such a condition may lead to strong reduction of the time step as shown by Manenti *et al.* (2018).

Extensive research has been carried out during the last two decades to overcome the main drawbacks of this method, however, there is still considerable ongoing research, being SPH still unconventional in comparison with other mesh-based methods (refer to Fig. 22). In the following sections, the current state-of-knowledge of some of these research areas is addressed, in particular for density correction techniques, boundary conditions, turbulence modelling, multiphase modelling and GPU computing. It is worth mentioning that this is a brief review, far from being exhaustive. Further description on the recent developments of the SPH method is available from Liu and Liu (2010), Gomez-Gesteira *et al.* (2010) and Violeau and Rogers (2016).

3.3. DENSITY CORRECTION IN SPH

The greatest advantage of the WCSPH approach is the ease of programming, however, there are also some drawbacks – a very small time-step is required, and small density errors cause significant non-physical pressure fluctuations. When Eq. (21) is used, a possible reason for the non-physical pressure fluctuations is the fact that pressure is a function of a high power of the density, through the equation of state (small errors on the density then yield very large errors on the pressure). In addition, small errors on the density may be amplified by the coefficient c_0 squared and this is why density smoothing procedures are necessary and widely used. Proposed solutions to circumventing such problems are (i) an incompressible approach (ISPH); (ii) the employment of a density filter (such as: a Monaghan type artificial viscosity term, Π_{ab} , in the physical pressure term; a density filter following Colagrossi and Landrini, 2003; the δ -SPH scheme by Antuono *et al.*, 2010, 2012; a density diffusion term following Brezzi and Pitkäranta, 1984); or (iii) Riemann solvers (e.g. Cha and Whitworth, 2003; Inutsuka, 2002). In the ISPH, pressure is treated separately and computed from a pressure Poisson equation, thus no longer a dependent variable (Cummins and Rudman, 1999). The use of an artificial viscosity term, Π_{ab} , added to the physical pressure term (in Eq. 17), in SPH is presented in literature by e.g. Monaghan (1992), and it is given by

$$\Pi_{ab} = \begin{cases} -\alpha_{\Pi} \bar{c}_{ab} \phi_{ab} + \beta_{\Pi} \phi_{ab}^2 & \mathbf{v}_{ab} \cdot \mathbf{r}_{ab} < 0 \\ 0 & \mathbf{v}_{ab} \cdot \mathbf{r}_{ab} \geq 0 \end{cases} \quad (23)$$

where α_{Π} and β_{Π} are constants with different values according to each problem, \bar{c}_{ab} is the average speed of sound between particles a and b , $\phi_{ab} = h \mathbf{v}_{ab} \cdot \mathbf{r}_{ab} / r_{ab}^2 + \eta^2$, being $\eta = 0.1h$. Modifications to the Monaghan type artificial viscosity were proposed such as that by Morris and Monaghan (1997).

Another possible strategy is to add a diffusive term inside the continuity equation (Eq. 16) as

$$\frac{d\rho_a}{dt} = \sum_b m_b (\mathbf{u}_b - \mathbf{u}_a) \cdot \nabla_a W_{ab} + \delta h c_0 D_a \quad (24)$$

where ρ_0 is the density of the fluid at rest, δ is related to the magnitude of the numerical diffusive contribution in the continuity equation added for stability purposes and $D_a = 2 \sum_b \psi_{ab} \nabla_a W_{ab} V_b$.

Molteni and Colagrossi (2009) and Ferrari *et al.* (2009) suggested the computation of ψ_{ab} following to Eq. (25) and Eq. (26), accordingly

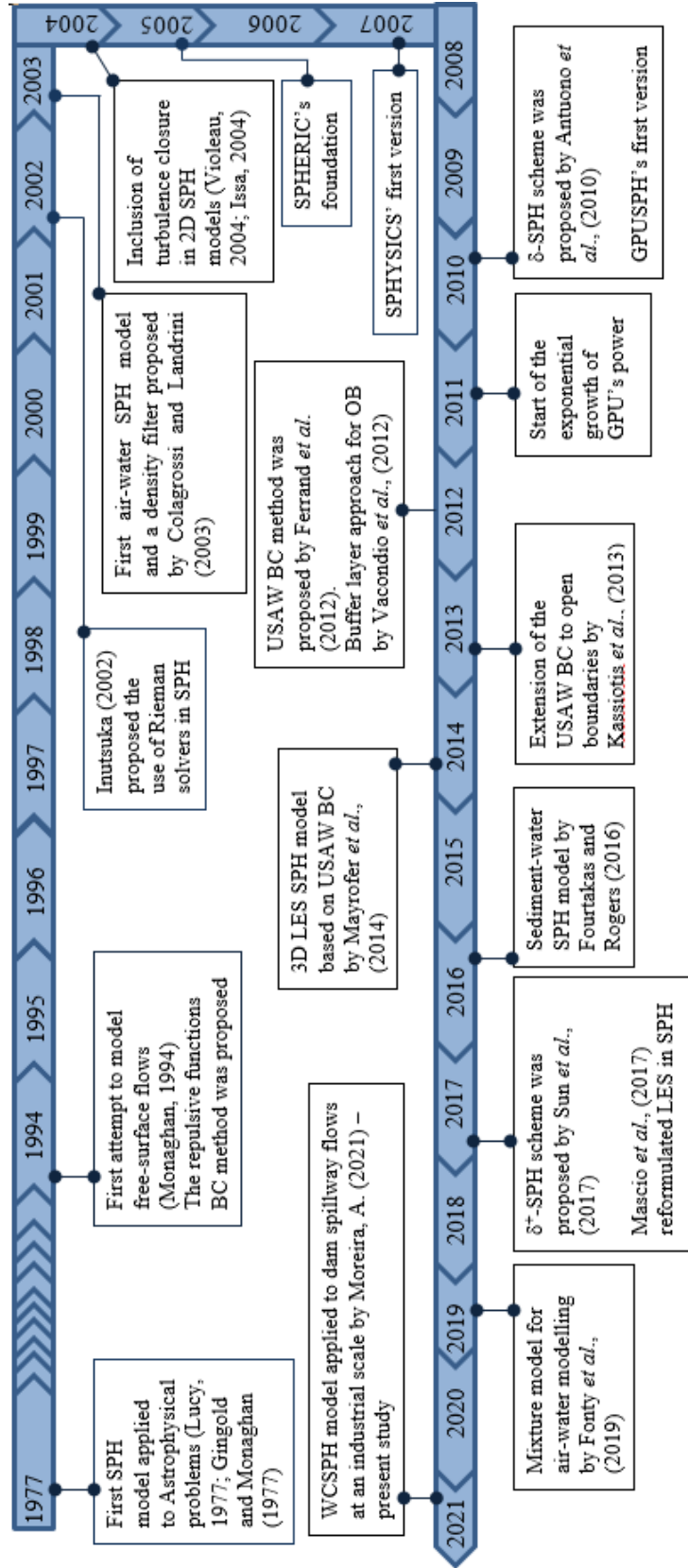


Fig. 22 - Timeline of some SPH developments (BC – boundary conditions; OB – open boundaries).

$$\psi_{ab} = (\rho_b - \rho_a) \frac{(\mathbf{r}_b - \mathbf{r}_a)}{|\mathbf{r}_b - \mathbf{r}_a|^2} \quad (25)$$

$$\psi_{ab} = (\rho_b - \rho_a) \frac{(\mathbf{r}_b - \mathbf{r}_a)}{2h|\mathbf{r}_b - \mathbf{r}_a|} \quad (26)$$

Since Eq. (25) and Eq. (26) demonstrated to be inconsistent close to the free-surface, Antuono *et al.* (2010) further improved the work by Molteni and Colagrossi (2009) to include a proper artificial diffusive term in the continuity equation. In this scheme, named as δ -SPH scheme, ψ_{ab} is computed as

$$\psi_{ab} = \left[2(\rho_b - \rho_a) - (\langle \nabla_\rho \rangle_b^L + \langle \nabla_\rho \rangle_a^L) \cdot (\mathbf{r}_b - \mathbf{r}_a) \right] \frac{(\mathbf{r}_b - \mathbf{r}_a)}{|\mathbf{r}_b - \mathbf{r}_a|^2} \quad (27)$$

Where $\langle \nabla_\rho \rangle^L$ is the renormalized density gradient. The δ -SPH scheme can be easily implemented and the main benefit with respect to the standard SPH is the stabilization of the scheme avoiding the occurrence of a non-physical energy flux to high-frequency modes (Sun *et al.*, 2017), reason why it has become quite popular for simulating hydrodynamics problems (e.g. Crespo *et al.*, 2015). More recently, Sun *et al.* (2017) proposed an improvement to the δ -SPH scheme, as it still presented some unsolved problems related to the tensile instability (Swegle *et al.*, 1995), named δ^+ -SPH, which main modification is linked to the introduction of a reformulated Particle Shifting Technique.

3.4. BOUNDARY CONDITIONS IN SPH

The implementation of boundary conditions in the SPH method is not as straightforward as generally it is for mesh-based methods (e.g. Neumann boundary conditions and Dirichlet boundary conditions). This has been regarded as a weak point of particle methods, for which a lot of research works have been published. When a fluid particle approaches a solid boundary, only the particles inside the domain are involved in the SPH interpolants. This incompleteness of the kernel can generate odd effects, because, on the solid surface, although the velocity is zero, other field variables such as density are not. Since the first SPH model for free-surface flows by Monaghan (1994), there have been many proposals for boundary treatments. They can be categorised in 3 groups: (i) repulsive functions, (ii) fictitious particles and (iii) boundary integrals (Fig. 23). The approaches falling in the first two groups (also called classical boundary conditions) are pragmatic but suffer from some disadvantages (as explained hereafter). On the other hand, the boundary integrals approach is rather accurate, however, it is complex and computationally expensive (Violeau and Rogers 2016).

The repulsive functions approach (Monaghan, 1994) is a classical way of imposing wall boundary conditions in SPH by discretising the boundary through particles and imposing repulsive forces between boundary particles and the free (fluid) particles. Generally, the repulsive force employed derives from the Lennard-Jones potential. This method is easy to implement even for complex geometries and is computationally cheap but leads to spurious behaviours of the particles as the SPH equations are inaccurately solved close to the boundaries. Improvements of this technique were proposed by Monaghan and Kos (1999) and Rogers and Dalrymple (2008).

Another very classical technique for modelling boundaries in SPH is the fictitious particles approach. The basic idea is to place two or more layers of ghost particles beyond the boundary, so as to fill the

void in the particle kernel. This approach includes three techniques: prescribed fluid particles, mirror particles and image transpose particles. The prescribed fluid particles technique is pragmatic but suffer from disadvantages such as not preventing particles from penetrating the boundary and creating unphysical separation and boundary layers. For engineering applications, enforcing solid impermeable boundaries is essential.

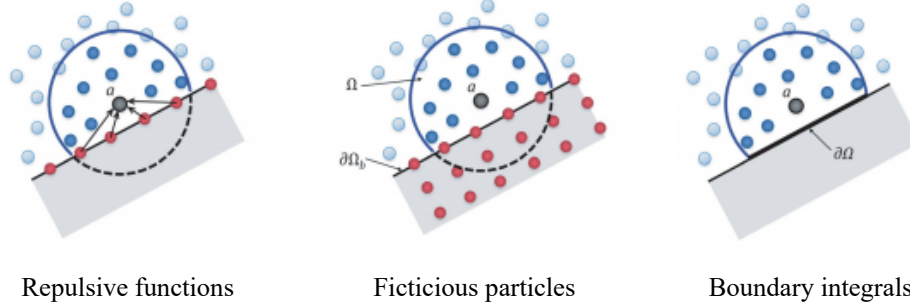


Fig. 23 - Generic SPH boundary treatments for rigid walls as particle approaches the boundary $\partial\Omega_b$. The grey shaded area is the solid boundary, the blue particles are fluid particles and the red particles are boundary particles (adapted from Violeau and Rogers, 2016).

In the mirror particles boundary technique, when a real particle is close to a boundary (the distance is shorter than the kernel smoothing length), a fictitious particle is generated outside of the system, which has the same density and pressure but opposite velocity, preventing particle penetration. This approach works well for simple geometries but for complicated geometries its implementation becomes prohibitively difficult (Børve, 2011). The image transpose particles boundary treatment takes images of the particles in the fluid domain and transposes them from a Lagrangian to an Eulerian frame of reference (Marongiu *et al.*, 2007; Narayanaswamy, 2009), then employs more conventional boundary treatments and transforms them back to the Lagrangian frame to impose the boundary condition.

More recently, other methods to model solid boundaries were proposed, that rely on the use of a wall renormalization factor in the SPH interpolation in order to compensate the lack of neighbouring particles outside of the fluid domain, so that the continuous SPH interpolation (Eq. 10) is then modified and reads

$$f(\mathbf{r}_a) = \frac{1}{\gamma_a} \int_{\Omega} f(\mathbf{r}_b) W(\mathbf{r}_a - \mathbf{r}_b, h) d\mathbf{r} \quad (28)$$

where γ_a is the kernel renormalization parameter, defined as

$$\gamma_a = \int_{\Omega} w(|\mathbf{r} - \mathbf{r}_b|) d\mathbf{r}^3 \quad (29)$$

γ_a is thus equal to 1 far from the boundary and lower than one when the kernel support is truncated. Then the discrete interpolation of a field, in place of Eq. (13), reads

$$f(\mathbf{r}_a) = \frac{1}{\gamma_a} \sum_b V_b f_b W_{ab} \quad (30)$$

This idea original by Kulasegaram *et al.* (2004), was followed by Feldman and Bonet (2007) and De Lefte *et al.* (2009). Ferrand *et al.* (2013) extended this approach to arbitrary wall boundary conditions

in what was called the Unified Semi-Analytical Wall (USAW) boundary conditions, including the Neumann condition for diffusion terms. This work was followed by Mayrhofer *et al.* (2013) and further simplification were proposed by Amicarelli *et al.* (2013) and Cercos-Pita (2015). Recently, this technique has proved to be very efficient in predicting near-wall phenomena with ISPH (Leroy *et al.*, 2014). The USAW boundary conditions is the wall boundary treatment used in the present research as it is particularly appropriate to model complex geometries and provides good accuracy of results. In this method, the fluid domain Ω comprises three different types of particles: fluid particles and vertex particles constituting the set P and boundary elements (triangles in 3D) constituting the set S (Fig. 24). At each summit of these boundary elements lays a vertex. The vertex particles make it possible to efficiently impose Dirichlet boundary conditions. The derivation of the wall boundary terms using continuous interpolation and the wall corrected operators in the discrete NSE for this technique can be read from Ferrand *et al.* (2013).

Open boundaries are required whenever one wants to simulate a large-scale flow, yet, their implementation in SPH is not straightforward since an open boundary is Eulerian by nature. The simplest way to treat inlet/outlet boundary conditions in SPH is to use a buffer layer where the values of the fields at the boundary are imposed on several layers of particles that complete the kernel support of free particles close to the open boundary (Vacondio *et al.*, 2012). At an inflow boundary, a particle that enters the domain is changed into a free particle and its physical quantities are not imposed anymore. On the other hand, at an outflow boundary, a particle that leaves the domain is changed into a buffer particle and its physical quantities are prescribed. However, such implementation can generate spurious shocks, which are difficult to fix and is problematic for complex inlets where the flow may not be parallel to the boundary normal.

To remedy these problems, the unified semi-analytical technique for imposing wall boundary conditions was extended to the imposition of open boundaries by Kassiotis *et al.* (2013). The idea is to use domain discretization described above (for the USAW boundary conditions) and to let the masses of the vertex particles belonging to open boundaries evolve over time as a function of the desired ingoing/outgoing mass flux through the open boundary segments (Fig. 25). The vertex particles are then used to create/delete fluid particles, which is done by setting a minimum and a maximum value for their mass, proportional to the mass of the free particles (Leroy, 2014). This technique ensures that the total mass variation is a continuous function of time, so that the particle creation/destruction does not introduce any perturbation on the density or on the momentum. Besides, it keeps a correct particle distribution near the open boundaries (Leroy, 2014). A more detailed description of this algorithm is given in Ferrand *et al.* (2017).

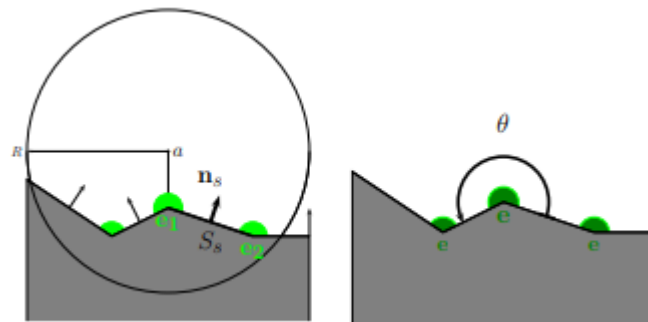


Fig. 24 - Sketch of the continuous medium discretisation with the USAW boundary conditions technique. Vertex particles, e , in green and segments, s , which have a surface, S_s , and an inward normal, \mathbf{n}_s (from Ferrand *et al.*, 2013).

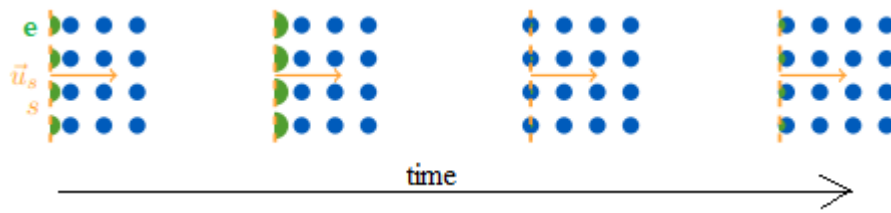


Fig. 25 - Sketch of the process of particles creation with vertex particles e in green, free fluid particles in blue and segments s at an inflow boundary (adapted from Ferrand et al., 2017).

When analytical open boundaries cannot be prescribed, a coupling strategy can be used to input some information into an SPH model from another model, which can be mesh-based. Such a coupling strategy allows the exploitation of the advantages of two different models. In this scope, Chiron (2017) proposed a coupling between SPH and FVM that made it possible to manage inputs / outputs between the two solvers in a generic and transparent way for both 2D and 3D simulations.

There has been steady progress in developing new boundary treatments in SPH, with improved behaviour for flows in the vicinity of boundaries. Yet, it is clear that there is no consensus in the SPH community on the best approach and there are numerous phenomena which are not adequately captured by current formulations (Violeau and Rogers, 2016).

3.5. TURBULENCE MODELLING IN SPH

In 1922, Richardson found out that the largest scales get kinetic energy out of the main flow and this energy is transferred to smaller scales (Kolmogorov's scale) until the energy is dissipated by viscous processes. This transfer of energy between different scales is called energy cascade. Reynolds was the first person to quantify the turbulence with a parameter, the Reynolds number, that depends on a characteristic velocity scale of the flow (U), a characteristic length scale (l) and the fluid's kinematic viscosity (ν).

$$Re = \frac{Ul}{\nu} \quad (31)$$

In the early applications of SPH to free-surface flows, turbulence was generally ignored since SPH proved particularly appropriate for representing violent flows, where inertia, pressure and gravity play a major role (Violeau and Rogers, 2016). This is because SPH broadly fits within the class of simulation techniques known as Large Eddy Simulations (LES) (Cleary *et al.*, 2007), namely the spatial interpolation used in SPH (Eq. 10) is formally identical to the spatial filtering used to construct LES methods.

Early attempts to use stochastic models based on the Langevin equations to deal with turbulence in SPH had limited success (Violeau *et al.*, 2002; Welton and Pope, 1997). Also, among the first papers on turbulence is the implementation of the α turbulence model (Holm, 1999) by Monaghan (2002). As with many numerical methods, SPH has been used for modelling turbulent flows through direct numerical simulation (DNS), more precisely with very refined resolution. Most of these attempts have been conducted for 2D simulations (e.g. Robinson, 2009; Robinson *et al.*, 2008; Valizadeh and Monaghan, 2012), with a limited meaning and restricted field of application⁷. A few attempts have been made with 3D simulations (Issa, 2004; Mayrhofer *et al.*, 2015) especially due to the high computational cost of

⁷ As turbulence is a three-dimensional phenomenon itself.

such simulations. However, the impressive development of GPU cards over the last few years and the adaptation of SPH codes to their architecture made massive parallelism financially accessible.

Despite the imposition of wall functions in turbulence models⁸ is inaccurate when using classical SPH boundary conditions, as explained by Leroy (2014), various authors developed LES and RANS SPH models using fictitious particles boundary conditions (e.g. Violeau and Issa, 2007; De Padova *et al.* 2013). To date, most of the SPH turbulence models used for engineering applications have been based on RANS approaches with first-order closure (eddy viscosity models), using the mixing length model (Violeau *et al.*, 2002) or $k-\epsilon$ models (Violeau, 2004; Violeau and Issa, 2007). The latter was successfully applied e.g. by Shao (2006) (to model wave overtopping, in association with ISPH) and De Padova *et al.* (2013) (to model 3D hydraulic jump). Other RANS models in SPH, like the $k-\omega$ model and explicit algebraic Reynolds stress models (Wallin and Johansson, 2000) are suggested by Violeau (2012) and some of them were tested by Violeau and Issa (2006) and Issa *et al.* (2010).

The $k-\epsilon$ turbulence model is widely used in the industry due to its simplicity and fairly good quality of results on most problems (despite its disadvantages of being inaccurate concerning non-inertial and streamline curvature effects, as well as severe deviation from local equilibrium). Basically, a SPH $k-\epsilon$ model consists in writing the standard $k-\epsilon$ equations using the SPH discrete operators presented in section “3.2. SPH formulation”.

$$\frac{dk_a}{dt} = P_a + L_a \left\{ \frac{v_{T,b}}{\sigma_k}, k_b \right\} - \epsilon_a \quad (32)$$

$$\frac{d\epsilon_a}{dt} = C_{\epsilon 1} \frac{\epsilon_a}{k_a} P_a + L_a \left\{ \frac{v_{T,b}}{\sigma_\epsilon}, \epsilon_b \right\} - C_{\epsilon 2} \frac{\epsilon_a^2}{k_a} \quad (33)$$

The eddy viscosity $\nu_{T,b} = C_\mu k_a^2 / \epsilon_a$ is then used in the momentum equation. The model constants σ_k , σ_ϵ , $C_{\epsilon 1}$, $C_{\epsilon 2}$ and C_μ are set as in Launder and Spalding (1974). The turbulent kinetic energy production rate, P_a , is computed from the velocity gradient tensor using the SPH gradient operator and L is a SPH Laplacian operator (Ferrand *et al.* 2013), which can be wrote as

$$L_a \{f_b\} = \sum_b f_b \nabla^2 W_{ab} \quad (34)$$

Various SPH Laplacian operators exist, like the one proposed by Cummins and Rudman (1999) or the Morris Laplacian operator (Morris *et al.* 1997).

Recently, the development of the USAW boundary conditions led to improvements of these turbulence models: in Ferrand *et al.* (2013) a $k-\epsilon$ model in WCSPH was proposed with much improved results compared to Violeau and Issa (2007). On the other hand, a 3D LES model based on the USAW boundary conditions was proposed in Mayrofer *et al.* (2014). In this work a LES simulation of a 3-D turbulent channel flow was performed, but the results showed a clear deviation from the DNS results on that case (Leroy, 2014).

Turbulence was identified as a key task by Violeau and Rogers (2016) for the next five years. As they stated, despite the efforts made over the past 10 years, advanced turbulence models for SPH are still

⁸ Which are required in RANS and LES models - see Section “2.3.5. Turbulence modelling”

poorly developed, requiring huge computation time even with GPUs (Mayrhofer *et al.*, 2015). Still, the work by Mascio *et al.* (2017) brought a new LES-SPH model formulation.

3.6. MULTIPHASE MODELLING IN SPH

In many circumstances, violent fluid–structure interactions lead to air entrapment and the development of multiphase flows. Both in coastal and dam engineering applications (e.g. Peregrine, 2003 and Manso *et al.*, 2009), the dynamics of the entrapped air at the impact may play a dominant role in the energy dissipation process, in the induction of pressure and in the free-surface elevation. A number of numerical techniques have been proposed to model flow fields with free-surfaces, most of them based on the use of an Eulerian grid where the fluid-flow equations are solved and coupled with a suitable technique to capture or track the interface. The Volume of Fluid (VoF) method (e.g. Lopes *et al.*, 2016) and the Level Set (LS) method (e.g. Qu *et al.* 2011) are two of the most well-settled ones. The weakness of the VoF method is the need to accurately calculate the spatial derivatives, mainly due to the volume fraction function discontinuity across the interface. The LS method is popular for computing two-phase flows with topologically complex interfaces, but it is unsatisfactory for maintaining mass conservation (Olsson *et al.*, 2007). A coupled VoF and LS method was proposed to overcome these limitations (Yin *et al.*, 2018), yet further validation of this method is needed to extend its applicability to engineering study cases.

Owing its Lagrangian nature, the SPH method is particularly suited to deal with multiphase flows and, to take advantage of such good ability multifluid SPH models have been extensively studied. However, as pointed out by Colagrossi and Landrini (2003) and Hu and Adams (2006), when large density ratios exist, like in air–water mixtures, severe instabilities develop along the fluid interface which prevent SPH to work. In the modelling of aerated flows, two main approaches can be considered (Fonty *et al.*, 2019):

- Two-fluid models in which each phase is described by a continuity and a momentum equations. Interfacial interactions introduce additional terms in these equations. They are closed by constitutive laws, depending on the flow regime, but their determination can prove to be tedious; and
- Mixture models in which the flow is seen as a single-fluid flow with one continuity and one momentum equation that rule the evolution of mixture quantities (mixture density and velocity, combinations of phase properties to be defined) complemented by an additional equation for the mass conservation of one phase. Some additional terms linked to the relative velocity between phases, computed through a closure law depending on the flow regime, appear in these equations. In the absence of relative velocity, one has a homogeneous fluid model.

The work by Colagrossi and Landrini (2003) was one of the first SPH studies to consider water–air flows at realistic density ratios of 1 to 1000. This two-fluid model used WCSPH with gradients recast in terms of volume (not density) to avoid issues around the density discontinuity at the water–air interface. The method also required an empirical adhesion term that physically resembled surface tension and maintained interface integrity. This work was extended by Grenier *et al.* (2009) who developed a multi-fluid SPH method derived from Lagrangian variational principles. Surface tension was included explicitly through the Continuum Surface Force approach, in addition to an empirical repulsive term in the pressure gradient that minimises the fragmentation of the interface (this term bears semblance to the cohesion force introduced by Colagrossi and Landrini, 2003). Both works - Colagrossi and Landrini (2003) and Grenier *et al.* (2009) - demonstrated good results for the chosen test cases, but both methods are based on WCSPH and are restricted to using non-physical speeds of sound. Monaghan and Rafiee (2013) presented a similar approach to model multi-phase flows with large density ratios,

however a larger sound speed is still required in the less-dense fluid. As these studies were based on the WCSPH formulation they lack accuracy in liquid pressure calculations. Therefore, ISPH was as well extended to multiphase flows by a number of authors (e.g. Hu and Adams, 2006). Following the idea that water–air flows of practical interest typically occupy flow regimes where air should be modelled as compressible, but water remains incompressible, some authors (e.g. Sun *et al.*, 2012 and Lind *et al.* (2016) presented two-phase incompressible-compressible SPH methods (ICSPH) for this type of flows, that employs WCSPH in the air phase and ISPH in the water phase. Sun *et al.* (2012) concluded that a two-phase flow consideration does not change the water movement significantly (in a dam break test case), but no quantitative validation was provided. Lind *et al.* (2016) validated their model using four different test cases, one of which a benchmark dam break case. The results from the method are promising, namely the pressure predictions for the dam break flow agreed well with experimental data up to the point of impact of the overturning front, when the flow becomes three dimensional. Subsequent pressure predictions do show a reduction in the spurious high frequency pressure oscillations observed with two-phase WCSPH, likely due to a more physical representation of the air pocket compressibility.

Mixture models are of particular interest for modelling flows with small-scale interfaces (e.g. dispersed air phase in a water flow). Using this approach in SPH results in having each individual SPH particle carrying the different phases with their respective volume fractions (rather than having different sets of particles for each phase). The reduced number of equations to solve is expected to limit the computations compared to two-fluid approaches with a different set of particles for each phase, as described in (Shi *et al.*, 2017) or (Kwon and Monaghan, 2015). A mixture model with a volume fraction formulation without phase exchanges between particles was implemented and compared to a multi-fluid formulation in Grenier (2009), showing the diffusion of the interfaces triggered by the mixture model. The multi-fluid formulation of SPH proved to perform better on the cases tested. Fonty *et al.* (2019) derived a realizable SPH mixture model and validated it with various test cases. Limits of the model were highlighted by a sand dumping case for which the model failed at reproducing the correct falling velocity and topology of a sand cloud at a given discretization compared to a two-velocity approach. Also, the pressure gradient computation for high density ratios needs more investigation.

Despite the valuable research done on this subject, it has not yet been proposed any robust and accurate enough multiphase SPH model to simulate complex turbulent and high-velocity flows such as those encountered in spillways and energy dissipators. This problem is an obstacle that hinders practical applications. Thus, further theoretical and computational research is required to address this problem. Within the subject of the present research, it is relevant to recall that:

- The majority of the multiphase formulations proposed for solving the closest-to-industry cases were applied for high-density ratios with low flow velocities (e.g. Nakayama *et al.*, 2016 simulated the skimming flow in a stepped channel using a multiphase SPH model achieving good qualitative agreement in terms of the air concentration near the steps' surface, but flow velocity was ~ 3 m/s, far from that found in prototype conditions). In high velocity flows (let's say 10 - 20 m/s) the compressibility of water could become significant and the severe cavitation could lead to the complex phase changes, so more advanced SPH models should be developed to account for these effects; and
- Accurately modelling multifluid phenomena with the usual SPH approach in the air-water case requires choosing a particle discretization of less than the size of an air bubble or water drop, which leads to high computational cost at the scale of practical interest for engineering applications (Fonty *et al.*, 2019). So, two-phase schemes validation has been limited to a small scale because of the computational costs incurred. High-performance computing achieved through the use of multiple GPU's may provide a solution to this issue.

Multiphase SPH sediment-water models have also been proposed, e.g. by Fourtakas and Rogers (2016), Ghaïatanellis (2017) and Zubeldia *et al.* (2018). SPH models to simulate bed erosion generally fall into two distinct categories: one is to treat the water and sediment media as two different fluid components and an interaction model is used to address the discontinuity of the two phases (Shakibaeinia and Jin, 2011), while another is to consider the critical velocity and shear stress of the flow acting on the sediment bed and treat the bed as an erodible solid wall (Hayashi *et al.*, 2003). Existing models are currently being validated against classical test cases and simple geometries tested in laboratory. Still, sediment scour problems in the scope of dam engineering are generally limited to event- and reach-level simulations, so modelling such scenarios more than a few hours of real-world time may be immensely computationally intensive. It is expected that its application to large-scale dam spillways will depend upon the hardware development and affordability, within the next years.

3.7. PARALLELIZATION THROUGH GPU COMPUTING

SPH has traditionally been an expensive computational method, especially because of the high number of interactions with neighbouring particles for each particle (approximately 250 in 3D), and the very small time-steps required, due to the use of explicit time integrators in WCSPH (Violeau and Rogers, 2016). This is a serious obstacle to the extension of the method to an industrial scale, but also to its development since even relatively small validation cases in 3D may take days or even weeks on sequential SPH codes (Leroy, 2014). Until recently, the implementation of hardware acceleration for CFD calculations was done by using High-Performance Computing (HPC) on supercomputers consisting of thousands of Central Processing Unit (CPU) cores. Even if they can be easily programmed, general purpose processors CPUs are not the very best architecture on which one can make fast scientific computations. For large computations with many millions of particles, exiting works (Maruzewski *et al.*, 2008) have shown that architectures such as BlueGene⁹ machines exhibit some limitations: parallel efficiency on thousands of cores tends to decrease dramatically. This approach may as well be technically difficult and expensive in terms of hardware investment and maintenance.

Lately, the growth of the computational power of GPUs, which are designed for three-dimensional graphics tasks, has been tremendous (Fig. 26). The capability of GPUs to simulate SPH was demonstrated by the pioneering work of Harada *et al.* (2007). Shortly after Harada's work, the advent of the Compute Unified Device Architecture (CUDA) programming language from Nvidia in 2007 allowed to fix most of the identified limitations by using advanced GPU programming features introduced by CUDA. Nowadays, simple C++ language can be used to access the mathematical power of the massively parallel cards. The first CUDA implementation of the SPH method was developed by Hérault *et al.* (2010). Owing to the specific suitability of SPH to the multi-processor parallel architecture of GPUs, several open-source GPU codes have been recently developed to be run on GPUs, including GPUSPH (Hérault *et al.*, 2010), DualSPHysics (Crespo *et al.*, 2015) and AQUAgpusph (Cercós-Pita, 2015).

Acceleration of the codes can be achieved either by using more advanced hardware and/or by optimizing the codes to better take advantage of the GPU characteristics. The later was investigated by Domínguez (2014). The performance of two different GPU cards was assessed upon a number of code optimizations and it was verified that these show different responses (in terms of speedup) to the various optimizations tested.

⁹ Supercomputers that can reach operating speeds in the PFLOPS (petaFLOPS) range, with low power consumption.

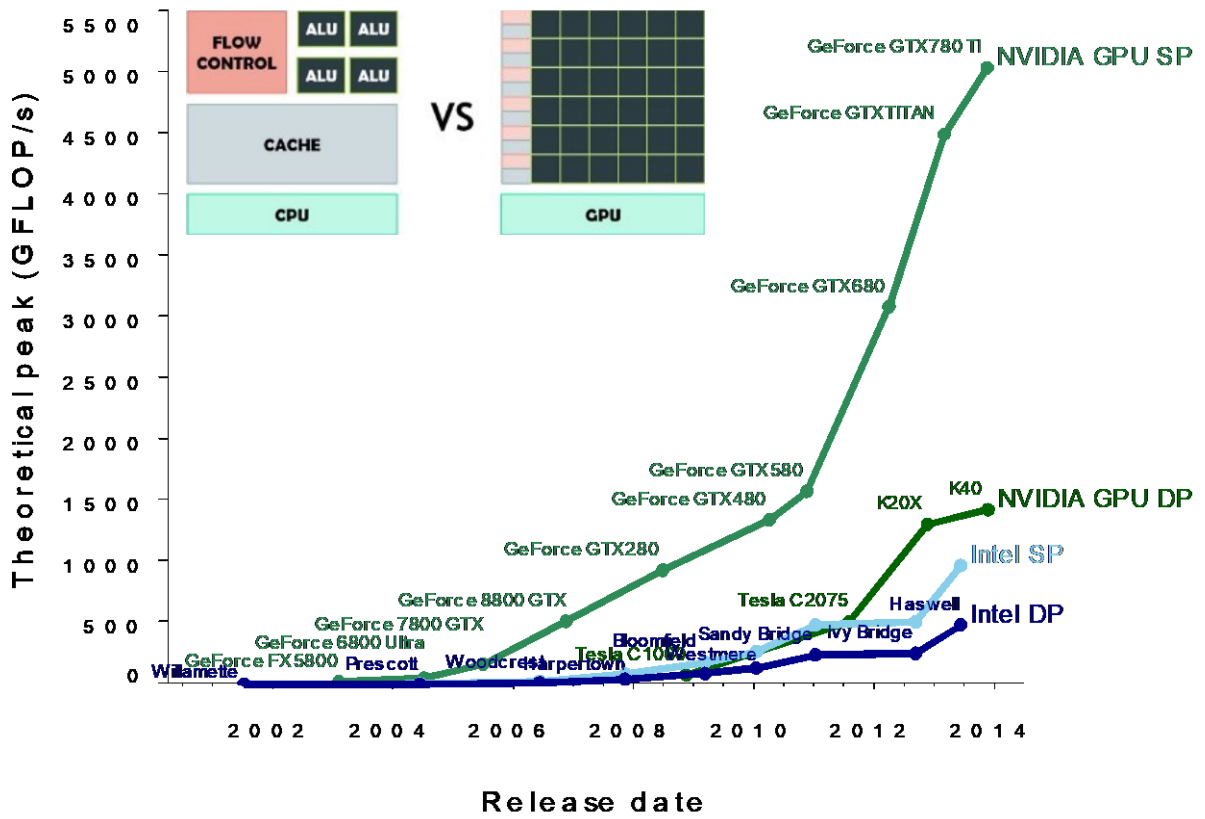


Fig. 26 - CPU and GPU performance evolution (adapted from <https://michaelgalloy.com>).

This means that optimizing a SPH code to be run on GPUs is dependent upon the GPU characteristics used (e.g. compute capability, number of cores, number of registers and cache memory), highlighting the complexity of this matter.

Fig. 27 and Fig. 28 present some numbers on the acceleration that can be achieved by using GPU computing instead of CPU computing and by optimizing the SPH programming to best suit the GPU’s architecture, accordingly. For simulating real-life problems, the use of multiple GPUs is recommended.

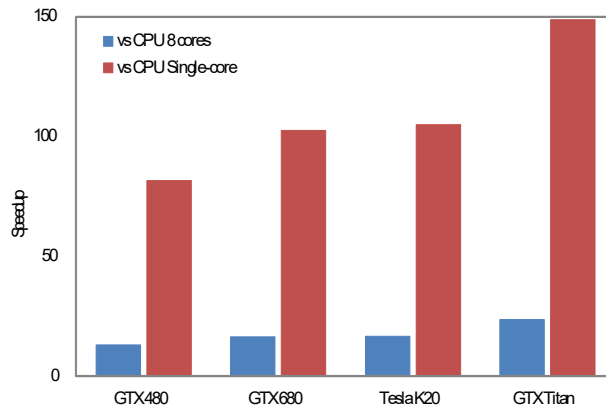


Fig. 27 - Speedups of GPU against CPU simulating 1 million particles (Domínguez, 2014).

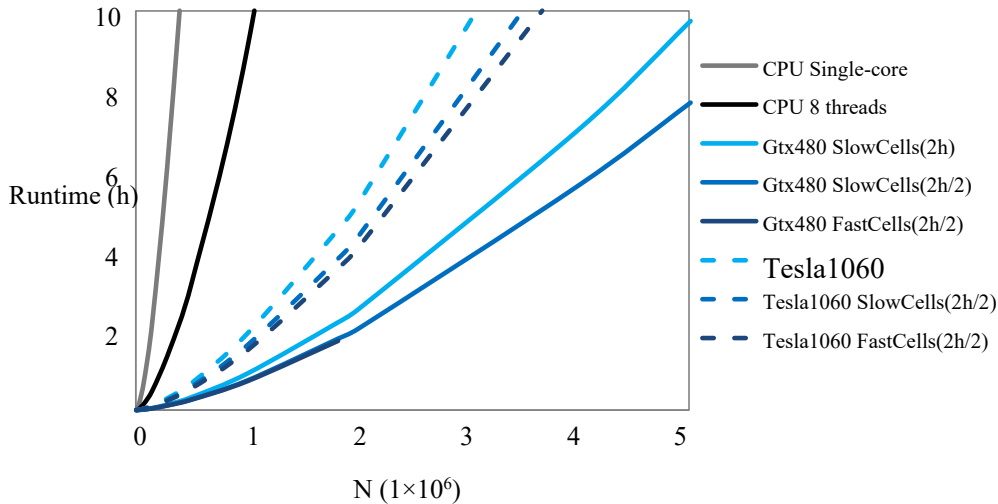


Fig. 28 - Runtimes for different CPU and GPU implementations as a function of the number of particles, N (adapted from Domínguez, 2014).

Combination of different devices can be done through Message Passing Interface¹⁰ (MPI) and CUDA, making possible the execution of SPH on heterogeneous clusters. In this approach, the physical domain of the simulation is divided into subdomains so that the size of the simulation scales with the number of machines.

3.8. SPH MODELLING OF FREE-SURFACE AND SPILLWAY FLOWS

As previously explained, meshfree methods present many advantages in the simulation of flows involving large deformations nevertheless they have been far less used in the numerical modelling of open-channel flows in comparison with mesh-based methods such as FVM or FEM. Mesh-based methods have provided useful and satisfactory results (e.g. Johnson and Savage, 2006; Kim *et al.*, 2010; Kumcu, 2016 and Moreira and Taveira-Pinto, 2017a, 2017b), however, their success largely rely on good quality meshes, and mesh adaptability and connectivity problems are likely to occur whenever large deformation of boundaries and interfaces exists. The SPH method is now becoming widely used for research applications on free-surface flows.

Within the last decade various SPH studies have been conducted addressing dam-related flows. These studies mainly addressed dam-break flows (e.g. Lee *et al.*, 2008 and Lee *et al.*, 2010), the estimation of the free-surface evolution over weirs of simple geometries (e.g. Ferrari, 2010) and hydraulic jump studies (López *et al.*, 2010b). Few industrial cases have been addressed, mainly for practical reasons based on the computational cost of this method, especially in three dimensions (Lee *et al.*, 2010). However, this research field has been progressing steadily and the current SPH state-of-knowledge along with the hardware technology improvements now permit the simulation of dam flows at an industrial scale, which means that complexities underlying real hydraulic structures (both in terms of structure geometry and hydrodynamics) can be taken into account in a numerical model.

In this section, an overview of the most relevant SPH studies published within this scope is presented. Some numerical aspects, potentialities and conditionals of the SPH method to model such flows are discussed. This overview shows how SPH developers reached the present state-of-knowledge. It does not cover the entire range of studies that could have been done, but it rather concentrates on the most

¹⁰ A library of functions that can be called from C, C++, and Fortran programs.

relevant published ones, for the sake of objectivity. Firstly, some conclusions from studies carried out on schematic geometries are reviewed. Yet, much attention is posteriorly given to industrial case studies, for which the reader may consult Table 8 (presented at the end of this section) to get a summary of some of their characteristics and quantitative validations done.

3.8.1. SCHEMATIC GEOMETRIES

The collapse of a water column, also designated as dam-break, has been extensively used by SPH researchers as a benchmark test for code validation. Many works have been published concerning this application (e.g. Lee *et al.*, 2008; Lee *et al.*, 2010; Crespo *et al.*, 2008; Albano *et al.*, 2014 and Jian *et al.*, 2015). Most of these have used theoretical or experimental data to validate the SPH model (e.g. Lee *et al.*, 2008, 2010, simulated the experiments by Kleefsman *et al.*, 2005, whereas Crespo *et al.*, 2008 described the development of the SPHysics code to model the experiments by Janosi *et al.*, 2004). Hydraulic jumps have been target of attention as well in e.g. López *et al.* (2010b) and Chern and Syamsuri (2013), and some simplistic simulations of spillway flows were addressed by various authors, such as Ferrari (2010) and Hussain (2016). These studies have led to relevant conclusions:

- ISPH yields smoother and more realistic velocity and pressure fields than WCSPH (Fig. 29) and provided, as well, a better qualitative representation of the splash behaviour. WCSPH results can approach ISPH results if a higher particle resolution is used (higher computation demand), especially at higher Reynolds numbers (Lee *et al.*, 2008);
- Leroy (2014) tested a 2D dam-break over an edge and found out that WCSPH can yield better pressure predictions when the USAW boundary conditions are used (Fig. 30) which allowed to conclude that computed pressures accuracy is as well related to the boundary conditions treatment employed;
- The CPU time required by ISPH is shorter than that by WCSPH, by about a factor of 2-20 depending on the cases, since it requires a larger time-step (Lee *et al.*, 2008 and Lee *et al.*, 2010), yet, it should be kept in mind that computational times are also dependent upon features as the wall boundaries approach used. For instance, Leroy *et al.* (2014) applied ISPH with USAW boundary conditions and observed that the additional time-step restriction due to the boundary integrals calculation actually increased the computational time for highly dynamic flows, so that ISPH and WCSPH presented similar performances;
- Both experimental flow depths and the bodies' movements in time were accurately fitted in 3D WCSPH simulations of a dam-break wave evolution involving two fixed structures and three mobile bodies, thus concluding that it can be used to evaluate the risks associated with floating bodies (Albano *et al.*, 2014);
- The features of the mixing interface of two water bodies in 2D dam-break flows were described in great detail, both from a qualitative and quantitative perspectives in Crespo (2008) and Jian *et al.* (2015);
- The traditional WCSPH model, with Monaghan artificial viscosity, allows investigation of water flows with low Froude numbers, nevertheless, with Froude numbers greater than 5 many differences have been found. The implementation of a more sophisticated turbulence model, such as $k - \epsilon$, or a modified viscosity model (modified α_π in Eq. 23), led to significant improvements in simulating hydraulic jumps with $Fr > 5$, however computational times were greater, especially using the $k - \epsilon$ model (almost double) (López *et al.*, 2010b);

- The effect of a corrugated bed on a hydraulic jump with respect to the conjugate depth, jump's length, shear stress and energy dissipation was correctly assessed with a 2D SPH model (Chern and Syamsuri, 2013);
- A 2D WCSPH simulation of a sharp-crested weir by Ferrari (2010) has been one of the first to consider an open boundary condition (namely, an outflow boundary) and it involved about half a million of fluid particles and was run on two of the most powerful High-Performance Computing (HPC) facilities in Europe. The computed free-surface profile was in close agreement with the experimental profile by Scimeni (1930);
- The flow depths and velocity profiles have been predicted with a maximum relative error of 7% and 6%, accordingly, in a 2D stepped spillway (Hussain, 2016). The author modified the open source code 2D SPHysics to satisfy the flow conditions in open channels by introducing a numerical SPH open boundary condition technique. The baseline for the numerical results validation was the experimental work by Meireles and Matos (2009); and
- The flow over a sharp-crested weir (previously studied from a physical model built at the Hydraulics Laboratory of the University of Liège) was simulated by Lodomez *et al.* (2014) with the application of a 2D SPH code developed by Lodomez (2014). Open boundaries were set to allow the inflow and outflow of particles to the computational domain. A satisfactory agreement was obtained between numerical results and experimental observations, concerning the upper and lower profiles of the jet over the sharp-crested weir.
- Nóbrega *et al.* (2020) simulated the flow over smooth and stepped spillways in the nonaerated, skimming flow regime using two-dimensional simulations. Continuous inflow fluid layers with constant height and uniform velocity were used to establish the flow rate on the broad crested weir. In general, the numerical flow depths compared well with the corresponding experimental data and with empirical formulas available in the literature. The velocity profiles, and the free-stream velocity, were also well reproduced by the SPH method; however, larger differences were obtained near the solid boundary.

The good results achieved with these simple geometries give confidence that SPH can be successfully applied to model rather complex hydraulic structures such as those addressed hereafter.

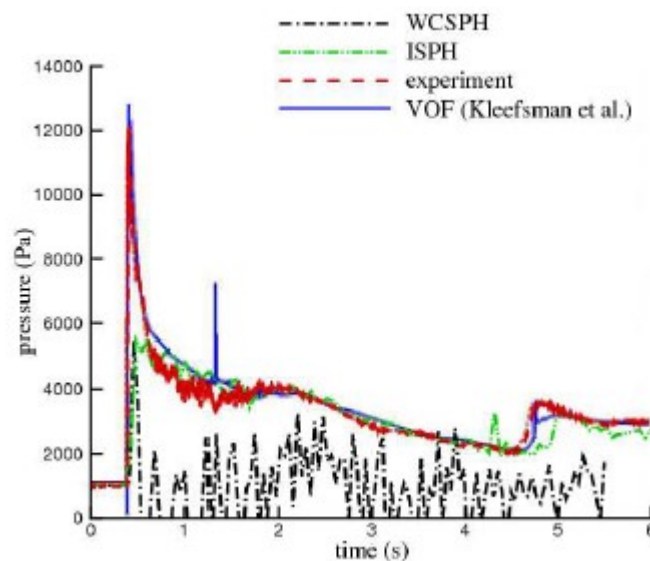


Fig. 29 - Time history of pressure at the toe of a square obstacle (Kleefsman *et al.*, 2005 experiments' configuration) according to WCSPH, ISPH, VoF and experiments (from Lee *et al.*, 2009, a fictitious particles approach was used for the boundary conditions treatment).

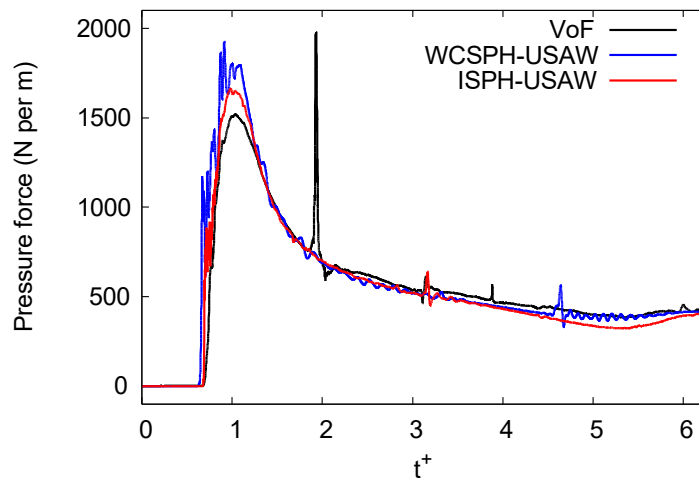


Fig. 30 - Comparison of the evolution of the pressure force applied on the left-side of the wedge between VoF, ISPH-USAW and WCSPH-USAW (from Leroy, 2014; $t^+ = t/\sqrt{gH}$).

3.8.2. INDUSTRIAL CASE STUDIES

The Goulours dam

The Goulours dam located in Midi-Pyrénées, France was originally equipped with a ski-jump spillway, however, this spillway was later proved to be insufficient to deal with the highest floods. Hence, a piano key weir was installed at the end of October 2006, as an additional floodwater evacuation system. This solution was studied with the construction of a physical model at the *Laboratoire National d'Hydraulique et Environnement* (LNHE) at *Électricité de France* (EDF) R&D. Fig. 31 shows a view of this model while the piano key weir is working.

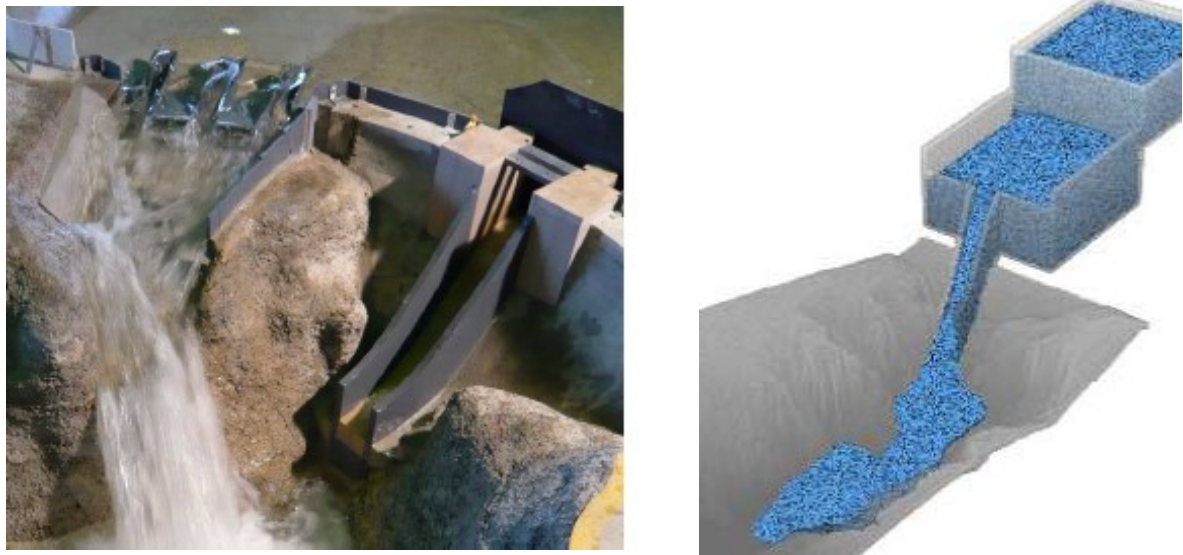


Fig. 31 - Spillway of Goulours dam from the physical model (left) and the numerical model (right) (from Lee *et al.*, 2009).

The model, built at the scale 1:20, provided experimental data of surface elevations upstream of the dam and along the ski-jump weir, among other data.

Lee *et al.* (2009) modelled the free-surface flow in the ski-jump spillway of the Goulours dam, using a WCSPH algorithm, namely the code *Spartacus-3D*, developed at EDF R&D together with the Saint-Venant Laboratory for Hydraulics. It has been validated on many cases and used in the context of industrial studies in two dimensions such as that by Violeau *et al.* (2008). The numerical model setup was subjected to many simplifications. To maintain a constant water level in the reservoir, a second reservoir upstream of the former was defined (see Fig. 31b). About 80 000 wall particles were used for the purpose of the spillway and reservoirs discretization, along with one layer of dummy particles (a boundary fictitious particles approach) everywhere. The valley, reservoirs and spillway geometry required a total of about 500 000 wall and dummy particles. The reservoirs were initially filled with about one million fluid particles. The total dimensions of the model including the valley and the reservoirs are 197 m \times 118 m \times 44 m.

The reported results were based on qualitative analysis (except for the pressure estimation at the top of the ski-jump) as the main objective so far was to examine the feasibility of such type of study. Qualitatively, the main features of the flow were well captured, the fluid particles behaved satisfactorily, and the bottom was perfectly impermeable. The shape of the ski-jump was designed to get a zero pressure at the top of it, and the computed results showed that the pressure at this location oscillates around zero, consistently with laboratory observations. However, the large oscillations in the modelled pressure were unsatisfactory. As explained earlier, the weakly compressible approach is mostly responsible for this. As stated by the authors, this issue must be properly addressed in order to estimate the force experienced by a structure and to predict the risk of cavitation on a concrete surface. The ISPH algorithm proposed in Lee *et al.* (2008), has been tested on SPHERIC test case number 2 (Kleefsman *et al.*, 2005's dam breaking experiment). Results showed that the method predicts well the pressure in the case of 3D free-surface flows in reservoirs (Fig. 29), as the computed pressures agreed well with measurements and VoF method results. The following was concluded from the work by Lee *et al.* (2009):

- The geometry of the hydraulic system under investigation was significantly simplified, in particular the geometry of the dam was not represented, and the ski-jump was slightly simplified. Indeed, the existence of two pillars immediately upstream the jump, which were not considered, were proved to control the flow over the weir. Therefore, further simulations should consider a more realistic geometry;
- The flow rate and the upstream water level need to be properly prescribed by means of 3D inlet boundary condition, on the basis of the developments proposed in Lastiwca *et al.* (2009) for 2D SPH flows. The solution of the two reservoirs used is rough and insufficient, especially for long-term simulations;
- Turbulence modelling should be considered in future simulations, in order to reproduce the energy dissipated by the flow past the ski-jump. For this purpose, the developments made at EDF R&D during the past years (Violeau and Issa, 2007) should be employed; and
- In virtue of the improved pressure predictions obtained with ISPH for SPHERIC test case number 2 (Kleefsman *et al.*, (2005)'s dam breaking experiment) in Lee *et al.* (2008), the authors suggested to test this approach on the present real study case, yet this would require parallelization of the ISPH code.

The authors foresaw that quantitative validations concerning pressure and velocity distributions, as well as surface elevation along the ski-jump will then be possible. The discharge coefficient, giving the flow rate as a function of the water elevation upstream the dam, will also be calculated and compared to measurements.

The Pala Tiloth dam

Saunders *et al.* (2014) used the 3D WCSPH method described in Cleary and Prakash (2004) to model the flow through a four bay, radial gated, submerged spillway system, including all near field dam components. According to the authors, this study was the first to use SPH to model a range of flow rates through a spillway in three dimensions and compare results with physical model data (namely, a reservoir water depth).

The spillway computations were performed at the same scale as the corresponding physical study for direct comparison and validation (Fig. 32). Efforts were firstly directed to the study of the effect of SPH resolution on the predicted water depths, in order to estimate the resolution required for highly accurate simulations. Six SPH resolutions, ranging from 0.01 to 0.035 m, were tested (which corresponds to 5392×10^3 to 242×10^3 fluid particles, respectively), at a discharge rate of 35.86 L/s. To set a fixed inflow rate, the discharge rate through the spillway was equal to the inflow rate and the reservoir water level was invariant. Boundary walls were modelled using a repulsive functions approach – the Lennard-Jones repulsive forces (see e.g. Monaghan, 1994). The simulation with the highest resolution took 28 days to reach a steady state (run in parallel using a dual Xeon 8-core E5-2650 machine), whereas, the lowest resolution simulation took 17 hours to reach a steady state.

The accuracy of the simulated spillway flow was found to be dependent upon the particle size used. Fig. 33 shows the percentage difference between the simulated water depth and the experimental water depth for the range of SPH resolutions tested. The percentage difference converged to a resolution independent value beyond a resolution of 0.02 m. Results for the particle size of 0.015 m are comparable to the highest resolution simulation of 0.01 m, with a relative difference of only 0.5% (Fig. 33). The particle size of 0.015 m was therefore used for the following simulations, as this resolution provides the desired balance between computational efficiency and accuracy.

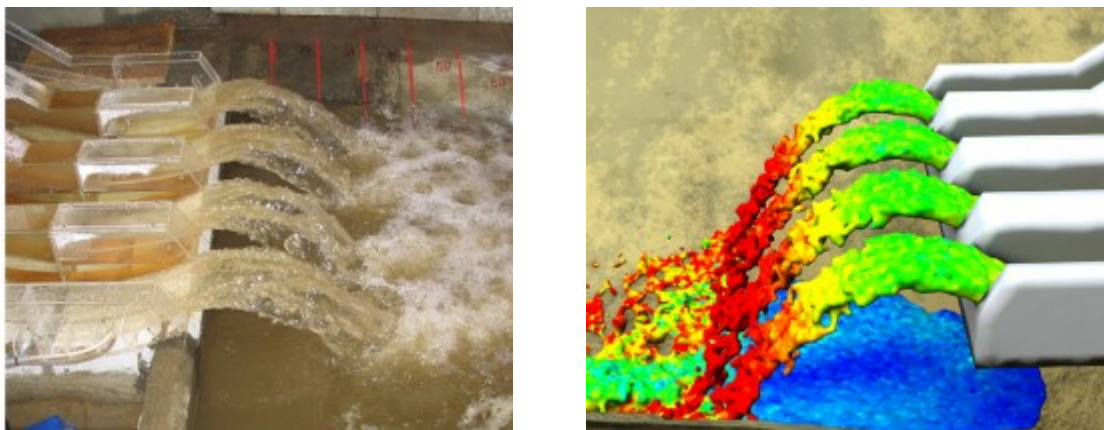


Fig. 32 - Physical model testing on the left and computed flow field on the right (from Saunders *et al.*, 2014).

Next, simulations for the remaining discharge rates (from 8.96 to 62.76 L/s, in model scale) were carried out and results were compared against experimental data, namely the reservoir water depth. However, there was an important limitation in this study – there was uncertainty in the location of the experimentally measured water depth. For this reason, the experimental water depths were compared against the corresponding computed values at different distances from the spillway crest. The maximum difference between the simulated and experimental water depth was 11.5%, which occurred at a discharge rate of 62.76 L/s. This depth was recorded in the center of the reservoir area. At the spillway crest the maximum difference was only 2.4% for a discharge rate of 8.96 L/s.

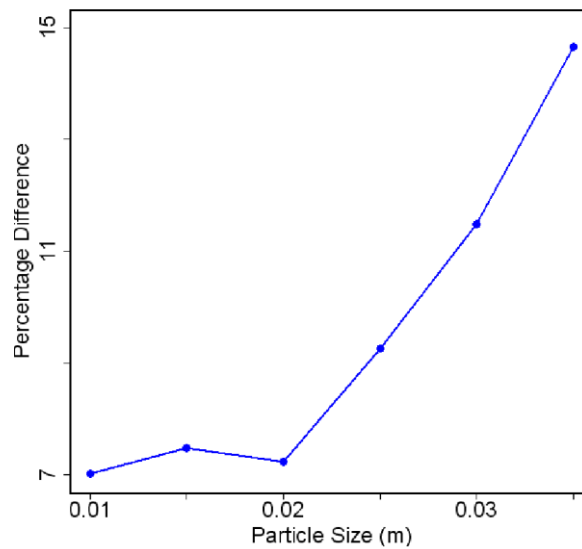


Fig. 33 - Percentage difference in simulated reservoir water depth for different SPH resolutions at a discharge rate of 35.86 L/s (from Saunders *et al.*, 2014).

Based on numerical results, Saunders *et al.* (2014) drawn the following main conclusions and observations:

- The flow behaviour of water down the spillway's ski-jump, posteriorly projected away from the spillway base, was qualitatively compared to the physical model study showing good agreement;
- The uncertainty in the physical sensor location impacted upon the interpretation of the accuracy of the simulated results. If the physical sensor was located close to the spillway crest, the SPH model agreement with the physical study is excellent. If the physical sensor location was more central to the reservoir area, the agreement with physical model results was good at low flow rates but decreased as the flow rate increased. If the latter is the case, factors of turbulence and boundary layer effects may be influencing the numerical results; and
- Results of this study formed the most in-depth quantitative validation of the SPH method for spillway flows to date. As future work, the authors suggested some research directions, such as, pressures on ski-jump, forces on the gate structures and effect of dynamically moving gate structures.

The Dahua dam

The Dahua dam, located in the Qinghai province in China, has a stepped spillway used to discharge flood waters during the rainy seasons. Gu *et al.* (2017) applied parallelSPHysics to reproduce the laboratory experiment previously done. In the feasibility study of this spillway, three different conditions had been proposed, with varying step numbers (namely, 31, 45 and 62). A 2D SPH model was set for each condition, comprising an upstream tank, a push-paddle for inflow generation and an ogee weir connected to the stepped spillway. Boundary walls were modelled using a fictitious particles approach – the dynamic boundary particles technique (Dalrymple and Knio, 2000 and Crespo *et al.*, 2007). Computed pressure profiles on the horizontal and vertical faces of the steps were compared with experimental data, nevertheless, it should be noted that only two measurement points were available for

the pressure profile on the vertical face of the 45-step spillway, and three measuring points were available for the remaining conditions. An error analysis showed that the normalized average errors between the numerical and experimental results were 0.8-4.3% in the horizontal steps pressures and 0.7-4.7% in the vertical steps pressures. The energy dissipation efficiency of the three stepped spillway configurations was validated as well, being the average errors 8.2%, 3.17% and 5.8% for the 62, 45 and 31-step cases, accordingly.

The CEDEX experience

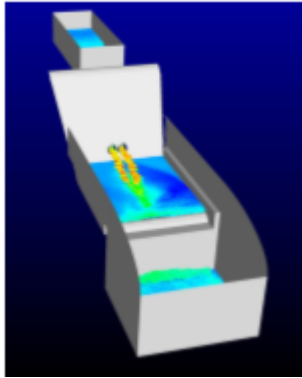
CEDEX (*Centro de Estudios y Experimentación de Obras Públicas*), an autonomous organisation of the central Spanish State Administration, has also developed a SPH code named MDST-MPI which has evolved since 2004, from a serial version (Grassa, 2004) to a parallel one using the standard Message Passing Interface (MPI) paradigm (Grassa, 2007). López *et al.* (2010a) addressed the calibration of the MDST-MPI model using prototype data of pressures from the dissipation basin of the Villar del Rey dam (Fig. 34). This study was motivated by the interest in deepening the knowledge about the physical phenomenon occurring at the dissipation basin, characterized by unstable and uneven eddies' development that was causing the overtopping of the basin walls. The numerical analysis of this hydraulic system allowed to understand the general flow features in the dissipation basin but also revealed some of the employed SPH model limitations. It showed that the repulsive forces between boundary and fluid particles reduced the outlet's effective section, so that, to discharge the targeted flow rate, the diameter of the outlet conduits was readjusted. Consequently, these repulsive forces affected the computed pressures (which translated to numerical noise, Fig. 35). This was acknowledged as an effect of the wall boundary conditions approach applied, namely, the Lennard-Jones repulsive forces. Still, the authors, underlined that the prediction of pressures in the vicinity of wall boundaries could be improved by virtue of the boundary treatment used.

Rebollo *et al.* (2010) demonstrated as well the SPH capabilities to compute, with a reasonable accuracy, the discharge rating curves of the gated spillway of the Alarcón dam (both with the gate totally opened or partially closed). The spillway of the Alarcón dam is composed by three openings of 15m wide, equipped with Tainter flood gates which discharge to three channels located over the dam. This structure was experiencing flow separation and high negative pressures on the spillway surface, so that the spillway crest design was altered in order to permit a softer flow transition between the crest and the discharge channel. The SPH model allowed to visualize the gate closing and its influence in the flow at different instants of its movement (Fig. 36).

Addressing mobile bodies in SPH is straightforward which is a great advantage for this sort of applications, in which the hydrodynamic functioning of gates should be assessed. Pressures over the spillway crest were also computed and compared with experimental data, but, since the flow circuit established was based on an iterative laborious process there was no certainty that the pressures were being compared exactly for the same flow rate.

To increase the drainage capacity of Calanda dam, a new spillway tunnel was projected on the right side of the dam. In this sense, a physical model was used for the spillway flow analysis. After a laborious tests process, the design showed several failures concerning the expected flow behaviour. To save time, the original design modifications were only carried out with the aid of SPH simulations. The MDST-MPI code aided to do a qualitative preliminary analysis of possible designs for a new spillway for the Calanda dam, including a morning glory and a labyrinth spillway (Fig. 37) (López, 2013).

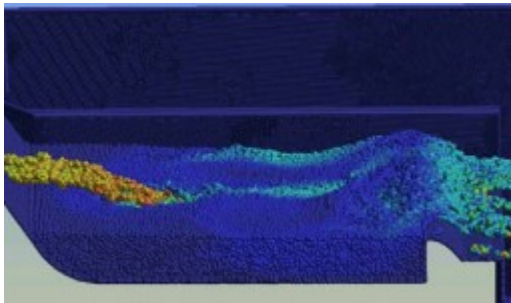
SMOOTHED PARTICLE HYDRODYNAMICS



(a)



(b)



(c)



(d)

Fig. 34 - Dissipation basin of the Villar del Rey dam: numerical model (a) and (c), the physical model (b) and prototype (d) (from López, 2013).

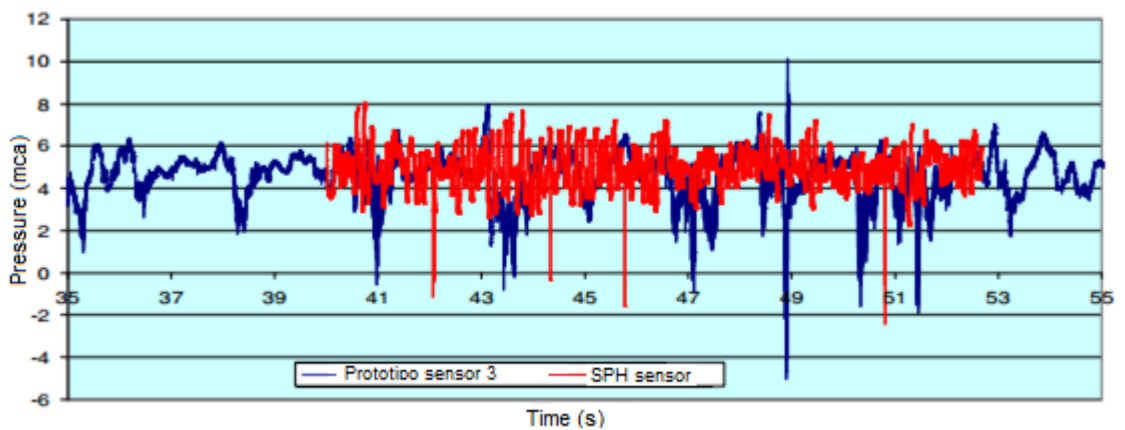


Fig. 35 – SPH vs. prototype pressure records for the Villar del Rey dam (adapted from López *et al.*, 2010a).

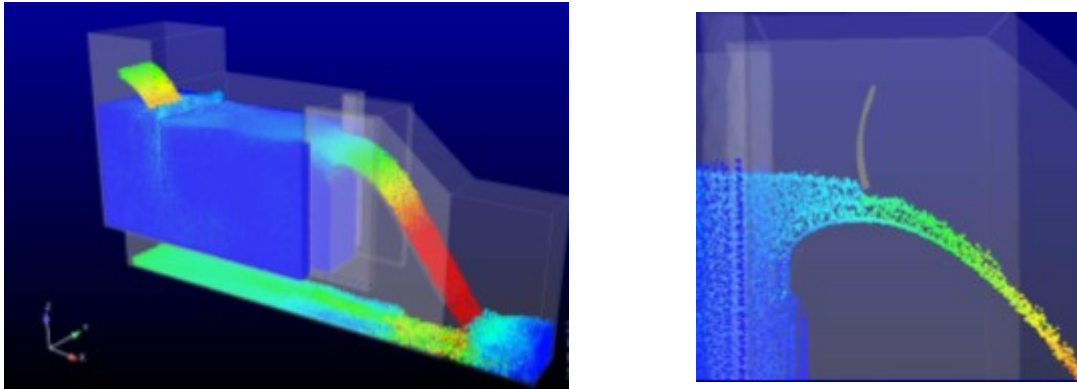


Fig. 36 - SPH model of the Alarcón dam. Plot according to particles velocity magnitude (blue – 0 m/s to red – 20 m/s) (from Rebollo *et al.*, 2010).

The numerical study allowed a general vision of the different alternatives in a short lapse of time, as well as the determination of the discharge rating curves. A labyrinth spillway was selected as the best solution. The same SPH code was used to simulate the flow in the bottom outlet of the Mularroya dam with the objective of verifying if the channel flow remains a free-surface flow (López *et al.*, 2012).

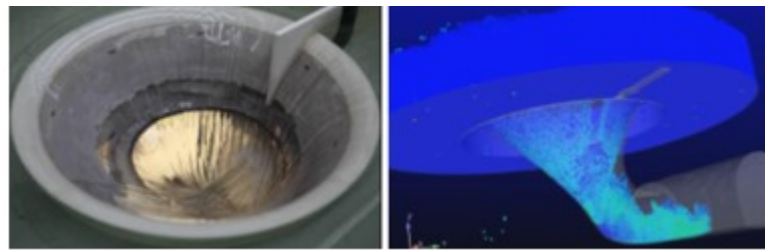
The experience with the MDST-MPI model was very hardworking due to the lack of proper open boundaries prescription. The stabilization of the flow was done on the basis of the establishment of a circuit. This methodology requires very long runs, until reaching a steady state, in an iterative manner. Moreover, it has a high computational cost because it requires a significant increment (sometimes the double) in the number of particles to generate the recirculation flow (López, 2013).

Posteriorly, a new version of the MDST-MPI model was developed - the SPHERIMENTAL code, which is run on graphic cards. This code has been applied, in a complementary manner, in multiple studies of technical assistance requested to CEDEX. These include the spillway of the Nagore dam and the intermediate spillway of the Bárcena dam. These experiences, described in brief in López *et al.* (2015), highlight the added-value of the SPH method in the industrial environment.

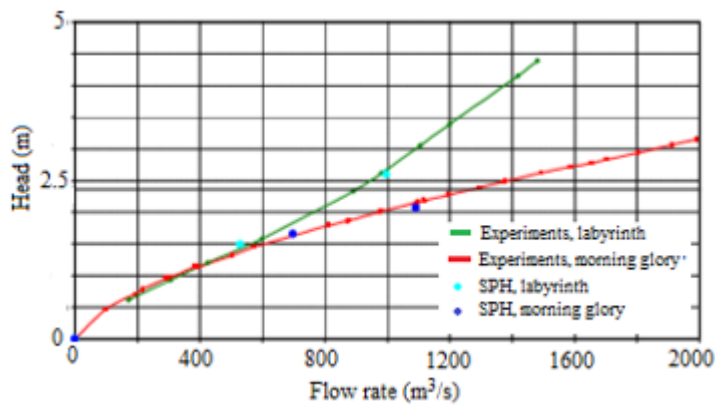
The Nagore dam is an embankment dam that was put into service recently. During its design stage, the SPHERIMENTAL code was applied to study the flow in the morning glory spillway, prior to physical model testing (López *et al.*, 2016). The numerical model allowed to analyse the transient phenomena during the initial working phase, when there is a mobile hydraulic jump which moves along the gallery depending on the flow rate, validating its hydraulic feasibility, improving some parts of its design and detecting the main aspects to assess in the posterior physical modelling (Fig. 38).

The discharge rating curve was computed. In this work, a new term was added to the Lennard-Jones forces equation in order to account for the wall roughness (Gómez *et al.*, 2012). The upgrading of the intermediate spillway of the Bárcena dam also benefited from the capabilities of the SPHERIMENTAL code. As explained in López *et al.* (2015), the customer has raised a number of amendments to simplify construction, providing a short period for the study.

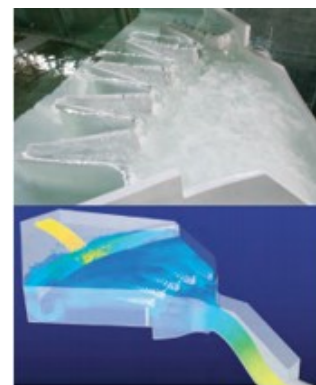
This work was performed within two months using this SPH code, allowing to analyse the flow at the drainage intake and check the velocity and vorticity field. Despite the scarce information available about the details of the numerical study performed for the Bárcena dam, López *et al.* (2015) evidenced how the SPH method allowed to deepen in the physical basis of the problems analysed, providing more information and helping to reduce time and costs typical from physical modelling.



(a)



(b)



(c)

Fig. 37 - Calanda dam spillway study: (a) Physical and SPH model of the morning glory spillway (López, 2013); (b) comparison between experimental and SPH discharge rating curves for the morning glory labyrinth spillway solutions (López, 2013); and (c) physical and SPH models of the labyrinth spillway solution (adapted from López *et al.*, 2015).

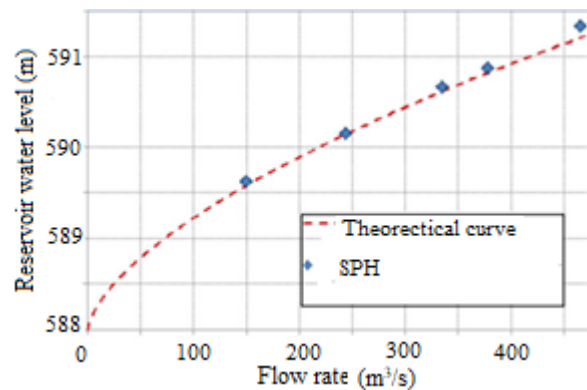
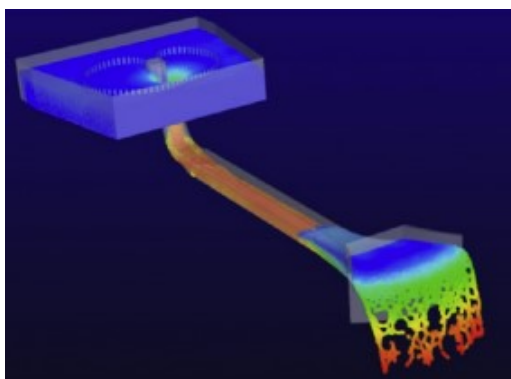


Fig. 38 – Nagore dam study: numerical model on the left and comparison between experimental and computed discharges on the right (from López *et al.*, 2016).

Table 8 - Summary of some SPH models' setup characteristics and quantitative validations carried out (Adapted from Moreira *et al.*, 2020).

Dam, location	Goulours, France	Villar del Rey, Spain	Alarcón, Spain	Pala Tiloth, India	Nagore, Spain	Dahua, China
SPH Code	3D WCSPH, SPARTACUS	3D WCSPH, MDST-MPI	3D WCSPH, MDST-MPI	3D WCSPH	3D WCSPH, SPHERIMENTAL	2D WCSPH, parallelSPHysics
No. of particles	936 600	667 858	750 000	415 to 7571	620 000 to 720 000	300 000
Particle diameter, dp (m)	ca. 1	Fluid: 0.4 Boundary: 0.25	Fluid: 0.7 Boundary: 1	0.01 to 0.035	Fluid: 0.2 Boundary: 0.5	0.004
Open boundaries	No	No	No	Yes	Yes	No
Wall boundary conditions	Fictitious particle	Repulsive functions	Repulsive functions	Repulsive functions	Repulsive functions	Fictitious particle
Turbulence modelling	No	No	No	No	No	Sub Particle Scale
Computational time/ physical time/ hardware	5 days/ 10s/ CPU with 1024 processors	NIA/ NIA/ CPU with 24 cores	NIA/ NIA/ Cluster with 24 cores	17h-28 days/ 65s/ run parallel on a dual Xeon 8-core E5-2650	NIA	20-26 days/ 20s/ CPU with 48 cores
Quantitative validation	DRC		✓		✓	
	WD			✓		
	CP		✓			
	SCP					✓
	DBP	✓				
	V					
	DE					
Comments	Merely qualitative study	Prototype results were available	A particles feedback circuit was established	A particle resolution study was done	A modified α_π in Eq. (23) was used	A push-paddle was used for inflow generation

Note: The Bárcena, Calanda and Mularroya dams are not addressed here because the information available about their SPH studies was far too scarce.

NIA: no information available; DRC: discharge rating curve; WD: water depth; CP: crest pressures; SCP: spillway chute pressures; DBP: dissipation basin pressures; DE: dissipation efficiency; V: flow velocity.

3.9. CONCLUSIONS

The basics of the SPH method and its most relevant applications to free-surface and spillways flows were presented here. A number of spillway projects have benefited from the SPH capabilities to model rapidly varying flows. These studies aimed at validating existing SPH codes, especially from a qualitative point of view, with the aim of providing insight into some of the most common tasks in spillway design, which are: (i) the assessment of the flow behaviour; (ii) the computation of the discharge rate or the discharge coefficient as a function of the upstream head; (iii) the evaluation of the

pressure distribution along the spillway; (iv) and the evolution of the free-surface profile. Presented SPH studies showed that the two first tasks have been successfully fulfilled yet with respect to providing accurate and useful quantification of pressures, flow velocities or free-surface configuration, more research is needed. At this stage the following observations are pertinent:

- All of the studies performed by CEDEX employed the repulsive forces approach for the wall boundary conditions imposition, which is known to be inaccurate, leading to excessive pressure noise. On the top of this decision was probably the computationally cheap nature of this technique as well as its ability to model complex geometries;
- The USAW boundary conditions showed promising results (Leroy, 2014) yet their accuracy has not been proved in a complex, industrial case simulation as far as the pressures computation is concerned;
- Turbulence modelling in industrial cases simulations has been put apart to date. Gu *et al.* (2017) used the Sub Particle Scale turbulence model in a 2D simulation, nevertheless, turbulence is a three-dimensional phenomenon; and
- Most of the studies did not employ open boundary conditions for in and out flow generation. A buffer-based approach has been used by Saunders *et al.* (2014) and in the studies done with the SPHERIMENTAL code. Still, this approach is associated with the development of spurious shocks.

DEVELOPMENT OF SPH APPLICATIONS

4.1. INTRODUCTION

The validity of the SPH method to provide engineers relevant information to support decision making was not proved yet, namely in the dam engineering field. This fact hinders the methods' application by the industry. The main objective is to quantify the SPH performance upon the assessment of the most common issues in the design and evaluation of spillways and energy dissipators, such as:

- Is it possible to define areas propitious to negative pressures development?
- How well can the risk of cavitation be quantified?
- How accurately are mean flow velocity magnitudes and velocity profile shapes captured?
- How well can be determined the maximum loading on a plunge pool?
- How well can complex free-surface configurations be captured when geometric singularities are present (e.g. channel contractions, curvatures)?

The answer to some of these questions is not as straightforward as one would like to. Yet, to all of them an answer/reflection is provided throughout the present and the following chapters.

In this chapter, three SPH models are set-up, corresponding to three distinct applications: an overgate discharge, a chute flow, and a jet's diffusion in a plunge pool (Table 9). The first two models are industrial applications as they correspond to dam prototypes. The third one, though it is based on a laboratory experiment, it corresponds to a large-scale facility in which the flow velocity magnitudes are as those found in engineering practice and near-prototype pool aeration is replicated.

The criteria used for the choice of these case studies was: *(i)* the availability of good quality and quantity experimental results for the validation of the SPH models; *(ii)* the availability of corresponding numerical results obtained with a mesh-based model for comparison purposes; and *(iii)* the relevance and complexity of the hydraulic phenomena being modelled.

The development of the three SPH models, within the framework of the GPUSPH code, was an iterative process, as some issues were observed during initial runs. It is relevant stating that, despite the geometric complexity of the hydraulic structures being modeled (i.e., the first two case studies which correspond to real dam structures), any simplification was made from the geometric point of view, thanks to the meshless nature of the method. In the second case study, the performance of SPH is compared with that of a mesh-based model.

Table 9 - Resume of some of the case studies' characteristics.

	Overgate discharge	Chute flow	Plunge pool
Background case	Crestuma dam	Caniçada dam	Laboratory facility at EPFL
Available experimental data	Free-surface elevation, flow velocities	Free-surface elevation, pressures, flow velocities, jet's length	Bottom pressures
Available numerical (mesh-based model) results?	no	yes	no
Targeted hydraulic phenomena	Hydraulic jump	Development of cross-waves and low/negative pressures, ski jump jets' configuration	Hydrodynamic loading on the pool bottom

4.2. GPUSPH

4.2.1. THE GPUSPH PROJECT

GPUSPH was the first implementation of the WCSPH to run entirely on GPU with Compute Unified Device Architecture - CUDA. CUDA is a parallel computing platform and programming model created by NVIDIA and implemented by the GPUs that they produce. The developer still programs in C, C++ or other supported languages, and incorporates extensions of these languages in the form of a few basic keywords. These keywords let the developer express massive amounts of parallelism and direct the compiler to the portion of the application that maps to the GPU. The present version of GPUSPH is open source, licensed under the GNU General Public License (www.gnu.org/licenses/gpl.txt). The GPUSPH source code is hosted on GitHub. The project's GitHub page is <http://github.com/GPUSPH/gpusph>. The main reason for using GPU computing to solve (parallelizable) problems in scientific research is the time saving. Some timing information can be found in Hérault *et al.* (2010), showing that using the GPU is far faster (orders of magnitude) than using a CPU to compute SPH models. Speedups of 100 can be achieved for parts of the code when compared to serial versions of the code (GPUSPH Installation Guide, 2016). In the present work the GPUSPH version 4.1 was used. It should be noted yet, that since then this SPH code has evolved to a 5.0 version released in Jun 2019, which includes some relevant developments, such as the possibility to create GPUSPH simulation scenarios using the SALOME platform, making the whole process of setting up a simulation rather user-friendly. In addition, since March 2019 a discourse group is available too. The following paragraphs sought to briefly describe the main features included in the code as well as schematize the process of setting up a numerical simulation.

4.2.2. RUNNING GPUSPH

GPUSPH delivers four options regarding the choice of the smoothing kernel. These are the cubic spline kernel, the quadratic spline kernel, the quintic Wendland kernel and the Gaussian kernel. The formulae for the different kernels and their derivatives are given in the GPUSPH Theory Guide (2016).

Another choice to be made is the SPH formulation, being available the following: SPH_F1, SPH_F2, and SPH_GRENIER. SPH_F1 is a WCSPH single-fluid formulation, SPH_F2 is a WCSPH multi-fluid

formulation and SPH_GRENIER is another multi-fluid formulation based on the Grenier's formulation (Grenier *et al.* 2009). In the context of the present research, the WCSPH single-fluid formulation is the adequate formulation to be used.

Several different boundary conditions are available for the SPH method, as described in Chapter 3, and a few selected ones are implemented in GPUSPH. Currently the following options available are: Lennard-Jones boundary conditions, Monaghan-Kajtar boundary conditions, semi-analytical boundary conditions, and dynamic boundary conditions. These types of boundary conditions are described in the GPUSPH Theory Guide (2016). With classical boundary conditions (Lennard-Jones, dynamic boundaries) the geometries of the problem are defined and filled with particles by GPUSPH itself. For simulations involving complex objects and/or open boundaries, the semi-analytical boundaries can be used. (GPUSPH User Guide, 2016). The semi-analytical wall boundary conditions developed by Ferrand *et al.* (2013) have shown promising results in the simulation of flows with complex boundaries using the SPH method. Recent efforts have pushed these boundary conditions towards practical applications (Mayrhofer *et al.* (2014); Leroy *et al.* (2014)). While the accuracy of these boundary conditions is outstanding, one of their downsides is their comparably high computational cost. The semi-analytical wall boundary conditions are the ones used in all of the study cases.

Another parameter is the viscosity model. There are five options in GPUSPH: artificial viscosity, kinematic viscosity, dynamic viscosity, Sub-Particle Scale Turbulence model and standard $k-\epsilon$ turbulence model. The implementation of extra functions in the simulation, such as the extra Ferrari diffusion term or an adaptive time step (determined based on a maximum CFL number) are available, among others.

To pre-process and run a simulation using semi-analytical boundaries in GPUSPH the main following steps, summarized in Fig. 39, should be undertaken:

- To prepare the geometry and mesh with a generic platform for pre-processing. SALOME open-source software was used here. The mesh of the boundaries should be exported as a binary .stl file: one file being the total domain's boundaries, other two files being each special boundary (that is, the open boundaries for inflow and outflow generation), and another file being the mesh for the free-surface. The meshes must be composed by triangles, as regular as possible.
- To check the triangles' dimensions with *testTriangle* algorithm. For the simulation to work correctly, the distance between particles, (to be set hereafter) should not be less than the maximum distance between the centre and the vertex of a triangle. *testTriangle* is used to get the maximum value of this magnitude for all triangles of the main geometry .stl file. The minimum value is also an output. This is to prevent irregularly distributed boundary particles, which may cause simulation issues later.
- Before running the simulation, the fluid domain must be initialised (i.e. filled with fluid particles). This task is done using CRIXUS, a pre-processing tool for SPH, and in particular GPUSPH. As input, it needs the .stl files describing the model geometry and, if applicable, the .stl file describing the free-surface and the special boundary meshes. In addition, one should specify the distance between particles. CRIXUS fills the fluid domain using a cartesian grid, as can be easily seen in Fig. 40, fluid particles are highly ordered. So, at the beginning of a simulation, fluid particles are rearranged, what creates fake and ephemeral pressure or velocity fields in the fluid domain. So, before really starting the numerical data registration, it is better to wait for some iterations in order to make those spurious fields vanish. The fluid initialization performed by CRIXUS, and stored in h5sph files, is then used by GPUSPH to start the simulation.

- To set up the simulation in GPUSPH the following information should be specified: (i) geometry: indicate the location of the h5sph files (previously created by CRIXUS) as these contain the boundary and fluid particles positioning; (ii) simulation parameters: there are several simulation parameters that need to be specified, concerning the time-step and total time of simulation, the frequency of the writing output or other specific SPH parameters; (iii) initial conditions: one should specify an initial value for each of the fields to be implemented on each particle; and (iv) boundary conditions. This process involves writing the source file, a .cu file.
- To build and compile source file.
- Once the source file is compiled, GPUSPH program can be run.
- To visualize the results, using e.g. the ParaView tool.

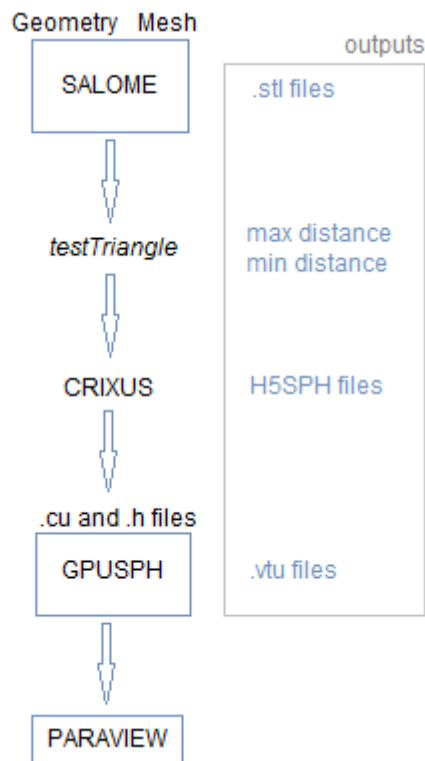


Fig. 39 - Work flow.

Lastly, Table 10 shows the characteristics of the GPU processors used in the numerical experiments.

Table 10 - Main characteristics of the Nvidia GPU processors used in the present work.

	Number of cores	Processor clock (GHz)	Memory space (GB)	Compute capability	Architecture
GTX Titan X	3072	1.08	12	5.2	Maxwell
GTX 980 Ti	2816	1.08	6	5.2	Maxwell
GTX 1070 Ti	2432	1.68	8	6.1	Pascal

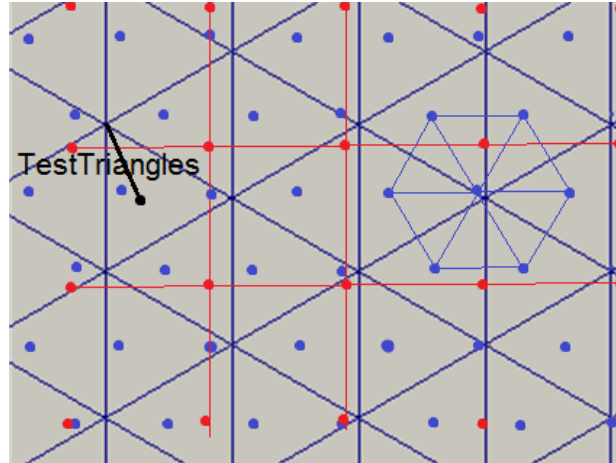


Fig. 40 – Exemplification sketch of the *testTriangle* algorithm. The triangular mesh represents the generated mesh used for the boundary particles positioning; the blue particles represent the boundary particles; and the red particles represent the fluid particles, initially placed on a cartesian grid.

4.3. OVERGATE DISCHARGE – CASE STUDY I

4.3.1. INTRODUCTION

The Crestuma dam is the last hydropower plant in the catchment basin of Douro river (Fig. 41). This dam, concluded in 1986, is a multipurpose one, intended essentially for the production of energy, fluvial navigation and fresh water supply to the regions of Porto and Vila Nova de Gaia (PNCOLD, 1992). The dam is of the gate-structure type, allowing discharges over and underneath their body or both simultaneously. Discharges are controlled by double slicing gates installed on eight spans of 28 m each and supported by 49 m length and 6 m width piles. When there is a major flooding, the eight gates are raised above water level and only the hydrodynamic piers remain to hinder the flow as if they were a bridge. Table 11 summarizes some of the characteristics of the Crestuma dam. The dam is founded on an alluvial bed and energy dissipation of the discharged flow occurs on a concrete slab stilling basin followed by a rock fill bed protection (Fig. 42). Two experimental studies were carried out to the Laboratory of Civil Engineering (LNEC), by the time of the design and construction of the dam (LNEC, 1972, 1985).



Fig. 41 - Overhead view of Crestuma dam (© IPTM, F. Piqueiro /Foto Engenho).

DEVELOPMENT OF SPH APPLICATIONS

Table 11 – Crestuma dam characteristics

Reservoir capacity	106 hm ³
Total installed capacity	105 MW
Annual energy production	399 GWh
Maximum flow rate	26 000 m ³ /s
Full reservoir level	13 m
Maximum flood level	21.5 m
Turbines (no. / type)	3 / Kaplan
Minimum hydraulic head	6.8 m
Maximum hydraulic head	12.6 m

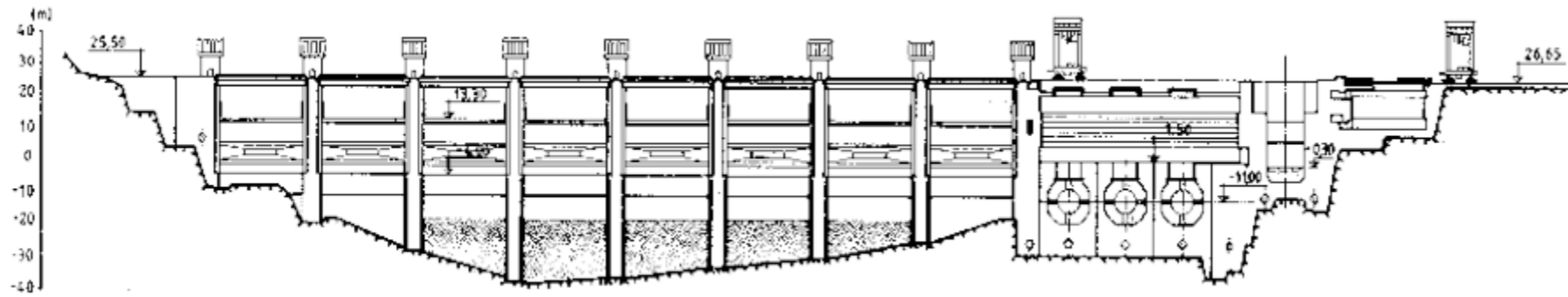
4.3.2. LABORATORY EXPERIMENTS

Lopes (2005) constructed and tested a physical model of the Crestuma dam in the water channel of the Hydraulics Laboratory (LH), at the Faculty of Engineering of the University of Porto (FEUP). The water channel has a length of 32.3 m, a width of 1 m and a bottom slope of 0.5%. The scaled model, made of Acrylic, was constructed with a 1:80 geometric scale, according to Froude similarity. This geometric scale has already been used in the experimental studies previously performed at LNEC. Considering the mentioned scale and the spatial restrictions of the available water channel, the portion of the Crestuma dam represented in the physical model includes: one central span, two piles and two lateral incomplete spans (approximately half spans), as represented in Fig. 43. The rock bed protection has 1 m length in the physical model.

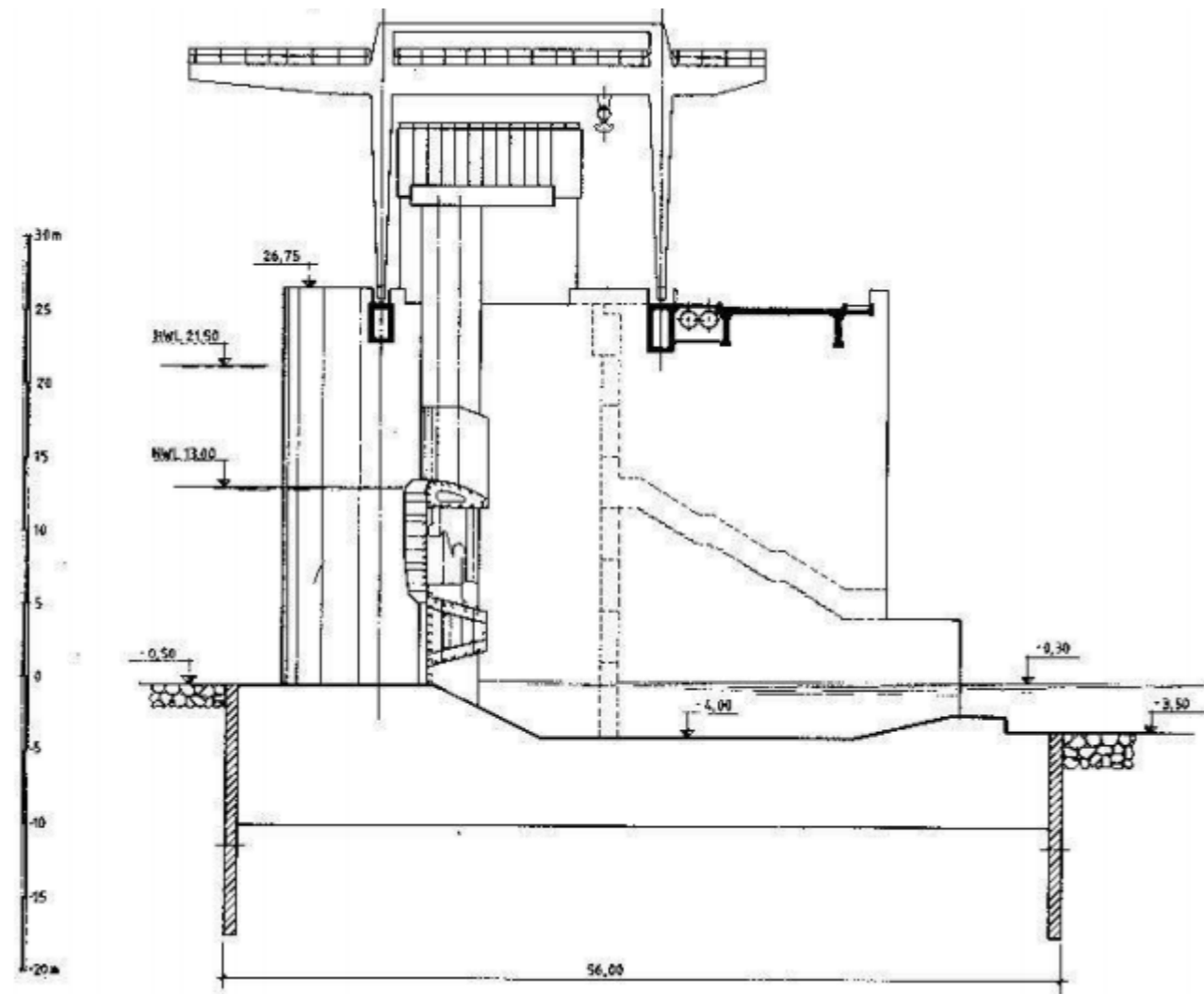
The free-surface was measured using a tape-measure stuck to the channel wall (error ± 0.5 mm). Measurements of the flow field over the rock bed protection were carried out with the aid of a Laser-Doppler Anemometer (LDA) on several profiles. In each profile, the velocity was measured along the vertical direction in points spaced of 2 mm (or 1 mm near the bottom). Fig. 44 shows the location of the profiles measured (from P-1 to P15).

Lopes (2005) considered three different flow conditions, which main features are presented in Table 12. Depending on the hydraulic conditions, the hydraulic jump can be confined in the stilling basin or can eventually form downstream of it, over the bed rock filling. In the latter situation, erosion of the bed may occur. A flow rate of 11.5 L/s/m corresponds to a situation in which the hydraulic jump is formed within the stilling basin slab. A small increase of 6% in the flow value (to 12 L/s/m), leads to the formation of a hydraulic jump showing much more unstable characteristics, with an oscillatory behaviour and a tendency to move away from the stilling basin slab. Fig. 45 shows some photographs from the experimental facility by Lopes (2005).

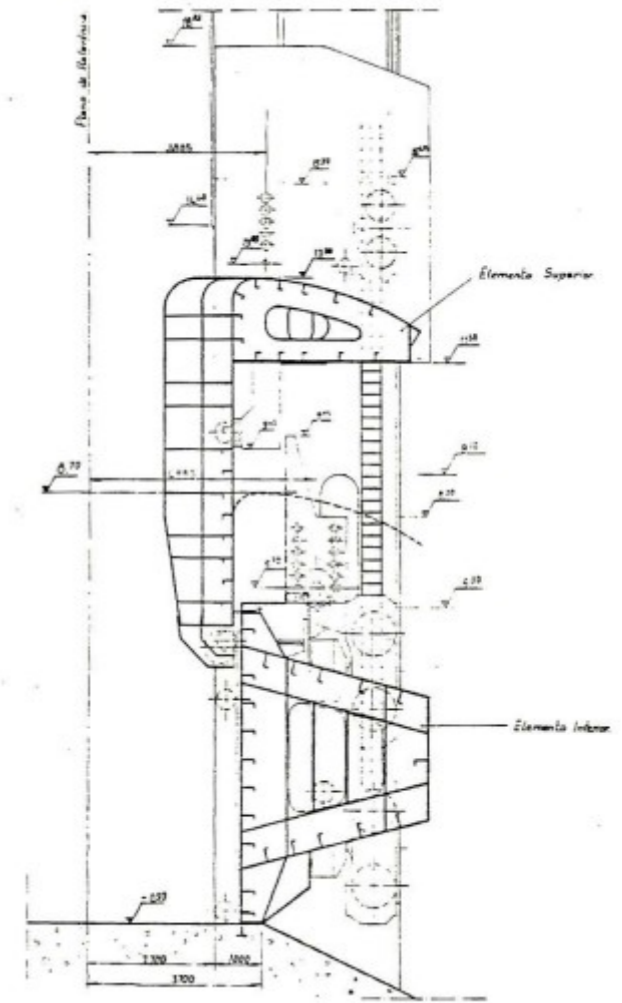
DEVELOPMENT OF SPH APPLICATIONS



(a)



(b)



(c)

Fig. 42 – Crestuma dam: (a) profile along the dam axis on top; (b) cut view (along the flow direction); and (c) gates' definition (from PNCOLD, 1992 and LNEC, 1985).

DEVELOPMENT OF SPH APPLICATIONS

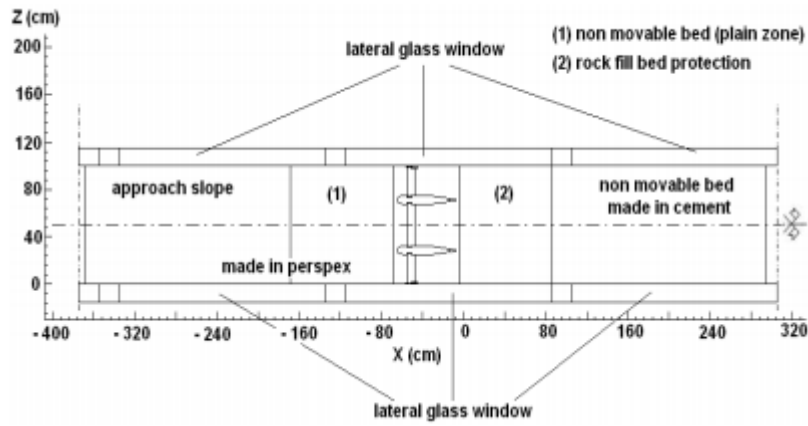


Fig. 43 - Crestuma dam physical model – plant view (Lopes *et al.*, 2006).

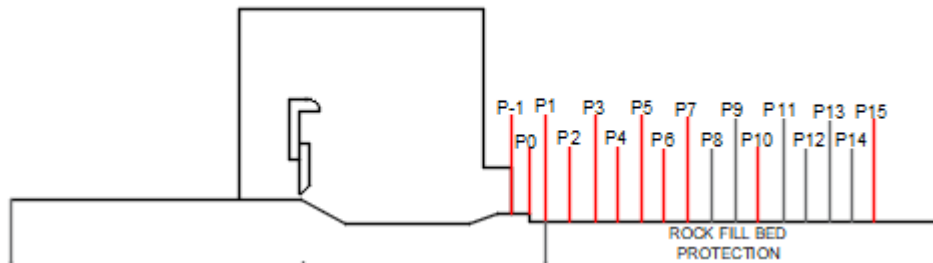


Fig. 44 - Location of the measured profiles (adapted from Lopes *et al.*, 2006).

Table 12 - Main flow characteristics applied in the experiments (in model dimensions).

Flow conditions	Flow rate	Gate opening	Downstream water depth,	Downstream flow velocity
	(L/s/m)	(-)	(m)	(m/s)
A	11.5 ± 0.1	Superior	0.0585	0.197
B	11.5 ± 0.1	Inferior	0.0585	0.197
C	12.2 ± 0.1	Inferior	0.0605	0.202

4.3.3. SPH MODEL SET-UP

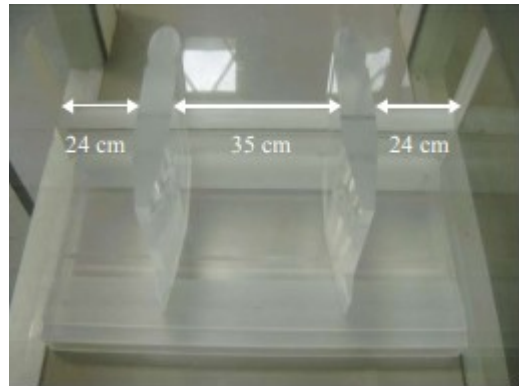
Geometry, mesh and initial conditions

The numerical model was designed with the same dimensions as the physical model by Lopes (2005) (Moreira *et al.*, 2018, 2019a). The numerical domain is 3 m long (x-direction), 0.98 m wide (y-direction) and 0.3 m high (z-direction). Fig. 46 shows the geometry of the computational model for this simulation and the origin of the coordinate system. The effect of the rugosity of rock fill bed protection were not included in this study, for simplicity. So, the numerical boundaries were considered to be smooth. A computational mesh constituted by triangles was created to aid in the placement of the boundary

particles. Fluid particles with a diameter, d_p , equal to 0.005 m were placed upstream of the gates at the initial time-step.



(a)



(b)



(c)



(d)

Fig. 45 - Experimental facility by Lopes (2005): (a) upper gate; (b) physical mode in the water channel; (c) measuring equipment (LDA); and (d) physical model testing for an over gate discharge of 11.5 L/s/m . All photographs from Lopes (2005).

These were placed following a cartesian grid, with zero initial velocity and the corresponding hydrostatic pressure. The number of fluid particles in the computational domain at the initial time-step was 2.60×10^5 , after which it increased to fill the water channel downstream of the gates, according to the water depth prescribed at the outlet, stabilizing around 16×10^5 fluid particles (out of 23.5×10^5 total particles). Hydrostatic pressure initialization was used.

Boundary conditions

The USAW boundary conditions were used to model the boundaries, that is, the channel bottom, walls and gates. Two types of open boundary conditions were used (following Ferrand's *et al.*, 2017 approach based on the USAW boundary conditions technique) – a velocity driven open boundary for inflow and a pressure driven open boundary for outflow. A logarithmic velocity profile with a varying water depth was imposed at the inlet section (X_{\min} section). The water depth at the inlet section was equal to 0.17 m (being the hydraulic head over the gate equal to 0.035 m).

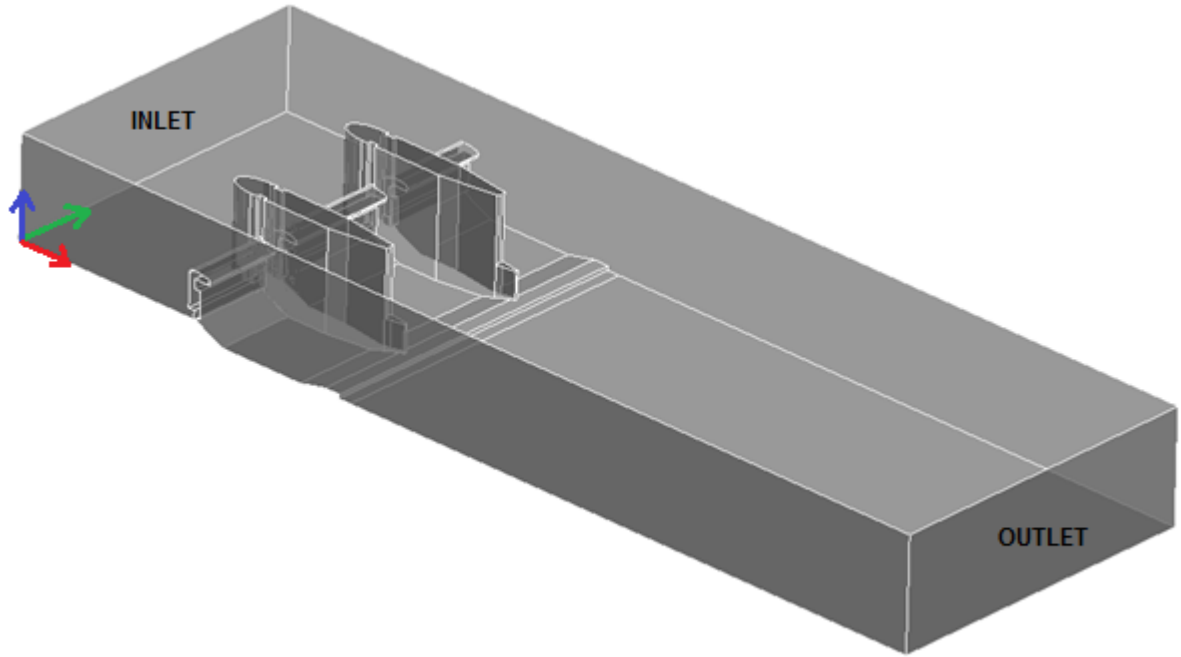


Fig. 46 - Numerical model's geometry for the simulation of the over gate flow in the Crestuma dam.

To recover the appropriate volume flow rate within the smooth turbulent regime, resulting imposed values are

$$u_x = u_* \left(\frac{1}{k} \ln \left(\frac{zu_*}{\nu} \right) + C_v \right) \quad (35)$$

$$k = \frac{u_*^2}{\sqrt{C_\mu}} \left(1 - \frac{z}{H} \right) \quad (36)$$

$$\epsilon = \frac{u_*^3}{\kappa z} \left(1 - \frac{z}{H} \right) \quad (37)$$

with u_x being the imposed velocity in the longitudinal axis of the geometrical model, u_* the shear velocity, k the turbulent kinetic energy, ϵ the dissipation rate, z the vertical coordinate and H the water depth, computed in the simulation through a tracking of the free-surface. The constants are $C_v = 5.2$ and $C_\mu = 0.09$.

Tests done using a pressure driven open boundary condition at the inlet section showed that the flow rate entering the computational domain did not stabilize which indicated that further research on this type of open boundary condition for inflow generation is probably needed¹¹. At the outlet (X_{\max} section) a hydrostatic pressure profile was prescribed, being the water depth equal to 0.059 m.

¹¹ This fact was verified both in the present research and in the work by Fonty *et al.* (2018).

In WCSPH computations, the free-surface conditions are naturally satisfied due to the meshfree nature of the method, kernel interpolation of density and the use of a relevant state equation. That is because it makes the density tends to zero when approaching the free-surface due to the absence of neighbours in the kernel support, which, due to the equation of state, makes the pressure tend to zero as well. Still, the incorporation of a free-surface detection algorithm (to distinguish the fluid particles that belong to the free-surface from those which do not) in the SPH solver is particularly interesting to allow an in-depth analysis of complex flow behaviours, especially when air entrapment is foreseen, such as in the present study. The free-surface detection technique used in this work is a simplification of the one proposed by Marrone *et al.* (2010).

Other numerical parameters

As far as the SPH particle approximation is concerned, the Wendland C^2 kernel (Wendland, 1995) was used. The particle approximations done in the SPH method depend on having a sufficient and necessary number of particles within the support domain of the kernel. A fixed smoothing scale, h , of 1.3 was considered in all simulations. The number of neighbouring particles throughout the simulation varied around 250 particles, which is a convenient value for a 3D simulation. To ensure stability, the time-step varied during the simulation to accomplish a maximum CFL number of 0.3. A density diffusion term following Brezzi and Pitkäranta (1984) was set through the Brezzi coefficient¹² (set to 0.1). Turbulence was modelled using the standard $k - \epsilon$ turbulence model, which is incorporated in the GPUSPH code.

The GTX Titan X GPU card was used. To run a physical time of 107 s it took a GPU time of approximately 13 days. A set of wave gages was defined along the x-direction of the model (at half model width), in order to register the free-surface evolution. Velocities were registered as well in the locations depicted in Fig. 44, through the definition of *testpoints*, which are like computational probes that register a certain quantity (e.g. velocity, pressure) at a given point in space (following a SPH interpolation), with a specified output frequency. This SPH interpolation is done taking the closest fluid particle to the given point in space. The speed of sound, c_0 , was set to 20 m/s (about an order of magnitude higher than the maximum expected fluid velocity).

4.2.3. ANALYSIS OF RESULTS

In this section, the numerical results obtained with the SPH model are presented. Flow conditions A (Table 12) were simulated with SPH. These correspond to hydrodynamic conditions for which the hydraulic jump is expected to take place within the stilling basin, thus, no erosion of the bed rock protection was verified in the physical model.

At the initial time-step, the free-surface is set at the height of the gates' crest. Within the first seconds of simulation, the water flows over the gate due to gravity, and the channel, initially emptied downstream of the gates, is filled with water until the water depth at the inlet and outlet are 0.17 m and 0.0585 m accordingly. Fig. 47 shows a 3D view of the fluid progress within the first 6 s of simulation. Fluid particles are coloured according to their velocity magnitude. The plot presented in Fig. 48 shows the number of fluid particles existent in the computational domain over the simulation time and the corresponding percentage variation. It can be seen that, during the initial 20 s there is a noticeable increase in the number of fluid particles, after which it tends to stabilize, indicating that the number of

¹² Formula 14 of the paper by Ferrand *et al.* (2017).

fluid particles entering and leaving the computational domain is approximately the same in the end of the simulation. This fact gives confidence that the numerical model reached a steady state condition.

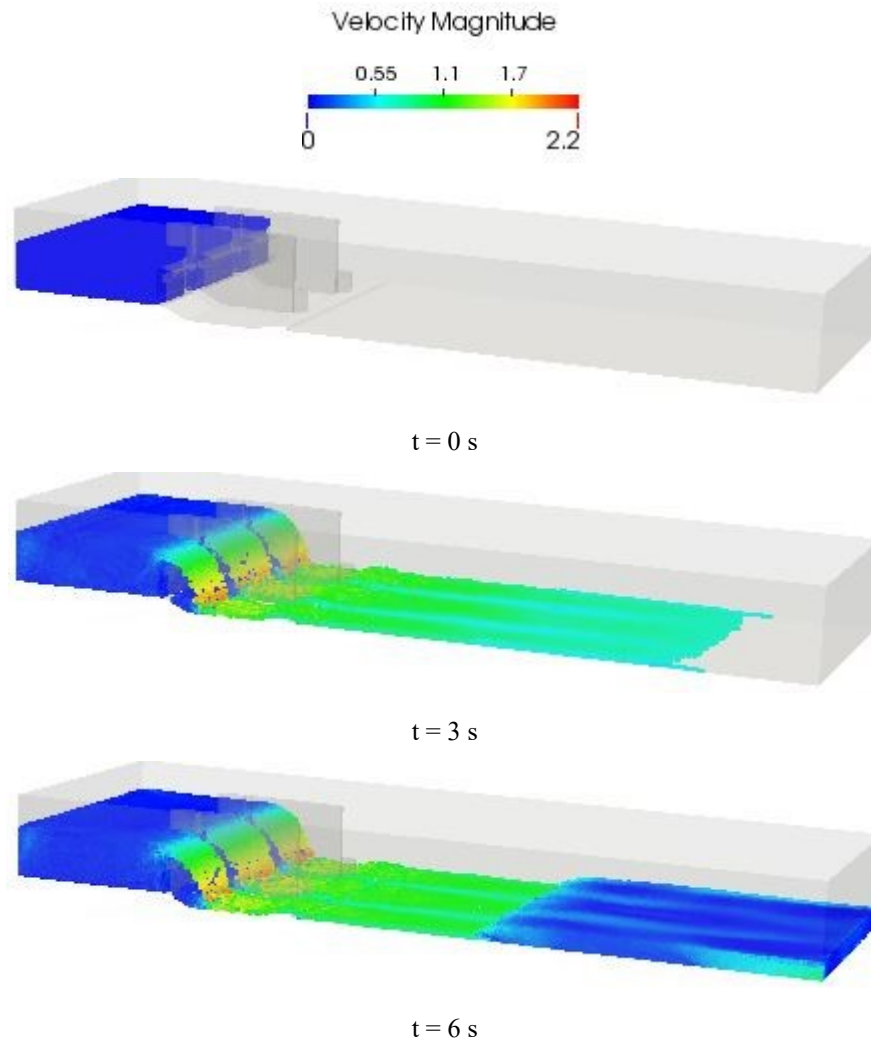


Fig. 47 - Flow visualization within the first 6 s of simulation. SPH particles coloured by their flow velocity in m/s.

After approximately 10 s of simulation, a particle leakage issue was identified, specifically near/in the downstream open boundary (Fig. 49). The number of particles leaving the domain varied from one time-step to another, stopping sometimes and starting again. Efforts were made to fix this issue but any of the made code fixes was successful. This difficulty is partly owned to the fact that the way that open boundaries are prescribed in SPH is still an open issue and consequently a current topic of active research. However, as the simulation run longer, it was verified that the particle leakage tended to cease (as the number of fluid particles in the simulation stabilized as well). Still, such aspects require further clarification in the future.

Qualitative validation

Fig. 50 shows the flow field at the end of the simulation (107 s). Four regions can be distinguished based on their flow characteristics: region 1 shows the nearly stagnant water in the reservoir; region 2 shows the rapid increase in the flow velocity as it flows over the gate (supercritical flow); region 3 consists of the hydraulic jump (as expected, located within the stilling basin), and region 4 in which the discharged flow stabilizes after the hydraulic jumps (subcritical flow).

DEVELOPMENT OF SPH APPLICATIONS

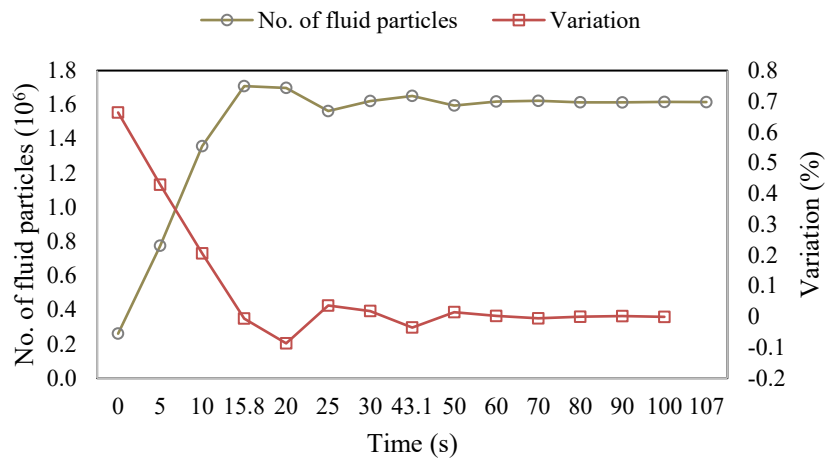


Fig. 48 - Number of fluid particles in the computational domain over the simulation time and corresponding percentage variation.

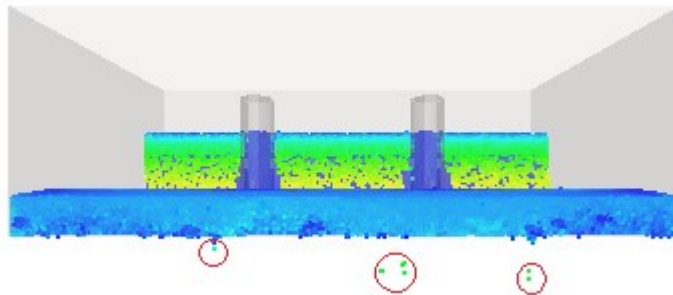


Fig. 49 - Particle leakage issue near/in the downstream open boundary.

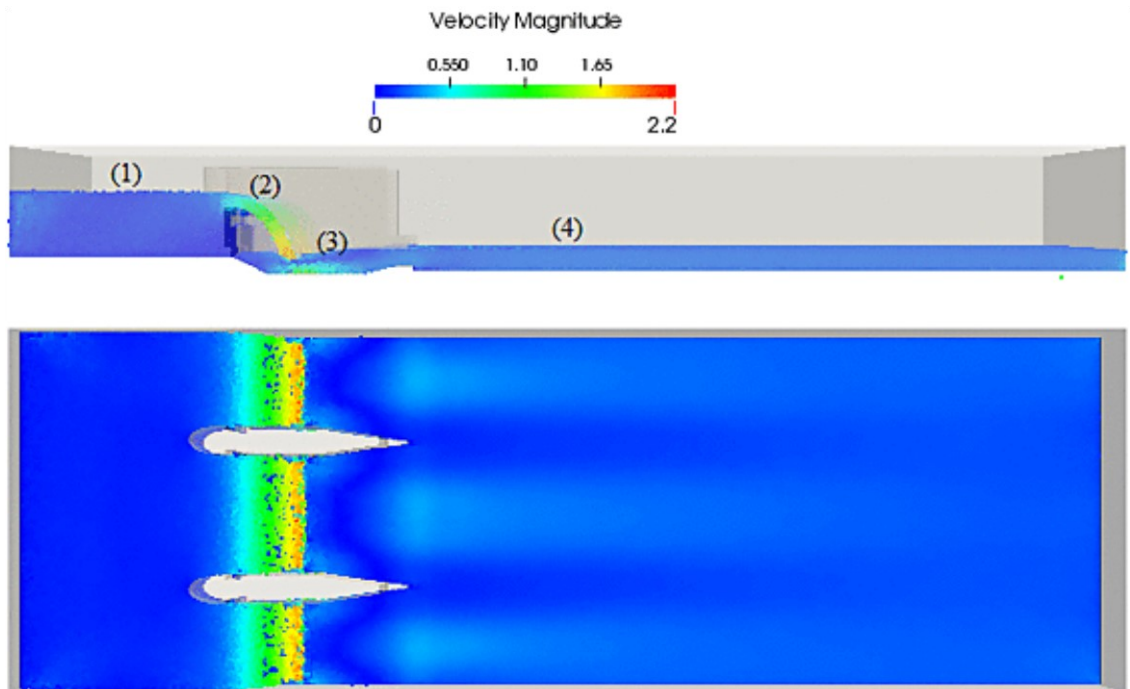


Fig. 50 - Simulated velocity field in the Crestuma dam (in m/s).

Fig. 51 shows the fluid particles coloured according to their turbulent kinetic energy, k . It gives information about the extension of the hydraulic jump and the zone where most of the energy dissipation occurs. It is seen from the pattern of the k plot, that the turbulence intensity assumes the highest values at approximately $x = 0.8$ m, immediately downstream of the water jet impact, after which it gradually decreases towards the end of the concrete basin. As experimentally verified, the hydraulic jump for the tested flow conditions occurs within the concrete basin.

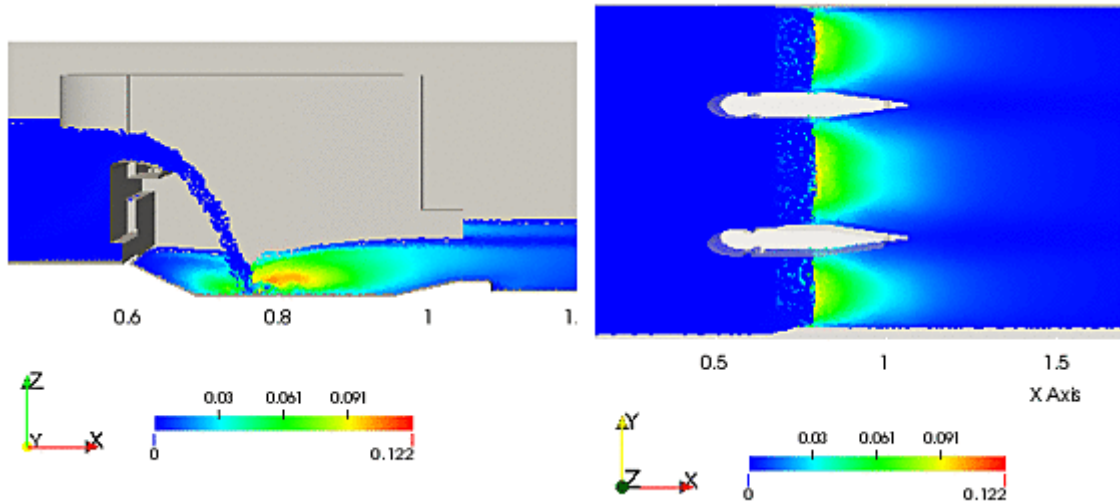


Fig. 51 - Crestuma dam simulation with GPUSPH. Computed turbulent kinetic energy, k (in m^2/s^2): side view at half channel width (on the left) and top view (on the right).

A dye was used in the experiments to allow a better visualization of the flow characteristics in the zones where debris are expected to accumulate. A similar analysis was done with SPH by plotting the fluid particles according to their ID at the end of the simulation. It was verified that fluid particles with the lower ID numbers (those existing in the computational domain at $t = 0$ s) remained merely upstream of lower gate, close to the channel bottom, which means that for these hydrodynamic conditions there is no dragging capacity there (Fig. 52).

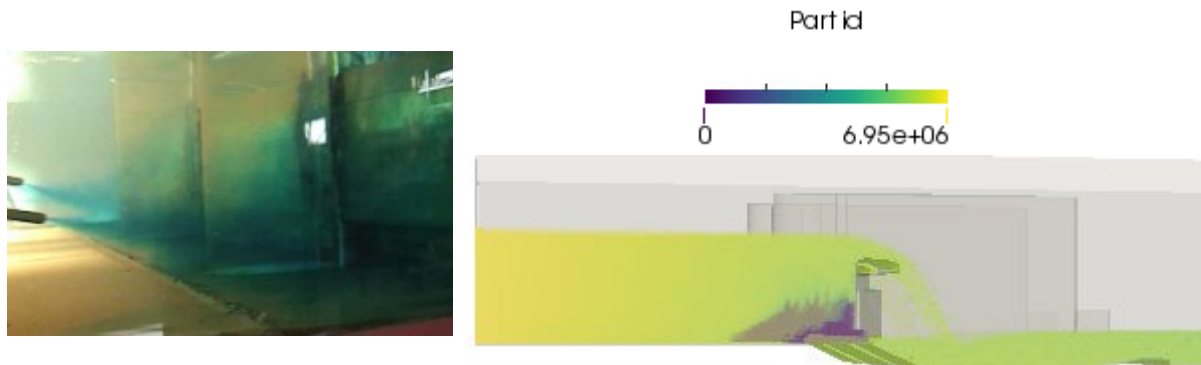


Fig. 52 - Details of the flow upstream of the gates for an overgate discharge from Lopes (2005) on the left and from the SPH model on the right.

Quantitative validation

The free-surface computed at the end of the simulation was compared with the available experimental data. Due to bias derived both from the digitalization and the measurement technique used to register the free-surface elevation (a tape with precision of 1 mm), the consideration of these data points is to be

done with caution. Fig. 53 shows the comparison between the computed and experimental data for the free-surface elevation, being the mean relative errors between 15% and 20%, in the hydraulic jump region. The turbulence characteristic of the hydraulic jump as well as the air entrainment are factors that may have also hindered the exact definition of the free-surface in the experiments. Indeed, as stated by Lopes (2005), the oscillations of the free-surface and turbulence observed, made the water depths vary, and consequently an average water depth was registered. Downstream of the hydraulic jump, results were good, with the mean error for the water depth being approximately 3%.

Though the jet's trajectory was not measured during the experiments it was computed with SPH and compared to that obtained with the following trajectory equation (presented in Chow, 1959, in a slightly modified form)

$$z = x \tan \theta_0 - \frac{x^2}{4h_u (\cos \theta_0)^2} \quad (38)$$

With θ_0 being the initial angle of the jet from horizontal and h_u the velocity head defined as $h_u = u_0^2/2g$, with u_0 the velocity of the jet as it leaves the dam crest. As can be seen in Fig. 54, the computed jet's trajectory is quite similar to that derived from Eq. (38), though Eq. (38) overpredicts the jets reach by about 5%. That is because this equation describes the motion of a projectile unaffected by wind resistance and the SPH modelling done does not account for this effect too. In reality, projectiles or free jets will always travel a distance somewhat shorter than that computed by these equations, due to wind resistance and jet's breakup.

As explained in Wahl *et al.* (2008), for modelling high velocity jets that might be subject to greater aeration and wind drag, modification of Eq. (38) with some correction factor may be appropriate, but further research is needed to determine appropriate values for this correction factor.

Vertical profiles for the velocity magnitude were computed downstream of the stilling basin (refer to Fig. 44). These were obtained by interpolation, considering a Gaussian kernel and the 200 closest SPH particles to each of the points in which the vertical profile was discretized. The height of each vertical profile was taken equal to the water depth and discretization was always done considering a hundred equally (vertically) spaced points. Fig. 55 to Fig. 58 show a comparison between the velocity profiles computed at sections P-1 to P7, P10 and P15 (as these were the ones with experimental data available for the simulated flow conditions) and the experimental data. The velocity profiles P-1 and P0 are located at the end of the stilling basin and are the ones showing a greater velocity magnitude, as expected. P1 is at the beginning of the rock protection. This velocity profile corresponds to a transition zone, after the negative step (or drop) immediately upstream. Further downstream, velocity decreases and the velocity profiles approach the logarithmic distribution. Computed profiles exhibited a greater velocity magnitude near the bottom. This is probably due to the non-consideration of the bed rock roughness in the SPH model. To better quantify these differences four parameters were evaluated at each profile: the maximum velocity, U_{max} , the mean velocity, U_{mean} , the water depth (or profile's height), H , and the vertical distance from the bottom to the point of maximum velocity, h' . Both computed and experimental data are summarized in Table A.1 of Appendix A. From Fig. 59 it is observed that a satisfactory agreement is obtained for U_{mean} , U_{max} and H but with regard to h' differences are significative. U_{mean} , U_{max} and h were predicted with mean relative errors of 4.8%, 9.2% and 6.7%, respectively, while the prediction of h' reached a mean relative error of 22%. The error statistics for these variables are depicted in the error bars in Fig. 60. It shows the minimum, maximum and mean errors as well as the quartiles of the distribution.

DEVELOPMENT OF SPH APPLICATIONS

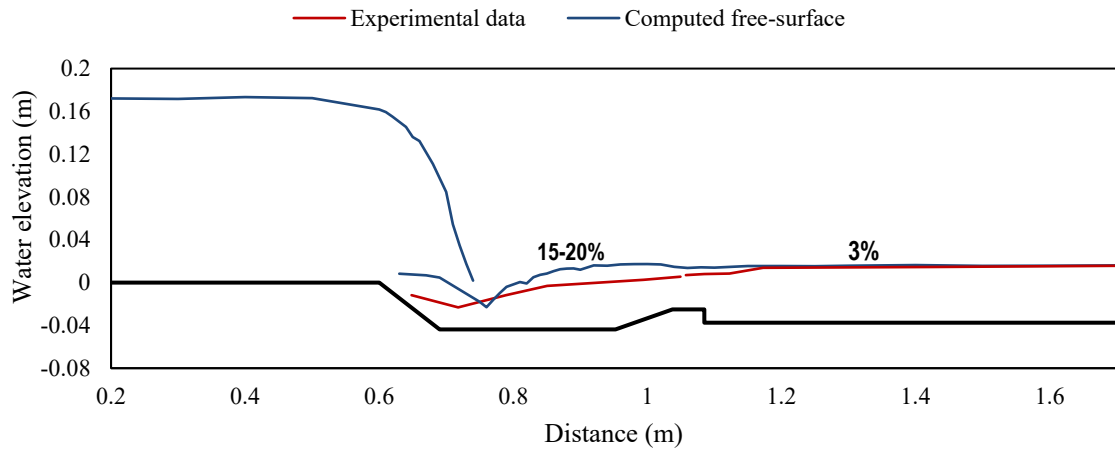


Fig. 53 - Computed vs. experimental free-surfaces profile. The experimental free-surface profile was digitized from Fig. 7.3 of Lopes (2005) work.

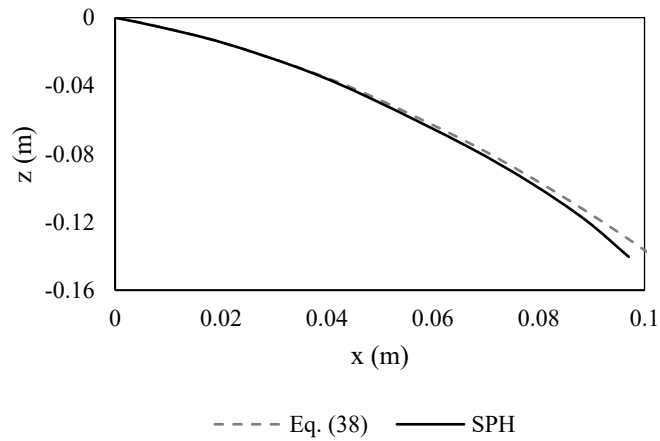


Fig. 54 – Comparison between the computed trajectory and that obtained with Eq. (38)

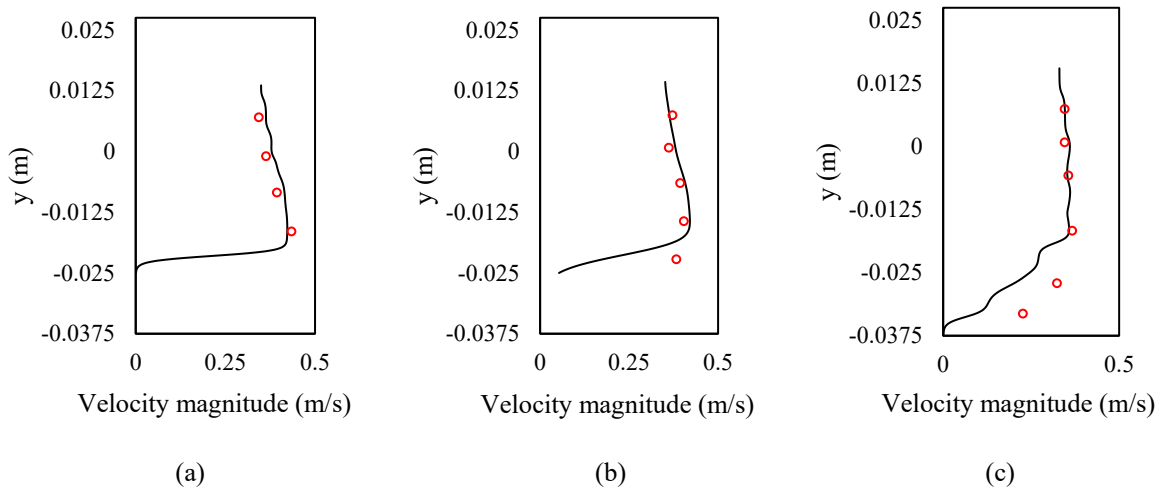


Fig. 55 - Computed (black line) vs. experimental (red circles) velocity profiles in sections: (a) P-1; (b) P0; and (c) P1. The experimental data was obtained through digitalization of Fig. 7.4 from Lopes (2005) work.

DEVELOPMENT OF SPH APPLICATIONS

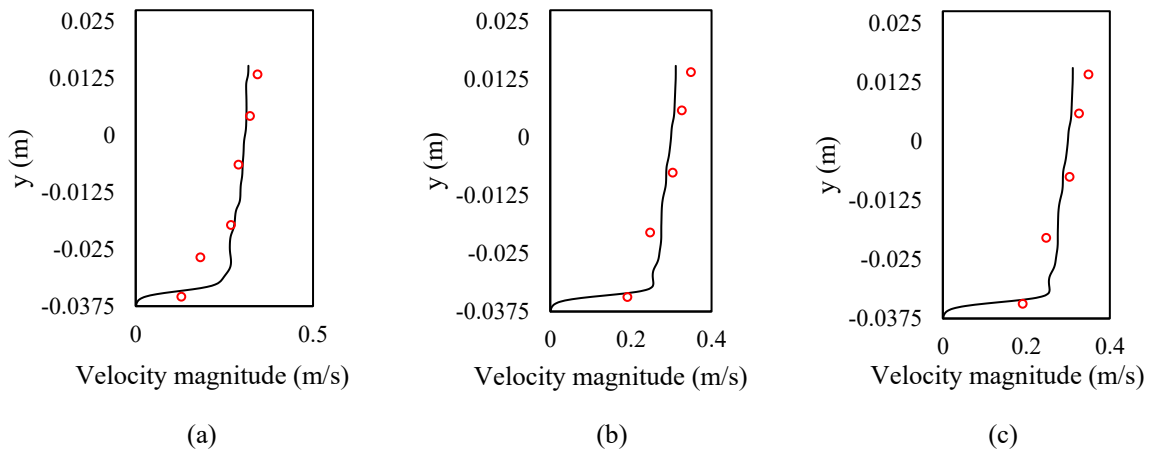


Fig. 56 - Computed (black line) vs. experimental (red circles) velocity profiles in sections: (a) P2; (b) P3; and (c) P4. Experimental data was obtained through digitalization of Fig. 7.4 from Lopes (2005) work.

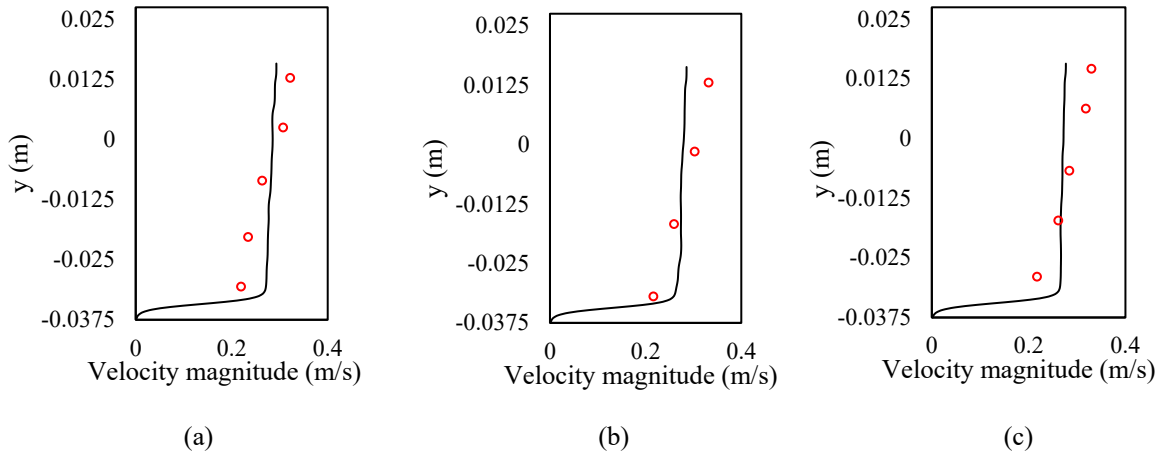


Fig. 57 - Computed (black line) vs. experimental (red circles) velocity profiles in sections: (a) P5; (b) P6; and (c) P7. Experimental data was obtained through digitalization of Fig. 7.4 from Lopes (2005) work.

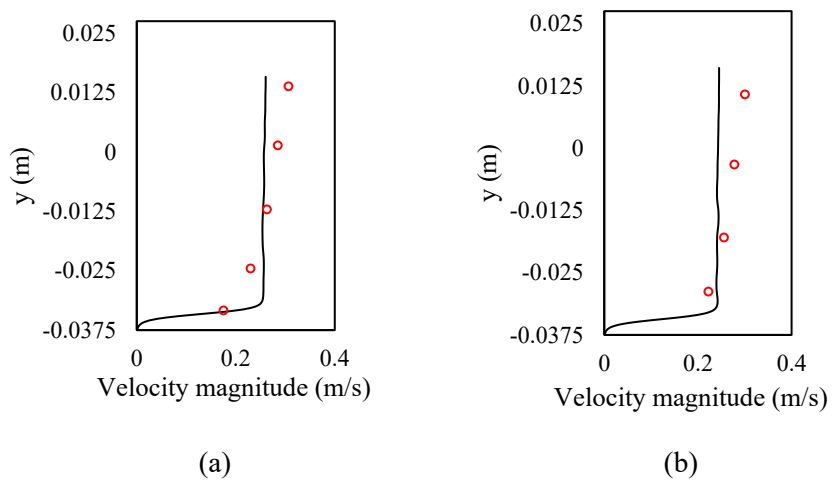


Fig. 58 - Computed (black line) vs. experimental (red circles) velocity profiles in sections: (a) P10; and (b) P15. Experimental data was obtained through digitalization of Fig. 7.4 from Lopes (2005) work.

DEVELOPMENT OF SPH APPLICATIONS

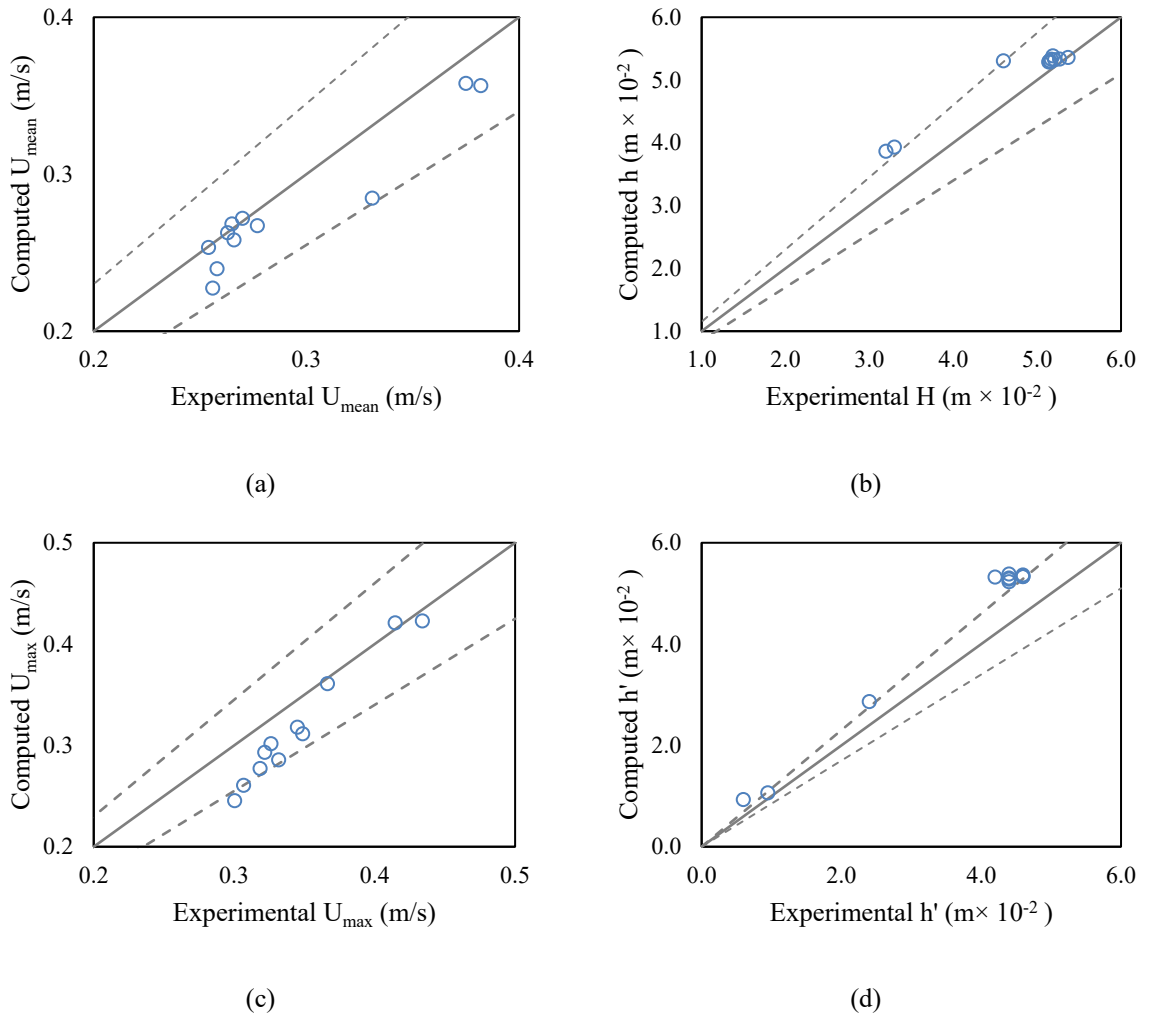


Fig. 59 - Computed vs. experimental U_{max} , U_{mean} , H and h' . The dashed lines represent the bounds for a relative error of 15%. The experimental data was obtained from Table B.1 of Lopes (2005) work.

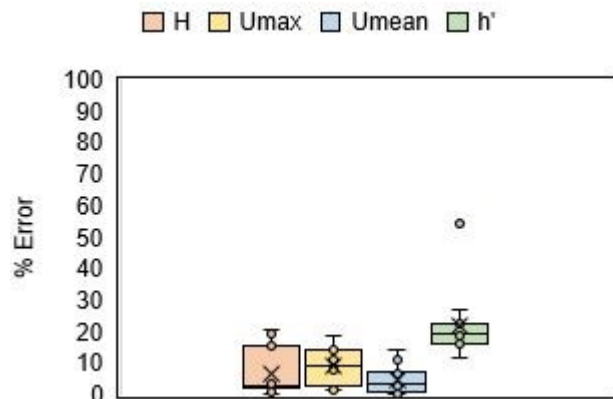


Fig. 60 - U_{max} , U_{mean} , H and h' errors' statistical distribution.

4.3.4. CONCLUSIONS

The experimental study by Lopes (2005) was used for the validation of a SPH model of the Crestuma dam, developed within the framework of the GPUSPH code. A three-dimensional model was set-up to

visualize the flow field and to determine the free-surface elevation and velocity profiles, downstream of the stilling basin. The following conclusions can be drawn:

- Generally, the behaviour of the turbulent flow inside the stilling basin was well represented, with the hydraulic jump being located inside the concrete basin and most of the kinetic energy being dissipated there, as expected;
- SPH results allowed the visualization of some flow features as the shape of the free overfall jet and its impact on the downstream water, the influence of the piers in the flow field, up and downstream of them, or even the existence of zones prone to debris accumulation (for specific operating conditions);
- The computed free-surface elevation agreed well with the measured values, especially after the concrete stilling basin, for which the water depths were computed with an average error of approximately 3%;
- Within the stilling basin, the computed values for the free-surface elevation overpredicted the experimental ones. Some sources of imprecision that may contribute to this significant mean relative error determined (15-20%), are, e.g., imprecisions in the experimental measurement procedure (a wall-mounted ruler) compounded by the turbulence and air entrainment characteristic of the hydraulic jump (that hinder the correct definition of the free-surface) and/or the low quality of the image used for the data points extraction;
- Over the rock protection computed velocities tend to decrease and the vertical velocity profiles gradually evolve to the logarithmic distribution, as in the experiments. U_{max} , U_{mean} , H and h' were computed with mean relative errors of about 9.2%, 4.8%, 6.7% and 22%, accordingly; and
- Even though particle leakage was identified (in particular near the outlet section), it ceased after some seconds of simulation. This effect is not desirable (because it is a non-physical behaviour), but the reason why it occurs is not clear yet (despite it is a well-recognized SPH issue).

In the initial simulations program, it was previewed the simulation of further hydrodynamic conditions for the present case study, namely an undergate discharge, however, such simulation was not successfully completed. This is because the existent gate opening was significantly small, leading to the need for a high particle resolution, which significantly increased the computational effort. By using a periodic boundary condition (taking advantage of the models' symmetry), as schematized at Fig. 61, the total number of particles could be reduced. Nonetheless, persistent leakage issues in the upstream reservoir, within the first seconds of simulation, prevented the completion of the numerical calculation. An increase in the upstream reservoir length could eventually have helped to solve this issue (though it would be computationally unfeasible). Futurely, the employment of a variable resolution approach may solve a number of limitations, as this one.

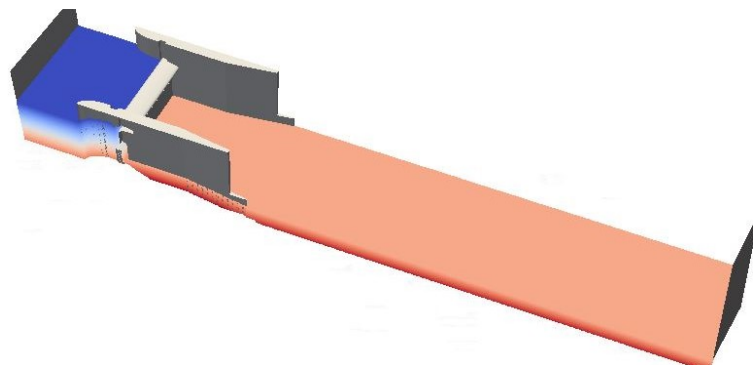


Fig. 61 – Model scheme of an under-gate discharge simulation using a periodic boundary condition. 11 million SPH particles.

4.4. CHUTE FLOW – CASE STUDY II

4.4.1. INTRODUCTION

The Caniçada dam is located in the north of Portugal, in Cávado river, 17 km downstream of the Salamonde dam. The construction of this hydropower plant goes back to 1955. This is a double-curved arch dam made of concrete, with a maximum height of 76 m from foundation. The Caniçada dam is part of the hydroelectric system of Cávado-Rabagão-Homem exploited by EDP *Produção*. The original flood discharge device is set in the central part of the dam body, near the crown, and comprises four rectangular orifices equipped with Stoney gates (Fig. 62).

Table 13 summarises some of the characteristics of the Caniçada dam. After safety analysis studies performed by EDP *Produção* in 2006, it was concluded that an additional discharge structure would be necessary to provide a greater discharge capacity and to accomplish the new dam safety regulation. This resulted in the project and construction of a complementary spillway for the Caniçada dam, which location with respect to dam body is depicted in Fig. 63, along with some photographs of the engineering works recently concluded. The complementary spillway of the Caniçada dam, also referred to as the new spillway of the Caniçada dam, is the hydraulic structure under study in the present section.



Fig. 62 - Caniçada dam (downstream view).

This new spillway is a gated one, controlled by an ogee crest which is followed by a tunnel with rather complex geometry, designed for free-surface flow. The ogee crest (which has a slope of 1:2/3) is divided into two spans (by a septum) controlled by radial gates. Following the ogee crest there is a tunnel, with variable section geometry, approximately 200 m long. In profile, the tunnel presents two stretches with slopes of 77% and 10%, connected by a circular curve with 50 m radius. In plant the tunnel presents a rectilinear axis. Along the first stretch, with approximately 60 m, there is a convergence of the section initially with a $2 \times 105 \text{ m}^2$ up to a constant section of about $2 \times 56 \text{ m}^2$.

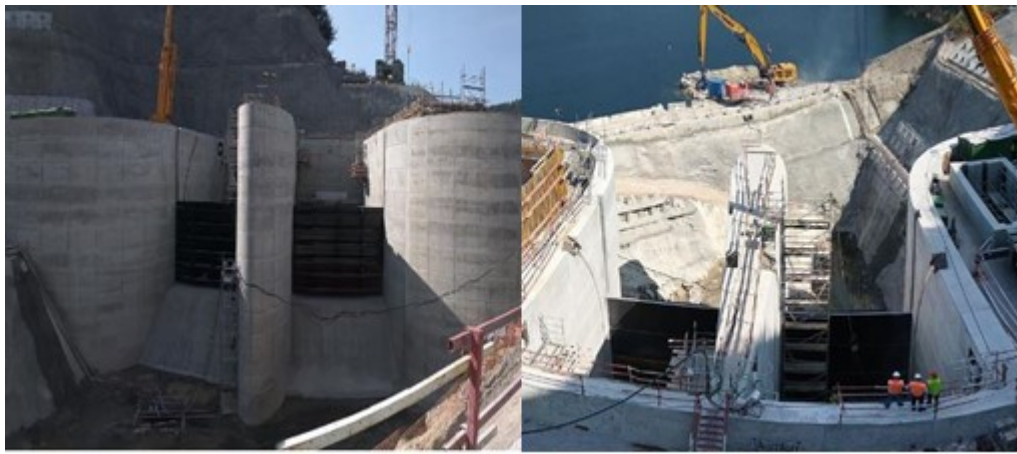
DEVELOPMENT OF SPH APPLICATIONS



(a)



(b)



(c)



(d)

Fig. 63 – New spillway of the Caniçada dam: (a) schematic location with respect to the dam body (from Brandão, 2015); (b) downstream view of the new spillway's outlet; (c) up and downstream view of the new spillway's intake; and (d) upstream view of reservoir and new spillway's intake. Photographs of the engineering works obtained from <https://afaplan.com/projecto>.

The final part of the spillway is opencast, being the outlet, a ski jump structure. To direct the jets into the river, in the final stretch there is a curve in plant that ends with a 15° angle with respect to the tunnel axis. In this final stretch there is also a decrease in the channel section width and a transversal incline of

the channel bottom. The design flow rate for this structure is 2062 m³/s, for a maximum flood level of 152.83 m.

Table 13 - Caniçada dam characteristics.

Reservoir capacity	153 hm ³
Total installed capacity	62 MW
Annual energy production	337 GWh
Maximum flow rate	1 700 m ³ /s
Full reservoir level	152.5 m
Maximum flood level	153 m
Turbines (No. / type)	2/ Francis
minimum hydraulic head	77 m
maximum hydraulic head	121 m

4.4.2. LABORATORY EXPERIMENTS

To validate and adjust the original project for the complementary spillway of the Caniçada dam, a physical model was built and tested in LNEC (Couto *et al.*, 2013; 2014). The physical model was constructed with a geometric scale of 1:62, using the Froude similarity (Fig. 64), and it is 2.3 m high, 13.3 m long and has a maximum width of 6.7 m. Besides the complementary spillway, the physical model also represented the double-curved arch dam, a significant extension of the upstream reservoir and the downstream river bed. The dam and spillway structures were moulded with cement and sand. In the areas bordering the flow, the structures have a cement paste coating that simulates the roughness of the concrete surfaces of the prototype.

The experimental campaign comprised the measurement of various quantities along different sections of the spillway, such as, water depths, pressures, flow velocities and jets length. Water depths were measured with a limnimeter (error < 0.2 mm) in 10 sections; pressures were measured with piezometers (error < 1 mm H₂O) in 36 points, 16 of them located on the left-side channel bottom (designated as P1 to P16) and 20 of them located on the right (e.g. P1R) and left (e.g. P1L) walls of the left-side channel; and flow velocities were registered using a propeller meter in 6 sections. The sections and points where these quantities were measured are schematized in Fig. 65.

The jets length was measured in relation to the alignment of the spillway septum. Registered values result from observations of the average maximum jets' length, so inaccuracies associated with parallax errors are foreseen. To measure flow velocities two propellers were used, depending on the flow velocities range. One propeller of dimensions 500 mm was calibrated for a range of speeds between 0.06 to 5 m/s, whereas another of dimensions 300 mm was calibrated for a range of speeds between 0.05 to 1 m/s. Measurements were done at approximately half water depth and half channel section width.



Fig. 64 - Downstream view of the physical model (Brandão, 2015).

These measurements represent a valuable tool for the validation of the numerical model developed. The flow conditions experimentally tested are presented in Table 14. In all tests the water level in the upstream reservoir was kept at the full reservoir level (152.50 m, which corresponds to a reservoir water depth of 21 m and a hydraulic head over the spillway ogee crest of 14 m). The ratio between the hydraulic head and the design hydraulic head of the spillway, H/H_d , is 1.13.

The experimental data available for the design flow rate refer to pressures, flow velocities and jets' length. For the flow rate 1, there are experimental data available concerning water depths, pressures, velocities and jets' length. For the flow rates 2 and there are experimental data concerning water depths, pressures and length of the jets.

Further details on the description of the physical model testing carried out for the complementary spillway of Caniçada can be found in Muralha *et al.* (2014) and Brandão (2015).

Table 14 - Hydrodynamic conditions tested and respective gate openings.

	Design flow rate, Q_{des}	Flow rate 1, Q_1	Flow rate 2, Q_2	Flow rate 3, Q_3
Q model (L/s)	66.6	29.6	22.8	17.4
Gate opening (m)	Totally opened	5.3	4	3
Q prototype (m ³ /s)	2062	896	690	527
Downstream water depth (m)**	10.3	6.9	6	5.3

*Gate opening is measured along z direction with respect to the gate positioning when it is closed.

** According to the downstream river flow model for the various flow rates under study.

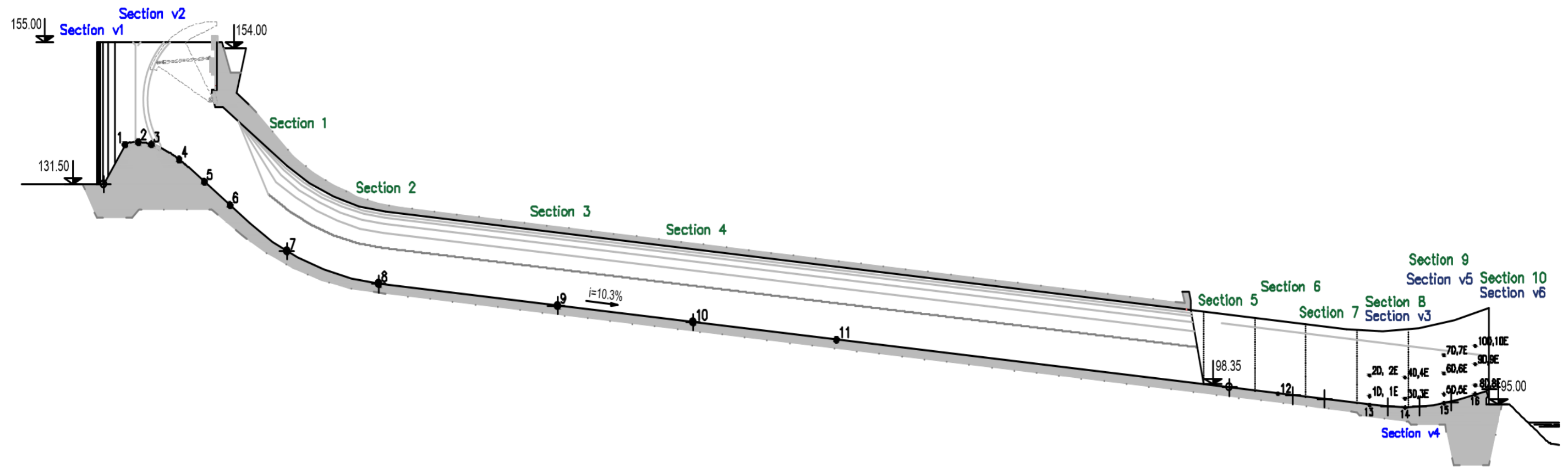


Fig. 65 - Measurement points and sections location

4.4.3. SPH MODEL SET-UP

Geometry, mesh and initial conditions

The numerical model geometry has the same dimensions as the prototype, which corresponds to a 3D numerical domain 510 m long, 119 m wide and 81 m high (Moreira *et al.*, 2018, 2019a). It comprises an upstream reservoir, the spillway structure itself and a downstream reservoir that represents the river. Fig. 66 shows the geometry of the computational model.

The adopted particle diameter, d_p , respects the condition of being smaller than a quarter of the gate opening. Initially, fluid particles were placed in the upstream and downstream reservoirs with a dp varying from 0.62 m to 0.72 m. Thus, the number of fluid particles in the computational domain increased within the first seconds of simulation, in order to fill in the spillway channels. Four flow conditions were simulated, in particular those referring to the following flow rates: Q_{des} , Q_1 , Q_2 and Q_3 . The particle resolutions, number of particles as well as the computational times are resumed in Table 15.

Table 15 – GPUSPH simulations' characteristics.

Flow rate	Particle diameter (m)	Total no. of particles (10^6)	Physical time (s)	Approximate GPU time (h)
Q_{des}	0.72	0.9	35	19 (9.25*)
Q_1	0.66	1.0	35	19
Q_2	0.63	1.1	35	24
Q_3	0.62	1.2	35	23

*without turbulence model

Boundary conditions and other numerical parameters

A velocity driven boundary condition was used upstream of the computational domain (X_{min} section). To recover the appropriate flow rate, a logarithmic velocity profile with a varying water depth was imposed following Eqs. (35), (36) and (37). The upstream water depth was 21 m in all the simulations. Downstream of the computational domain (Y_{max} section), a pressure driven boundary condition was set, considering the downstream water depths presented in Table 14. The hydrostatic pressure initialization was disabled which means that at $t = 0$ s all fluid particles have equal and null pressure. The USAW boundary conditions were used.

The standard $k - \epsilon$ turbulence model was used (with $C_\mu = 0.09$ and $\kappa = 0.41$ – refer to Eq. (32) and Eq. (33)). A simulation without turbulence model was also carried out for comparison purposes. Near the walls, the flow is assumed to be in a smooth turbulent regime. The non-consideration of the wall roughness is not expected to have a significant influence in the numerical results of both study cases, because the material used in the experiments (Acrylic, PVC) along with the magnitudes of the observed velocities, yields a wall friction Reynolds number lower than 5 (smooth regime). Particle approximation was done with the Wendland C^2 kernel (Wendland, 1995). A fixed smoothing scale, h , of 1.5 was considered in all simulations.

DEVELOPMENT OF SPH APPLICATIONS

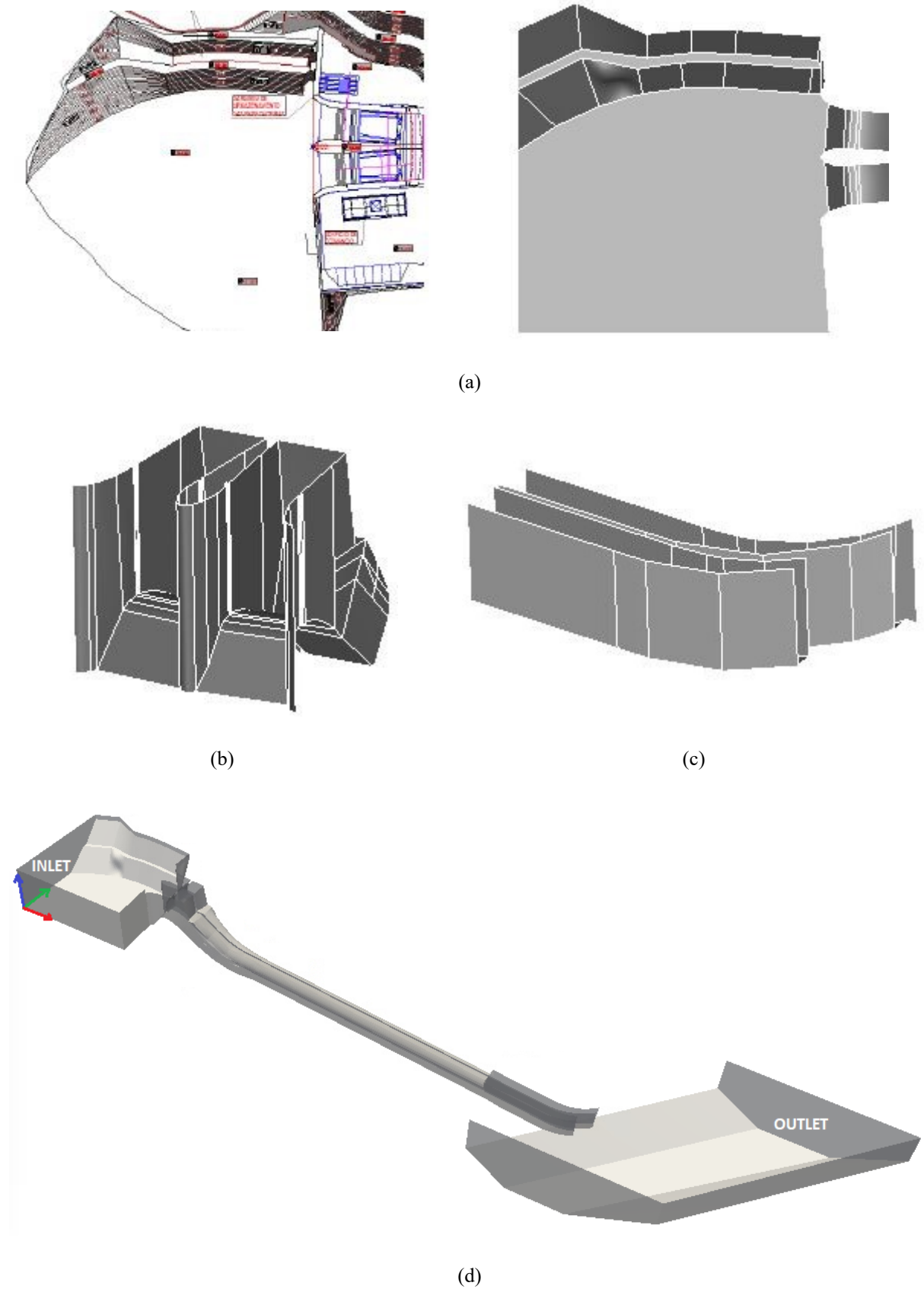


Fig. 66 - Numerical model's geometry: (a) upstream reservoir; (b) spillway's intake; (c) ski jump structure; and (d) general view.

Stability was favoured with the imposition of a maximum CFL number of 0.3. As in the previous case study, density diffusion was treated following Brezzi and Pitkäranta (1984) through the definition of the Brezzi coefficient as 1.0. The reason why this coefficient is greater in the present case study than it was in the previous one is because now one is interested in an extensive computation of pressures over the spillway bottom and walls, and a greater Brezzi coefficient may smooth out the pressure field commonly affected by noise.

A set of wave gages was defined to track the free-surface evolution in the sections under study (refer to Fig. 65), in the reservoir (to monitor the water depth and check if the reservoir depth was approximately 21 m) and at the spillway's intake. To obtain the pressure values, computational probes were set up. To further improve the pressures' computation, a change in the GPUSPH code was made so that pressures were computed taking the closest vertex particle (refer to Fig. 24), instead of the closest fluid particle as done in the study case I, which is expected to minimize pressure noise (because the base point for interpolation is always the same). The GTX TITAN X GPU card was used. The speed of sound, c_0 , was set to 250 m/s.

4.4.4. ANALYSIS OF RESULTS

As verified for the study case I, the number of particles in the simulations tended to stabilize. This condition, which means that the number of fluid particles leaving and entering the computational domain is roughly the same, along with the stabilization of some of the quantities being measured (e.g. the flow velocity at a certain point) was used to judge the convergence of the numerical solution. All simulations were run for 35 s of physical time which took between 19-23 h of computational time.

Fig. 67 shows a general view of the computed flow field in the spillway of the Caniçada dam, at the end of the simulation for the flow rate $890 \text{ m}^3/\text{s}$ and a view of the physical model testing. Flow velocities increase gradually along the spillway channel, reaching values of approximately 30 m/s ($\sim 3.8 \text{ m/s}$ in the physical model). Validation of the results was done for the water depths, pressures on the channel bottom and walls, flow velocities and jets' length.

Water depths

Firstly, the free-surface elevation at the approach of the spillway channel was assessed, near the guiding walls and the pier that divides both channel spans, to verify the functioning of the intake structure. The flow behaviour along the spillway chute is strongly affected by the flow pattern at the entrance of the spillway, which is influenced by the guiding walls configuration. The choice of an optimized design for the guiding wall has a great effect on rising the ability of the spillway to safely pass the probable maximum flood, so any nonuniformity in flow in the approach channel can cause reduction of spillway capacity, reduction in the discharge coefficient of the spillway, and even increase the probability of cavitation development. Fig. 68 and Fig. 69 show the computed and the experimentally measured free-surface elevation, at the spillways' intake. From the experiments it was verified that the free-surface elevation is greater near the left guiding wall in comparison to the right one, however, the SPH model suggest that this difference is negligible. As for both sides of the pier, the physical model suggests an opposite behaviour, that is, a higher free-surface elevation on the right side of the pier, whereas the SPH model does not register significant differences. The unevenness in the free-surface elevation near the flow boundaries is likely due to a "suction effect" of the spillway intake and the fact that it is positioned on the left margin of the dam's reservoir. In the SPH model such effect was probably lost because the portion of the reservoir being modelled was smaller. The velocity vectors field depicted in Fig. 70 indeed confirm this.

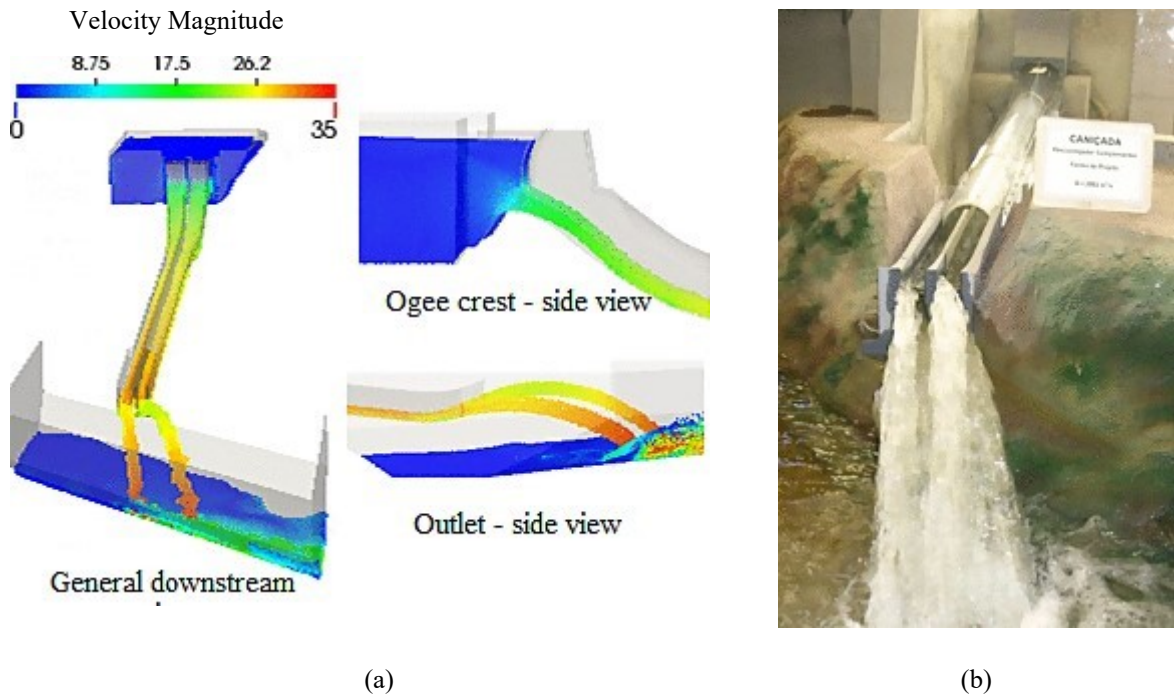


Fig. 67 - Caniçada dam: (a) numerical velocity flow field (in m/s), obtained with GPUSPH (GPUSPH), for the flow rate 890 m³/s; (b) physical model being tested.

The comparison between the computed and experimental water depths, in various sections, for the studied flow rates allowed to verify the capability of a SPH model to correctly simulate the free-surface behaviour. As previously mentioned, there are not experimental water depths available for the design flow rate, so, comparisons were done only for the flow rates Q_1 to Q_3 . Fig. 71 to Fig. 75 show the shape of the free-surface elevation for these flow rates (view from upstream to downstream). These are representative of a vertical cut along the YZ plane, in the measurement section. The free-surface representations were obtained thanks to the definition of wave gases, distanced ~ 0.6 m from each other.

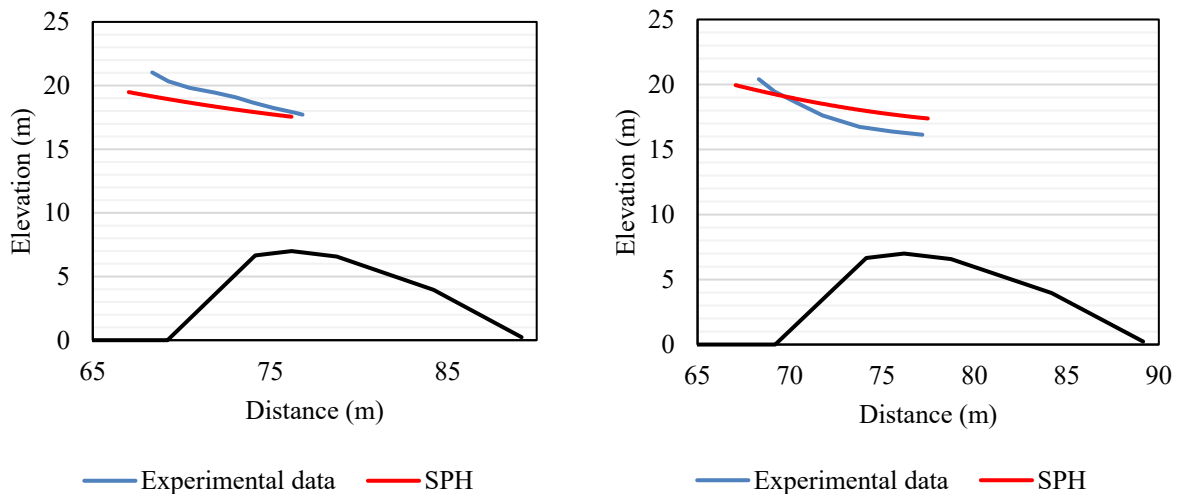


Fig. 68 - Computed vs. experimental free-surface elevation, at the spillways' intake, on the right guiding wall (on the left) and on the left guiding wall (on the right), for the design flow rate, Q_{des} . The thick black line schematizes the ogee crest profile.

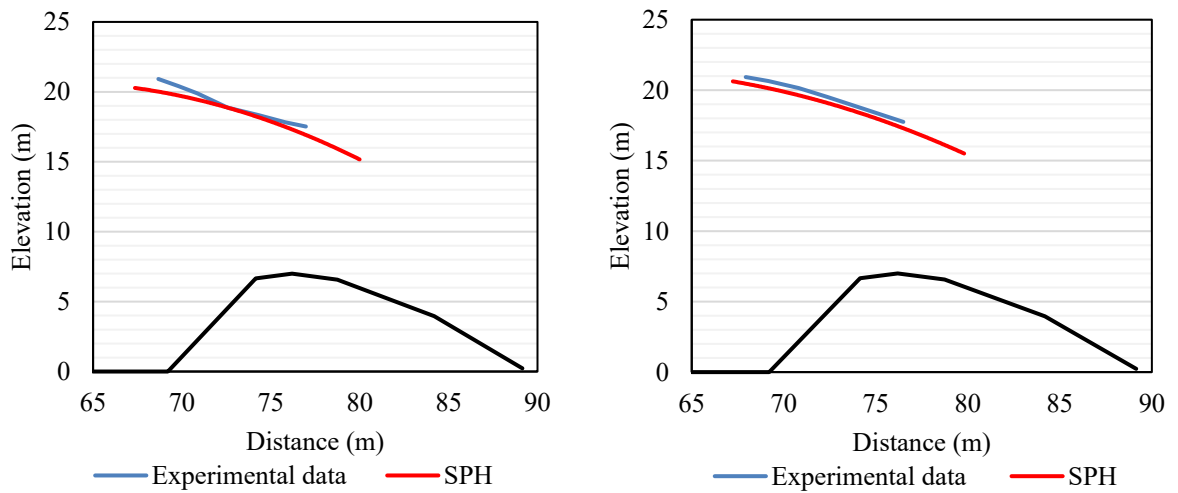


Fig. 69 - Computed vs. experimental free-surface elevation, at the spillways' intake, on the right side of the pier (on the left) and on the left side of the pier (on the right), for the design flow rate, Q_{des} . The thick black line schematizes the ogee crest.

The shape of the computed free-surface for the flow rate of $896 \text{ m}^3/\text{s}$ is represented in the Fig. 71 to Fig. 75 by the red line. It is clear the generic symmetry between the two spans of the spillway, with the exception of the final sections, located in the ski jump structure. The free-surface shape for the flow rate of $690 \text{ m}^3/\text{s}$ is visible through the green line. For this flow rate there is also the above-mentioned symmetry of the free-surface shape, with respect to the central septum, for all sections, except for sections 9 and 10. The water depths are smaller than those obtained for the flow rate of $896 \text{ m}^3/\text{s}$. The free-surface obtained for a discharge of $527 \text{ m}^3/\text{s}$ is represented by the blue line. The free-surface configuration is like that of the flow rates Q_1 and Q_2 , yet, smaller water depths were computed, as expected.

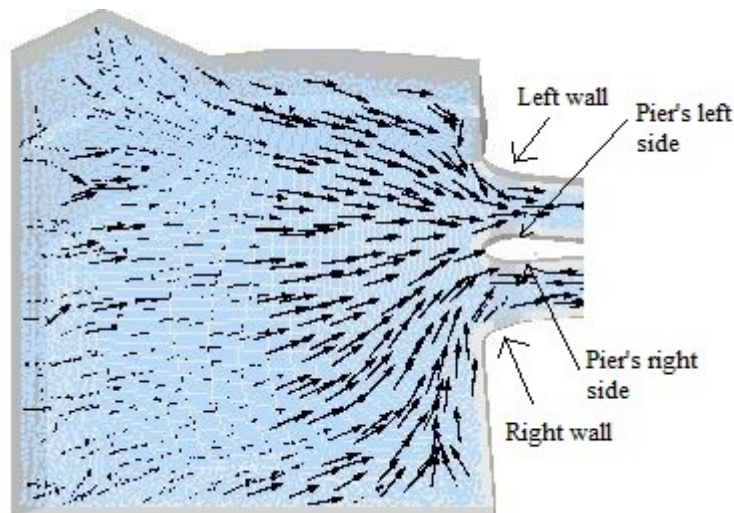


Fig. 70 - Flow pattern in the approach channel for the design flow rate.

DEVELOPMENT OF SPH APPLICATIONS

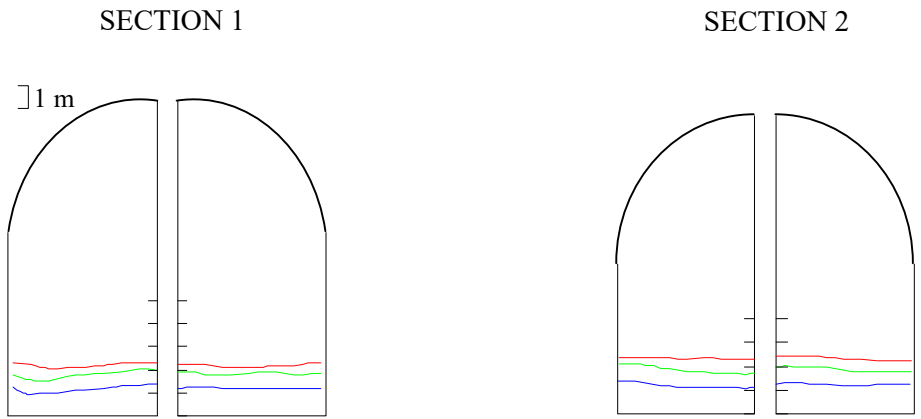


Fig. 71 - Free-surface shape in sections 1 and 2: flow rate 896 m³/s - red line; flow rate of 690 m³/s - green line; and flow rate of 527m³/s – blue line.

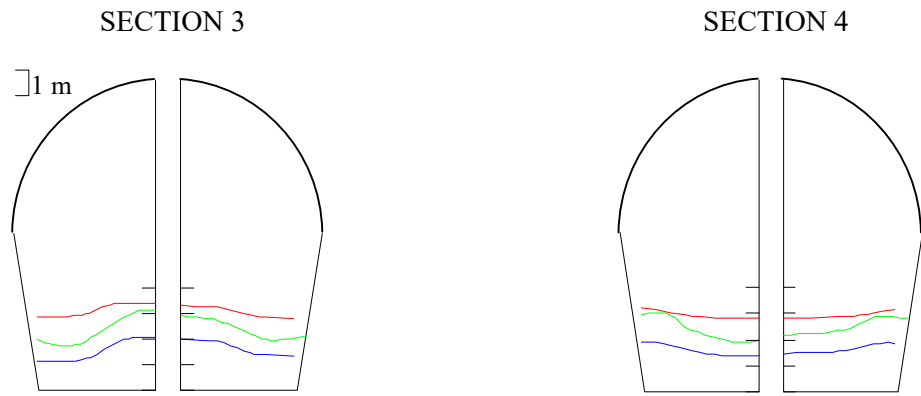


Fig. 72 - Free-surface shape in sections 3 and 4: flow rate 896 m³/s - red line; flow rate of 690 m³/s - green line; and flow rate of 527 m³/s – blue line.

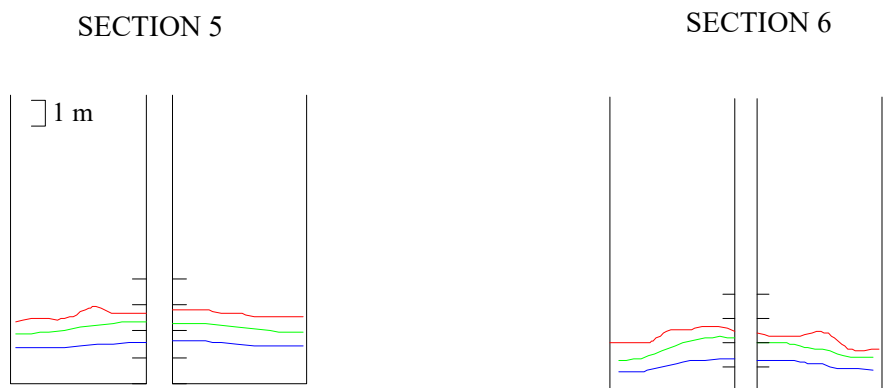


Fig. 73 - Free-surface shape in sections 5 and 6: flow rate 896 m³/s - red line; flow rate of 690 m³/s - green line; and flow rate of 527 m³/s – blue line.

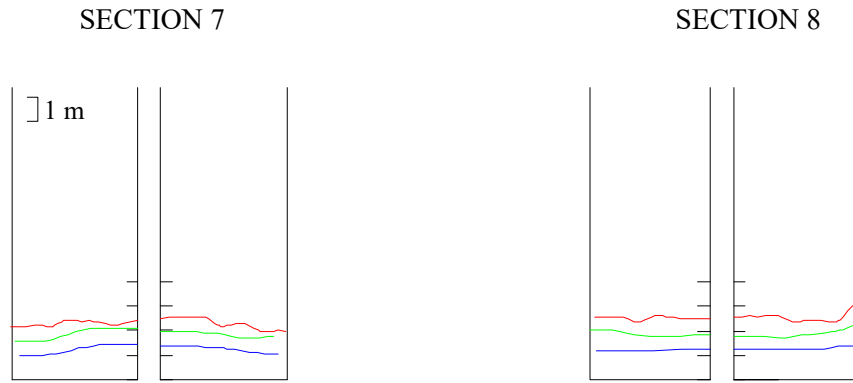


Fig. 74 – Free-surface shape in sections 7 and 8: flow rate 896 m³/s - red line; flow rate of 690 m³/s - green line; and flow rate of 527 m³/s – blue line.

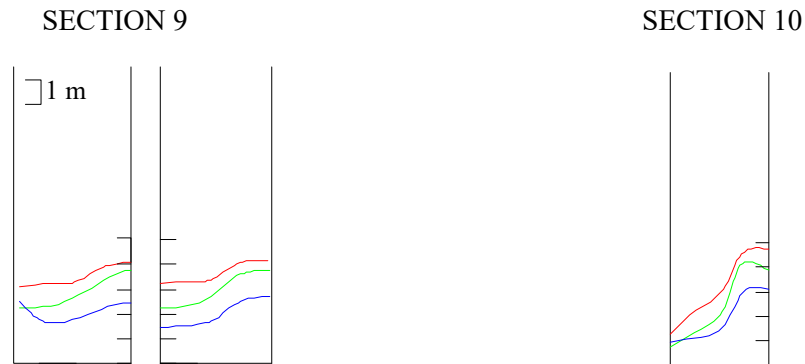


Fig. 75 – Free-surface shape in sections 9 and 10: flow rate of 896 m³/s - red line; flow rate of 690 m³/s - green line; and flow rate of 527 m³/s – blue line.

The comparison between the free-surface shape derived from the experiments and GPUSPH, for the flow rate of 896 m³/s is presented in Fig. 76 to Fig. 80. Globally, GPUSPH tended to underpredict the water depth. The agreement is reasonable for sections 1 to 5 (up to the end of the constant sloped stretch). From section 6 to 10, which are located in the final stretch of the spillway, discrepancies become greater. GPUSPH seems to fail in the water depth prediction in this stretch and it is then important to point out some possible explanations for this behaviour.

The fact that, at the end of the chute the flow is aerated (as verified in the experiments) may contribute to the referred GPUSPH underprediction, as entrained air is surely a cause for a water depth increase. In Appendix B, Fig B.1 to Fig B.10, the comparison between the computed and experimental free surface shape for the flow rates 690 m³/s and 527 m³/s is shown. The comparison is pretty much alike to that described for the flow rate of 896 m³/s.

Given that there exist changes in the cross-section, direction and inclination along this spillway, it is relevant to verify the development of cross-waves. The generic evolution of the free-surface elevation throughout the spillway channels was assessed for Q_{des} and Q_1 flow rates (Fig. 81).

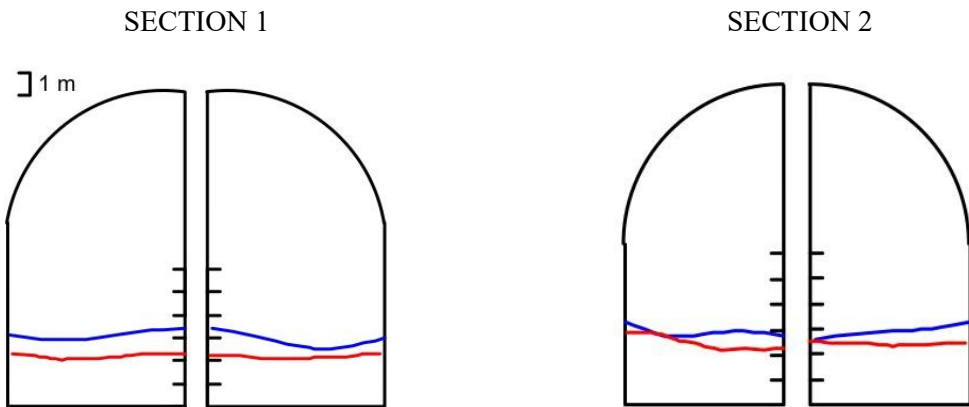


Fig. 76 - Graphic comparison of the free surface for sections 1 and 2 for the flow rate of 896 m³/s: Experimental results - blue line; GPUSPH results - red line.

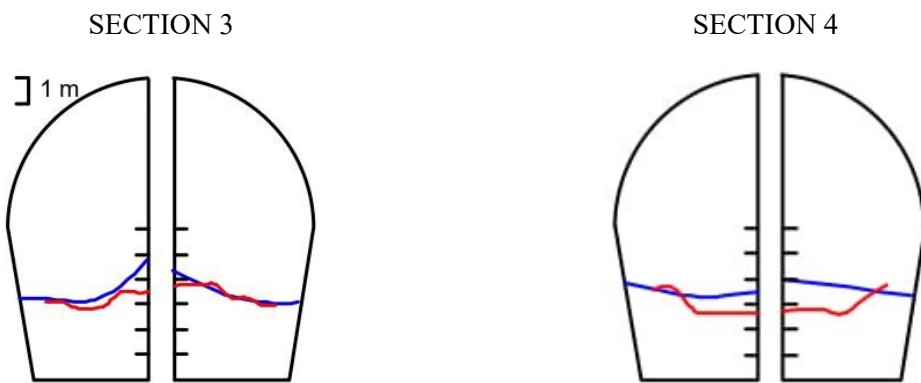


Fig. 77 - Graphic comparison of the free-surface for sections 3 and 4 for the flow rate of 896 m³/s: Experimental results - blue line; GPUSPH results - red line.

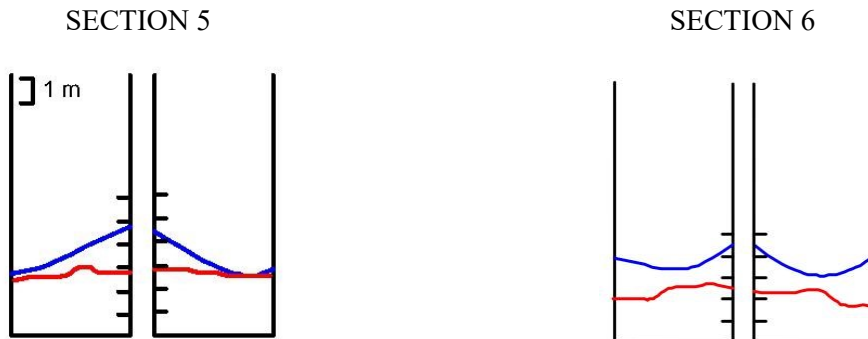


Fig. 78 - Graphic comparison of the free-surface for sections 5 and 6 for the flow rate of 896 m³/s: Experimental results - blue line; GPUSPH results - red line.

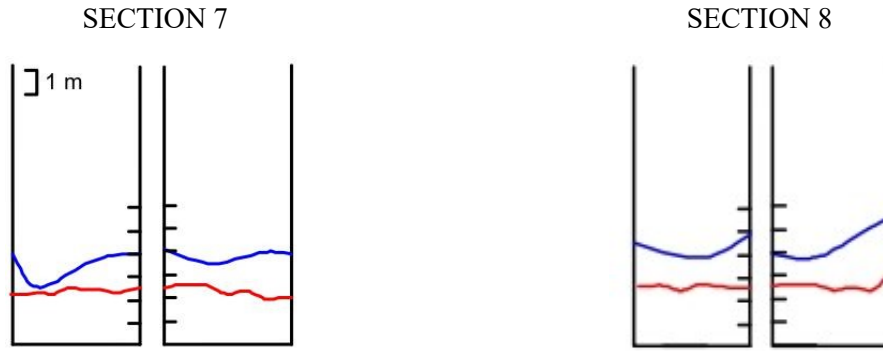


Fig. 79 - Graphic comparison of the free-surface for sections 7 and 8 for the flow rate of 896 m³/s: Experimental results - blue line; GPUSPH results - red line.



Fig. 80 - Graphic comparison of the free surface for sections 9 and 10 for the flow rate of 896 m³/s: Experimental results - blue line; GPUSPH results - red line.

The elevation of each fluid particle with respect to the channel bottom, Z , was considered as $Z = Z_{absolute} - Z_{channel\ bottom}$, being $Z_{absolute}$ the absolute z -coordinate of each particle in the SPH simulation and $Z_{channel\ bottom}$ the z -coordinate of the channel bottom. $Z_{channel\ bottom}$ was obtained through the approximation of the spillway channel profile by polynomial regressions (with correlation coefficients, R^2 , of 0.9999 – 1). The numerical results suggest the development of cross-waves, especially for the flow rate Q_1 .

Pressures

The pressure history was recorded with a sampling frequency of 10 Hz, throughout the simulations. The exact locations where pressures were computed are presented in Table B.1, in Appendix B. Fig. 82 shows the pressure signal as registered by GPUSPH at the locations P2 and P3 for the flow rate 690 m³/s. Table 16 and Table 17 present the computed pressures based on the average of the pressures within the last 20 s of simulation. For the design flow rate, it was verified that the highest channel bottom pressures are recorded at locations P13 to P16, that is, along the ski jump structure. The smallest channel bottom pressures are recorded in the spillway crest. With respect to the lateral wall pressures, it was verified that higher values are recorded in the right-side wall, consequence of the geometry of the spillway's final stretch, which configures a curve in plant to the left. For the flow rate of 896 m³/s it is

worth noticing the increase in the crest pressures, due to the hydraulic head increase, consequence of the gate closing.

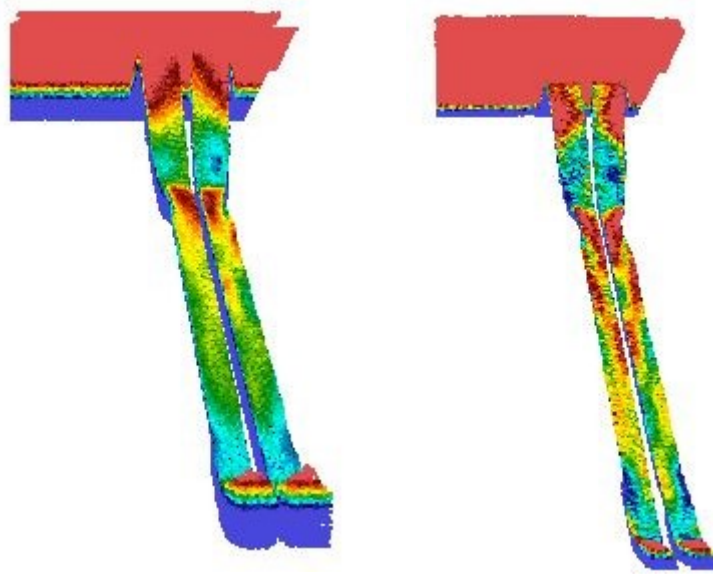


Fig. 81 – Numerical cross-waves development in the complementary spillway of the Caniçada dam. Fluid particles coloured by their elevation with respect to the channel bottom, Z , for the design flow rate, Q_{des} (on the left – blue, 5 m, to red, 9m), and the flow rate of $896 \text{ m}^3/\text{s}$, Q_1 (on the left – blue, 2 m, to red, 3.5 m).

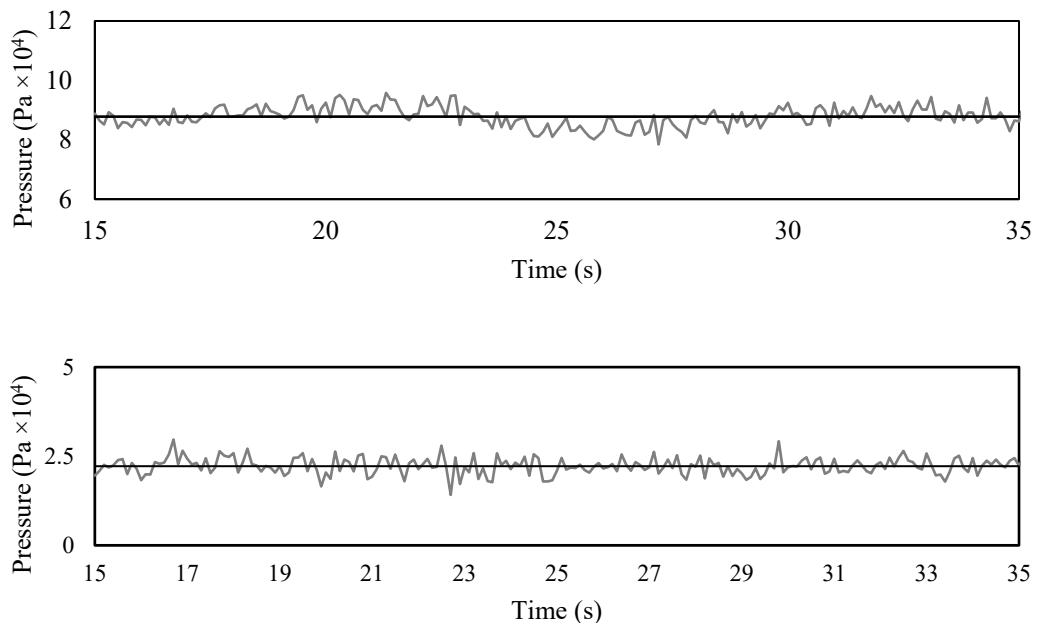


Fig. 82 - Computed pressure history at P2 (above) and at P3 (below) for the flow rate of $690 \text{ m}^3/\text{s}$.

With respect to the lateral wall pressures, null values were recorded for the measurement points P2R, P2L, P4R, P4L, P6L, P7R, P7L, P9L, P10R, P10L, because of insufficient water depth. For the flow rates of $690 \text{ m}^3/\text{s}$ and $527 \text{ m}^3/\text{s}$, the crest pressures tend to increase as the flow rate decreases. Also, the

channel bottom pressures over the ski jump structure decrease with the decrease of the flow rate. For a discharge of 690 m³/s, null values were recorded for the same measurement points as for 896 m³/s. For the flow rate of 527 m³/s the measurement points P2R, P2L, P4R, P4L, P5R, P5L, P7R, P7L, P8R, P8L, P9R, P9L, P10R and P10L registered null values.

Table 16 - Computed pressures for the measuring points in the channel bottom.

ID	Pressure (Pa ×10 ⁴)			
	Q_{des}	Q_1	Q_2	Q_3
P1	4.93	10.59	12.47	13.27
P2	2.31	6.72	8.79	10.55
P3	1.60	2.42	2.23	2.84
P4	1.31	0.60	0.66	0.79
P5	6.72	1.74	1.28	0.35
P6	6.71	3.20	2.27	3.98
P7	11.12	4.61	3.12	1.75
P8	12.14	6.65	5.16	4.00
P9	8.01	3.57	2.74	2.07
P10	7.83	3.35	2.62	1.94
P11	7.79	3.41	2.70	2.03
P12	7.52	2.62	1.90	1.84
P13	15.94	4.36	3.22	2.05
P14	20.32	8.88	6.78	4.39
P15	17.30	8.24	6.70	4.37
P16	13.13	7.09	5.54	4.15

Fig. 83 shows the comparison between the computed and experimental bottom pressures (both with and without the employment of the standard $k - \epsilon$ turbulence model) for the design flow rate, Q_{des} . It can be seen that not including a turbulence model results in a significant accuracy loss, while by including it SPH can provide interesting results. The greater differences between experimental and computed results were observed in the crest of the spillway, with GPUSPH overpredicting pressures. Also, at locations P10 and P11 some discrepancies were registered. The physical model registers a negative pressure at P3. As expected, GPUSPH cannot predict realistic negative pressures as it is based on a WCSPH formulation¹³. Concerning the lateral wall pressures, results are satisfactory, especially for P1 to P6 (Fig. 84). GPUSPH always computes greater pressures in the right wall, which agrees with the deformation observed in the free-surface shape, in the ski jump stretch, caused by the geometry of the spillway. However, in the experiments, in the piezometers P8 and P9 the opposite occurred.

Fig. 85 shows the comparison between experimental and numerical bottom pressures for the flow rate of 896 m³/s, Q_1 . Overall, pressures were predicted with a good accuracy with the exception of P4, where sub atmospheric pressure was registered in the experiments and P8, P10 and P11. For the lateral wall pressures results were satisfactory except for the piezometer P8L (Fig. 86). The physical model registered a much higher pressure in the left wall (P8L) than GPUSPH. Fig. 87 shows the comparison between experimental and numerical bottom pressures for the flow rate of 690 m³/s, Q_2 . For this flow

¹³ Possible negative pressures computed with a WCSPH formulation would likely be numerical artifacts.

rate, a sub atmospheric pressure was recorded at P4. Again, greater discrepancies occur for P8, P10 and P11. The wall pressures results were satisfactory for piezometers P1, P3 and P5L (Fig. 88). P5R and P8L registered the significant discrepancies.

Table 17 - Computed pressures for the measuring points in the lateral channel walls.

ID	Pressure (Pa $\times 10^4$)			
	Q_{des}	Q_1	Q_2	Q_3
P1R	15.07	4.20	3.33	1.25
P1L	11.96	2.96	2.53	1.26
P2R	7.02			
P2L	6.34			
P3R	18.47	7.59	6.47	3.66
P3L	16.46	5.03	4.50	0.84
P4R	10.47			
P4L	7.08			
P5R	16.71	9.01	5.02	5.14
P5L	14.45	5.29	2.80	2.06
P6R	9.82	0.69	0.15	
P6L	6.51			
P7R	3.81			
P7L	0.62			
P8R	11.49	5.58	4.60	5.38
P8L	8.33	1.86	0.86	0.09
P9R	6.18	0.73	0.25	0.02
P9L	2.96			
P10R	2.54			
P10L	0.35			

Fig. 89 shows the comparison between experimental and numerical bottom pressures for the flow rate of $527 \text{ m}^3/\text{s}$, Q_3 . For this flow rate greater differences were observed, particularly in the constant sloped stretch at P6, P8, P10, P11, P12 and P13. The comparison made for the lateral wall pressures for this flow rate showed greater discrepancies in relation to the flow rates previously presented (Fig. 90). Despite the differences observed, the evolution of the pressures in the spillway bottom and walls was generally well captured.

As previously mentioned, a WCSPH model (as GPUSPH) is not able to compute negative pressures. However, the developed SPH model is capable of showing if and where such negative pressures are likely to occur. This qualitative assessment was made by evaluating the renormalization factor values, γ , (refer to Eq. 29), all over the fluid particles. The γ value is related with the kernel truncation, being 1 if the kernel is fully complete and 0 for a fully incomplete kernel. As can be seen in Fig. 91, the fluid particles tend to detach from the spillway surface (flow separation - $\gamma \sim 1$) near the crest, which is coherent with the development of negative pressures (as verified in the experiments). In fact, for hydraulic heads greater than the design hydraulic head (which is the case as $H/H_d = 1.13$), negative pressures tend to develop on the spillway crest.

DEVELOPMENT OF SPH APPLICATIONS

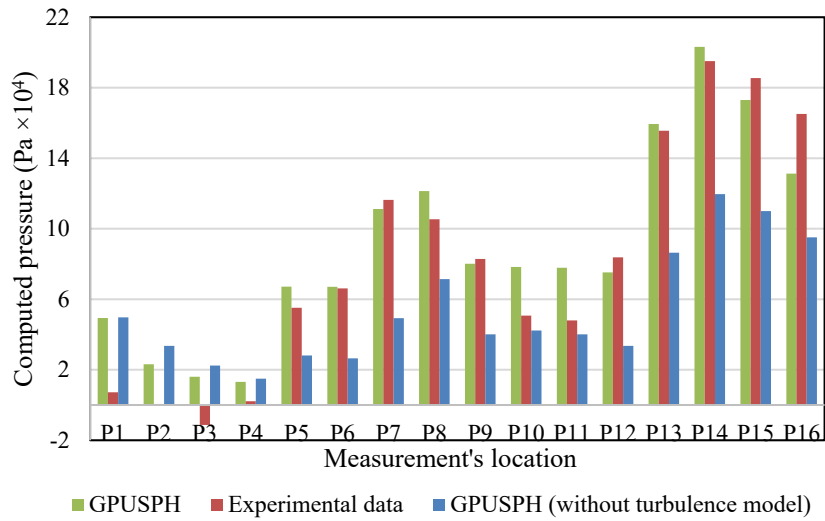


Fig. 83 - Experimental vs. computed pressures, on the spillway bottom, for the flow rate of 2026 m³/s, Q_{des} .

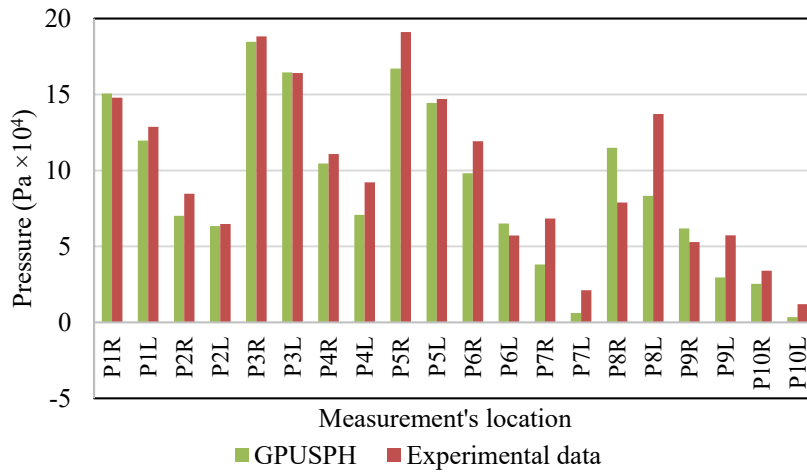


Fig. 84 - Experimental vs. computed pressures, on the spillway walls, for the flow rate of 2026 m³/s, Q_{des} .

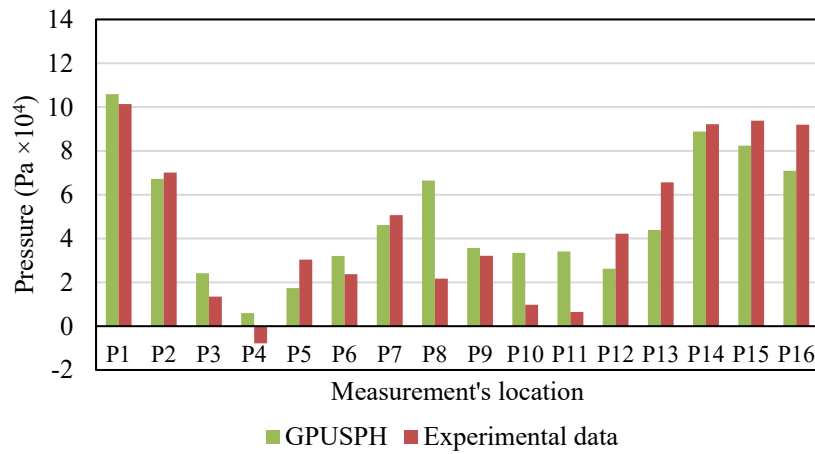


Fig. 85 - Experimental vs. computed pressures, on the spillway bottom, for the flow rate of 896 m³/s, Q_1 .

DEVELOPMENT OF SPH APPLICATIONS

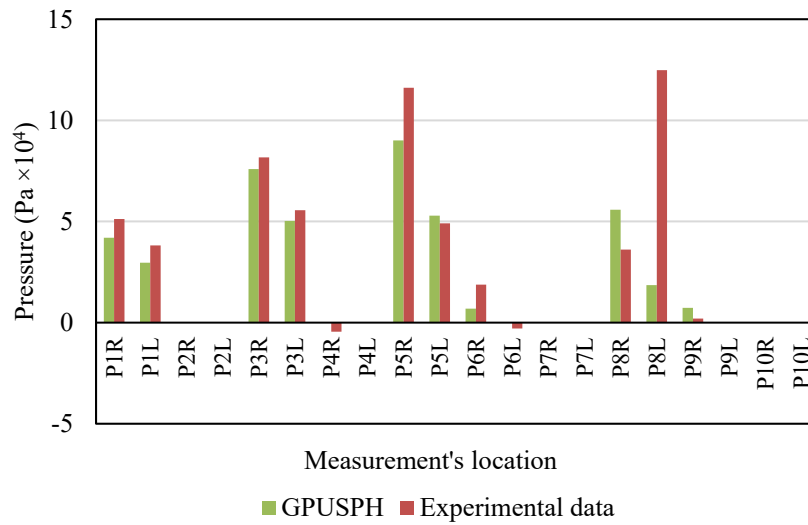


Fig. 86 - Experimental vs. computed pressures, on the spillway walls, for the flow rate of 896 m³/s, Q_1 .

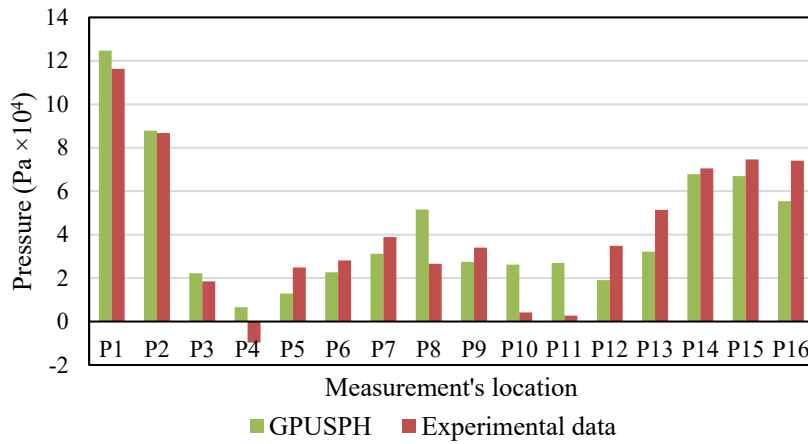


Fig. 87 - Experimental vs. computed pressures, on the spillway bottom, for the flow rate of 690 m³/s, Q_2 .

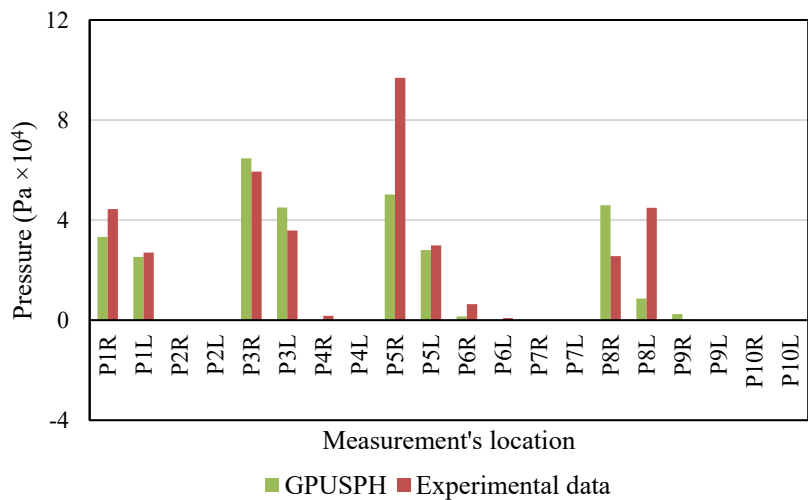


Fig. 88 - Experimental vs. computed pressures, on the spillway walls, for the flow rate of 690 m³/s, Q_2 .

DEVELOPMENT OF SPH APPLICATIONS

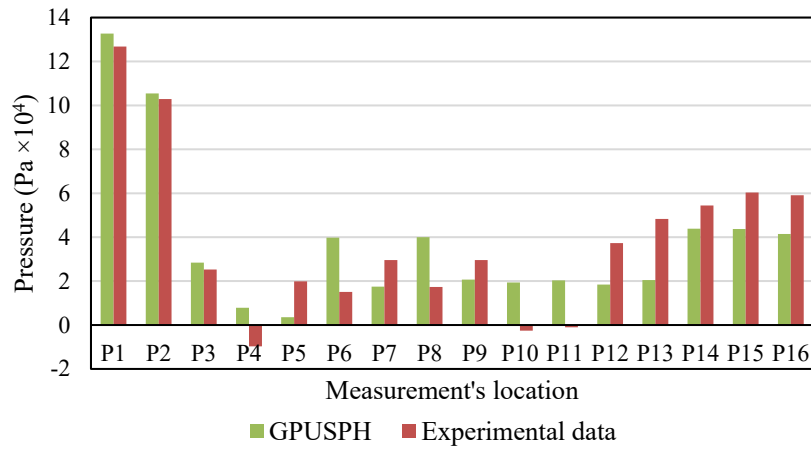


Fig. 89 - Experimental vs. computed pressures, on the spillway bottom, for the flow rate of 527 m³/s, Q_3 .

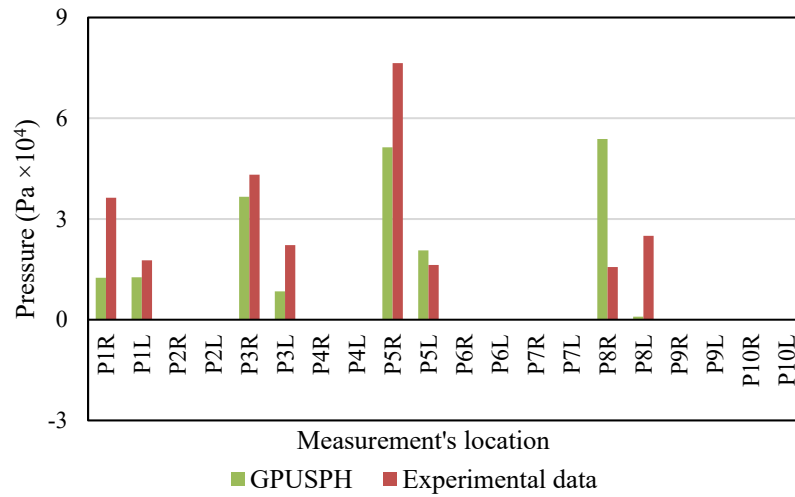


Fig. 90 - Experimental vs. computed pressures, on the spillway walls, for the flow rate of 527 m³/s, Q_3 .

A ratio H/H_d slightly greater than the unit is commonly used in practice as it increases the discharge coefficient, increasing the discharge capacity of the structure. This effect should, however, be limited due the potential for cavitation.

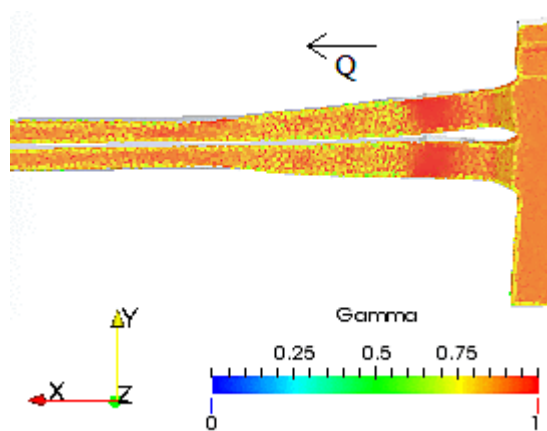


Fig. 91 – Fluid particles coloured by their renormalization factor value r, γ , for the flow rate of 890 m³/s, Q_1 . (bottom to top view).

Flow velocities

The characterization of the flow velocity magnitude in sections V1 to V6 was done for the simulations carried out with the design flow rate the flow rate of 896 m³/s. To do so, the velocity at approximately half water depth was computed at each section using a Gaussian interpolation over the 250 closest particles (roughly, the number of neighbours throughout the simulations). The reported values correspond to an average of the velocity over a time range of at least 20 s. Fig. 92 shows that variations in the computed flow velocities are small which indicates that the numerical model reached a steady state.

Table 18 and Table 19 show the computed and experimental velocities for Q_{des} and Q_1 , respectively. For Q_{des} , it is worth noticing the discrepancies obtained for V1 and V5. In the entrance of the spillway channel, at V1, GPUSPH underpredicted the velocity for both flow rates tested, however the underprediction is greater for the design flow rate. The mean relative error obtained for the comparison between computed and experimental flow velocities was 17.5% for Q_{des} and 28.4% for Q_1 .

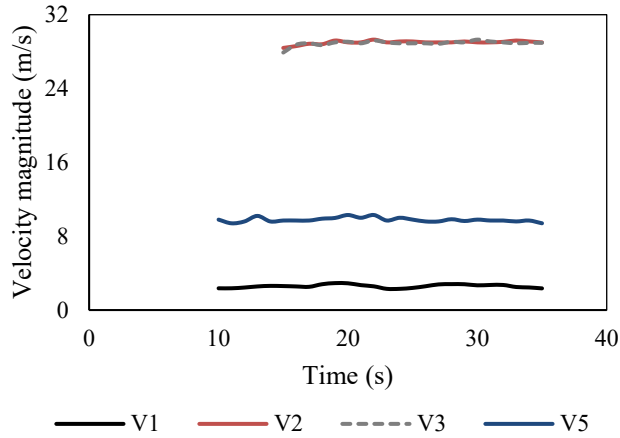


Fig. 92 - Evolution of the velocity magnitude over time, at sections V1, V2, V3 and V5 for the flow rate of 896 m³/s, Q_1 .

Table 18 – Comparison of the velocity magnitude, U , at sections V1, V3, V5 and V6 for the design flow rate, Q_{des} .

	Measurement location	Experimental U (m/s)	GPUSPH U (m/s)
Right span	Section V1	11.0	5.5
	Section V3	7.0	27.1
	Section V5	38.8	28.2
Left span	Section V1	9.9	5.4
	Section V6	22.4	26.6

DEVELOPMENT OF SPH APPLICATIONS

Table 19 – Comparison of the velocity magnitude in sections V1 to V6 for the flow rate of 896 m³/s, Q_1 .

	Measurement location	Experimental U (m/s)	GPUSPH U (m/s)
Right span	Section V1	3.7	2.6
	Section V2	13.5	9.8
	Section V3	26.9	29.0
	Section V5	40.4	28.9
Left span	Section V1	3.5	2.7
	Section V2	11.9	9.9
	Section V4	26.9	27.5
	Section V6	26.2	27.3

Experimental results evidence a great difference between the velocities achieved in the ski jump structure on the right and left spans. Despite the measurement sections are different (that is V5 and V6), the magnitude of the flow velocities differs in more than 70%. This, together with the reported uncertainty associated with measurement technique, concur that this comparison must be taken with some reserves. In fact, the size of propellers used in the experimental campaign (30 mm and 50 mm) were significant in comparison to the dimensions of the physical model channel (ranging from ~180 mm, in the entrance of the spillway channel, to ~60 mm in the ski jump structure). Moreover, difficulties in stabilizing the propeller meter were reported. Still, despite the results obtained at V5, the other computed velocities in the ski jump structure are in agreement with the experiments.

Jets' trajectory and length

Though the jets' trajectory was not measured during the experiments, the computed jets' trajectory was analysed considering the mass point dynamics theory. Juon and Hager (2000) demonstrated that both the upper and the lower jet trajectories from circular-shaped buckets are parabolic-shaped. With z_0 equal to 0 or equal to the water depth at take-off for the lower and upper jets, respectively, and α_j as the virtual jet take-off angle, the trajectory equation reads

$$z(x) = z_0 + \tan(\alpha_j) x - \frac{gx^2}{2U_0^2 (\cos \alpha_j)^2} \tag{39}$$

Being U_0 the average approach velocity, determined as a function of the flow rate, Q , the approach water depth, h_0 , and the channel width, b , as $U_0 = Q/(bh_0)$.

Data normalization is a common way of facilitating results comparison and interpretation, as it eliminates the units of measurement. Here, the trajectory normalization proposed by Heller *et al.* (2005)

was used. With it, the maximum jet elevation is used for the normalization, which can be obtained from the derivative of the trajectory parabola by setting $dz/dx = 0$, resulting in the following normalized trajectory coordinates (X, Z)

$$X = \frac{2x}{h_0 F_0^2 \sin(2\alpha_j)} \quad (40)$$

$$Z = \frac{2z}{h_0 F_0^2 (\sin \alpha_j)^2} \quad (41)$$

With F_0 being the Froude number of the approach flow ($F_0 = U_0 / \sqrt{gh_0}$). α_j is the virtual jet take-off angle used to fit the data to the general mass-point parabola, so that the trajectory maxima is at $X = Z = 1$ and the take-off location is at $X = Z = 0$. It means that the normalized data should fit the equation

$$Z = 2X - X^2 \quad (42)$$

Fig. 93 shows the upper and lower normalized SPH trajectories (of the left jet, for the design flow rate, Q_{des}), and Eq. (42) fitted both to SPH normalized results and the experimental normalized results by Schmocker (2006) and Balestra (2012). The SPH normalized data follow well Eq. (42) resulting in a coefficient of determination of R^2 of 0.997 and 0.998 for the lower and upper trajectory, respectively. Schmocker (2006) and Balestra (2012) data were fitted to Eq (42) with a R^2 of 0.94 (upper and lower jet trajectory data analysed together). Thus, the trajectory shape follows the standard parabolic profile, provided the take-off angle of both the lower and upper jet trajectories are correctly accounted for. As shown by Pfister *et al.* (2014), and also verified with the SPH results, the virtual take-off angle, α_j , is generally smaller than the geometrical take-off angle, α , so, using α for trajectory computation is inadequate, typically resulting in too long jets (Fig. 94).

To define the computed jet's length, a plot according to the z-component of the velocity, U_z , was used to determine the point where the jet hits the downstream water, as at this point a rapid change in U_z occurs. The jets' length was determined considering the furthest distant point with respect to the furthest downstream point of the spillway, considering its final alignment.

Fig. 95 to Fig. 98 depict the jets' shape at the end of the simulations. These evidence the changes in the jets' characteristics for the various flow rates, not only in terms of the jets' length but also in terms of its width. The jet issued from the right span evidences a greater velocity in comparison to the left jet.

Table 20 shows a comparison among the jets' length derived from GPUSPH and the physical model. The jet's length derived from GPUSPH tend to decrease with decreasing flow rate and are greater for the jets issued from the left span. This behaviour is in agreement with that observed in the physical model, however, jets' length are overpredicted by GPUSPH, especially for lower flow rates and for the jet issued from the right span.

DEVELOPMENT OF SPH APPLICATIONS

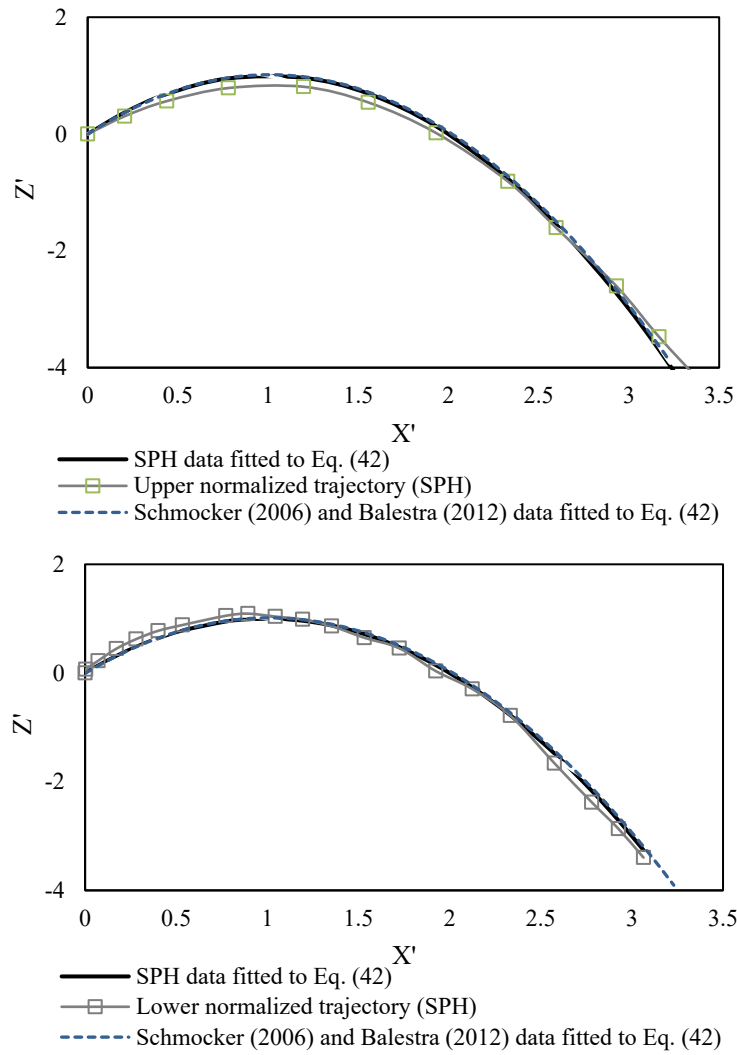


Fig. 93 – Normalized upper (above) and lower (below) SPH jet trajectories and corresponding fit to Eq. (41). Comparison with Eq. (41) fitted to the normalized experimental results by Schmocker (2006) and Balestra (2012).

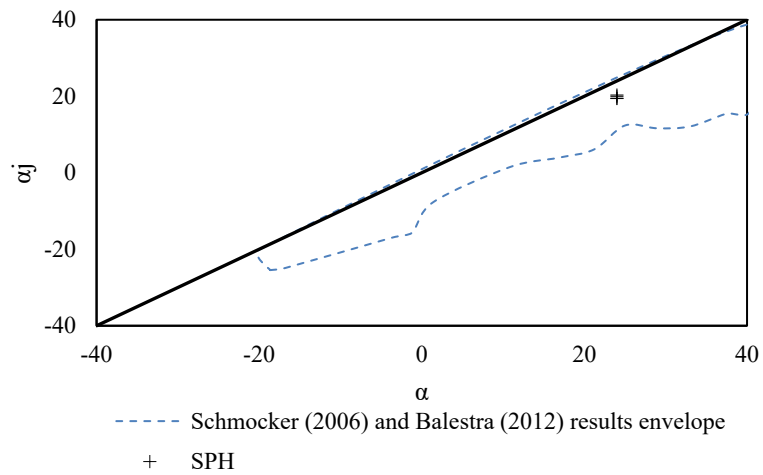


Fig. 94 - Comparison between the geometrical take-off angle, α , and the virtual take-off angle α_j obtained for the SPH results (right and left jets, for the design flow rate, Q_{des}). Comparison with the results envelope for the experimental data by Schmocker (2006) and Balestra (2012).

DEVELOPMENT OF SPH APPLICATIONS

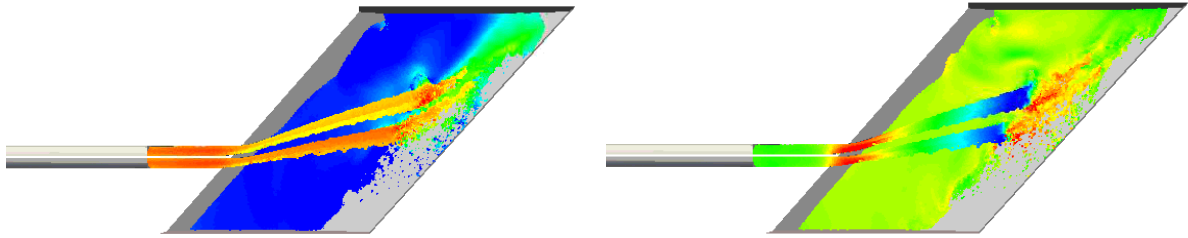


Fig. 95 - Jets' configuration for the design flow rate, Q_{des} : horizontal component of velocity, U_x , on the right (blue, 0 m/s, to red, 32 m/s) and vertical component of velocity, U_z , on the left (blue, -20 m/s, to red, 10 m/s).

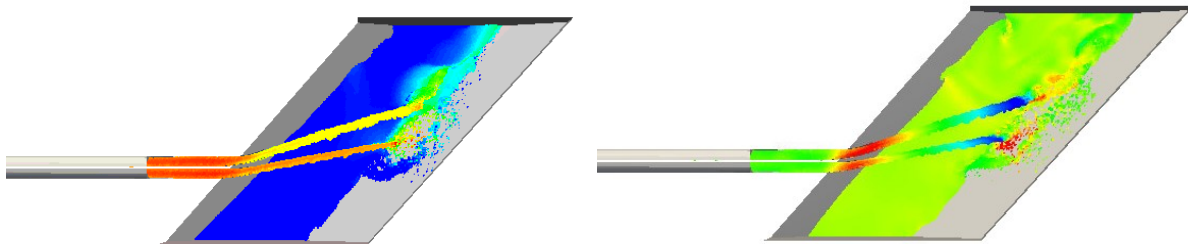


Fig. 96 - Jets' configuration for the flow rate of $896 \text{ m}^3/\text{s}$, Q_1 : horizontal component of velocity, U_x , on the right (blue, 0 m/s, to red, 32 m/s) and vertical component of velocity, U_z , on the left (blue, -20 m/s, to red, 10 m/s).

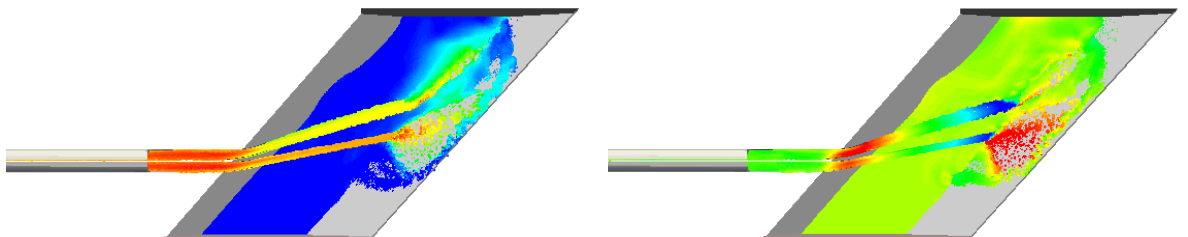


Fig. 97 - Jets' configuration for the flow rate of $690 \text{ m}^3/\text{s}$, Q_2 : horizontal component of velocity, U_x , on the right (blue, 0 m/s, to red, 32 m/s) and vertical component of velocity, U_z , on the left (blue, -20 m/s, to red, 10 m/s).

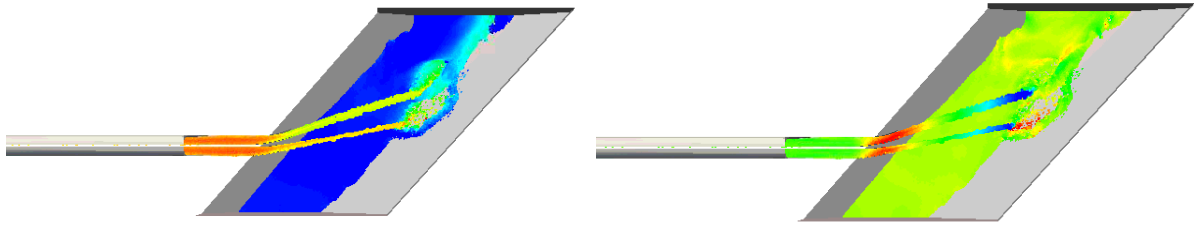


Fig. 98 - Jets' configuration for the flow rate of 527 m³/s, Q_3 : horizontal component of velocity, U_x , on the right (blue, 0 m/s, to red, 32 m/s) and vertical component of velocity, U_z , on the left (blue, -20 m/s, to red, 10 m/s).

The dispersion of jets in prototype trajectory basins is a highly complex phenomenon of which viscosity, surface tension, air entrainment and turbulence are variables. In the presented results comparison, the following should be borne in mind:

- Simulated jets are more compact than those in the experiments because surface tension and air entrainment were not modelled. This is coherent with the referred overprediction of the jet's length;
- Jets studied under laboratory conditions are normally small in diameter what causes the effects of surface tension and viscosity to be significant. Jets' disintegration and length depend on the Reynolds and Weber numbers, so, the scale effects derived from a physical model scaled to Froude similarity may be relevant; and
- Ervine and Falvey (1987) studied the mechanisms of jet spreading and break-up in the air. They found out that the key parameter governing jet's deformation in the air is the jet's initial turbulence intensity. As previously stated, the turbulence model used can be inaccurate to predict the flow features in the downstream portion of the spillway. As such, the turbulent kinetic energy and consequently the turbulence intensity computations will be subjected to inaccuracies, because these quantities relate to each other. In fact, intensity of turbulence is generally characterized by the rate of formation of turbulent kinetic energy, that is, the rate at which energy is transferred from the mean flow to the turbulent eddies.

So, the computed jets' length accuracy may be affected due to both the turbulence model used and the non-consideration of the air phase. Moreover, the jet's geometry at issuance is as well affected by the underprediction of the water depth.

Table 20 – Computed vs. experimental jets' length.

Flow rate	Left span jet (m)			Right span jet (m)		
	Experimental	GPUSPH	% variation	Experimental	GPUSPH	% variation
Q_{des}	80.6	85.9	6.6	70.1	77.2	10.1
Q_1	74.4	82.9	11.4	64.8	75.1	15.9
Q_2	70.1	77.1	10.0	60.1	73.9	23
Q_3	68.2	77.1	13.0	58.3	72.1	23.7

4.4.5. GPUSPH *VS.* MESH-BASED MODEL RESULTS

A quantitative validation of the SPH model was presented above, for the water depths, pressures on the channel bottom and walls, flow velocities and jets' length, by comparison with the corresponding available experimental data. Still, another objective of this research was the comparison with a mesh-based model results. In this section, the GPUSPH performance is compared with that obtained by Brandão (2015) using the commercial FLOW-3D software¹⁴, which is based on the FVM, with the VoF technique for the free-surface tracking (FLOW- 3D Documentation 2014), for the same case study. Table 21 summarizes some of the characteristics of each numerical model. Since both numerical models were set at prototype dimensions, whilst the experimental results used for the validation were derived from a scaled physical model, it is important to ponder on the effects that can eventually arise from this comparison. A physical model scaled upon a Froude similarity may result in fluid flow properties such as the capillary forces and the viscous forces being incorrectly reproduced, affecting phenomena as air entrainment (Pfister and Chanson, 2014). Since a single-phase SPH model was used, air entrainment will not be modelled, regardless of the numerical model scale, so a prototype scale was taken (allowing for a rather direct comparison with the mesh-based model results).

Table 21 - GPUSPH vs. FLOW-3D models' characteristics.

	GPUSPH	FLOW-3D
Resolution	Particle diameter, dp , varied from 0.65 m to 0.72 m among the various simulations	Cell dimensions: 0.5 m \times 0.5 m \times 0.5 m
Scale	1:1	1:1
Multi-phase modelling	Single phase	Application of an air entrainment model
Turbulence modelling	Standard $k - \epsilon$ (Pope, 2001)	RNG $k - \epsilon$ (Yakhot and Orszag 1986)
Physical time (s)	35	100
Computational time	19h	\sim 1 week
Hardware	Run on GPU	Run on CPU*

*No information is available with regard to the mesh-based model being run in parallel or series.

Fig. 99 shows a comparison among GPUSPH, the mesh-based model and the experimental results for the water depths along the spillway, for the flow rate Q_1 (view from upstream to downstream). Globally, GPUSPH tended to underpredict the water depths, being this effect rather pronounced along the spillway's final stretch, such as at section 9. This behaviour was equally observed for the other flow rates tested. As far as the mesh-based model results are concerned, these seem to better approach the experimental results, especially in the final stretch of the spillway. Thus, the most likely justification for the GPUSPH results discrepancies may lay on the fact that in the final stretch of the spillway the flow is aerated despite a single-phase SPH code has been employed. All over the spillway channel, it is

¹⁴ FLOW-3D software is nowadays widely used for engineering simulations of dam spillways.

expected that the air concentration in the water will smoothly increase, what may rise the water depth. Even if aeration is limited in the scaled model due to existing low Reynolds and Weber numbers (Pfister and Chanson, 2014), the spillway chute is probably long enough to trigger air entrainment. For gated structures (chutes), Toso and Bowers (1988) estimate the distance needed for the boundary layer to reach the surface to be about 50 times the gate opening. It turns out that the water depth over the ski jump structure is very probably influenced by some air entrainment, and the jet issued is aerated too (as visible in the experiments depicted in Fig. 67). This can possibly justify why the mesh-based model performed better in predicting the water depths in the downstream portion of the spillway, as it considered the effect of air entrainment.

Besides that, it is expected that the flow features in the final stretch of the spillway are rather complex because this stretch configures a set of geometrical changes, such as, a cross-section narrowing, a spanwise rotation (curve in plant) and the bottom curvature characteristic of a ski jump structure. As seen in Fig. 99, at section 9, the water depth is slightly greater at the convex border and a little shallower at the concave border, so that the free-surface is not flat but displays the characteristic depression toward the axis of the spinning fluid. This aspect was qualitatively well-reproduced by GPUSPH. When water moves in a circular motion, a pressure gradient results from the concave border towards the other border and the water near the concave border flows at a relatively higher speed, whereas the water at the convex border flows more slowly.

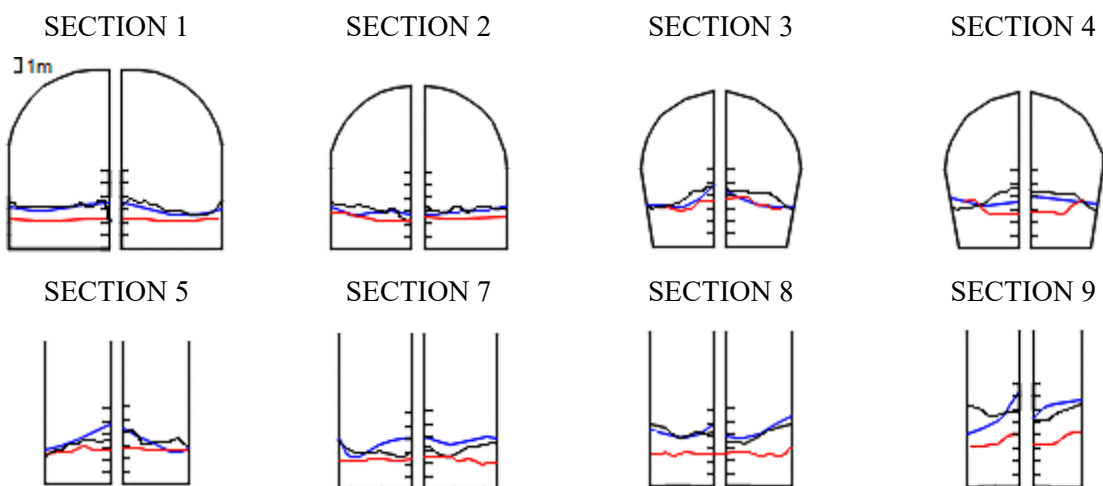


Fig. 99 - Graphic water depths comparison for sections 1, 2, 3, 4, 5, 7, 8 and 9, for the flow rate of $890 \text{ m}^3/\text{s}$, Q_1 . Blue line: experimental results; red line: GPUSPH results; and black line: FLOW-3D results.

The isotropic eddy viscosity assumption taken in the standard $k - \epsilon$ turbulence model used in GPSPH can then not be accurate enough to model the water behaviour in this stretch, as the normal Reynolds stress differences may be significant.

Turbulent channel flow subjected to rotation about the spanwise direction displays several phenomena of interest to engineering applications and turbulence modelling. Two-equation models with an isotropic eddy viscosity, such as the standard $k - \epsilon$ turbulence model, have yielded reasonably acceptable predictions for fully developed secondary flows in curved ducts with moderate to strong curvature ratios (Bradshaw, 1987). In order to analyse curved duct flows for a range of curvature ratios, or under developing conditions, anisotropic eddy viscosity models or second-order closure models, respectively, are needed (Speziale, 1993). In the present case, the flow is not fully developed when it reaches the ski

jump structure (because the section is gradually narrowing and gradients of velocity and pressure are not null) thus, it is expected that the standard $k - \epsilon$ turbulence model is not sufficiently accurate to predict the flow features in this zone. The RNG $k - \epsilon$ turbulence model is an improved version of the standard $k - \epsilon$ model, more suitable to model swirling flows with streamline curvature. It was employed in the mesh-based model, fact that may help justifying the better performance at the downstream stretch of the spillway, as far as water depths prediction is concerned.

The fact that GPUSPH is implemented for the smooth turbulent behaviour can also have impact in the results at this specific stretch of the spillway since the occurrence of greater friction losses and rather relevant near wall effects may occur. Despite the possible numerical sources of errors previously pointed out, it is worth judging the assumption of the physical model measurements correctness. Still, the water depth differences observed are relevant, which strengthens the fact that results discrepancies are numerically-based, deriving from the model's limitations.

To investigate if the low-quality results obtained for the free-surface elevation in sections 6 to 10 were due to insufficient particle resolution a new simulation was set with a dp equal to 0.3 m. It was verified that there was a leakage problem in the upstream reservoir, which could not be solved in time, despite the multiple attempts (Fig. 100). Alternatively, the inlet boundary condition was changed from a velocity driven inlet to a pressure driven inlet. This change solved the leakage problem but created a wavy pattern for the free-surface elevation in the reservoir, which is not physically sound but a numerical error.

As formerly mentioned, this issue has been equally acknowledged by Fonty *et al.* (2018) when using a pressure driven boundary conditions for inflow. Still, the free-surface elevation was analysed in the ski jump structure (for this new model with a different inflow condition) and it was verified that the increase in the particle resolution did not changed the water depths significantly, which strengthens the idea that the underpredicted water depth along the ski jump structure is linked to other numerical issues, rather than insufficient particle resolution.



Fig. 100 – Illustration of a particle leakage problem in the upstream reservoir.

Pressures' computation revealed a quite satisfactory accuracy of GPUSPH. This was partly owed to the USAW boundary conditions technique used but also to some other numerical artefacts used (mentioned in section 4.4.3). Fig. 101 and Fig. 102 evidence the dispersion of the computed results *vs.* the experimental results for the four flow rates tested, both for GPUSPH and the mesh-based model results. The dispersion pattern looks similar for both numerical models.

A similar assessment was done for the computed flow velocities. A comparison between both numerical models' performance is depicted in Fig. 103. GPUSPH results approach the experimental data slightly better. The mean relative error obtained for the comparison between GPUSPH and FLOW-3D flow velocities was 8.6% for Q_{des} and 19.7% for Q_1 , lower than those obtained for the comparison between GPUSPH and experimental results.

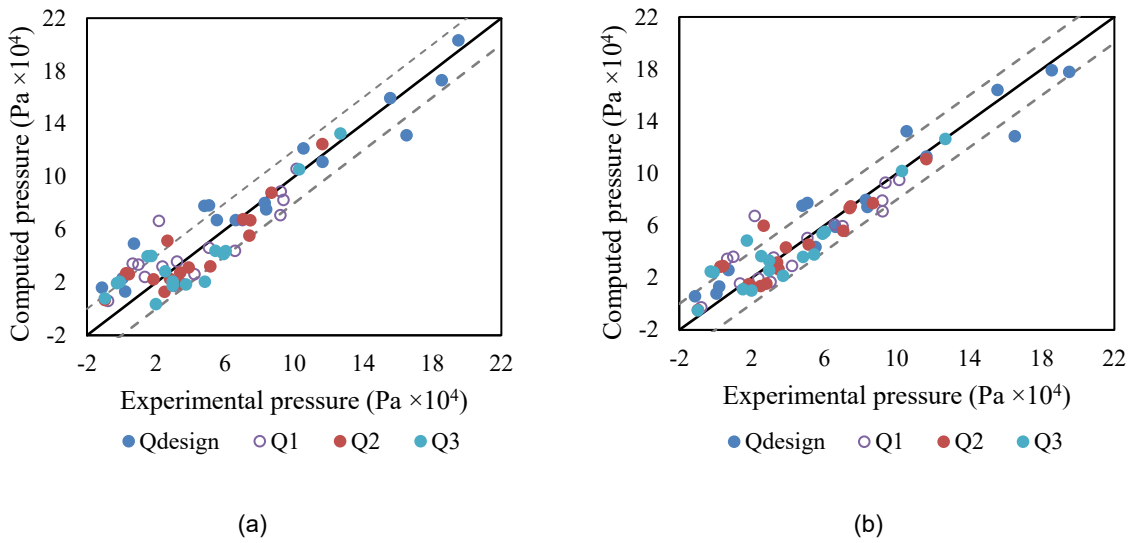


Fig. 101 – Dispersion of results comparison for the bottom channel pressures: (a) GPUSPH vs. experimental results; and (b) Mesh based model (Brandão, 2015) vs. experimental results. The dashed lines represent the bounds for a variation of 2×10^4 Pa.

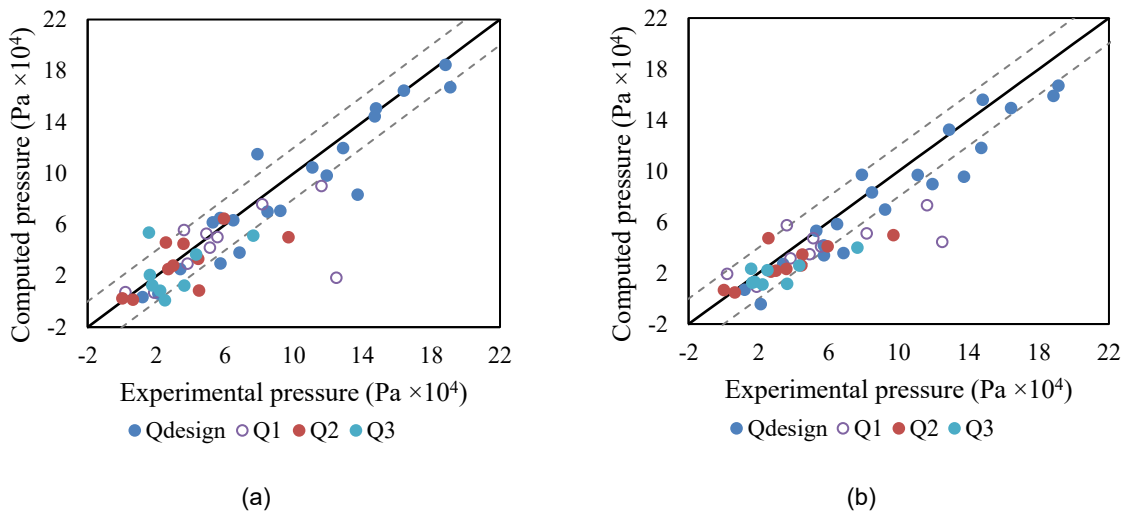


Fig. 102 - Dispersion of results comparison for the wall channel pressures: (a) GPUSPH vs. experimental results; and (b) FLOW-3D (Brandão, 2015) vs. experimental results. The dashed lines represent the bounds for a variation of 2×10^4 Pa.

The accuracy of the jets’ length prediction with both numerical models was also compared in Fig. 104. The jets’ length derived from GPUSPH were overpredicted (especially for the jet issued from the right span), whereas the mesh-based model showed an opposite tendency (underprediction). Still, the mesh-based model results better approached the experimental data.

As explained before, discrepancies between GPUSPH results and the experimental data may be caused by the non-inclusion of the air-phase and limitations of the turbulence model. The fact that air entrainment and a more sophisticated turbulence model were incorporated in the mesh-based model may justify its better performance in the prediction of jets’ length.

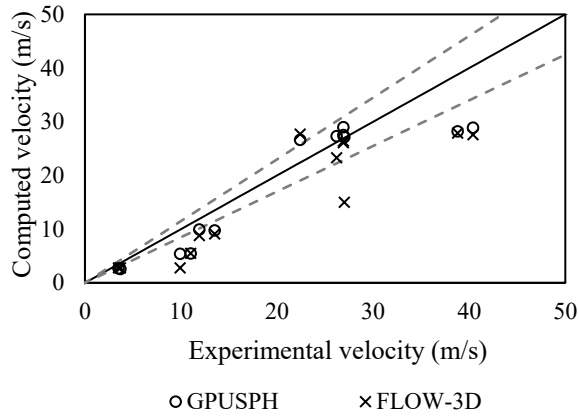


Fig. 103 - Dispersion of results comparison for the flow velocity, in sections V1 to V6, for the flow rates Q_{des} and Q_1 , for both numerical models. The dashed lines represent the bounds for a relative error of 15%.

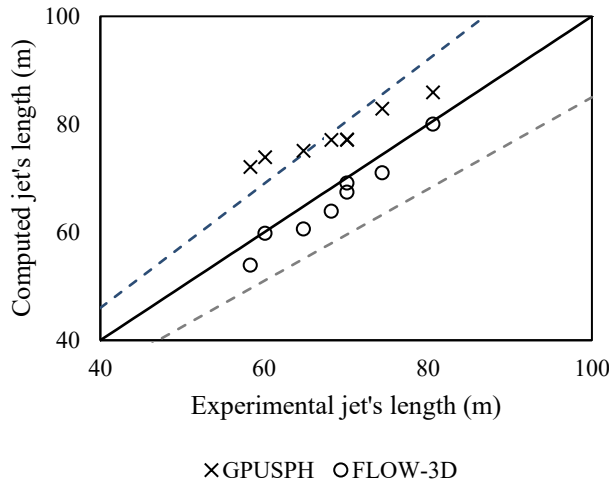


Fig. 104 - Dispersion of results comparison for the jets' length, for the flow rates Q_{des} , Q_1 , Q_2 , and Q_3 , for both numerical models. The dashed lines represent the bounds for a relative error of 15%.

4.4.6. CONCLUSIONS

The results derived from a SPH model of the complementary spillway of the Caniçada dam were analysed and compared against the experimental study by Couto *et al.*, (2013; 2014) and the numerical study by Brandão (2015). The analysis focused on the quantification of water depths, pressures and flow velocities along the chute and the length of the jets issued from the ski jump structure, for various flow rates. The following conclusions can be drawn:

- SPH results allowed the visualization of some free-surface shape singularities, such as the development of cross-waves;
- The computed water depth agreed well with the measured values, up to the downstream portion of the chute (the ski jump structure), where differences became significant. The inability of SPH

to accurately compute the water depth in this stretch is probably related to the high complexity of the flow dynamics;

- Computed pressures on the channel bottom and walls showed a general good agreement with the experimental data, and an accuracy comparable to that obtained with a mesh-based model (though the SPH model provided these results within a significant lower period of time);
- The mean relative errors obtained for the comparison between SPH and experimental flow velocities were 17.5% for Q_{des} and 28.4% for Q_1 , lower than those obtained for the comparison between FLOW-3D and experimental flow velocities (18.8% for Q_{des} and 43.6% for Q_1).
- Computed jets' length overpredict the experimental ones which may be link to the fact that the computed jets are more compact (given that air entrainment is not modelled). Differences are greater for the lower flow rates in comparison to the greater flow rates (with mean relative errors ranging from 6 to 24%). Additionally, the computed jet's length decreases with decreasing flow rate and are greater for the jets issued from the left span, which is in agreement with that observed in the physical model.
- A Particle leakage problem (in the upstream reservoir) prevented the completion of a simulation using a higher particle resolution. The cause of this problem could not be found in time.

With the exception of the water depths prediction along the ski jump structure, GPUSPH showed a satisfactory performance to predict the flow features of a real chute flow, comparable to that got for a commercial mesh-based code.

4.5. HIGH-VELOCITY JET – CASE STUDY III

4.5.1. INTRODUCTION

Many high head dams often make use of plunging jets (Fig. 105). The Caniçada dam is an example of a dam which discharge is made through impinging jets, issued from four rectangular orifices located in the central part of the dam body (main discharge device). In recent years, the re-evaluation of the maximum probable floods (as longer hydrological series are now available), along with the acknowledged impact of climate change on the frequency of incoming extreme events (e.g. Todeschini, 2012), has prompted reviews to the spillway's capacity and operation scenarios. The inadequacy of many spillways' capacity raises the possibility that these dams might be overtopped during extreme floods, which may create new hydrodynamic loading scenarios and raise questions about scour development and dam structural safety. In order to avoid the possible construction of expensive concrete slabs for energy dissipation, a thorough assessment of the dynamic pressures on the pool bottom and scour evolution is mandatory.

On prototype, a large range of jet conditions can be distinguished, depending on the jet-issuing structure (e.g., overfall weirs, orifices and ski jumps) and the hydrodynamic conditions (e.g. approach velocity, aeration degree or submergence level). For example, jets issuing from overfall weirs, like an ogee crest, are often quite compact and non-aerated (Manso, 2006), whereas jets issuing from ski jumps at the end of long chutes, such as in the case of the new spillway of the Caniçada dam, have their core generally aerated, which reduces surface tension and compactness and enhances jet's disintegration. The energy dissipation that occurs in a plunging jet discharge is due to a combination of mechanisms of (i) aeration and disintegration of the jet during its fall, (ii) air entrainment and diffusion of the jet in the tailwater pool, and (iii) impact on the pool bottom (e.g. Manso, 2006). In literature, scour holes as big as 18 times the jet diameter have been documented, being the Kariba Dam in the Zambeze river, an example. Within

its first twenty years of operation (from 1959 to 1979), a large scour hole of 87.5 m below the initial river formed, despite the existing tailwater level of about 40 m.

In this section, a SPH model was set-up to simulate the hydrodynamic conditions investigated in the laboratory work done by Manso (2006), which show the same behaviour of orifices, free-falling high-velocity undeveloped nappes and submerged outlets encountered in practice, with non-aerated cores at issuance. The aim is to understand the physics of the jet's diffusion in the pool for various pool depths, as such analysis is hampered in a physical model due to the high ratio of entrained air, and to provide quantification of the pressures acting on the pool bottom.

4.5.2. PREVIOUS STUDIES

The investigation of impact pressures generated by the diffusion of turbulent high-velocity aerated jets presents many difficulties for experimental research due to the complex two-phase environment, and, because of this, the hydrodynamic flow field is often extrapolated from non-aerated, low-turbulence and free-diffusion conditions, which are easier to reproduce in laboratory (e.g. Castillo, 1989; Ervine *et al.*, 1997; Bollaert and Schleiss, 2003; Melo *et al.* 2006; Castillo and Carrillo, 2013). In the following years, Manso (2006) consolidated and further developed previous work while investigating different pool geometries and Federspiel (2011) focused on the behaviour of loose blocks in the jet impact zone.



Fig. 105 – (a) Caniçada dam impinging jets (Image from www.meteopt.com, forum (<https://www.meteopt.com/forum/topico/seguimento-rios-e-albufeiras-2014.7457/pagina-2>)). (b) Bottom outlet jet of the Baixo Sabor dam, Portugal, 2016 (image from <https://akisabor.blogspot.com/2014/04/descarga-de-fundo.html>)

The characterization of the pressures due to jet impingement on the pool bottom has been studied using different media (e.g. air/air, air/water, water/water) and different jet geometries (e.g. plane and circular jets). Experimental investigation done so far using different scale models lead to the establishment of some empirical formulae to characterize the pressures on the bottom of flat plunge pools, at the stagnation point (e.g. Hartung and Häusler, 1973; Ervine *et al.*, 1997, Melo, 2001; Bollaert, 2002). In general, these consider the pressure as a function of the falling height, the water depth of the plunge pool and the jet's characteristics (thickness, velocity, turbulence and air content). Analysis of radial mean pressures was done by e.g. Cola (1966) and Hartung and Häusler (1973). Gutmark *et al.* (1978) also gave their contribution to the knowledge by attempting to determine the location where the impingement

zone starts. A brief overview of the characteristics of some of these experimental studies is given in Table 22.

Numerical investigations were also used to characterize plunging jets. Most of them applied the well-settled Volume of Fluid (VoF) method (e.g. Lopes *et al.* 2016) and the Level Set (LS) method (e.g. Qu *et al.*, 2011) to track the free-surface evolution. The weakness of the VoF method is the need to accurately calculate the spatial derivatives, mainly due to the volume fraction function discontinuity across the interface. The LS method is popular for computing two-phase flows with topologically complex interfaces, but it is unsatisfactory for maintaining mass conservation (Olsson *et al.*, 2007). A coupled VoF and LS method was proposed to overcome these limitations (Yin *et al.*, 2018), yet further validation of this method is needed to extend its applicability to engineering study cases.

The present numerical study was grounded on a set of experiments on plunging jets conducted by Manso (2006) at the Laboratory of Hydraulic Constructions (LCH) of the *École Polytechnique Fédérale de Lausanne* (EPFL). The experimental facility, initially used by Bollaert (2002) and later improved by Manso (2006)¹⁵, produces circular jets with velocities, U , up to 30 m/s (or 120 L/s), corresponding to a maximum Reynolds number of 1.87×10^5 (maximum Froude number of 35).

Table 22 - Characteristics of some experimental studies on jets.

Author	Type of jet	Jet velocity (m/s)	Additional information
Cola (1966)	P W submerged	< 4.8	Nozzle outlet to bottom of the basin = 0.82 m.
Hartung and Häusler (1973)	P/C W plunging	NIA	The first to show the destructive effect of the dynamic pressure inside rock fissures ($Y/D = 10$)
Gutmark <i>et al.</i> (1978)	P A impinging	35	Nozzle outlet to impinging plate distance = 1.3 m.
Ervine <i>et al.</i> (1997)	C W plunging	< 25	First near-prototype scale jet facility. $1.3 < Y/D < 20$
Bollaert (2002)	C W plunging	< 30	Study of pressures in joints and formation of rock scour; $2.1 < Y/D < 12.3$
Manso (2006)	C W plunging	< 30	Even if the experimental facility is the same as that by Bollaert (2002), Manso (2006)'s jets were more stable at issuance

C – circular; P – plane; W – water; A – air; NIA – no information available; Y/D – pool water depth to nozzle diameter ratio. Note: in all of these studies the depth is limited, the jet's axis is normal to the boundary (a basin bottom or plate) and the water jets are non-aerated at issuance.

¹⁵ The placement of a honeycomb grid and an air vent in the hydraulic system, upstream of the nozzle, allowed the generation of more stable jets, eliminating swirl and achieving an almost uniform velocity profile at the nozzle exit.

These velocities are similar to those found in typical prototype applications in large dams and reproduce correctly the aeration of the plunge pool due to the jet's impact. Moreover, it is worth stressing that all jets produced are axisymmetric circular jets, have undeveloped, non-aerated cores at issuance and their impact onto the pool bottom can be classified into two categories, according to the pool depth, namely core jet impact and developed jet impact. The exact value of the pool water depth to nozzle diameter ratio, Y/D , for which core jet impact transforms into developed jet impact is not clearly defined. For practice a value of 4 to 6 is appropriate (Bollaert, 2002). Therefore, a third type of jet diffusion and impact can be distinguished: the transitional jet impact. A transitional jet impact will approach a core jet impact for high velocities (around 15 m/s) and a developed jet impact below this threshold.

The experimental facility comprises a 0.300 m diameter water supply conduit which ends up in a cylindrical jet outlet with a nozzle diameter, D , of 0.072 m, and a 3 m diameter cylindrical basin that simulates the plunge pool. The nozzle outlet jet is located 0.7 m above the pool bottom and the pool depth, Y , is variable (Fig. 106). Water is evacuated by two rectangular boxes equipped with variable height weirs symmetrically placed regarding the plunging jet, thus, the pool flow is not fully symmetrical. Enhanced by this unevenness, circulatory flows tend to develop, which were clearly visible at high jet velocities. Y/D varied from 2.8 to 9.3 in the experimental campaign, which corresponds to travel lengths in the air ranging from 0.63 to 0.03 m for the shallowest and deepest pools tested, respectively. For ratios of Y/D that are common in practice¹⁶ and for near-prototype jet velocities, the facility allows to generate frequency spectra of the turbulence intensity of the jet at impact that are very close to reality. The ratio between the tested pool water depth, Y , and the jet diameter, D , was within a 1/1 to 1/20 geometric scale of target prototype applications.

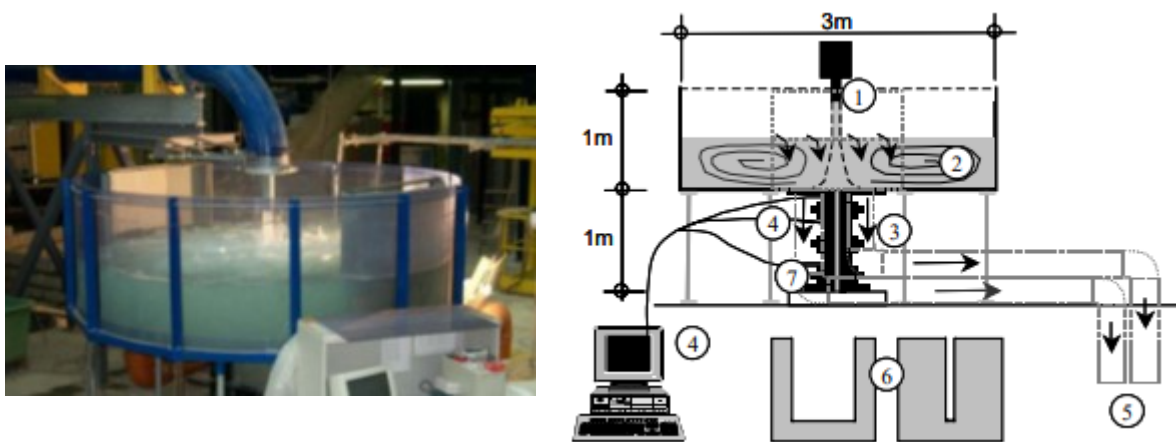


Fig. 106 – Ongoing experiment and side view of the facility assembled at the LCH-EPFL (Bollaert, 2002): 1) cylindrical jet outlet, 2) reinforced plastic cylindrical basin, 3) pre-stressed two-plate steel structure, 4) PC-DAQ and pressure sensors, 5) restitution system, 6) thin steel sheeting pre-stressed between steel structure (defining the form of artificial 1D and 2D joints), 7) pre-stressed steel bars.

Pressure measurements were taken with a number of piezo-resistive micro-transducers of type KULITE XTL-190-17BAR-A (accuracy of $\pm 0.1-1\%$) placed at the pool bottom (at 0.025, 0.050, 0.075, 0.095, 0.150 and 0.200 m radially from the stagnation point). The results analysis allowed the assessment of the dynamic pressures created by the impact of high-velocity turbulent jets plunging into a water pool

¹⁶ For impact dissipation basins Y/D ratios are frequently ranging from 2-5. For eroding basins this ratio may be greater.

with flat bottom. The pressure signal was sampled at 1 kHz during 65 s (each run). Discharge measurements were performed with an electromagnetic flow meter of 1% accuracy. A complete description of the test series performed can be consulted in Manso (2006).

Fig. 107 illustrates the experimental facility geometry, the notation used, and the three major flow regimes of a vertical plunging jet: (i) the free jet region, (ii) the impingement region, and (iii) the wall jet region. In the free jet region, the jet develops by shear with the surrounding fluid independently of the presence of the obstacle on the bottom. This region can be divided into two sub-regions: the zone of flow development is where the core of the jet persists, and centreline velocities are thus constant, and the zone of developed flow beyond core break-up where the centreline velocity decreases with distance from the issuance section. The impingement region is characterized by strong curvature of the flow streamlines as well as strong velocity and pressure gradients due to the impact of the jet with the pool bottom. Finally, the wall jet region is characterized by flow parallel to the bottom. An important parameter is the jet's length of core decay, L_c , as it influences the impact conditions (core jet impact or developed jet impact). Jet core diffusion is closely related to the issuing conditions and travel distance (Manso *et al.*, 2008). For long trajectories in the air, the jet becomes completely broken-up or developed, consisting mostly of blobs of water that disintegrate into successively finer drops (e.g. Ervine *et al.*, 1997; Guyot *et al.*, 2016). In water, the diffusion of the plunging jet namely the rate of mixing with the surrounding fluid, eddies generation and the distance influenced by the jet will depend on its entry velocity in the pool, density and turbulence intensity, as well as jet and pool dimensions. In this situation, a fully turbulent two-phase shear layer impacts the bottom, generating significant pressure fluctuations. When the jet impinges the bottom after a travel distance smaller than L_c , the jet's core persists, and high impact pressures are generated combined with a turbulent shear layer.

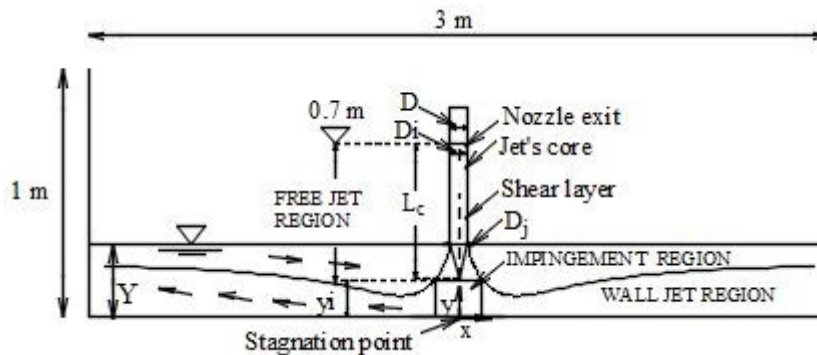


Fig. 107 - Schematic plot of the three major flow regimes of a vertical plunging jet.

4.5.3. SPH MODEL SET-UP

Geometry and boundary conditions

The numerical model has the same dimensions as the physical model previously described. Preliminary simulations (done with a particle diameter, dp , of 0.009326 m) revealed that the mean flow velocity at the exit of the 0.072 m diameter nozzle was significantly higher than the theoretically expected value of 29.5 m/s (it was approximately 36 m/s, which corresponded to a relative error of 22%). To investigate this effect, a particle resolution sensitivity analysis was performed to the upstream part of the numerical model (i.e., the nozzle) (Moreira *et al.*, 2019b). For simplicity, a non-dimensional resolution number, D/d_p , was defined as the ratio between the nozzle diameter and the particle diameter. Simulations with smaller particle diameters (of 0.004194 m and 0.002111 m) were run, which corresponded to D/d_p

ratios from 7.7 to 34.1. It was verified that (Fig. 108): the fluid particles tend to detach from the nozzle wall and this effect is greater for the smaller D/d_p ratios; flow acceleration is significant for the lower resolution, which is compatible with the visible reduction in the effective nozzle diameter; for the simulation having a higher D/d_p it is clearly visible the higher velocities in the centre of the nozzle but, near the wall instabilities occur; and the mean outlet velocity for the higher D/d_p better approaches the theoretically expected value (it was approximately 32.2 m/s, which corresponded to a relative error of 9.1%).

Thus, it is likely that, in confined flows, coarse particle resolutions compound the reduction of effective diameters, leading to inaccurate computations of the flow field. Higher resolutions are needed in such cases to resolve the velocity profile that will occur due to the presence of a developing boundary layer on the wall. This has been acknowledged as well by e.g. Pereira *et al.* (2018) who simulated the water flow through a high-pressure nozzle with a SPH model¹⁷.

Also relevant to this matter is the modelling of physical boundaries as fluid and boundary particles will interact with each other. With coarse resolutions the “mesh” of the nozzle may be too inaccurate and the gamma values, γ , taken for the SPH interpolation near the boundaries are not really those of a cylindrical shape. In fact, for the tested resolutions, the average gamma values of the nozzle boundary particles ranged from 0.44 to 0.49 (coarse to fine resolution, respectively).

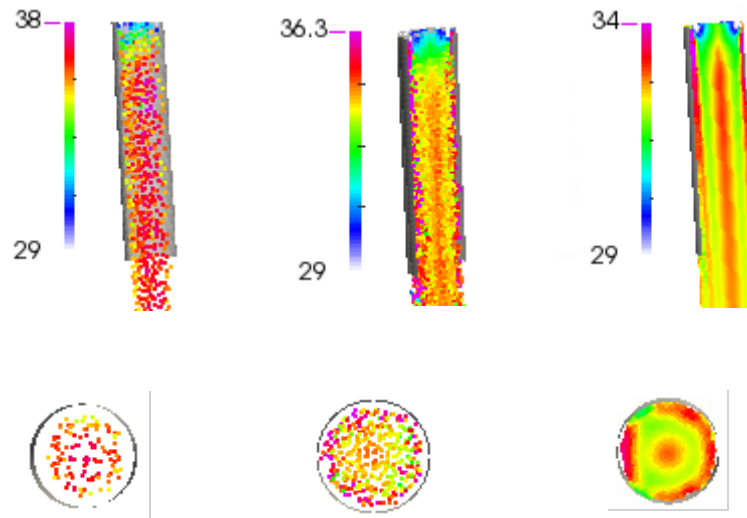


Fig. 108 - Flow conditions inside the 0.072 m diameter nozzle, for different particle resolutions: $D/d_p=7.7$ on the left, $D/d_p=17.2$ in the middle and $D/d_p=34.1$ on the right. Plot according to particles' velocity (in m/s)

It was concluded that the particle resolution had to be improved to correctly reproduce the flow inside the tube, however, such would be prohibitive from a computational point of view, because, even for the shallowest pool water depth ($Y = 0.2$ m), the total number of fluid particles, in the beginning of the simulation, in the plunging pool would be 150 million particles (considering a $d_p = 0.0021$ m, Fig. 109).

¹⁷ Pereira *et al.* (2018) considered a resolution number, D/d_p , of 8 to be acceptable (maximum nozzle exit velocity relative error was 9.4%, for a $U = 21.3$ m/s). Wall boundaries were modelled with a repulsive functions approach – the Lennard-Jones repulsive forces (see Monaghan, 1994).

This could be significantly reduced in the future by implementing a variable resolution approach (Vacondio *et al.*, 2013; Chiron *et al.*, 2017). At the present stage, possibilities were (i) increasing the tube diameter (but there would be a different jet diameter at impact), (ii) decreasing the flow rate (this would have to be done in an iterative non-efficient manner), or (iii) removing the nozzle. A final model configuration without the nozzle was set, so that there was no need to use computationally prohibitive particle resolutions.

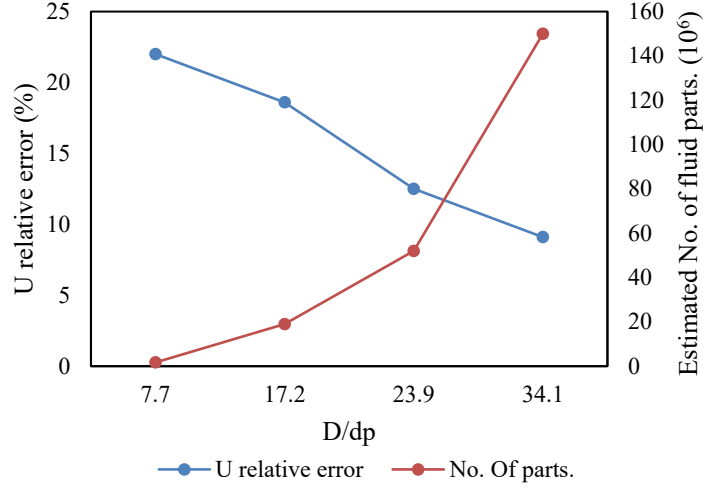


Fig. 109 - Relative error in the mean exit velocity, U , vs. estimated number of fluid particles in the simulation.

The inlet section was materialized by a circular section, perpendicular to z -direction, located right where the nozzle ended, at $z = 0.7$ m. A velocity boundary condition was prescribed at this section with the following logarithmic velocity profile, turbulent kinetic energy, k and dissipation rate, ϵ

$$u_z = u_* \left(\frac{1}{k} \ln \left(\frac{(R-r) u_*}{\nu} \right) + 5.2 \right) \quad (42)$$

$$k = \frac{u_*^2}{\sqrt{C_\mu}} \left(1 - \frac{R-r}{R} \right) \quad (43)$$

$$\epsilon = \frac{u_*^3}{\kappa \max(R-r, 0.01)} \left(1 - \frac{R-r}{R} \right) \quad (44)$$

with u_z being the imposed vertical velocity, u_* the shear velocity, R is the radius of the circular section (equal to 0.072 m) and r is the horizontal coordinate along the radius. The constants are $C_\mu = 0.09$ and $\kappa = 0.41$ (von Karman's constant) (Launder and Spalding, 1972).

As explained by Manso *et al.* (2008), for high flow velocities (i.e. $U > 25$ m/s), the velocity profile at the nozzle exit is quasi uniform, mainly due to the extreme contraction produced by the nozzle. This

was further evident when upstream swirling was reduced thanks to the implementation of the honeycomb and air vent. Thus, imposing a logarithmic profile at the nozzle exit section is expected to produce a reasonable approximation, at a manageable computational time (**Erro! A origem da referência não foi encontrada.**). Because a logarithmic profile was imposed at the inlet, the flow can be considered established at this section, as the logarithmic profile was derived for the boundary layer flow - far away from a solid wall (the free-stream zone), the flow is free from the friction, whereas near the wall (the boundary layer zone), the flow is subject to the friction from the wall.

Two outlets were symmetrically located on the lateral wall of the pool, to mimic the lateral weirs of the physical model. Hydrostatic pressure profiles were prescribed there, considering the pool water depth, Y . These guaranteed an approximately constant level in the circular tank throughout the simulation.

In WCSPH computations, the free-surface conditions are satisfied due to the meshfree nature of the method. That is because the density tends to zero when approaching the free-surface due to the absence of neighbours in the kernel support, which, due to the equation of state, makes the pressure tend to zero. Still, the incorporation of a free-surface detection algorithm (to distinguish the fluid particles that belong to the free-surface from those which do not) in the SPH solver is particularly interesting to allow a better qualitative analysis of complex flow behaviours, especially when air entrapment is foreseen, such as in the present study. The free-surface detection technique used in this work is a simplification of the one proposed by Marrone *et al.*, (2010).

The solid wall boundaries were treated using the Unified Semi-Analytical Wall (USAW) boundary conditions technique by Ferrand *et al.* (2017). A density diffusion correction term (after Brezzi and Pitkäranta, 1984) was used in the continuity equation, adapted to the USAW boundary conditions by Ghäitanellis *et al.* (2015), to smooth out the density/pressure field and the standard $k - \epsilon$ turbulence model was employed after Ferrand *et al.* (2013).

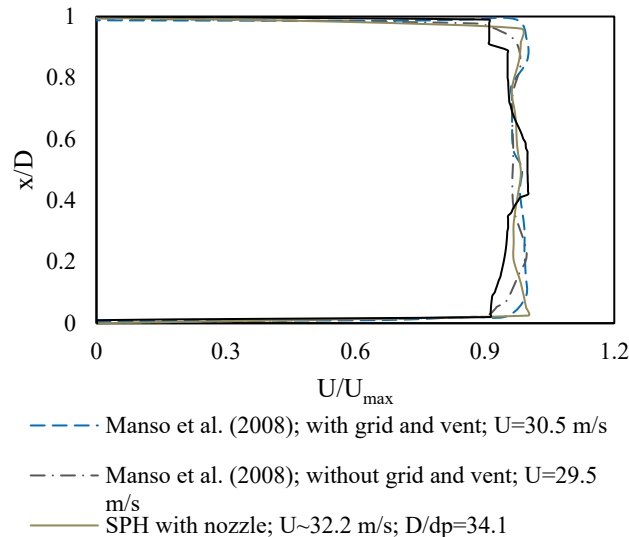


Fig. 110 - Comparison between experimental and computed velocity profiles obtained along the nozzle diameter, at the exit section. Experimental profiles were obtained from pressure measurements.

Hydrodynamic conditions and simulation's characteristics

A flow rate of 120 L/s was imposed at the inlet section in all of the simulations. The pool water depth, Y , varied from 0.2 m to 0.67 m. Table 23 summarizes the hydrodynamic conditions and some of the

SPH model characteristics in each simulation (designated as SIM 1 to SIM 7). To assess the influence of particle resolution, two simulations were performed for the shallowest pool case (SIM 1 with $d_p = 0.0093$ m and SIM 2 with $d_p = 0.0125$ m ($D/d_p = 5.7$))¹⁸. It was verified that the use of a higher d_p did not lead to a significant improvement in the accuracy of the computed pressures, considering the additional computational time (more than double). For this reason, the lower particle resolution was used in the subsequent simulations.

All jets reproduced in this study have non-aerated cores and their impact onto the pool bottom can be classified into two categories, according to the pool depth, namely core jet impact and developed jet impact. The exact value of the ratio Y/D for which core jet impact transforms into developed jet impact is not clearly defined. For practice a value of 4 to 6 is appropriate (Bollaert, 2002). Therefore, a third type of jet diffusion and impact can be distinguished: the transitional jet impact. A transitional jet impact will approach a core jet impact for high velocities (around 15 m/s) and a developed jet impact below this threshold. SPH interpolation was based on the 3D Wendland C^2 function and a smoothing length factor of 1.3. This factor has direct influence on the efficiency of the computation and the accuracy of the solution as it controls the number of particles contributing to the SPH interpolation. The speed of sound, c_0 , in the Tait equation of state was taken as $c_0 = 10 \times U_{max}$, considering a U_{max} of 35 m/s. Simulation runs correspond to 10 s of physical time, which lead to significant computational times. The high computational cost of each simulation relates to the SPH formulations used, in particular, the USAW boundary conditions implemented which is known to be time-consuming. For instance, the employment of a fictitious particles approach for wall modelling could have decreased computational times to about a factor of about 12, but these present some disadvantages as not preventing particles penetrating the boundary and creating unphysical separation (Violeau and Rogers, 2016). Moreover, inflow and outflow boundary conditions are not available in version 4.1 of GPUSPH with USAW boundary conditions. The time frame of 10 s was defined for all of the simulations because it was verified that the computed mean pressures did not vary significantly when a longer physical time is simulated. Fig. 111 shows that the percentage variation of the computed mean pressure after 10 s is lower than 1,5%). As for the maximum pressures, it is empirically known that they tend to be greater as the acquisition time increases (Toso and Bowers, 1988; Manso, 2006). The variation of the computed maximum pressures during a 15-s simulation is depicted in Fig. 112.

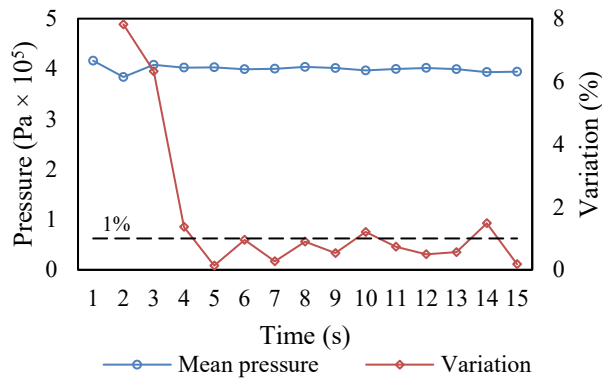


Fig. 111 - Evolution of the computed mean pressure at 0.025 m from the stagnation point and corresponding percentage variation, in a 15-s simulation (with $Y/D = 4.2$), sampled at 40 Hz.

¹⁸ A minimum of four fluid particles across the jet's diameter (minimum dimension) should be guaranteed (Moreira *et al.*, 2019a).

DEVELOPMENT OF SPH APPLICATIONS

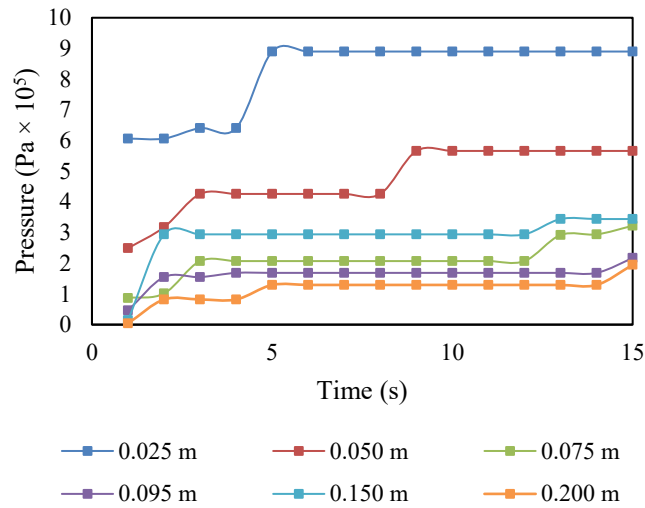


Fig. 112 - Evolution of the computed maximum pressures at 0.025, 0.050, 0.075, 0.095, 0.150 and 0.200 m from the stagnation point, in a 15-s simulation (with $Y/D = 4.2$), sampled at 40 Hz.

Table 23 - Numerical simulations characteristics.

	SIM 1	SIM 2	SIM 3	SIM 4	SIM 5	SIM 6	SIM 7
Y (m)	0.2	0.2	0.3	0.4	0.5	0.6	0.67
Y/D	2.8	2.8	4.2	5.6	6.9	8.3	9.3
L (m)	0.5	0.5	0.4	0.3	0.2	0.1	0.03
L/L_c	0.32-0.35	0.32-0.35	0.26-0.28	0.19-0.21	0.13-0.14	0.06-0.07	0.02
d_p (m)	0.0093			0.0125			
Total no. of particles* (10^6)	2.6	1.3	1.6	2.0	2.3	2.7	2.9
Computational time (days)	55	22	27	29.5	46.5	39.5	43
NVIDIA®	GeForce®	GeForce®	GeForce®	GeForce®	GeForce®	GeForce®	GeForce®
Graphic processor	TITAN X	TITAN X	GTX 980 Ti	GTX 1070 Ti	TITAN X	GTX 1070 Ti	GTX 1070 Ti

*at the end of simulation;

L - length of jet travel in the air;

L/L_c - relative degree of jet break-up (L_c being the jet's length of core decay)

4.5.1. RESULTS AND DISCUSSION

Flow characteristics

At the beginning of the simulation the high-velocity jet impinges into the pool. The high momentum of the jet cuts through the water mass. At small pool water depths, the jet's momentum is such that the jet directly impinges on the pool bottom, so that there is a clear distinction between the jet and the surrounding mass of water in the pool. As the water jet impinges into the shallow pool a "wave" forms due to the interaction of the high velocity jet with the stagnant water (Fig. 113).

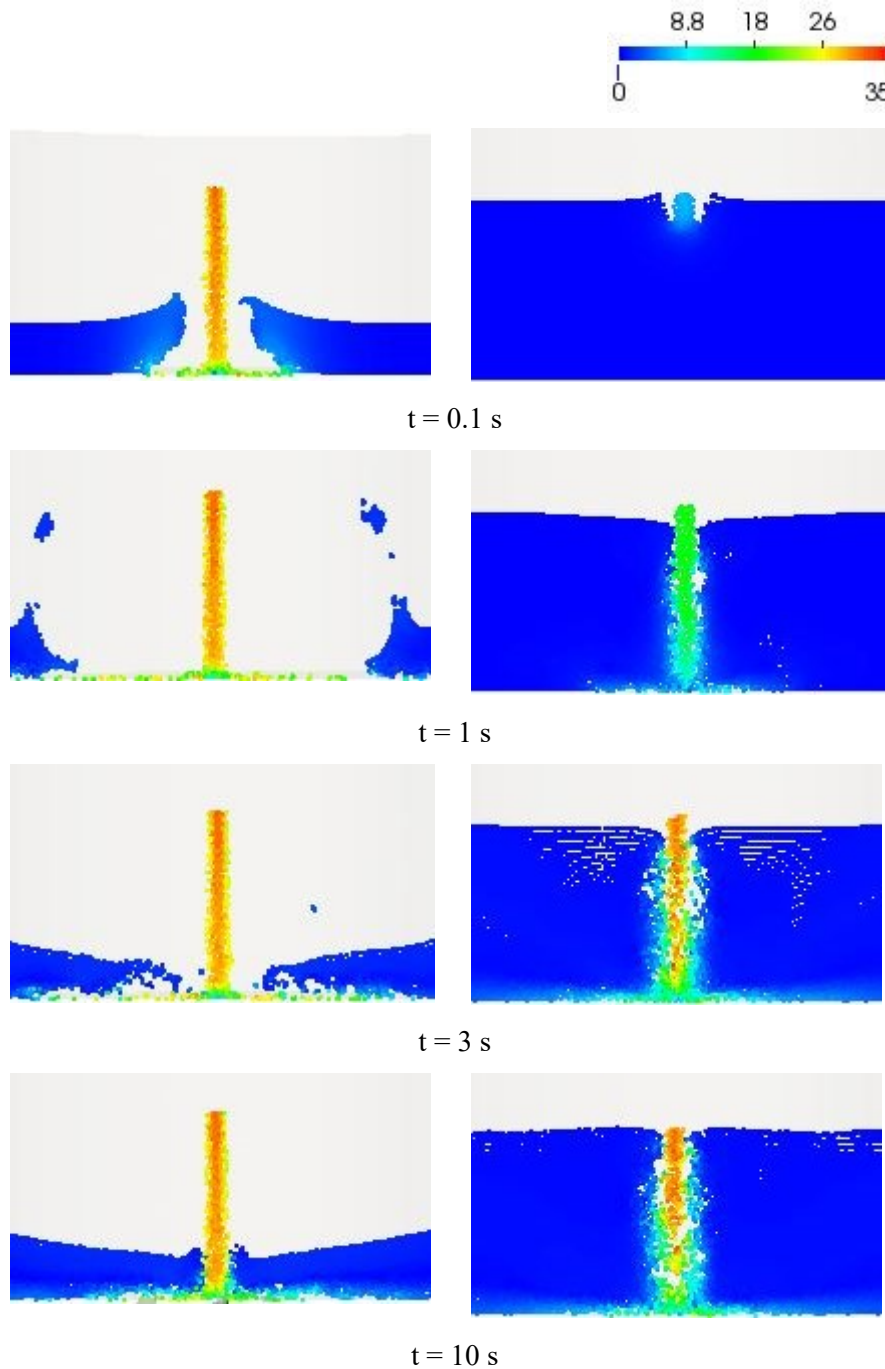


Fig. 113 – Flow evolution throughout the simulation: shallow pool, $Y/D = 2.8$, on the left and deep pool, $Y/D = 9.3$, on the right. Fluid particles coloured by their velocity magnitude in m/s.

For higher plunge pool depths, the jet cannot maintain this situation and it is drawn by the strong recirculation currents, becoming surrounded by a submerged hydraulic jump. Fig. 114 represents the free surface shape (at a radial plane) for the various pool water depths simulated, at the end of the simulation. Free-surface particles (represented in red) were detected below the water surface, up to the pool bottom, which is coherent with the experiments that showed a highly aerated flow inside the pool, hampering the visualization of the flow behaviour inside the pool. These free-surface particles were dragged into the pool, just as air is in the experiments. Given that the air phase was not modelled with SPH, it is remarkable that “air” pockets can be seen, showing that the method can provide an good qualitative description of the flow features in highly aerated flows, even if a single-phase approach is used. In a mesh-based model, such evaluation would require additional equations to be solved (e.g. a Volume Fraction equation in the VoF method).

Fig. 115 illustrates the 3D flow configuration in the pool at the end of the simulation. The free-surface exhibited different shapes according to the pool water depth.

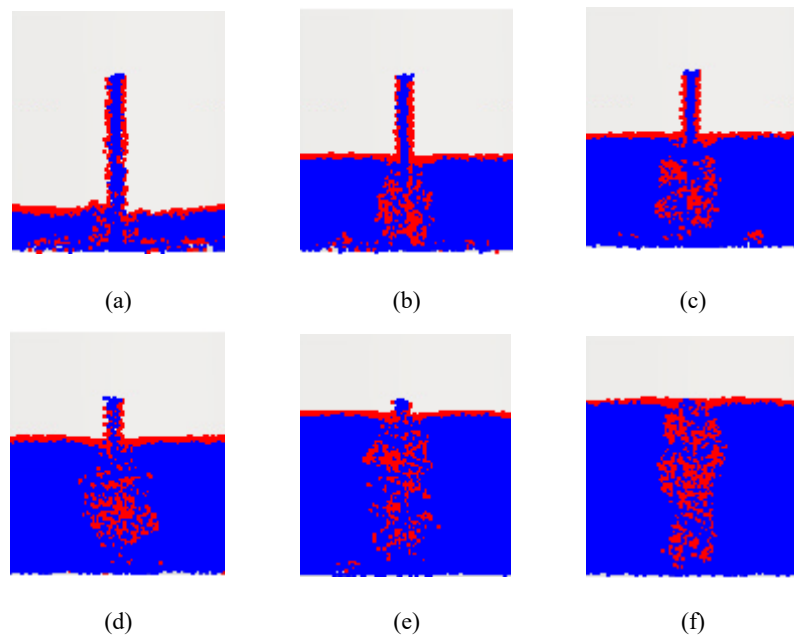


Fig. 114 - Free-surface shape (at a radial plane) for the tested hydrodynamic conditions: (a) $Y/D = 2.8$; (b) $Y/D = 4.2$; (c) $Y/D = 5.6$; (d) $Y/D = 6.9$; (e) $Y/D = 8.3$; and (f) $Y/D = 9.3$. The red particles represent the fluid particles identified as free-surface particles (zero pressure).

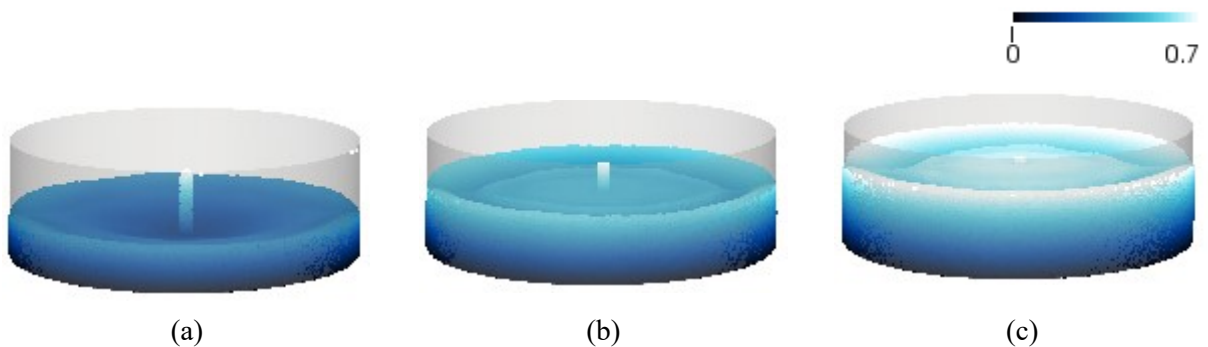


Fig. 115 - Free-surface shape in the plunge pool at the end of the simulations: (a) $Y/D = 2.8$; (b) $Y/D = 5.6$; and (c) $Y/D = 8.3$. Plot coloured according to the z-coordinate of the fluid particles

To better understand the flow behaviour inside the plunge pool, the flow velocity and turbulent kinetic energy, k , fields were analysed. For core jet impact conditions, the core persists and impinges the pool bottom almost directly. Upon impact on the pool bottom, the plunging jet divides into wall jets and recirculation eddies are formed around the falling jet (Fig. 116). For higher pool water depths, shear eddies develop starting shortly after the jet's entry in the pool, providing energy dissipation. This is mainly due to the dramatic velocity change caused by friction with the surrounding pool water. Such process is clearly seen in the k plots (Fig. 117), as these show the locations where most of the energy dissipation occurs. After the impact on the pool bottom, the plunging jet divides into wall jets and large eddies are formed around the falling jet (i.e. a submerged hydraulic jump), drowning it, which constitutes a macroturbulent zone. According to SPH results, the location of the maximum k varies depending on the pool water depth: for small water depths it tends to occur downstream of the impinging jet, whereas for greater pool water depths it further concentrates on the impingement area and the diffusing jet area.

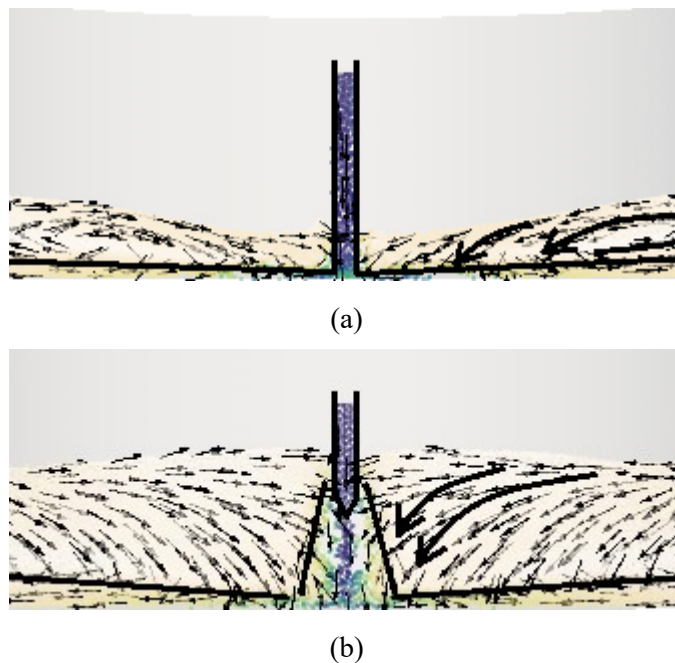


Fig. 116 - Velocity field (m/s) for core jet impact conditions ($Y/D = 2.8$, top image) and developed jet impact conditions ($Y/D = 5.6$, bottom image). Black thick lines added in post-processing for clarification of main flow features.

Centreline velocity decay

It is well known that the velocity at the jet's centreline is a significant parameter used to investigate the hydraulic characteristics of a vertical plunging jet. According to experimental benchmark data of impinging air jets by Giralt *et al.* (1977) (for jet exit velocities, $U_0 < 48$ m/s), the centreline velocity along the longitudinal axis of a jet will vary little near the jet's exit, while the core persists (core region), and, subsequently to the disintegration of the core, the centreline velocity reduces smoothly (established flow region). If an obstacle is present (which is the case of an impinging jet rather than a free jet), an abrupt velocity reduction is observed due to the proximity of the obstacle (impingement region), so that velocities must be reduced to zero. If the obstacle is sufficiently near the issuing section, a zone of established flow may not develop.

The normalised centreline velocity decay along the jet's axis was computed by SPH and plotted as a function of the relative depth below issuance y / D . Results are shown in Fig. 118, in which the shaded region in each panel covers the minimum and maximum either sides of the average profile from the decelerating jet. For $Y/D = 2.8$ it can be seen that a very slight decay is registered up to the proximity of the pool bottom, meaning that the centreline velocity remains similar to the mean jet's exit velocity up to approximately $8.5 y/D$, which is characteristic of a compact jet. No established flow region exists for this type of impinging jet. This agrees with the fact that for shallow pool conditions, a core jet impact occurs. As the water depth in the pool increases the velocity fluctuations are greater. This is due to the turbulence fluctuations generated by the dispersion of the jet in the pool water. For $Y/D = 8.3$, the velocity decay and fluctuations are further evident after the disintegration of the core (axis origin considered to be at the nozzle exit, oriented downwards).

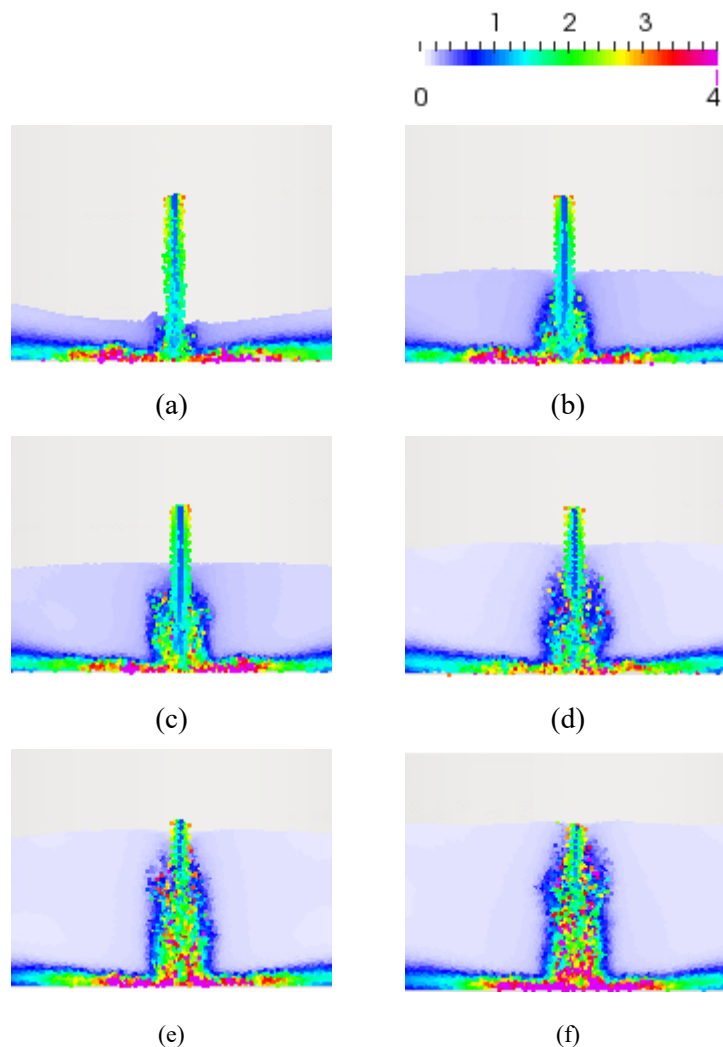
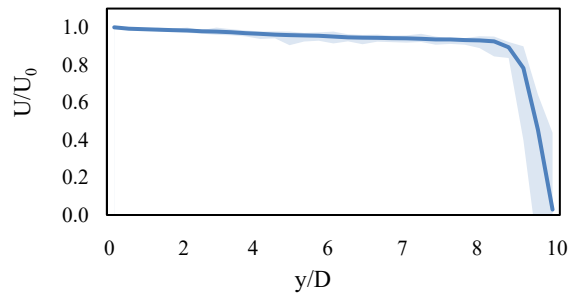


Fig. 117 - Fluid particles coloured by their turbulent kinetic energy, k , (m^2/s^2) for different ratios of plunge pool water depth Y to jet diameter D : (a) $Y/D = 2.8$; (b) $Y/D = 4.2$; (c) $Y/D = 5.6$; (d) $Y/D = 6.9$; (e) $Y/D = 8.3$; and (f) $Y/D = 9.3$

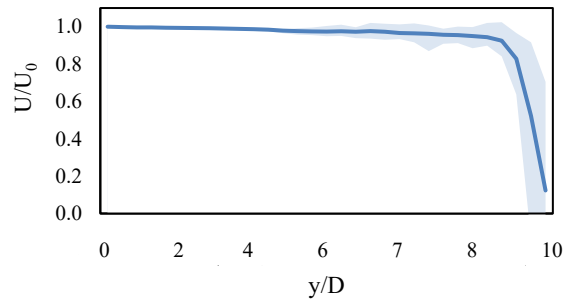
At the simulated hydrodynamic conditions, due to the small ratio y/D (jets were issued at a distance from the bottom $y/D = 9.58$), that is, a small travel distance, and the high jet's exit velocity, the zone of established flow is almost imperceptible. Duarte *et al.* (2014) did a similar analysis for experimental

test results carried out with a 0.072 m diameter nozzle, for plunging water jets issued 1 m above the pool bottom, and a pool depth, Y , of 0.8 m ($4.9 < U_0 < 22.1$ m/s). The authors found out that jets with a different issuance velocity produce different normalized lengths of core decay, L_c/D , namely, greater issuing velocities lead to greater lengths of core decay. According to Duarte *et al.* (2014) results, for a $U_0 = 22.1$ m/s, L_c/D was approximately 8. This may justify the almost imperceptible zone of established flow in the simulated jets.

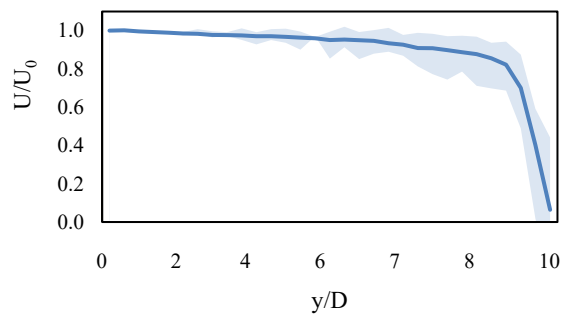
Moreover, they postulated that the impingement region should have different limits for air jets in comparison to water jets, since none of the cases showed a steeper rate of velocity decay when approaching the pool bottom than that in the established flow region, in the positions measured with a double-optic probe. Such is not confirmed with the findings of the present investigation, which indeed show a sudden velocity decay near the pool bottom (as suggested by Giralt *et al.*, 1997 for air jets).



(a)



(b)



(c)

Fig. 118 - Centreline velocity decay of the tested jets for different Y/D ratios: (a) $Y/D = 2.8$; (b) $Y/D = 5.6$; and (c) $Y/D = 8.3$. The shaded region represents the minimum and maximum bounds either sides of the average profile.

Apart from small differences in the nozzle height and jet velocity, differences between Giralt's *et al.* (1997) and Duarte's *et al.* (2014) works are mainly due to the measurement principle (based on cross-correlation of two optic signals along a given flow streamline) which loses accuracy in the impingement

region due to the strong curvature of the flow streamlines. The complementary between experimental and computational works is here again proven, since air-water flow velocities close to the pool bottom remain a major challenge for research in hydraulics.

According to the SPH results, the impingement zone starts approximately 0.1 m above the pool bottom (y_i in Fig. 107). This agrees well with the findings by Giralt *et al.* (1997) who suggested that for nozzle heights larger than $y/D_i=6.8$, the impinging zone location with respect to the pool bottom, y_i , is given by

$$y_i = 0.153 (D_i + Y) \tag{45}$$

Which yields a value of 0.12.

Other authors such as Cola (1966) and Gutmark *et al.* (1978) also attempted to determine the location where the impingement zone starts, through the definition of η_A (being $y_i = Y \times \eta_A$), which relates to the free diffusion length β_A , as $\beta_A = 1 - \eta_A$. Based on their results for submerged water plunging jets with exit velocities up to 4.8 m/s, Cola (1966) suggested a β_A/Y in the range of 0.65-0.75, which yields a y_i of about 0.17 m. Gutmark *et al.* (1978) suggested a β_A/Y of 0.75 from their experiments on submerged air jets with exit velocities of 35 m/s, which yields a y_i of 0.17 m.

Pressure distribution near the stagnation point

The jet impingement in the pool bottom results in a pressure build-up that decreases the centreline velocity rapidly towards zero and in a jet deflection parallel to the obstacle plane. Pressures estimation on or near the stagnation point is key because these relate to the maximum possible damage. Pressures were computed 0.025 m away from the stagnation point (as done by Manso, 2006 - closest location possible to the jet vertical axis in the experimental set-up for practical reasons). Fig. 119 shows an example of the pressure signal computed by SPH under the jet's centreline.

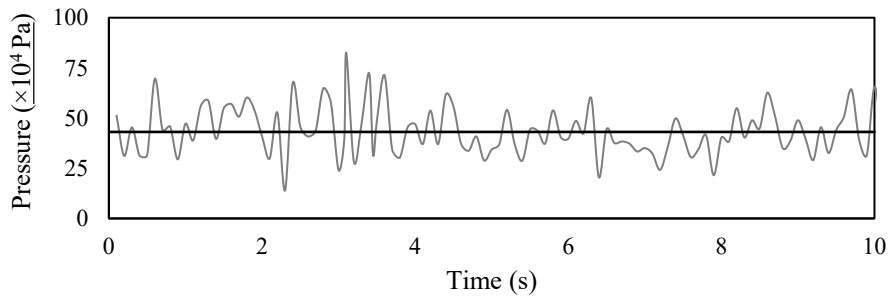


Fig. 119 - Pressure signal in the time domain, computed by SPH under the jet's centreline, at the plunge pool bottom, for $Y/D = 2.8$.

Fig. 120 shows the evolution of the maximum, mean and minimum pressures near the stagnation point with respect to the ratio Y/D , from the SPH model and the experimental data by Manso (2006). The SPH results show a decrease in the mean pressure as the pool depth increases which is compatible with the fact that, at higher pool depths, the two-phase turbulent shear layer created generates lower mean pressures and significant pressure fluctuations at impact with bottom (May and Willoughby, 1991). Differences between both sets of results are significant for the mean pressures (relative errors were in

the range 20-40%), but, for the maximum pressures SPH agrees well with the experimental results, being the relative error in the range 1.1-9.3%. The differences observed in the mean pressures are due (not exclusively, though) to the non-consideration of the air phase. Despite the air phase was not modelled in the SPH model, still some free-surface particles are dragged into the pool, some of them reaching the pool bottom (as seen in Fig. 114). As these particles are by definition at zero pressure, they will likely decrease the computed mean SPH pressures. In fact, entrained air bubbles vary in pressure and geometry across the pool under the influence of the falling jet, inducing changes in local turbulence and compressibility (Manso *et al.*, 2004; Manso, 2006; Duarte *et al.*, 2015). Other factors that may have influenced the comparison of results are (i) the difference between the computational and experimental acquisition times (being the increase of the former computationally prohibitive for now), and (ii) the output frequency considered for the computed SPH pressures (which could be assessed in the future), knowing that, although a greater output frequency can help to capture some pressure peaks, it can be tricky as well because some pressure peaks can be numerical (not physical). As for the maximum pressures, it also should be kept in mind that in turbulent flows such as those under investigation the instantaneous maximum pressures relate to the acquisition frequency and the duration of the run and tend to be greater as the acquisition period increases. For instance, Toso and Bowers (1988) measured extreme values in a hydraulic jump and found that the extreme values for a 24-hour test run were about twice the magnitude of the 10-min observations. Pressures were computed at a frequency of 40 Hz, during a 10-s simulation, yet experimental maximum and minimum pressures correspond to 3-min ergodic runs sampled at 1 kHz (Manso *et al.*, 2007).

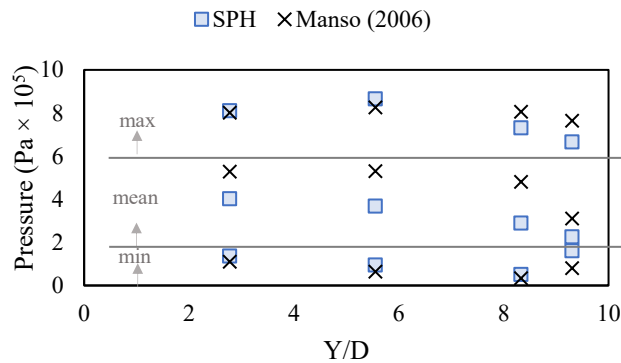


Fig. 120 - Computed vs. experimental minimum, mean and maximum pressures at 0.025 m from the stagnation point, for various pool depths ratios Y/D , sampled at 40 Hz during a 10-s run. Comparison with experimental minimum, mean and maximum pressures by Manso (2006), sampled at 1 kHz during a 3-min run, for the same hydrodynamic conditions ($U = 29.5$ m/s).

The non-dimensional mean dynamic pressure coefficients, C_p were determined following the expression

$$C_p = \frac{P_{stagnation} - \gamma}{\phi U_0^2 / 2g} \quad (46)$$

Where $P_{stagnation}$ is the mean pressure at the stagnation point, γ_w is the water's specific weight, g is the modulus of gravitational acceleration and ϕ is a correction coefficient for the kinetic energy $U_0^2 / 2g$

as a function of the mean jet exit velocity U_0 . At high-velocity jets, such as those being tested, a typical value for ϕ is 1.05 (Bollaert, 2002).

Fig. 121 depicts the mean dynamic pressure coefficients, obtained with SPH, as a function of the ratio Y/D_j , being D_j the jet diameter at impact with the pool water. According to the best-fit of available literature data on circular vertical impinging jets by Ervine *et al.* (1997), the envelope of Bollaert (2002) results, and the data by Manso (2006), a similar trend is obtained – initially, the increase in the pool depth has little influence in the C_p coefficient which assumes a value of about 0.86, yet, after a certain threshold C_p decreases with increasing Y/D_j . The SPH model suggests a smoother transition between both patterns of C_p variation in comparison to the experimental outputs by Ervine *et al.* (1997) and Bollaert (2002). This can be justified by the higher air entrainment at increasing Y/D_j (which tends to decrease the mean hydrodynamic loading – as acknowledged by Melo *et al.*, 2006) that can not be modelled in a single-phase approach. Thus, a relevant improvement in the future will be the consideration of a two-phase SPH model. However, such improvement is not straightforward because dealing with a large density ratio (e.g. air/water) in WCSPH is linked to numerical instability leading to the crash of the simulation. Several techniques have been proposed to overcome this issue (Hu and Adams, 2006; Grenier *et al.*, 2009; Monaghan and Ashkan, 2013; Fonty *et al.*, 2018), including a recent simple strategy proposed by Manenti (2018) to assure SPH stability without numerical correctives and maintaining low computational cost. Still, modelling aerated flows with WCSPH at the scale of practical interest for engineering applications requires choosing a very fine particle discretization (compatible with the air bubbles size), which is extremely demanding from the computational point of view.

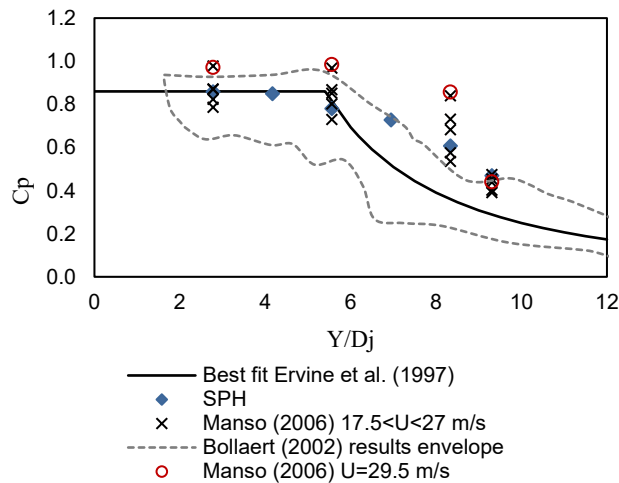


Fig. 121 - Computed vs. experimental non-dimensional mean dynamic pressure coefficients, C_p , at 0.025 m from the stagnation point, for various Y/D_j ratios. Comparison with Manso (2006)'s results for equivalent hydrodynamic conditions ($U = 29.5$ m/s) and Ervine *et al.* (1997)'s best fit of data obtained for circular plunging water jets, sampled at 100-230 Hz during 2-min runs ($U < 25$ m/s).

The non-dimensional pressure coefficient, $C_{p'}$, was equally set for the fluctuating part of the dynamic pressure measured near the stagnation point, on the basis of the RMS value, σ :

$$C_{p'} = \frac{\frac{\sigma}{\gamma_w}}{\phi U_0^2 / 2g} \quad (47)$$

Results obtained with SPH are presented in Fig. 122 in which they are compared with the best-fit of available literature data by Ervine *et al.* (1997) and the envelope of Bollaert (2002) results. The general form of the relationship between the RMS values and the Y/D_j ratio agrees with previous findings and with theoretical considerations on turbulence. Turbulence firstly increases with increasing pool depth (increased jet break-up) up to a maximum value and then decreases again with the pool depth (due to increasing diffusion). Comparison with the bandwidth of available data from Ervine *et al.* (1997) shows that the SPH model results significantly overpredict these, yet, SPH results fit within the results envelope from the experiments performed by Bollaert (2002). Such may be explained by the generation of a turbulent shear layer with near prototype spectral characteristics on large-scale models (such as the LCH facility) much closer to reality than on small-scale models (such as in the facility by Ervine *et al.* 1997).

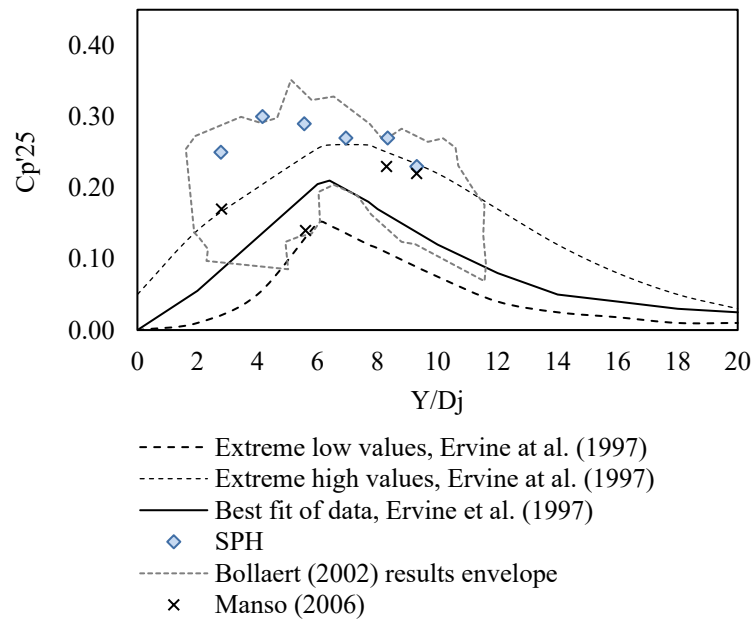


Fig. 122 - Computed non-dimensional fluctuating dynamic pressure coefficient C_p , at 0.025 m from the stagnation point, for various Y/D_j ratios.. Comparison with the experimental values by Manso (2006), Ervine et al (1997)'s best fit of data and Bollaert (2002)'s results envelope obtained from circular plunging water jets sampled at 1 kHz during ~1-min runs ($U < 30$ m/s).

Radial pressure distribution

The assessment of the radial pressure distribution is important to define the radial extent of possible damage and eventually inform about the shape and extension of the scour hole or required protection measures. The obtained SPH results were compared with those obtained by Manso (2006) in Fig. 123. It was verified that the pressures determined experimentally are greater than those computed by SPH. Such deviation may be due to the existence of air bubbles entrained and the non-consideration of the air phase modelling. Thus, the existence of free-surface particles near the pool bottom (pressure zero), translates to lower pressures being computed by SPH, as these particles may be in the neighbourhood of the point where pressures were computed.

Still a similar tendency was found – pressures decrease occurs mostly within 100 mm radius from the stagnation point. Also, a monotonic decreasing trend was observed for the mean pressures both in SPH

and experimental results (Fig. 123a). However, with regard to the maximum pressures, such tendency is not clearly perceived both in SPH and experimental results (Fig. 123b).

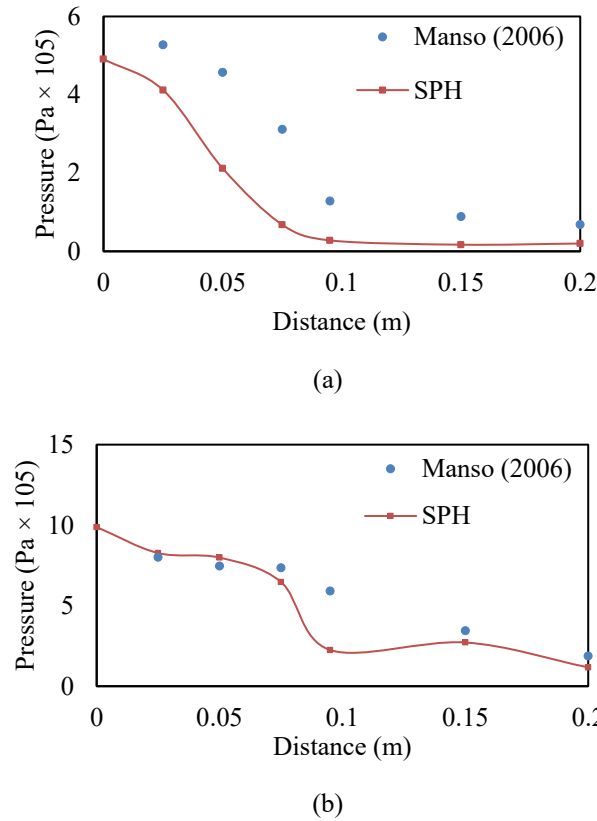


Fig. 123 - Computed absolute mean pressures (a) and maximum pressures (b) along the plunge pool's radial direction for $Y/D = 2.8$ m. Comparison with the experimental data by Manso (2006) for the equivalent hydrodynamic conditions.

This can be related with the fact that maximum registered pressures are dependent upon the acquisition time, as previously explained. Moreover, given that the amount of free-surface fluid particles varies along the radial direction, it is expected that the non-consideration of the air phase has different influence in the computed radial pressures.

Additionally, the SPH pressures were also compared with those derived from the empirical formulae proposed by Castillo (1989) (Eq. 17), which are based on the analysis of results from previous studies (namely Cola, 1966 for one-phase flow and Hartung and Häusler, 1973 for two-phase flow).

$$\frac{P-Y}{P_{stagnation}-Y} = e^{-\phi'(x/Y)} \quad (48)$$

Where P is the mean pressure on the pool bottom, $P_{stagnation}$ is the mean pressure at the stagnation point and x is the horizontal distance from the stagnation point to the considered point. The parameter ϕ' varies for each data set and can be read in Castillo *et al.* (2014). The inflection points of non-dimensional Gaussian type curves (Fig. 124) are further away from the stagnation point in the cases in

which the air entrainment is considered, revealing greater diffusion angles in these cases. SPH results approach well the results by Hartung and Häusler (1973), showing that pressures are reduced by approximately 85% within a radius of about $0.4 x/Y$.

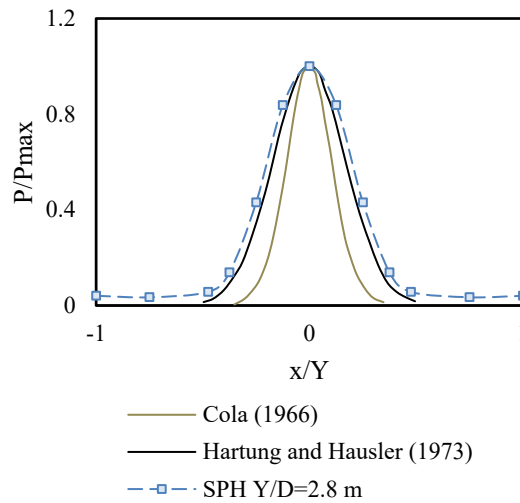


Fig. 124 - Experimental vs. computed non-dimensional pressures along the plunge pool's radial direction for $Y/D = 2.8$ m.

4.5.2. CONCLUSIONS

An SPH model of high-velocity plunging jets at near-prototype scale was developed with the objective of assessing the hydrodynamic loading produced on a flat plunge pool bottom. A resolution study performed to the upstream part of the model (the nozzle) revealed that a very fine particle resolution is needed to accurately simulate the confined flow, which lead to the simplification of the model's geometry. This underlined the importance of including a variable resolution approach into a SPH model. The final SPH model enabled improved understanding of the physical flow processes occurring inside the plunge pool, in particular of the flow features with high spatial resolutions and of air entrainment (even if employing a single-phase model).

A range of comparisons between SPH simulations and experiments was satisfactory. Maximum pressures near the stagnation point were computed with a relative error within 10% of experiments, which indicates that this technique has a good predictive capacity for modelling this highly complex turbulent flow. Computed mean pressures near the stagnation point exhibited a less accurate agreement (relative error within 20-40%) which was probably enhanced by the lack of explicit air phase modelling. Still, it should be kept in mind that these relative errors are compounded by the fact that in the experimental study by Manso (2006) the decrease in the mean pressures near the stagnation with the increasing pool depth was (unexpectedly) little pronounced, mainly due to the fact that the produced jets were too compact, with low turbulence intensities. The study of the bottom pressures along the radial direction showed that within a radius of about $0.4 x/Y$ pressures are reduced by approximately 85%, which agreed well with previous findings for two-phase flow jets (Moreira *et al.* 2021).

Given the complexity and costs associated to prototype measurements (Viseu *et al.*, 2018) more experimental and numerical studies are necessary to characterise the phenomena produced by plunging jets on dissipation basins. It would be highly desirable for the SPH simulation of plunging jets to include a variable resolution approach, as the use of a single resolution limits the resolution given to the jet in

favour of a manageable number of fluid particles in the plunge pool. Yet, given the significant challenge that variable resolution implementation poses in SPH, existing developments did not yet achieve their maturity to solve such complex simulations.

4.6. CONCLUSION

In this chapter the development of SPH applications was presented, including the setup of different SPH models and corresponding extensive quantitative validations. Three 3D case-studies were presented to show that WCSPH (with USAW boundary conditions) is able to accurately model complex, high-Reynolds turbulent flows, even in the presence of complex geometries. Two dam spillways were simulated with little to no simplifications in their geometry which evidences a great advantage that the SPH model offers to simulate such hydraulic systems at an industrial scale. All developed SPH applications employed open boundaries for in and outflow and a RANS-based turbulence model. The quantitative validation carried out leaned on the most common physical quantities of interest in dam spillways engineering, like flow depths and velocities and pressures on surfaces.

Obtained results are overall promising and evidence the potentialities of the method. Moreover, it was possible to verify that the accuracy of the employed SPH model can be similar to that obtained with a well-established mesh-based model, which at the present stage motivates the ongoing research for improved SPH formulations. On this subject, it is worth mentioning the δ^+ -SPH variant (by Sun *et al.*, 2017) of the standard WCSPH model, which has shown to be robust in solving violent fluid-structure interactions, such as those under study. It is anticipated that this new formulation may help to minimize some of the limitations encountered in the present research, namely, the pressures fluctuations estimation and the leakage issues. Extensive validation for this new WCSPH scheme is being undertaken against several challenging benchmark cases (Sun *et al.*, 2019).

PRACTICAL RECOMMENDATIONS

5.1. INTRODUCTION

The majority of the available literature on applying CFD models to simulate spillway flows comes from studies using three of the most popular software packages, namely FLOW-3D, ANSYS CFX, and ANSYS Fluent. Each of these has been successfully applied to model advanced problems involving fluid-solid interactions and thus, general guidelines for their application can be found in literature. For general CFD applications (that is, of mesh-based models), the ERCOFTAC¹⁹ Best Practice Guidelines (Casey and Wintergerste, 2000) is still the most complete document. Yet, this does not happen for the SPH method. Despite all of the characteristics that make it especially interesting for this type of applications (section “3.1. Introduction”), still very little is published concerning recommendations for a successful application of the SPH method to model dam spillway hydraulics, especially at an industrial scale. As such, this section is aimed at giving a contribution to that knowledge mostly taking advantage of the experience gained with the application of the SPH-based code, GPUSPH, to the previously described study cases. Guidance and indications are given concerning aspects including design and meshing or hardware issues. The following recommendations are not restricted to the simulation of spillway flows, but were found from the present experience, and thus should be particularly relevant for future similar numerical attempts.

5.2. PROBLEM STATEMENT


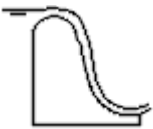
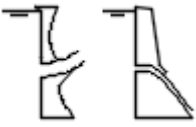
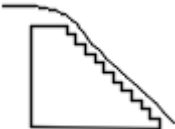

The overall objective of modelling is to provide the basis for making well-founded decisions. It should be seen as an evolving, iterative process which reflects the development and understanding of the phenomena being simulated. As such, before considering any numerical set-up for the hydraulic system under study, it is important to have the theoretical knowledge of the hydrodynamic processes expected to take place. This knowledge is important to guide the decisions to be made in subsequent phases of the numerical modelling.

For instance, in spillways having a long chute, three major phenomena that may influence the structure design are: the potential danger of cavitation, the occurrence of shock waves and the aeration of the flow (and consequent bulk of the flow depth). Depending on the objective(s) of the study, the engineer may benefit better from a certain SPH formulation over another. Table 24 summarizes the main flow features that may be present in some generic hydraulic systems.

¹⁹ ERCOFTAC stands for European Research Community on Flow, Turbulence and Combustion. SPHERIC is one of the Special Interest Groups created by ERCOFTAC.

PRACTICAL RECOMMENDATIONS

Table 24 - Summary of some flow characteristics in common spillway schemes^a.

ID	Spillway	Scheme	Aeration	Flow features / concerns
1	WES weir with a short chute (on the dam body)		<ul style="list-style-type: none"> • At issuance: insignificant • At falling: significant, with spreading and break-up (especially if splitters exist) • At plunge pool: significant due to jet impingement 	<ul style="list-style-type: none"> • Turbulent shear flow in the plunge pool with vortex formation. • Significant impact forces on the plunging pool • Energy dissipation by jet diffusion and deflection
2	WES weir with a long chute (on the dam body or as a side channel)		<ul style="list-style-type: none"> • Gradually increases from the inception point onwards • Bulking of the air-water mixture along the chute • The jet from a ski jump as a partially or fully aerated core 	<ul style="list-style-type: none"> • Cavitation potential at: the crest depending on crest shape/ existence of gates; at protruding concrete joints or small offsets (<10 mm); at baffles (if any); or at abrupt concave/convex surfaces • Shock waves development due to: overflow pier ends; or chute contractions, expansions or slope changes. • Rotating flow at chute bends
3	Orifice high-head		<ul style="list-style-type: none"> • At the intake: it depends on submergence (the shallower the more relevant) • At the dissipation basin: significant 	<ul style="list-style-type: none"> • If the orifice is deep-seated the cavitation potential should be assessed • Energy dissipation processes are dependent upon the orifice design, existence of a trajectory basin and the tailwater depth • Significant impact forces if a plunging pool is used
4	Stepped		<ul style="list-style-type: none"> • Much air is entrained from the inception point onwards 	<ul style="list-style-type: none"> • Flow instabilities associated with transitory regime nappe/skimming flow • Spray action • The upstream part (up to the inception point) may be prone to cavitation damage at large discharges
5	Shaft		<ul style="list-style-type: none"> • An air-core should exist to prevent cavitation and vibrations 	<ul style="list-style-type: none"> • Open channel flow with a rotational velocity component (swirling flow) • Energy dissipation through wall friction is relevant • Shock waves may lead to abrupt transitions from free-surface to pressurized pipe flow • Cavitation potential at the transition between shaft and tunnel should be assessed.

^a From literature review (e.g. Vischer and Hager, 1998 and Tanchev, 2005) and author experience

A dam may have its own specificities and one may find the occurrence of one or more of the flow features mentioned above in the same structure. The choice of the approximate equations to describe the flow has the largest impact on the modelling errors and uncertainties referring to the flow physics.

Results may always be interpreted having a clear knowledge of the numerical limitations of the SPH code being employed. For a SPH application, at this stage it is convenient to:

- Estimate the order of magnitude of the maximum flow velocities in the numerical model, u_{max} , as these are used to compute the speed of sound, c_0 , (as explained in section “3.2. SPH formulation”). An incorrect computation of c_0 can make the simulation unfeasible, crashing it. The estimation of the order of magnitude of the maximum flow velocities can be done using experimental or prototype data (if existing) or using the approximation $u_{max} \cong \sqrt{2gH}$, being H the hydraulic head and g the gravity acceleration;
- Define the physical quantities being measured in the numerical model and how these will be computed in SPH (e.g. interpolation features, data registry frequency) and posteriorly processed. Computation of physical quantities in GPUSPH can be done with the definition of *wave gages* (which track the free-surface level evolution) or *test points* (which compute a physical quantity, such as flow velocity or pressure, at a given point, by performing a weighted average using the neighbouring particles within the influence radius of the Kernel function);
- Verify the possible occurrence of certain phenomena such as air entrainment, secondary flows, rotating flows, negative pressures (related to the cavitation potential) and foresee the impact of the SPH code limitations on the simulation of these features, e.g.: (i) if air entrainment is expected to have a relevant role in the fluid dynamics, losses of accuracy when computing the pressure and velocity fields may occur when using a single-phase SPH code. As seen in the high velocity jets case study, SPH can qualitatively give evidence of the flow “aeration”, as some free-surface fluid particles (having zero pressure) can enter the core of the flow (refer to Fig. 114). However, the pressure of real air pockets should be different from zero; (ii) if curved ducts are present, the effects of streamline curvature and swirl on the turbulent flow may play a role and a secondary flow may develop. In such cases using an isotropic eddy viscosity turbulence model, as the standard $k - \epsilon$ model, may be insufficiently accurate;
- Evaluate the inclusion of a turbulence model in the SPH model. SPH has succeeded in many fields (Monaghan, 1992) to simulate high speed turbulent flows because it broadly fits within the class of simulation techniques known as Large Eddy Simulations (LES), as the spatial interpolation done in Eq. (10) is formally the same as the spatial filtering used to construct LES methods. Still SPH is not a true turbulence method because it lacks a suitable sub-grid scale model and correct transport of energy between different scales. However, it is often able to make very good predictions for high speed turbulent flows just by reasonably representing the energy transfer in the larger length scales (Cleary *et al.*, 2007). Turbulence of the flow over the spillway of the Caniçada dam was simulated with the $k - \epsilon$ turbulence model and without a turbulence model to verify the impact of lacking a turbulence model on the results accuracy. It was verified that the non-inclusion of the turbulence model impacted the computed pressures accuracy, significantly. Thus, it is recommended that a turbulence model is included when simulating a spillway flow; and
- To define monitoring key values in the region of interest and select an acceptable level of convergence based on the rate of change of these targeted parameters. These key values should include the variables that are representative of the goals of the simulation and those that can be compared with the corresponding experiments. This should be done in addition to the verification of the mass flow balance in inlets and outlets (to guarantee mass conservation). In SPH, the mass flow balance may be assessed through the control of the number of particles in the computational domain throughout the simulation (e.g. Fig. 48).

The determination of instantaneous pressures in SPH is normally bounded to pressure noise, especially in the WCSPH approach, being reported in literature that normally ISPH can produce better results (e.g. Lee *et al.*, 2008; Leroy *et al.*, 2014). Indeed, as verified by Leroy *et al.* (2014), ISPH produces better results in comparison to the WCSPH, as verified on academic test cases. Yet, this difference seems to be more remarkable for confined flows in comparison to free-surface flows (e.g. Lee *et al.*, 2008; Lind *et al.*, 2012; Nomeritae *et al.*, 2016). As verified in the Caniçada dam simulations, a WCSPH formulation can produce accurate pressure results. This is largely owed to the accuracy of the USAW boundary conditions employed, but also to some numerical artefacts that aided to smooth out the pressure field, such as:

- Increasing the Brezzi coefficient. A reasonable range for this coefficient can be 0.1-1.0;
- Increasing the kernel's smoothing scale, h . A reasonable range can be 1.1-1.8; and
- Taking the closest vertex particle for the computation of pressures on the walls instead of the closest fluid particle (this can be done by changing the way that physical quantities are computed in SPH – *test points* in the case of GPUSPH). In GPUSPH, by default the closest fluid particle is taken for the interpolation which is disadvantageous when pressures are compute on a wall boundary.

To quantitatively determine the occurrence of negative pressures, an ISPH scheme is required, however, these can still be qualitatively assessed with an WCSPH scheme by evaluating the kernel renormalization parameter values, γ , Eq. (29), all over the fluid particles (as shown in Fig. 91). This assessment may show the locations where the occurrence of phenomena of flow separation or negative pressures is possible. In fact, for heads, H , greater than the design hydraulic head, H_d (which is the case of the spillway of Caniçada, in which $H/H_d = 1.13$), negative pressures tend to develop on the spillway crest. Still, a ratio H/H_d slightly greater than one is commonly used in practice as it increases the coefficient of discharge increasing the discharge capacity of the structure. This effect should be limited due to the potential for cavitation problems. Still within the scope of pressures prediction it is relevant to point out the δ^+ -SPH model (that combines a Particle Shifting Technique with the δ -SPH model), which has seen various improvements in past couple of years. This variant of the standard WCSPH model has shown remarkable improvements in solving some challenging benchmark test cases characterized by negative pressures, though some consistency issues still exist (Sun *et al.*, 2017). Sun *et al.*, (2019) presented a rather consistent approach to particle shifting in the δ^+ -SPH model.

5.3. DESIGN AND MESHING

Even though SPH is a mesh free method, still a mesh needs to be drawn in the pre-processing stage. This mesh aids in the positioning of the boundary particles that design the geometric model and confine the fluid particles. This can be done by using a pre-processing interface like SALOME. It is relevant noticing that, even though it is necessary to create a mesh of the boundaries, it is not necessary to mesh the whole fluid domain with SPH, which is a relevant advantage compared to mesh-based methods. This is particularly important for large-scale transient free-surface flows, where the volumes of space that would need to be meshed would be significantly larger than the volume of the fluid that is of interest.

During the design and meshing phase, the existence of small characteristic dimensions should be verified. These can be represented by a small exit or pipe diameter (e.g. a bottom outlet) or generally a thin passage for fluid particles (e.g. a small gate opening), in comparison to the whole model scale. To obtain a reasonable representation of the flow in such small passages the following practical recommendations may be considered:

- As a rule of thumb, the minimum resolution of the particles must be a quarter of the minimum characteristic length. This is particularly applicable for short-length flow contractions such as those caused by a small gate opening. When the flow contraction has a significant length, such as in a conduit, greater particle resolutions should be required, as seen in section “4.5. High-velocity jets – case study III”;
- When the resolution required to correctly reproduce the flow dynamics in a conduit or pipeline is such that it can not be applied to the whole fluid domain, due to computational restrictions, a variable resolution formulation, if available, is expected to provide an effective solution. If a variable resolution formulation is not implemented, this can translate into a very high number of particles in the computation domain (and unfeasible computational times as it is impossible to apply a high resolution to the entire fluid domain). As an alternative, if adequate, the stretch requiring a finer resolution may be replaced by a boundary condition (as did in the high velocity jet’s case study with respect to the nozzle);
- If energy dissipation through wall friction is relevant (as it can be in a shaft spillway), a very high resolution may be needed to more accurately resolve flow behaviours in such regions. In grid-based methods, a variable resolution approach is generally employed so as to use a finer mesh near the wall boundaries, in order to resolve the near-wall flow scales. In SPH, a homogenous discretization is still used, so that a wall function is usually applied, such as in the studies of Violeau and Issa (2007) or Mayrhofer *et al.* (2015), to account for the wall effect; and
- A resolution study may be carried out whenever possible;

Nowadays, some works are already published on variable resolution formulations (López *et al.*, 2013; Barcarolo *et al.*, 2014; Vacondio *et al.*, 2016), yet, the main SPH free access codes – SPHysics (Crespo *et al.*, 2015) and GPUSPH (as well as the remaining majority of current SPH solvers), do not provide it yet for potential users. As stated by Violeau and Rogers (2016), robust variable resolution schemes that give the user control over how it is employed over the potentially large range of temporal and spatial scales still poses a significant challenge. Also, in the context of modelling dam spillways, it would be necessary that the variable resolution implementation was done together with some features that are (generally) required in dam spillways modelling, such as open boundaries and robust wall boundary conditions formulations. This will be an important development concerning the application of SPH to this engineering topic, since bottom outlets sometimes have small diameters in comparison to the reservoir dimensions and small gate openings are often used.

Particle leakage problems may also hinder the simulations, as occurred in the present research. The reason why it happens is not straightforward and this is probably because boundary conditions (including open boundaries) in SPH still have some open issues, being presently a topic of active research. In literature, there are some possible formulations to implement them. In the present research, only the USAW boundary conditions was tested as these have proven to be accurate in simulating complex geometries. When a problem of particle leakage happens, it is important to identify where it starts. Generally, when it starts it tends to progress rapidly. If it happens through a wall boundary, possible reasons can be:

- Connectivity issues in the mesh (resulting from the design stage, e.g. overlapping faces or edges, incorrectly unbounded faces, etc). A good practice that can be used to verify the existence of connectivity issues is to verify the values of the renormalisation factor, γ , at the boundary particles in the beginning of a simulation. This will help to identify, e.g. if there are separated faces where they should be linked (see Fig. 125);
- Incorrect normals’ orientation of the faces composing the geometry: all normals must be oriented inwards. If this does not happen, leakage will happen through such faces; and

- Irregular meshing: meshes must be as regular as possible. Furthermore, irregular meshing can locally increase the number of neighbouring particles, which is computationally inefficient. SALOME has some mesh control utilities to help evaluating mesh regularity. For example, one can assess the distribution of the cells area. Irregularly distributed boundary particles may as well be prevented by keeping the ratio between the maximum and the minimum distances existent between the centre and the vertex of the mesh triangles (the mesh cell's preferable geometry) below 10 (refer to Fig. 40). This can be controlled using the *testTriangles* tool that comes with CRIXUS.

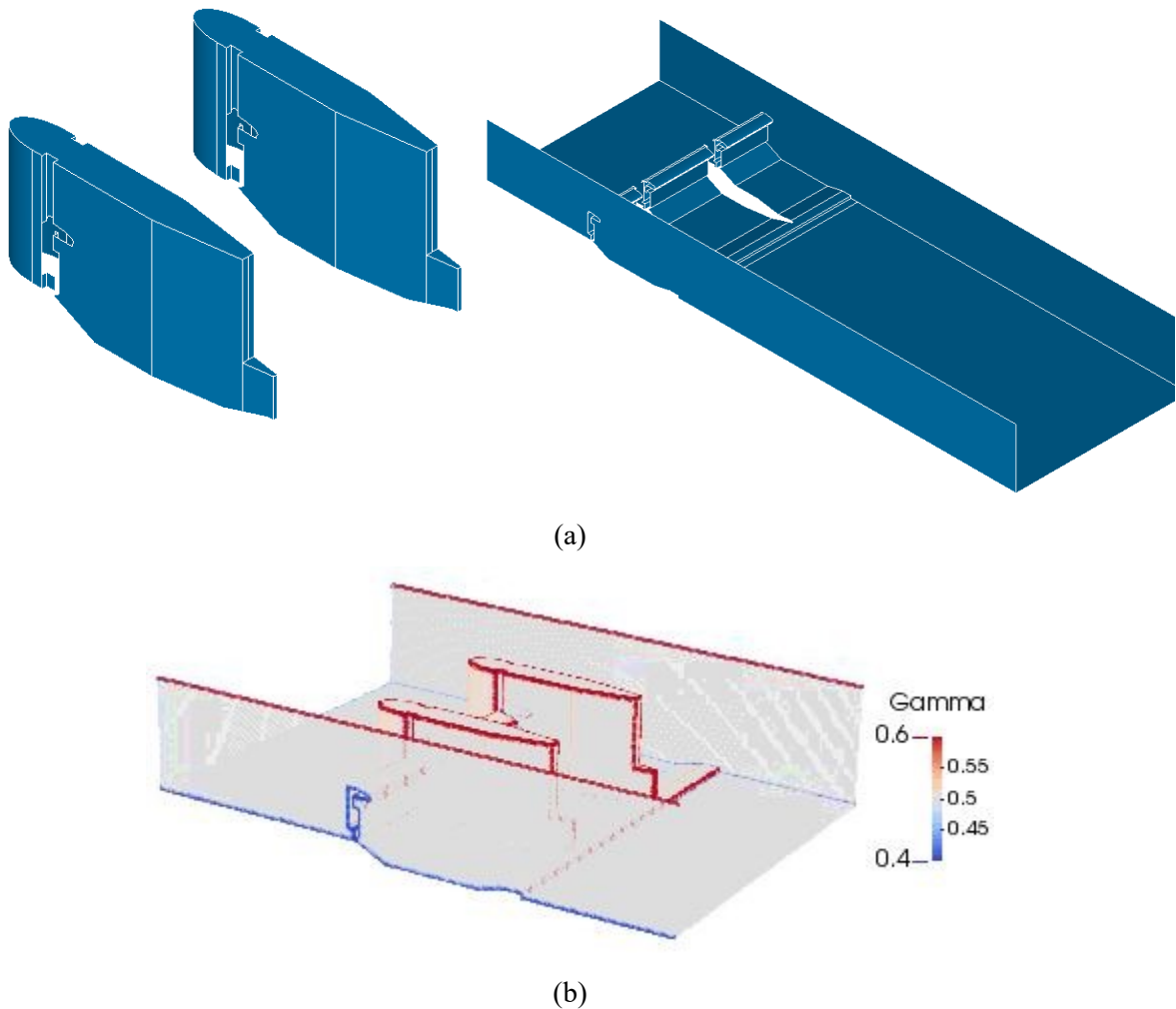


Fig. 125 - Design and meshing of the Crestuma dam model (a) Geometry model showing the two piers cut (by the gates) in order to get a correct mesh connectivity, without overlapped faces; (b) boundary particles plotted according to its renormalization factor values.

If particle leakage happens near an open boundary it can be due to:

- Insufficient distance from the inlet section to the weir (or control section);
- Irregular meshing of the open boundary face (in 3D);
- Incorrect prescription of the velocity profile at the inlet, if a velocity-driven open boundary is prescribed.

To verify if the open boundaries prescription is being done correctly throughout the simulation (whenever the USAW boundary conditions approach is being used), one can verify if the mass of the vertex particles is varying over time— that is, increasing in the inflow boundary and decreasing in the outflow boundary.

Given that the SPH method is computationally expensive, it is important to optimize the numerical calculation. This can be done by e.g.:

- Defining efficient problem domain sizes, keep the model's size as small as possible. If the geometry of the structure being modelled is symmetric, a periodic boundary condition can be employed at the symmetry plane to decrease the computational effort. The application of a periodic boundary condition requires a special treatment during the mesh generation phase - all geometry edges in which the periodic boundary condition is to be applied must have the same number of elements (thus, boundary particles) in both sides. If this correspondence is not respected, issues may appear during the simulation. In SALOME, this can be done with the creation of *submeshes* in groups of *edges* (the symmetric edges);
- Using the results of a coarser simulation as an initial state for a refined simulation, in order to converge faster towards the steady state. Such methodology was employed by Fonty *et al.* (2017) with the GPUSPH code.

Lastly, whenever an existing structure is being modelled it may be relevant to verify if the spillways' surface is not damaged (thus the actual spillways' profile will not be that defined at the design stage). Small defects on the spillways' surface are known to trigger cavitation. Still, modelling such small geometry particularities will require a variable resolution SPH formulation.

5.4. HARDWARE RELATED ISSUES

Also important are the considerations to be made about the properties of the hardware being used. As stated, the SPH method can be quite time-consuming in 3D simulations owing to the high number of neighbours to be computed. The use of GPU processors appears as a sound solution for this, thanks to the parallelizable nature of the method. The computational time will depend on the hardware characteristics and the complexity of the SPH model setup (e.g. the type of boundary treatment or turbulence modelling approach used). The maximum number of particles that the user can fit in a simulation is limited by the hardware characteristics and it scales linearly with the amount of available RAM of the GPU processor(s). Moreover, in problems involving open boundaries, the user should be aware that the number of fluid particles can significantly increase during the simulation. The following recommendations can be considered:

- When employing USAW boundary conditions, as a rule of thumb, the user should be able to fit around 5 million particles in 6 GB of RAM. For example, for the GPU processor used in the present work (the GeForce Titan X, a Maxwell card) one should be able to fit about 10 million particles (refer to Table 10). Nevertheless, with particle-type boundary conditions, e.g. dynamic boundaries in GPUSPH, larger simulations can be run with similar hardware properties;
- In the beginning of a simulation, the SPH code will allocate a certain amount of memory, which is expected to be needed during the calculation. In GPUSPH, the allocated memory is based on the initial number of particles times a maximum number of particles factor (*max_parts*) times the maximum number of neighbours (*maxneibsnum*). A preliminary estimate of the maximum number of particles that will be in the computation domain, in the converged numerical solution, is useful to define a function that limits it. For example, a *max_parts* factor of 2 would mean

that the number of fluid particles can double since the beginning up to the end of the simulation. The optimization of this factor is key to optimize the GPU processor's memory usage. It should be as smaller as possible to guarantee that there isn't memory being allocated but unused. The *maxneibnum* value may as well be optimized (as smaller as possible too), knowing that it is typically 30 in 2D and 250 in 3D, although these values can be higher depending on the geometry and mesh characteristics;

- Besides the RAM memory another concern may be the hard drive memory. In large simulations, the output files (.vtu files) can have a significant dimension. The user can vary the output frequency to meet the available space on the disk to store results; and
- Acceleration in SPH can be obtained either by using multi-GPU (GPU processors plugged to a single motherboard) or multi-node simulations (more than one motherboard to plug two or more GPU processors). These capabilities can make it possible to significantly reduce the computational times, compared to single-GPU simulations. Moreover, it is recommendable the use of GPU processors of the same generation, that is, of the same compute capability, as not doing so may eventually result in some errors. Still, more tests are needed to better assess the robustness of GPUSPH with respect to hardware heterogeneity.

5.5. SPILLWAY3D CASE EXAMPLE

For the industry, besides the performance of the numerical models themselves, an important aspect to consider is their availability. Numerical tools to simulate spillway flows can be home-made, open-source or commercial codes. With regard to SPH, existing codes mostly fall within the two first categories. Home-made and open-source codes are generally more flexible (and cheaper) than commercial codes, which is positive, but they are generally less well-documented, and it is more difficult to get advice for their usage. Also, it is worth noting that typical model files are generally difficult to find. Typically, everybody has to create his/her own models from scratch (which requires considerable expertise), sometimes gathering information from various simpler available file templates. Because of this, modelling spillway flows is still a specialized topic, mostly accessible to graduate students or researchers, especially when it comes to less-tested numerical methods, such as SPH.

Therefore, besides the improvement of the SPH model itself (which has been SPHERIC's goal over the past years) other conditions that may be necessary to move SPH towards industrial applications is the improvement of the availability and easiness-of-use of simulation tools. Like this, dam engineers may jump much more quickly to the core of their analysis without the need to be expert programmers. This is particularly important, as many dam designers from the industry were not trained as computer scientists, and therefore, they cannot spend time to learn a complex code.

As a contribute to that, a case example of an ogee spillway is presented here. It has the purpose of being included in the GPUSPH directory to provide a "ready-to-run" dam spillway application, for potential users. The core of the simulation setup, the .cu file, is shown and explained. It gathers the features employed in both simulations of the spillways of the Crestuma and Caniçada dams (such as the USAW boundary conditions, $k - \epsilon$ turbulence model, logarithmic velocity profile at the inlet section, among others).

The present case example consists of a 3D typical ogee spillway which geometry and dimensions follow the experimental work by Savage and Johnson (2001). The spillway design parameters, such as the design head, H_d , and the design flow rate, Q_d are 0.301 m and $0.376 \text{ m}^3/(\text{s} \cdot \text{m})$, accordingly. The first steps to undertake a GPUSPH simulation consist of the geometry design itself and respective meshing. This can be done, e.g., in the SALOME software using the corresponding modules. SALOME offers

several options to create a geometry, such as: (i) to create the geometry by hand; (ii) to import a geometry; (iii) to import an .stl file and convert it to a geometry (SALOME 7.2 and older). Fig. 126 shows the model geometry and dimensions designed by hand in SALOME. It shows a plane as well at $z = 0.75$ m which correspond to the free surface level at the initial time step (it serves as a top limit for the CRIXUS filling). The computational dimensions (2 m length, 0.5 m width and 1.5 m height) were set as to keep the computational time manageable, giving the academic nature of this simulation. The geometry design resulted then in the creation of two shells²⁰ - one for the model itself and another for the free-surface shape. Next, meshes were created for each of these shells. For the geometry model itself separate meshes should be created for the inlet and the outlet sections (the creation of groups from geometry in SALOME allows to do this). Triangle (metfisto) in 2D and wire discretization (using a local length) in 1D are two possible mesh generation algorithms that work well within the present context. The mesh generated for the free-surface shell should simply be quite coarse. Completing these steps results in the following .stl files:

- Spillway3D.stl
- Spillway3D_freesurf.stl
- Spillway3D_grid1.stl
- Spillway3D_grid2.stl

Which are available in gpusph/data_files folder (Fig. 127).

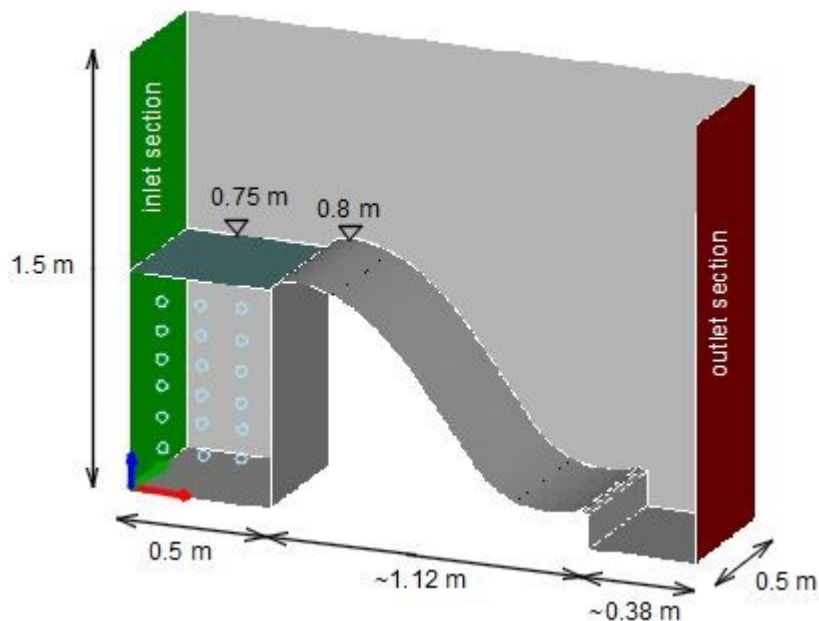


Fig. 126 – Model's geometry and dimensions.

Before filling the computational domain with SPH particles (both fluid and boundary particles) using CRIXUS, the mesh triangles size need to fulfil a certain criterion (see Fig. 40). This is only necessary for the geometry itself mesh, thus no control need to be done for the free-surface mesh which should

²⁰ Topological object in SALOME's geometry module.

ideally be quite coarse. To check whether this is met, a dedicated tool exists in the resources folder of CRIXUS, which is called test-triangle-size. It can be compiled using:

```
gcc test-triangle-size.c -lm -o testTriangle
```

and then run using

```
$(CRIXUS_PATH)/resources/testTriangle path/to/file.stl 0.1
```

where 0.1 is the particle size to be used and should be changed as needed. This will indicate whether all triangles meet the criterion or not. It also determines the maximum and minimum distances between the centre and the vertex of a triangle, which is a good measure to check mesh regularity as recommended in section “5.3. Design and meshing”.

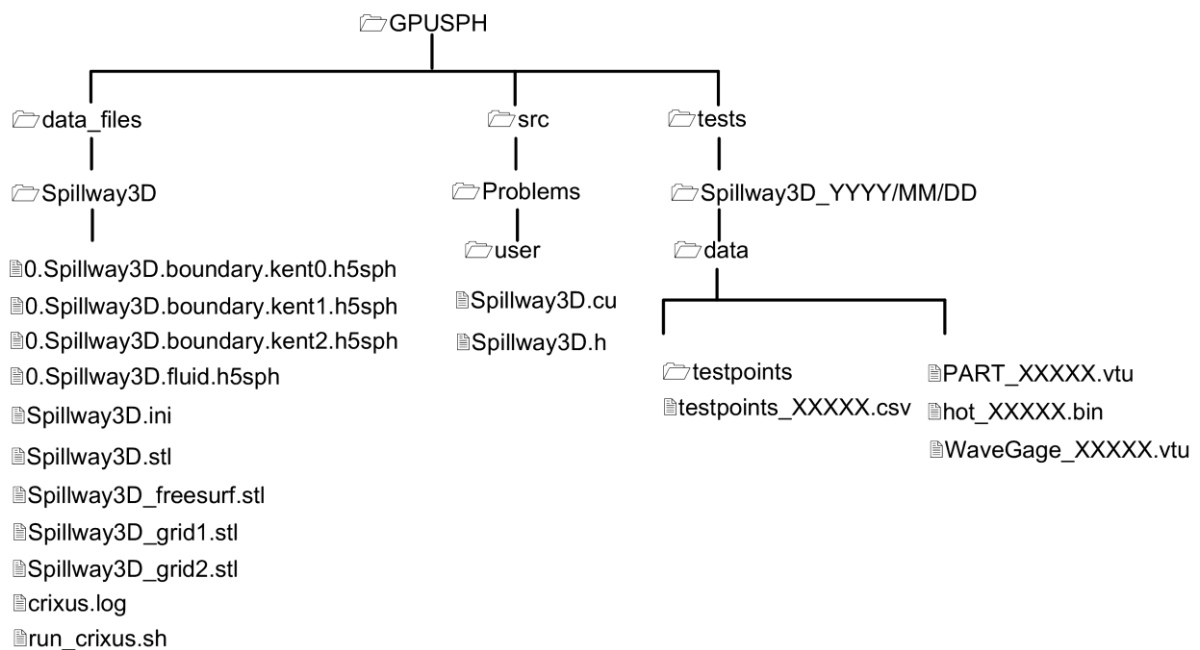


Fig. 127 - GPUSPH directory tree. For simplicity not all of the folders and files in the GPUSPH directory are represented.

CRIXUS can then be run in order to fill the geometry with SPH particles. It can be run inside the SALOME interface, through a plugin or in the terminal provided that an .ini file is prepared. The completion of this step results in the creation of the following .h5sph files:

- 0.Spillway3D.boundary.kent0.h5sph
- 0.Spillway3D.boundary.kent1.h5sph
- 0.Spillway3D.boundary.kent2.h5sph
- 0.Spillway3D.fluid.h5sph

These files can be found in folder data_files inside the GPUSPH folder and are needed (along with the .cu .h files) to run the code.

The solver setup can be done either through the new GPUSPH plugin for SALOME, which allows to generate the.cu and .h files in a user-friendly way, or by directly writing the referred files, which may

PRACTICAL RECOMMENDATIONS

allow greater flexibility. The .cu file for the present case example (named as Spillway3D.cu) is presented, explained and commented in appendix C. It can be found in folder gpusph/src/problems. In order to compile the Spillway3D.cu the user can type

```
Make compute=61 spillway3D
```

with 61 referring to the compute capability of the GPU card to be used, 6.1 in the present example.

And then GPUSPH can be run by typing

```
./GPUSPH _device0,1
```

with 0 and 1 referring to the GPUs device ID to be used, in the case where two GPUs will be used (though less or more GPU's can be used).

5 s of physical time can be simulated in approximately 7 min of computational time. Though, it should be noted that the particle resolution employed may be too coarse for quantitative validation purposes in favour of the speediness of results. The result files are .vtu files that can be find in folder gpusph/tests. Fig. 128 shows the flow evolution within the first 5 s of simulation.

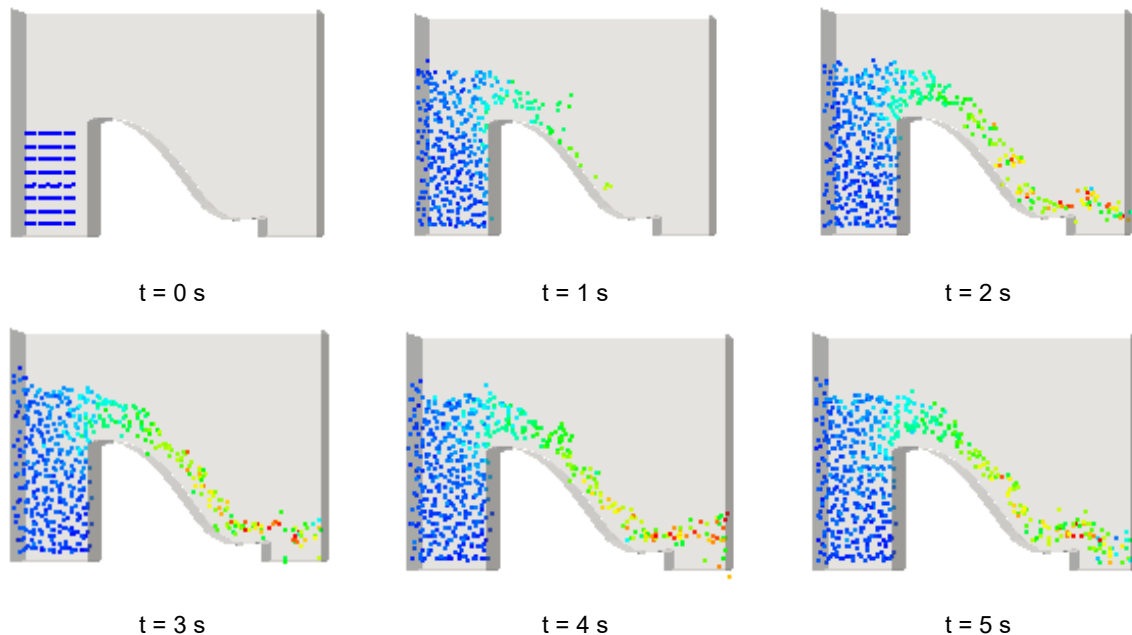


Fig. 128 - Schematic 3-D flow over an ogee spillway. Shape of the free-surface and velocity field obtained with GPUSPH within the first 5 s of simulation.

The user may find it useful to stop and restart the simulation at any time. This can be done by typing:

```
./GPUSPH --resume path/to/file.bin
```

The .bin files required to resume a simulation are written in the tests folder.

The provided .cu file is expected to work with any other user application (that is, other 3D hydraulic system) as long as the computational domain has two rectangular open boundaries (one for inflow and another one for outflow), provided that the following problem-specific parameters are adjusted in the .cu file:

PRACTICAL RECOMMENDATIONS

- Particle diameter;
- Computational domain dimensions;
- Maximum particles velocity;
- Desired probes and gages locations;
- Water depth at pressure driven open boundaries;
- Width of the inlet section;
- Flow rate imposed at the inlet section.

And as long as the user creates the .stl and .h5sph files for their own simulation following the generic given guidelines.

Some changes can be done to the provided .cu file to better suit the user goals, such as, imposing a variable flow rate (e.g. a flood hydrograph), imposing a different velocity profile at the inlet section (e.g. linear, from experimental data), introduce a movable body, use a periodic boundary condition, among others.

5.6. CONCLUSIONS

As the available time to complete a project normally has significant financial implications, the value of time when running CFD models in industrial context limits the choice of a software on the basis of its easiness of use and confidence. The compilation of recommendations given in this chapter is an attempt to present relevant information in regards to setting up a SPH model to simulate spillways of all kinds, though, as much of the research emphasis has been on chute flow and overgate (free) discharge, it may be rather relevant to such spillway schemes. Though it is not exhaustive, it should give the engineer the insight to properly consider some of the facets involved in a successful SPH spillway model set-up. As with any other set of practical recommendations of this kind, new research and experience may have an impact on the usefulness and validity of some of them. Additionally, a 3D spillway case example was presented with the objective of providing/describing a “ready-to-run” dam spillway application, within the GPUSPH framework, for potential users. As explained, it can be simply adapted to any other spillway application provided that the corresponding geometry files are created.

CONCLUSIONS AND FUTURE DEVELOPMENTS

6.1. SUMMARY

The present thesis was dedicated to the SPH modelling of dam spillways, with the ultimate purpose of investigating the viability of SPH for real-life applications of highly turbulent free-surface flows. The lack of quantitative validation of this method, towards industrial engineering applications, commonly referred in literature, was addressed. Three major outcomes were obtained with the present research: *(i)* the assessment of the SPH method performance to model engineering applications of dam spillways, by providing extensive quantitative validation; *(ii)* the comparison between SPH and a mesh-based model performances, based on a wide range of data results; and *(iii)* the compilation of a set of practical recommendations to simulate dam spillways using the SPH method. The first two outcomes were addressed in chapter 4 whereas the third composed chapter 5. Specific concluding remarks were already provided throughout this thesis. However, in this chapter, the broader conclusions and achievements are summarised.

Current methodologies for assessing spillway flow behaviour largely rely on commercial versions of mesh-based numerical methods and, ultimately, on physical models. Therefore, good quality numerical results are often affected by mesh quality and adaptivity issues. On the other hand, constructing physical models is also expensive, time-consuming and subjected as well to a few error sources and modelling constraints.

- Most of the SPH applications to model spillway flows at an industrial scale focused on a primary goal of providing sound qualitative results, letting apart pertinent issues as turbulence modelling, open boundary prescription for flow generation, or further accurate boundary conditions. These aspects were taken into account in the present investigation.
- The completion of three distinct case studies (i.e., overgate discharge, chute flow and high velocity jet) allowed to conclude that overall, the SPH method can accurately predicted the flow dynamics in dam related problems, especially in what concerns to flow depths, velocities and pressures, even if the model had some simplifications (e.g. single phase). As long as the prediction of water depths is concerned, the quality of the prediction seemed to be influenced by the complexity of the flow features, that is, its turbulence and anisotropy, so that, at some stretches it was satisfactory while at others it was poor.
- The promising results achieved by Leroy (2014) with the use of USAW boundary conditions were further exploited in this investigation with its application to challenging problems. This

boundary condition formulation along with some numerical tricks (mentioned in section “5.2. Problem statement”) showed quite positive results especially in terms of pressures’ prediction.

- At the present state-of-knowledge it was important to verify if an SPH model could deliver as accurate results as a commercial mesh-based model can, for such complex industrial applications. The comparison between the SPH and a mesh-based model performances, presented in section “4.4.5. GPUSPH vs. mesh-based model results”, showed that these can be identical, especially in terms of flow velocities and pressures prediction, with the SPH model delivering results even within a shorter period of time. Such finding motivates the continuous development of the method in favour of its already mentioned advantages.
- The three addressed case studies permitted a deep contact with the methodology and made it possible to identify some issues that may difficult or hold back future applications. Particle leakage through the domain boundaries was probably the most recurrent issue, highlighting one of the weaknesses of the method – the boundaries treatment. This, along with the unavailability of a variable resolution formulation limited the scope of the research, as it prevented, e.g., the simulation of further hydraulic conditions in the Crestuma dam (due to the existence of a relatively small gate opening) or the simulation of the upstream nozzle in the third case study.
- Still very little is published concerning recommendations for a successful application of SPH to model spillway flows, therefore, as no established guidance on the setup of SPH simulations exists at present, a set of practical recommendations for the SPH application to dam hydraulics was presented in chapter 5, based on the hands-on experience gained throughout the present research. Such recommendations focus on the design and meshing stage and hardware issues, but also discuss relevant aspects of the problem statement and underlying adequate SPH formulations. This non-exhaustive set of recommendations aims at paving the way for the settlement of general best practice guidelines by the SPHERIC’s community.
- This objective was further completed with the presentation of a generic spillway case example in section “5.5. Spillway 3D case example” as a “ready-to-run” dam spillway application, so that consultants in the dam engineering sector may orient their modelling efforts more effectively.

Besides the conclusions obtained with the present research and their associated limitations, the main idea of this research is that the application of SPH as a tool to improve dam spillways design and safety is close to hand and that it can be an interesting complement to well-established mesh-based methods, and ultimately to physical modelling.

6.2. FUTURE DEVELOPMENTS

In the framework of the long-term research line of the SPH method development for turbulent free surface flow applications since 1994 (Monaghan, 1994), this research can be regarded in line with those efforts, as a wrap-up of what has been achieved up to this date. With the results of the present research, a better understanding of the performance of SPH to model dam spillway hydraulics could be acquired. In the following paragraphs, the author points out some research directions for future investigations in the scope of dam spillways modelling with SPH.

- The performance of further SPH validations, at an industrial scale, is needed. Still many of the proposed method formulation improvements (with interest to the dam engineering sector) at this stage have only been validated against theoretical case examples. It is important to recognize that SPH codes can only be validated for a class of problems involving specific variables. If the application involves an area where the code is not fully verified there is more risk of

inaccuracies. The δ^+ -SPH variant appears as an interesting alternative to the standard WCSPH to model dam spillway hydraulics, especially when the pressure field can attain negative values (underlying cavitation damage), though its validation is still limited. Consistent method validation should ultimately lead to the definition of proper reliability indices, without neglecting that both computational and physical models are approximate representations of the real behaviour.

- A robust variable resolution SPH formulation is deemed necessary for dam engineering simulations to account for aspects as small dimensions in the geometry, sudden variations in flow depth (e.g. from a reservoir to a spillways' intake or conduit), or even localized flow perturbations. It is not computationally efficient nor adequate to model large reservoirs and e.g. jets or chute flows with the same particle resolution.
- To develop and validate a two-phase SPH model that could accurately address the air-water interactions commonly found in spillways flows is key, as air may be entrained in water flows in several ways: (i) free surface aeration in high-speed flows; (ii) local aeration by impinging jets into a plunge pool; (iii) air entrainment into hydraulic jumps; (iv) free jet entrainment through the atmosphere, (v) aeration at transitions from free-surface to conduit flow, or (vi) local air supply by aerators (Kobus, 1985). The non-inclusion of the air-phase in the presented SPH applications was frequently discussed throughout this thesis. To develop this research further, including the air phase in the SPH model should be considered, following, e.g., the recent developments by Fonty *et al.* (2018).
- The study of the phenomena produced by plunging jets on dissipation basins was successfully introduced at the present research, but this is still a broad and open scope for future investigation with SPH. At present, pressures induced by an impinging jet on a flat and rigid bottom were satisfactorily predicted (though greater simulation times are still required to strengthen these predictions), but the topic of the SPH modelling of scour on dissipation basins is still in great need for research. To this end, multi-phase SPH formulations have significantly evolved in recent years (e.g. Zubeldia *et al.*, 2018).
- In the present research, turbulence modelling was merely addressed with the standard $k - \epsilon$ model. A promising alternative to RANS turbulent closures are large eddy simulation (LES) turbulence models, which are superior in modelling turbulent eddies and vortices. Moreover, the LES approach should be most suited for the structure of the SPH itself. Mascio *et al.* (2017) reformulated, in a rigorous and general way, LES modelling in the SPH but still further research is needed, in particular the extension of the proposed model in finite domains, so that dam engineering applications may benefit from a whole family of LES-SPH schemes in the future.
- Modelling transient effects due to moving gates is another pertinent research vector for future, giving the suitability of SPH to model moving bodies.

To conclude, the application of SPH models in dam hydraulics engineering still poses major challenges to which is justified further research. Since SPH codes are being monthly improved, with some institutions releasing significant updates on a yearly basis, it is expected that many of the current limitations will be overtaken over the next decade and its application to real-life turbulent flows will witness relevant developments.

CONCLUSIONS AND FUTURE DEVELOPMENTS

REFERENCES

- Aghebatie, B. and Hosseini, K. (2016). Investigation on the formation of roll waves in chutes, *Water and Environment Journal*, 30(1-2): 113-118.
- Albano, R., Amicarelli, A., Mirauda, D., Agate, G., Sole, A., and Taramasso, A. C. (2014). Experimental validation of a 3-D SPH model for the simulation of a dam-break event involving multiple fixed and mobile bodies, *7th WSEAS International Conference on Engineering Mechanics, Structures, Engineering Geology*, Salerno, Italy.
- Alias, N.A., Mohamed, T.A., Ghazali, A.H., and Noor, M.J. (2008). Impact of takeoff angle of bucket type energy dissipater on scour hole, *American Journal of Applied Sciences*, 5(2): 40-45.
- Amicarelli, A., Agate, G. and Guandalini, R. (2013). A 3D fully Lagrangian smoothed particle hydrodynamics model with both volume and surface discrete elements, *International Journal for Numerical Methods in Engineering*, 95(5): 419–450.
- Antuono, M., Colagrossi, A. and Marrone, S. (2012). Numerical diffusive terms in weakly-compressible SPH schemes, *Computers Physics Communications*, 183, 2570-2580.
- Antuono, M., Colagrossi, A., Marrone, S. and Molteni, D. (2010). Free-surface flows solved by means of SPH schemes with diffusive terms, *Computer Physics Communications*, 181, 532-549.
- Balestra, A.A. (2012). *Einfluss von Zuflussgefälle auf Skisprünge [Effect of chute slope on ski jumps]*, MSc Thesis, Eidgenössische Technische Hochschule, Zurich, Switzerland, (unpublished, in German).
- Ballofe, A. (1961). Pressures on spillway flip buckets, *Journal of the Hydraulics Division*, 87(5): 87-98.
- Barcarolo, D., Touzé, D., Oger, G. and Vuyst, F. (2014). Adaptive particle refinement and derefinement applied to the smoothed particle hydrodynamics method, *Journal of Computational Physics*, 273: 640–657.
- Basco, D. R. and Adams, J. R. (1971). Drag forces on baffle blocks in hydraulic jumps, *Journal of the Hydraulics Division*, 97(12): 2023–2035.
- Bazargan, J. and Aghebatie, B. (2015). Numerical analysis of roll waves in chutes, *Water Science & Technology Water Supply*, 15(3): 517–524.
- Benson, D. (2013). *Introduction to Arbitrary Lagrangian–Eulerian in Finite Element Methods*, John Wiley & Sons, Inc.
- Bessaih, N. and Rezak, A. B.A. (2002). Effect of baffle block with sloping front face on the length of the jump, *Journal of Civil Engineering, The Institution of Engineers Bangladesh*, 30(2): 101-108.

REFERENCES

- Bhajantri, M.R., Eldho, T.I. and Deolalikar, P.B. (2006). Hydrodynamic modelling of Flow Over a Spillway Using a Two Dimensional Finite Volume Based Numerical Model, *Sadhana*, 31(6): 743-754.
- Bollaert, E. F. R. (2002). *Transient water pressures in joints and formation of rock scour due to high-velocity jet impact*, Ph.D. Thesis, École Polytechnique Fédérale de Lausanne, Lausanne, Switzerland.
- Bollaert, E. (2004). A comprehensive model to evaluate scour formation in plunge pools, *Hydropower and Dams* (1): 94-101.
- Bollaert, E. and Schleiss, A. (2003). Scour of rock due to the impact of plunging high velocity jets part I: a state-of-the-art review, *Journal of Hydraulic Research*, 41(5), 451–464.
- Bollaert, E. and Schleiss, A. (2005). Physically based model for evaluation of rock scour due to high velocity jet impact, *Journal of Hydraulic Engineering*, 131(3): 153–165.
- Bordbar, A., Jahromi, H., Bajestan, M. and Sedghi, H. (2010). Step effects investigation on the flow regime and cavitation in stepped morning glory spillways, *World Applied Sciences Journal*, 10(9): 1024-1031.
- Børve, S. (2011). Generalized ghost particle method for handling reflective boundaries, *6th SPHERIC International Workshop*, Hamburg, Germany.
- Bradshaw, P. (1987). Turbulent secondary flows, *Annual Review of Fluid Mechanics*, 19: 53-74.
- Brandão, L. (2015). Modelação numérica 3D de escoamentos em descarregadores de cheia, Aplicação ao descarregador de cheias complementar do aproveitamento hidroelétrico da Caniçada [3D numerical modeling of spillways flows, Application to the flood unloader complementary to the Caniçada hydroelectric plant], MSc Thesis, Faculdade de Engenharia da Universidade do Porto, Porto, Portugal, (in Portuguese).
- Brow, A., Müller, S. and Dobrotková, Z. (2011). Renewable energy markets and prospects by technology, *International Energy Agency*, Paris.
- Campomaggiore, F., Di Cristo, C., Iervolino, M. and Vacca, A. (2016). Inlet effects on roll-wave development in shallow turbulent open-channel flows, *Journal of Hydrology and Hydromechanics*, 64(1): 45–55.
- Cardoso, C., Santos, D., Almeida, I., Chambel, J., Gomes, P., and Mourão, R. (2013). A produção hidroelétrica em Portugal: Como se desenvolverá o sistema Hidroelétrico futuro em Portugal? [Hydroelectric production in Portugal: How will the future Hydroelectric system be developed in Portugal?], Projeto FEUP, Faculty of Engineering of the University of Porto, Porto, Portugal (in portuguese).
- Casey, M. and Wintergerste, T. (2000). *Quality and Trust in Industrial CFD: Best Practice Guidelines*, ERCOFTAC.
- Castillo, L. (1989). *Metodología experimental y numérica para la caracterización del campo de presiones en los dissipadores de energía hidráulica. Aplicación al vertido libre en presas bóveda [Experimental and numerical methodology for the characterization of the pressure field in hydraulic dissipators. Application to free discharge in vault dams]*, Ph.D. Thesis, Universitat Politècnica de Catalunya, Spain, (in Spanish).
- Castillo, L. and Carrillo, J. (2013). Analysis of the scale ratio in nappe flow case by means of CFD numerical simulation, *35th IAHR World Congress*, Chengdu, China.

REFERENCES

- Castillo, L., Carrillo, J. and Sordo-Ward, A. (2014). Simulation of overflow nappe impingement jets, *Journal of Hydroinformatics*, 16(4): 922-940
- Cercós-Pita, J. L. (2015). AQUAgpusph, a new free 3D SPH solver accelerated with OpenCL, *Computer Physics Communications*, 192, 295–312.
- Cha, S-H. and Whitworth, A. P. (2003). Implementations and tests of Godunov-particle hydrodynamics, *Monthly Notices of the Royal Astronomical Society*, 340: 73-90.
- Chanson, H. (1988). *Study of air entrainment and aeration devices on spillway model*, Ph.D. Thesis, University of Canterbury, Christchurch, New Zealand.
- Chanson, H. (1993). Self-aerated flows on chutes and spillways, *Journal of Hydraulic Engineering*, 119(2): 220-243.
- Chanson, H. (1994). Hydraulics of nappe flow regime above stepped chutes and spillways, *Australian Civil Engineering Transactions*, 36(1): 69-76.
- Chanson, H. (1995). *Hydraulic design of stepped cascades, channels, weirs and spillways*, Pergamon, Oxford, United Kingdom.
- Chanson, H. (1997). *Air bubble entrainment in free-surface turbulent shear flows*, Academic Press, London, United Kingdom.
- Chanson, H. (1999). *The hydraulics of open channel flow: An introduction basic principles, sediment motion, hydraulic modelling, design of hydraulic structures*, Butterworth-Heinemann, United Kingdom.
- Chanson, H. (2002). *Hydraulics of stepped chutes and spillways*, A. A. Balkema, Lisse, The Netherlands.
- Chanson, H. and Toombes, L. (1997). *Flow aeration at stepped cascades*, Research Report No. CE155, Department of Civil Engineering, University of Queensland, Australia.
- Chern, MJ. and Syamsuri, S. (2013). Effect of corrugated bed on hydraulic jump characteristic using SPH method, *Journal of Hydraulic Engineering*, 139(2): 221-232.
- Chiron, L. (2017). *Couplage et améliorations de la méthode SPH pour traiter des écoulements à multi-échelles temporelles et spatiales [Coupling and improvements of the SPH method to treat flows with temporal and spatial multiscale]*, Ph.D. Thesis, École centrale de Nantes, Nantes, France, (in French).
- Chiron, L., Oger, G., De Lefte, M. and Le Touzé, D. (2017). Analysis and improvements of Adaptive Particle Refinement (APR) through CPU time, accuracy and robustness considerations, *Journal of Computational Physics*, 354: 552-575.
- Chow, V. T. (1959). *Open-channel hydraulics*, McGraw-Hill, New York, USA.
- Cleary, P., Prakash, M., Ha, J., Stokes, N. and Scott, C. (2007). Smooth Particle Hydrodynamics: status and future potential, *Progress in Computational Fluid Dynamics, an International Journal*, 7(2-4): 70-90.
- Cola, R. (1966). Diffusione di un getto piano verticale in un bacino d'acqua d'altezza limitata [Diffusion of a vertical plane jet in a water basin of limited height], *L'Energia Elettrica*, 43(11): 649-664 (in Italian).

REFERENCES

- Colagrossi, A. and Landrini, M. (2003). Numerical simulation of interfacial flows by smoothed particle hydrodynamics, *Journal of Computational Physics*, 191: 448–475.
- Cornish, V. (1934). *Ocean Waves and Kindred Geophysical Phenomena*, Cambridge University Press, London, United Kingdom.
- Costa, A. S. (2016). A Eletricidade Renovável –Desafios futuros e o papel da energia hídrica [Renewable Electricity - Future challenges and the role of hydropower], APREN, *HYDRO'storming – Series of lectures*, Faculty of Engineering of the University of Porto (in Portuguese).
- Couto, L. T., Melo, J. F., Muralha, A. (2013). *Barragem de Caniçada. Descarregador de cheias complementar. Estudo em modelo hidráulico reduzido. Definição das formas alternativas da plataforma de aproximação e estrutura de entrada [Caniçada Dam. Complementary spillway. Study in reduced physical model. Definition of alternative forms of approach platform and inlet structure]*, LNEC, Lisboa, Portugal (in Portuguese).
- Couto, L. T., Muralha, A., Alvarez, T., Sardinha, R., Oliveira, M. and Dias da Silva, J. (2014). Descarregador complementar da barragem de caniçada: projeto e ensaios hidráulicos em modelo reduzido [Complementary spillway of the Caniçada dam: design and hydraulic tests in a reduced model], *12º Congresso da Água / 16º ENASB / XVI SILUBESA*, Lisboa, Portugal.
- Creager, W. P. (1917). *Engineering of masonry dams*, John Wiley & Sons, New York, USA.
- Crespo, A., (2008). *Application of the Smoothed Particle Hydrodynamics model SPHysics to free-surface hydrodynamics*, Ph.D. Thesis, Universidade de Vigo, Ourense, Spain.
- Crespo, A., Gómez-Gesteira, M. and Dalrymple, R. (2007). 3D SPH simulation of large waves mitigation with a dike, *Journal of Hydraulic Research*, 45(5): 631-642.
- Crespo, A., Gómez-Gesteira, M. and Dalrymple, R. (2008). Modelling dam break behavior over a wet bed by a SPH technique, *Journal of Waterway, Port, Coastal and Ocean Engineering*, 134(6): 313-320.
- Crespo, A., Domínguez, J., Rogers, B., Gómez-Gesteira, M., Longshaw, S., Canelas, R. and García-Feal, O. (2015). DualSPHysics: Open-source parallel CFD solver on Smoothed Particle Hydrodynamics (SPH), *Computer Physics Communications*, 187: 204–216.
- Cummins, S. and Rudman, M. (1999). An SPH projection method, *Journal of Computational Physics*, 152(2): 584–607.
- Dalrymple, R. and Knio, O. (2001). SPH modelling of water waves, *4th Conference on Coastal Dynamics*, Lund, Sweden.
- Dalrymple, R. and Rogers, B. (2006). Numerical modeling of water waves with the SPH method, *Coastal Engineering*, 53(2–3): 141–147.
- De Leffe, M., Le Touzé, D. and Alessandrini, B. (2009). Normal flux method at the boundary for SPH, *4th SPHERIC International Workshop*, Nantes, France.
- De Padova, D., Mossa, M., Sibilla, S. and Torti, E. (2013). 3D SPH modelling of hydraulic jump in a very large channel, *Journal of Hydraulic Research*, 51(2): 158–173.
- Dehnen, W. and Aly, H. (2012). Improving convergence in smoothed particle hydrodynamics simulations without pairing instability, *Monthly Notices of the Royal Astronomical Society*, 425(2): 1068-1082.

REFERENCES

- Deng, J., Xu, W. L. Qu, J. X. and Dong, J. W. (2002). Measurement and calculation of air concentration distribution of self-aerated flow in spillway tunnel, *Journal of Hydraulic Engineering*, 4(1): 64-68 (in Chinese).
- Deng J., Xu, W. L. Qu, J. X., Yang Z., and Yang, Y. (2003). The influence of aeration on average velocity of self-aerated chute flow, *Journal Hydraulic Eng.* 83(1): 88-94 (in Chinese).
- DNV GL. (2015). *The hydropower sector's contribution to a sustainable and prosperous Europe*, Main Report, DNV GL – Energy, June 2015.
- Domínguez, J. (2014). *DualSPHysics: Towards High Performance Computing using SPH technique*, Ph.D. Thesis, Universidade de Vigo, Ourense, Spain.
- Domínguez, J., Crespo, A., Gómez-Gesteira, M. and Marongiu, J. (2011). Neighbour lists in smoothed particle hydrodynamics, *International Journal for Numerical Methods in Fluids*, 67(12): 2026-2042.
- Dong, Z. and Su, P. (2006). Cavitation control by aeration and its compressible characteristics, *Journal of Hydrodynamics*, 18(4): 499-504.
- Duarte, R., Schleiss, A. and Pinheiro, A. (2014). Discussion on “CFD analysis of the effect of nozzle stand-off distance on turbulent impinging jets”, *Canadian Journal of Civil Engineering*, 41: 270-271.
- Duarte, R., Schleiss, A. and Pinheiro, A. (2015). Influence of jet aeration on pressures around a block embedded in a plunge pool bottom, *Environmental Fluid Mechanics*, 15(3): 673–93.
- Džebo, E., Žagar, D., Krzyk, M., Četina, M. and Petkovšek, G. (2014). Different ways of defining wall shear in smoothed particle hydrodynamics simulations of a dam-break wave, *Journal of Hydraulic Research*, 52(4): 453-464.
- Ellis, J. and Pender, G. (1982). Chute spillway design calculations, *Proceedings of the Institution of Civil Engineers*, 73(2): 299–312.
- Eloubaidy, A. and Al-Baidhani, J. (1999). Dissipations of hydraulic energy by curved baffle blocks, *Pertanika Journal of Science and Technology*, 7(1): 69-77.
- Ervine, D. and Falvey, H. (1987). Behaviour of turbulent water jets in the atmosphere and in plunge pools, *Proceedings of the Institution of Civil Engineers*, 83: 295–314.
- Ervine, D. and Oliver, G. (1980). The full scale behavior of air regulated siphon spillways, *Proceedings of the Institution of Civil Engineers*, 69: 687-706.
- Ervine, D., Falvey, H. and Withers, W. (1997). Pressure fluctuations on plunge pool floors, *Journal of Hydraulic Research*, 35(2): 257–279.
- Environment Agency. (2008). *Post-incident reporting for UK dams*, Annual Report. www.publications.environment-agency.gov.uk.
- Falvey, H. (1990). *Cavitation in chutes and spillways*, Engineering monograph, 42, USBR, Denver.
- Federspiel, M. (2011). *Response of an embedded block impacted by high-velocity jets*, Ph.D. Thesis No. 5160, École Polytechnique Fédérale de Lausanne, Switzerland.
- Felder, S. and Chanson, H. (2016). Simple design criterion for residual energy on embankment dam stepped spillways, *Journal of Hydraulic Engineering*, 142(4): 04015062.
- Feldman, J. and Bonet, J. (2007). Dynamic refinement and boundary contact forces in SPH with applications in fluid flow problems, *International Journal for Numerical Methods in Engineering*, 72(3): 295–324.

REFERENCES

- FEMA (2010). *Outlet works energy dissipators*, Technical Manual, available from <https://damsafety.org/content/technical-manual-outlet-works-energy-dissipators-fema-p-679>.
- Ferrand, M., Laurence, D., Rogers, B., Violeau, D. and Kassiotis, C. (2013). Unified semi-analytical wall boundary conditions for inviscid, laminar or turbulent flows in the meshless SPH method, *International Journal for Numerical Methods in Fluids*, 71(4): 446–472.
- Ferrand, M., Joly, A., Kassiotis, C., Violeau, D., Leroy, A., Morel, F. and Rogers, B. (2017). Unsteady open boundaries for SPH using semi-analytical conditions and Riemann solver in 2D, *Computer Physics Communications*, 210: 29-44.
- Ferrari, A. (2010) SPH simulation of free surface flow over a sharp-crested weir, *Advances in Water Resources*, 33: 270-276.
- Ferrari, A., Dumbser, M., Toro, E. and Armanini, A. (2009). A new 3D parallel SPH scheme for free surface flows, *Computers and Fluids*, 38(6): 1203–1217.
- Foster, M., Fell, R. and Spannagle, M. (2000). The statistics of embankment dam failures and accidents, *Canadian Geotechnical Journal*, 37(5), 1000-024.
- Fonty, T., Leroy, A., Violeau, D., Joly, A., Asiain, J. and Guyot, G. (2017). Numerical Modelling of the Undersluices of the Rance Tidal Power Station with SPH, *12th SPHERIC International Workshop*, Ourense, Spain.
- Fonty, T., Leroy, A., Joly, A., Violeau, D. and Ferrand M. (2018). An upwind scheme for conservative, realizable two-phase mixture SPH model with high density ratios, *13th SPHERIC International Workshop*, Galway, Ireland.
- Fonty, T., Ferrand, M., Leroy, A., Joly A. and Violeau, D. (2019). Mixture model for two-phase flows with high density ratios: A conservative and realizable SPH formulation, *International Journal of Multiphase Flow*, 111: 158-174.
- Fourtakas, G. (2014). *Modelling multi-phase flows in nuclear decommissioning using SPH*, Ph.D. Thesis, University of Manchester, United Kingdom.
- Fourtakas, G. and Rogers, B. (2016). Modelling multi-phase liquid-sediment scour and resuspension induced by rapid flows using Smoothed Particle Hydrodynamics (SPH) accelerated with a Graphics Processing Unit (GPU), *Advances in Water Resources*, 92: 186-199.
- Ghadampour, Z., Hashemi, M., Talebbeydokhti, N. and Neill, S. (2015). Some numerical aspects of modelling flow around hydraulic structures using incompressible SPH, *Computers and Mathematics with Applications*, 69: 1470-1483.
- Ghaïtanellis, A. (2017). *Modélisation du charriage sédimentaire par une approche granulaire avec SPH*, Ph.D. Thesis. Université Paris-Est, Paris, France.
- Gharangik, A. and Chaudhry, M. (1991). Numerical simulation of hydraulic jump, *Journal of Hydraulic Engineering*, 117(9): 1195–1211.
- Gingold, R. and Monaghan, J. (1977). Smoothed Particle Hydrodynamics: theory and application to non-spherical stars, *Monthly Notices of the Royal Astronomical Society*, 181: 375-389.
- Giralt, F., Chia, C. and Trass, O. (1977). Characterization of impingement region in an axisymmetric turbulent jet, *Industrial and Engineering Chemistry Fundamentals*, 16: 21-28.
- Giridhar, M., Madavi, M., Anirudh, R. and Goud, E. (2014). Analysis of Pressures on Nagarjuna Sagar Spillway, *EC Agriculture*, 1(1): 17-28.

REFERENCES

- Goffin, L., Ercicum, S., Dewals, B. J., Piroton, M. and Archambeau, P. (2014). Validation of a SPH model for free surface flows, *Simhydro*, Nice, France.
- Gómez, D., Colmenarejo, R., Moncalvillo, M. and Cillán, J. (2012). SPH methods applied to hydraulic structures. Friction boundary condition, *4th IAHR International Symposium on Hydraulic Structures*, Porto, Portugal.
- Gómez-Gesteira, M., Cerqueiro, D. Crespo, A. and Dalrymple, R. (2005). Green water overtopping analysed with an SPH model, *Ocean Engineering.*, 32(2): 223-238.
- Gómez-Gesteira, M., Rogers, B., Dalrymple, R., and Crespo, A. (2010). State-of-the-art of classical SPH for free-surface flows, *Journal of Hydraulic Research*, 48(Extra issue): 6–27.
- Gonzalez, C. and Chanson, H. (2007). Hydraulic design of stepped spillways and downstream energy dissipators for embankment dams, *Dam Engineering*, 17(4):223–244.
- Gosh, S. N. (1999). *Flood control and drainage Engineering*, A. A. Balkerma Publishers, Taylor & Francis Group, London, United Kingdom.
- GPUSPH Installation Guide, version 4.0, October 2016, available from <http://www.gpusph.org/documentation/install-guide/>.
- GPUSPH Theory Guide, version 4.0, October 2016, available from <http://www.gpusph.org/documentation/user-guide/>.
- GPUSPH User Guide, version 4.0, October 2016, available from <http://www.gpusph.org/documentation/theory-guide/>.
- Grassa, J. M. (2004). El método SPH. Aplicaciones en Ingeniería marítima, *Revista de Ingeniería Civil*, 133 (in Spanish).
- Grenier, N., Antuono, M., Colagrossi, A., Le Touzé, D. and Alessandrini, B. (2009). An Hamiltonian interface SPH formulation for multi-fluid and free surface flows, *Journal Computational Physics*, 228: 8380–8393.
- Gu, S., Ren, L., Wang, X., Xie, H., Huang, Y., Wei, J. and Shao, S. (2017). SPHysics Simulation of experimental spillway hydraulics, *Water*, 9(12): 973.
- Guyot, G., Pfister, M., Matas, J. P. and Cartellier, A. (2016). Experimental study of large scale plunging jets, *6th International Symposium on Hydraulic Structures*, Portland, USA.
- Gutmark, G., Wolfshtein, M. and Wygnanski, I. (1978). The plane turbulent impinging jet, *Journal of Fluid Mechanics*, 88(4), 737-756.
- Habibzadeh, A., Wu, S., Ade, F., Rajaratnam, N. and Loewen, M. R. (2011). Exploratory study of submerged hydraulic jumps with blocks, *Journal of Hydraulic Engineering*, 137(6): 706–710.
- Habibzadeh, A., Loewen, M. and Rajaratnam, N. (2012). Performance of baffle blocks in submerged hydraulic jumps, *Journal of Hydraulic Engineering*, 138(10): 902-908.
- Hager, W. (1989). Supercritical flow in channel junctions, *Journal of Hydraulic Engineering*, 115(5): 595–616.
- Hager, W. (1991). Uniform aerated chute flow, *Journal of Hydraulic Engineering*, 118(6): 528-533.
- Hager, W. (1996). Performance of a counter-current type stilling basin, *Hydropower and Dams*, (4): 78-84.

REFERENCES

- Hager, W., Schwalt, M., Jimenez, O. and Chaudhry, M. (1994). Supercritical flow near an abrupt wall deflection, *Journal of Hydraulic Research*, 32(1): 103–118.
- Hayashi, M., Gotoh, H., Sakai, T. and Ikari, H. (2003). Lagrangian gridless model of toe scouring of seawall due to tsunami return flow, *Asian and Pacific Coast*, Makuhari, Japan.
- Harada T., Koshizuka S. and Kawaguchi Y. (2007). Smoothed Particle Hydrodynamics on GPUs, *Computer Graphics International*, Rio de Janeiro, Brazil.
- Hartung, F. and Häusler, E. (1973). Scours, stilling basins and downstream protection under free overfall jets at dams, *11th Congress on Large Dams*, Madrid, Spain.
- Head, C. R. (1975). Low-head air-regulated siphons, *Journal of the Hydraulics Division*, 101(3): 329-345.
- Hepler, T. (2013). *Spillway design issues*, Presentation at National Dam Safety Program – Technical Seminar No. 20 “overtopping of Dams”, National Emergency Training Center.
- Heller, V., Hager, W. and Minor, H. (2005). Ski jump hydraulics, *Journal of Hydraulic Engineering*, 131(5): 347–355.
- Hérault, A., Bilotta, G. and Dalrymple, R. (2010). SPH on GPU with CUDA, *Journal of Hydraulic Research*, 48(Extra Issue): 74–79.
- Herbich, J. and Walsh, P. (1972). Supercritical flow in rectangular expansions, *Journal of Hydraulic Division*, 98(9): 1691–1700.
- Ho, D., Boyes, K. and Donohoo, S. (2001). Investigation of spillway behaviour under increased maximum flood by computational fluid dynamics technique, *14th Australasian Fluid Mechanics Conference*, Adelaide, Australia.
- Howard, T.R. (1982) Statistical analysis of embankment dam failure, *19th Annual Engineering Geology and Soils Engineering Symposium*, Pocatello, USA.
- Hu, X. and Adams, N. (2006). A multi-phase SPH method for macroscopic and mesoscopic flows, *Journal of Computational Physics*, 213: 844–861.
- Hunt, S. (2008). *Design of converging stepped spillways*, Ph.D. Thesis, Colorado State University, USA.
- Hunt, S., Kadavy, K., Abt, S. and Temple, D. (2008). Impact of converging chute walls for roller compacted concrete stepped spillways, *Journal of Hydraulic Engineering*, 134(7): 1000–1003.
- Hussain, S. (2016). Open boundary condition for a numerical SPH method to characterize the flow in open channels, *1st International Conference on Engineering and Innovative Technology*, Kurdistan, Iraq.
- ICOLD. (1995). *Dam failures statistical analysis*, International Commission on Large Dams (ICOLD), Bulletin 99.
- ICOLD (1984). *Lessons from dam incidents*, ICOLD, Paris.
- Inutsuka, S. I. (2002). Reformulation of smoothed particle hydrodynamics with Riemann solver, *Journal of Computational Physics*, 179(1): 238-267.
- IPCC. (2011). *Renewable Energy Sources and Climate Change Mitigation*, Special Report, Working Group III-Mitigation of Climate Change, Intergovernmental Panel on Climate Change (IPCC).

REFERENCES

- Dolf, G. (2012). Renewable energy technologies: cost analysis series, Bonn: The International Renewable Energy Agency 11-50.
- IRENA. (2018). *Renewable capacity statistics 2018*, International Renewable Energy Agency (IRENA), Abu Dhabi.
- Ippen, A. and Dawson, J. (1951). High-Velocity Flow in Open Channels: A Symposium: Design of Channel Contractions, *Transactions of the American Society of Civil Engineers*, 116(1): 326–346.
- Ippen, A. and Harleman, D. (1956). Verification of theory for oblique standing waves, *Transactions of the American Society of Civil Engineers*, 121(1): 678–694.
- Issa, R. (2004). *Numerical assessment of the Smoothed Particle Hydrodynamics gridless method for incompressible flows and its extension to turbulent flows*, Ph.D. Thesis, University of Manchester, United Kingdom.
- Issa, R., Lee, E.-S., Violeau, D. and Laurence, D. (2005). Incompressible separated flows simulations with the Smoothed Particle Hydrodynamics gridless methods, *International Journal for Numerical Methods in Fluids*, 47:1101-1106.
- Issa, R., Violeau, D., Lee, E.-S. and Flament, H. (2010). *Modelling nonlinear water waves with RANS and LES SPH models*, Advances in Numerical Simulation of Nonlinear Water Waves, World Scientific Publishing Co Pte Ltd
- Yakhot, V. and Orszag, S. (1986). Renormalization group analysis of turbulence, *Journal of Scientific Computing*, 1(1): 3-51.
- Yin, Z. Jia, Q. Li, Y. Wang, Y. and Yang, D. (2018). Computational study of a vertical plunging jet into still water, *Water*, 10(8): 989.
- Janosi, I., Jan, D., Szabo, K. and Tel, T. (2004). Turbulent drag reduction in dam-break flows, *Experiments in Fluids*, 37: 219–229.
- Jansen, B. (1988). *Advanced dam engineering*, Van Nostrand Reinhold, New York.
- Jian, W., Liang, D. and Shao, S. (2015). SPH study of the evolution of water-water interfaces in dam break flows, *Natural Hazards*, 78: 531-553.
- Johnson, M. and Savage, B. (2006). Physical and Numerical Comparison of Flow over Ogee Spillway in the Presence of Tailwater, *Journal of Hydraulic Engineering*, 132(1): 1353-1357.
- Jonsson, P., Jonsén, P., Andreasson, P., Lundström, T. and Hellström, J. (2015). Modelling dam break evolution over a wet bed with Smoothed Particle Hydrodynamics: a parameter study, *Engineering*, 7(5): 248-260.
- Jordaan, J. M. and Bell, A. (2009). *Hydraulic structures, equipment and water data acquisition systems*, Vol. 1, Eolss Pub. Co. Ltd., Oxford, United Kingdom.
- Juon, R. and Hager, W. H. (2000). Flip bucket without and with deflectors, *Journal of Hydraulic Engineering*, 126(11): 837–845.
- Kassiotis, C., Ferrand, M. and Violeau, D. (2013). Semi-analytical conditions for open boundaries in SPH, *8th SPHERIC International Workshop*, Trondheim, Norway.
- Kerman-Nejad, J., Fathi-Moghadam, M., Lashkarara, B. and Haghighipour, S. (2011). Dynamic pressure on flip bucket jets, *World Applied Sciences Journal*, 12(9): 1448-1454.

REFERENCES

- Kim, S., Lee, H. and An, S. (2010). Improvement of hydraulic stability for spillway using CFD model, *International Journal of the Physical Sciences*, 5(6): 774-780.
- Khatsuria, R. (2005). *Hydraulics of spillways and energy dissipators*, Dekker, New York, USA.
- Kleefsman, K., Fekken, G., Veldman, A., Iwanowski, B. and Buchner, B. (2005). A Volume-of-Fluid based simulation method for wave impact problems, *Journal of Computational Physics*, 206: 363–393.
- Kobus, H. (1985). *An introduction to air-water flows*, Instituts. für Wasserbau, Germany.
- Koschitzky, H.-P. (1987). *Dimensionierungskonzept für Sohlbelüfter in Schussrinnen zur Vermeidung von Kavitationsschäden [Design concept for chute aerators to avoid cavitation damage]*, Ph.D. Thesis, Institut für Wasserbau, Universität Stuttgart, Germany, (in German).
- Koskinas, A., Aristoteles T., Penelope, T., Panayiotis, D. Theano, I., Panos, P., Demetris, K. and Tracey Williamson. (2019). Insights into the Oroville Dam 2017 Spillway Incident, *Geosciences*, 9(37)
- Kramer, K. (2004). *Development of aerated chute flow*, Ph.D. Thesis, Eidgenössische Technische Hochschule Zürich, Germany.
- Kumcu, S. (2016). Investigation of flow over spillway modeling and comparison between experimental data and CFD analysis, *KSCE Journal of Civil Engineering*, 21: 994–1003
- Kulasegaram, S., Bonet, J., Lewis, R. W. and Profit, M. (2004). A variational formulation based contact algorithm for rigid boundaries in two-dimensional SPH applications, *Computational Mechanics*, 33: 316-325.
- Kwon, J., Monaghan, J. (2015). Sedimentation in homogeneous and inhomogeneous fluids using SPH, *International Journal of Multiphase Flow*, 72: 155–164.
- Landrini, M., Colagrossi, A., Greco, M. and Tulin, M. P. (2007). Gridless simulations of splashing process and near-shore bore propagation, *Journal Fluid Mechanics*, 591: 183-213.
- Lastiwka, M., Basa, M. and Quinlan, N. (2009). Permeable and Non-reflecting Boundary Conditions in SPH, *International Journal for Numerical Methods in Fluids*, 61(7):709 – 724.
- Launder, B. and Spalding, D. (1972). *Mathematical models of turbulence*. London: Academic Press.
- Lee, E.-S., Moulinec, C., Xu, R., Violeau, D., Laurence, D. and Stansby, P. (2008). Comparisons of weakly compressible and truly incompressible SPH algorithms for 2D flows, *Journal of Computational Physics*, 227(18): 8417–8436.
- Lee E-S, Violeau D, Issa R, Ploix, S. and Marc, R. (2009). Simulating a Real Dam Spillway Flow with 3-D SPH, *4th International SPHERIC Workshop*, Nantes, France.
- Lee E-S, Violeau D, Issa R and Ploix, S. (2010). Application of weakly compressible and truly incompressible SPH to 3-D water collapse in waterworks, *Journal of Hydraulic Research*, 48(Extra Issue): 50–60.
- Leroy, A. (2014). *A New Incompressible SPH model: Towards industrial applications*, Ph.D. Thesis. Université Paris-Est, France.
- Leroy, A., Violeau, D., Ferrand, M. and Kassiotis, C. (2014). Unified semi-analytical wall boundary conditions applied to 2-D incompressible SPH, *Journal of Computational Physics*, 261: 106–129.

REFERENCES

- Lind, S., Stansby, P. and Rogers, B. (2016). Incompressible-compressible flows with a transient discontinuous interface using smoothed particle hydrodynamics (SPH), *Journal of Computational Physics*, 309: 129-147.
- Lind, S., Xu, R. Stansby, P. and Rogers, B. (2012). Incompressible smoothed particle hydrodynamics for free-surface flows: A generalised diffusion-based algorithm for stability and validations for impulsive flows and propagating waves, *Journal of Computational Physics*, 231(4): 1499-1523.
- Liu, G. and Liu, M. (2003). *Smoothed particle hydrodynamics. A meshfree particle method*, Singapore: World Scientific Publishing Co Pte Ltd.
- Liu, M. and Liu, G. (2010). Smoothed Particle Hydrodynamics (SPH): an overview and recent developments, *Archives of Computational Methods in Engineering*, 17: 25-76.
- LNEC (1972). *Estudo Hidráulico em modelo reduzido do aproveitamento de Crestuma [Hydraulic study in a reduced model of the Crestuma dam]*, 1º Relatório, Maio 1972, (in Portuguese).
- LNEC. (1985). *Barragem de Crestuma – Estudo hidráulico em modelo reduzido – operação das comportas [Crestuma Dam - Hydraulic study in reduced model - operation of the gates]*, Relatório 230/85 – NHE, julho de 1985, (in Portuguese).
- Lodomez, M., (2014). *Determining the characteristics of a free jet in 2-D by the SPH model*, MSc Thesis, University of Liège, Belgium.
- Lodomez, M., Erpicum, S., Dewals, B., Piroton, M. and Archambeau, P. (2014). Comparison between Experimental and SPH Models over a Sharp-crested Weir, *5th IAHR International Junior Researcher*, Spa, Belgium.
- Lopes, A.I. (2005). *Dissipação de energia em estruturas hidráulicas assentes sobre fundos móveis [Energy dissipation in hydraulic structures based on movable bottoms]*, MSc Thesis, Faculdade de Engenharia da Universidade do Porto, Portugal, (in Portuguese).
- Lopes, A., Proença, M. and Maia, R. (2006). Energy dissipation downstream of dams established in alluvial beds, *River flow*, Lisbon, Portugal.
- Lopes, P., Tabor, G., Carvalho, R. and Leandro, J. (2016). Explicit calculation of natural aeration using a Volume-of-Fluid model, *Applied Mathematical Modelling*, 40: 7504–7515.
- López, D. (2013). Aplicación del método numérico SPH 3D en el diseño de aliviaderos de presas [Application of the SPH 3D numerical method in the design of dam spillways], *Jornada Técnica Avances en investigación aplicada en seguridad hidráulica de presas*, Madrid, Spain (in spanish).
- López, D., Diaz, R., Rebollo J. and Cuellar, V. (2015). SPH application in the design of hydraulic structures, *Hidrolink*, 3: 76-77.
- López, D., Diaz, R., Rebollo J. Ramos, T., Andrés, F. and Berga, M. (2016). Aplicación del método SPH al estudio hidráulico de estructuras. Análisis hidrodinámico del aliviadero en pozo de la presa de Nagore (Navarra) [Application of the SPH method to the hydraulic study of structures. Hydrodynamic analysis of the shaft spillway in the Nagore dam (Navarra)], *Ribagua – Revista Iberoamericana del Agua*, 3: 1–7 (in Spanish).
- López D., Marivela R. and Aranda F. (2010a). Análisis hidrodinámico de estructuras hidráulicas con modelos SPH. Estudio del cuenco de amortiguamiento de la presa de Villar del Rey [Hydrodynamic analysis of hydraulic structures with SPH models. Study of the dissipation basin of the Villar del Rey dam], *Comunicaciones de las IX Jornadas Españolas de Presas*, Valladolid, Spain, (in Spanish).

REFERENCES

- López, D., Marivela, R. and Garrote, L. (2010b). Smoothed particle hydrodynamics model applied to hydraulic structures: a hydraulic jump test case, *Journal of Hydraulic Research*, 48(Extra Issue): 142-158.
- Lucy, L. (1977). Numerical approach to testing the fission hypothesis, *Astronomical Journal*, 82: 1013-1024.
- May, R. and Deamer, A. (1989). *Performance of aerators for dam spillways*, Hydraulics Research Wallingford, Report SR 198, United Kingdom.
- May, R. and Willoughby, I. (1991). *Impact pressures in plunge basins due to vertical falling jets*, Hydraulics Research Wallingford, Report SR 242, United Kingdom.
- Manenti, S. (2018). Standard WCSPH for Free-Surface Multi-Phase Flows with a Large Density Ratio, *International Journal of Ocean and Coastal Engineering*, 1(2).
- Manenti, S., Amicarelli, A. and Todeschini, S. (2018). WCSPH with limiting viscosity for modeling landslide hazard at the slopes of artificial reservoir, *Water*, 10(4): 515.
- Manso, P., Fiorotto, V., Bollaert, E. and Schleiss, A. (2004). Discussion of “Effect of Jet Air Content on Plunge Pool Scour” by Stefano Canepa and Willi H. Hager, *Journal of Hydraulic Engineering*, 130 (11).
- Manso, P. A. (2006). *The influence of pool geometry and induced flow patterns on rock scour by high-velocity plunging jets*, Ph.D. Thesis, École Polytechnique Fédérale de Lausanne, Switzerland.
- Manso, P., Bollaert, E. and Schleiss, A. (2007). Impact pressures of turbulent high-velocity jets plunging in pools with flat bottom, *Experiments in Fluids*, 42: 49–60.
- Manso, P., Bollaert, E. and Schleiss, A. (2008). Evaluation of high-velocity plunging jet-issuing characteristics as a basis for plunge pool analysis, *Journal of Hydraulic Research*, 46(2): 147–157.
- Manso, P. A., Bollaert, E. and Schleiss, A. (2009). Influence of plunge pool geometry on high-velocity jet impact pressures and pressure propagation inside fissured rock media, *Journal of Hydraulic Engineering*, 135(10): 783-792.
- Marrone, S., Colagrossi, A., Le Touzé, D. and Graziani, G. (2010). Fast free-surface detection and level-set function definition in SPH solvers, *Journal of Computational Physics*, 229(10): 3652–3663.
- Marongiu, J. C., Leboeuf, F. and Parkinson, E. (2007). Numerical simulation of the flow in a Pelton turbine using the meshless method smoothed particle hydrodynamics: a new simple solid boundary treatment, *Proceedings of the Institution of Mechanical Engineering - Part A, Journal of Power and Energy*, 221(6): 849–856.
- Martins, R. (1977). *Cinématica do jacto livre no âmbito das estruturas hidráulicas [Kinematics of the free jet in the field of hydraulic structures]*, LNEC, Lisbon, Portugal (in Portuguese).
- Mayrhofer, A., Ferrand, M., Kassiotis, C., Violeau, D. and Morel, F. (2014). Unified semi-analytical wall boundary conditions in SPH: analytical extension to 3D, *Numerical Algorithms*, 68(1):15-34.
- Mayrhofer, A., Laurence, D., Rogers, B. and Violeau, D. (2015). DNS and LES of 3-D wall bounded turbulence using Smoothed Particle Hydrodynamics, *Computers and Fluids*, 115:86-97.
- Mayrhofer, A., Rogers, B. D., Violeau, D. and Ferrand, M. (2013). Investigation of wall bounded flows using SPH and the unified semi-analytical wall boundary conditions, *Computer Physics Communications*, 184: 2515–2527.

REFERENCES

- Maruzewski, P., Oger, G., Le Touzé, D. and Biddiscombe, J. (2008). High performance computing 3D SPH model: Sphere impacting the free surface of water, *3rd International SPHERIC Workshop*, Lausanne, Switzerland.
- Mascio, A., Antuono, M. Colagrossi, A. and Marrone, S. (2017). Smoothed particle hydrodynamics method from a large eddy simulation perspective, *Physics of Fluids*, 29(3): 035102.
- Meireles, I. and Matos, J. (2009). Skimming flow in the non-aerated region of stepped spillways over embankment dams, *Journal of Hydraulic Engineering*, 135(8): 685-689.
- Mendes, V. (2017). *Os aproveitamentos hidroelétricos da EDP em Portugal, A Hidroeletricidade em Portugal – Perspetivas Futuras [The hydroelectric hdropower plants of EDP in Portugal, Hydropower in Portugal - Future Prospects]*, Instituto Superior Técnico, Lisboa, Portugal.
- Melo, J. (2001). *Acções hidrodinâmicas em soleiras de bacias de dissipação de energia por jactos [Hydrodynamic loads acting on floor slabs of energy dissipation basins by plunging jets]*, Ph.D. Thesis, Instituto Superior Técnico, Portugal (in Portuguese).
- Melo, J., Pinheiro, A. N. and Ramos, C. M. (2006). Forces on plunge pool slabs: influence of joints location and width, *Journal of Hydraulic Engineering*, 132(1): 49–60.
- Molteni, D., Colagrossi, A. and Colicchio, G. (2007). On the use of an alternative water state equation for SPH, *2nd International SPHERIC Workshop*, Madrid, Spain.
- Molteni, D. and Colagrossi, A. (2009). A simple procedure to improve the pressure evaluation in hydrodynamic context using the SPH, *Computer Physics Communications*, 180(6): 861–872.
- Monaghan, J. (1982). Why particle methods work (hydrodynamics), *SIAM Journal on Scientific and Statistical Computing*, 3: 422-433.
- Monaghan, J. (1992). Smoothed particle hydrodynamics, *Annual Revue on Astronomy and Astrophysics*, 30: 543–574.
- Monaghan, J. (1994). Simulating free surface flows with SPH, *Journal of Computational Physics*, 110: 399–406.
- Monaghan, J. (2002). SPH compressible turbulence, *Monthly Notices of the Royal Astronomical Society*, 335(3), 843–852.
- Monaghan, J. (2005). Smoothed particle hydrodynamics, *Reports on Progress in Physics*, 68: 1703–1759.
- Monaghan, J. and Ashkan, R. (2013). A simple SPH algorithm for multi-fluid flow with high density ratios, *International Journal for Numerical Methods in Fluids*, 71: 537–561.
- Monaghan, J. and Kos, A. (1999). Solitary waves on a Cretan beach, *Journal of Waterway, Port, Coastal, and Ocean Engineering*, 125(3): 145–154.
- Monaghan, J. J. and Rafiee, A. (2013). A simple SPH algorithm for multi-fluid flow with high density ratios, *Int. J. Numer. Methods Fluids*, 71(5): 537–561.
- Moreira, A., A. Leroy, D. Violeau, and F. Taveira-Pinto. (2018). Simulating spillway flows with the SPH method, *13th International SPHERIC Workshop*, Galway, Ireland
- Moreira, A., Leroy, A., Violeau, D. and Taveira-Pinto, F. (2019a). Dam spillways and the SPH method: two case studies in Portugal, *Journal of Applied Water Engineering and Research*, 7(3).

REFERENCES

- Moreira, A., Leroy, A., Violeau, D. and Taveira-Pinto, F. (2020). Overview of large-scale Smoothed Particle Hydrodynamics modelling of dam hydraulics, *Journal of Hydraulic Engineering*, 146(2).
- Moreira, A., Manso, P., D. Violeau, and F. Taveira-Pinto. (2019b). SPH simulation of vertical high-speed jet flow from a circular nozzle with stagnation pressures prediction, *14th International SPHERIC Workshop*, Exeter, United Kingdom.
- Moreira, A., Manso, P., D. Violeau, and F. Taveira-Pinto. (2021). Single-phase SPH modelling of plunge pool dynamic pressures at a near-prototype scale, *Journal of Hydraulic Research*, in press: accepted in 9 November 2020.
- Moreira, A. and F. Taveira-Pinto. (2017a). Numerical modelling of hydraulic jumps. The Crestuma dam study case, *2nd Doctoral Congress in Engineering*, Porto, Portugal.
- Moreira, A. and Taveira-Pinto, F. (2017b). Modelação numérica do escoamento no descarregador de cheias da barragem da Caniçada [Numerical modelling of the flow in the Caniçada dam spillway], *11^{as} Jornadas de Hidráulica, Recursos Hídricos e Ambiente*, Porto, Portugal (in Portuguese).
- Morris, J., Fox, P. and Zhu, Y. (1997). Modelling low Reynolds number incompressible flows using SPH, *Journal of Computational Physics*, 136: 214-226.
- Nakayama, A., Leong, L. and Kong, W. (2016). Simulation of turbulent free surface flow with two phase SPH method, *Journal of Japan Society of Civil Engineers*, 72(4): 523-528.
- Narayanaswamy, M. (2009). A hybrid Boussinesq-SPH wave propagation model with applications to forced waves in rectangular tanks, Ph.D. Thesis, The Johns Hopkins University, USA.
- Nie, M. (2001). Cavitation prevention with roughened surface, *Journal of Hydraulic Engineering*, 127(10): 878-880.
- Nigam, U., Das, S. and Choudhury, M. R. (2015). Overview of energy dissipators and stilling basins with design aspects of hydraulic jump type energy dissipators, *3rd National Conference on Innovative and Emerging Technologies*, Dabhi, India.
- Nóbrega, J., Matos, J., Schulz, H. and Canelas, R. (2020). Smooth and Stepped Spillway Modelling Using the SPH Method, *Journal of Hydraulic Engineering*, 146: 8.
- Nomeritae, N., Daly, E. Grimaldi, S. and Bui, H. (2016). Explicit incompressible SPH algorithm for free-surface flow modelling: a comparison with weakly compressible schemes, *Advances in Water Resources*, 97: 156-167.
- Novak, P., Moffat, A., Nalluri, C. and Narayanan, R. (2006). *Hydraulic structures*, CRC Press, Taylor & Francis Group, London, United Kingdom.
- Olsson, E., Kreiss, G. and Zahedi, S. (2007). A conservative level set method for two phase flow II, *Journal of Computational Physics*, 225(1): 785–807.
- Oñate, E. and Owen, R. (2011). *Particle-based methods: fundamentals and applications*, Springer The Netherlands.
- Omidvarinia, M. and Jahromi, S. H. (2013). Effect of wedge shape deflector on dissipating energy in triangular flip buckets, *Journal of Civil Engineering and Urbanism*, 3(2): 56-61.
- Panwar, A. and Tiwari, H.L. (2014). Hydraulic Energy Dissipators – a review, *International Journal of Scientific Engineering and Technology*, 3(4): 400-402.

REFERENCES

- Pan, S. and Shao, Y. (1984). Scale effects in modeling air demand by a ramp slot, *IAHR Symposium on Scale Effects in Modelling Hydraulic Structures*, Esselingen, Germany.
- Peregrine, H. (2003). Water-wave impact on walls, *Annual Review of Fluid Mechanics*, 35: 23–43.
- Pereira, G., Cleary, P. and Serizawa, Y. (2018). Prediction of fluid flow through and jet formation from a high pressure nozzle using Smoothed Particle Hydrodynamics, *Chemical Engineering Science*, 178: 12-26
- Peterka, A. J. (1953). The effect of entrained air on cavitation pitting, *Proceedings of the Joint Meeting of the International Association for Hydraulic Research and the American Society of Civil Engineers*, Minneapolis, USA.
- Peterka, A. (1978). *Hydraulic design of stilling basin and energy dissipators*, U.S Bureau of Reclamation.
- Peterka, A. (1983). *Hydraulic design of stilling basins and energy dissipators*, Engineering Monograph 25, U. S. Bureau of Reclamation, Denver, USA.
- Pfister, M. (2008). *Schussrinnenbelüfter: Lufttransport ausgelöst durch interne Abflussstruktur [Chute aerators: Air transport due to internal flow features]*, Ph.D. Thesis, Eidgenössische Technische Hochschule, Zurich, Switzerland (in German).
- Pfister, M. and Chanson, H. (2014). Two-phase air-water flows: Scale effects in physical modelling, *Journal of Hydrodynamics*, 26: 291–298.
- Pfister, M., Hager, W. and Boes, R. (2014). Trajectories and air flow features of ski jump-generated jets, *Journal of Hydraulic Research*, 52(3): 336–346.
- PNCOLD. (1992). *Large Dams in Portugal*, Portuguese National Committee on Large Dams, Lisbon, Portugal.
- Pope S. (2001). *Turbulent Flows*, Cambridge University Press, United Kingdom.
- Qu, X., Khezzar, L., Danciu, D., Labois, M. and Lakehal, D. (2011). Characterization of plunging liquid jets: A combined experimental and numerical investigation, *International Journal of Multiphase Flow*, 37(7): 722–731.
- Rajaratnam, N. and Murahari, V. (1971). A contribution to forced hydraulic jumps, *Journal of Hydraulic Research*, 9(2): 217–240.
- Rebollo, J., de Blas, M., Diaz, R. and Marivela, R. (2010). Hydrodynamic verification with SPH of under gate flow in the Alarcon spillway (Spain), *1st European IAHR Congress*, Edinburgh, United Kingdom.
- Reinauer, R. and Hager, W. (1998). Supercritical flow in chute contraction, *Journal of Hydraulic Engineering*, 124(1): 55–64.
- Reisi, A., Salah, P. and Kavianpour, M. (2015). Impact of Chute Walls Convergence Angle on Flow Characteristics of Spillways using Numerical Modeling, *International Journal of Chemical, Environmental and Biological Sciences*, 3(3): 2320-4087.
- REN (2017). *Dados Técnicos '17 [Technical data]*, Rede Energética Nacional (available from <https://www.ren.pt/pt-PT/media/publicacoes/>, accessed in December 2018).

REFERENCES

- REN21. (2016). *Renewables 2016 Global Status Report*, REN21, (available from http://www.ren21.net/wp-content/uploads/2016/05/GSR_2016_Full_Report_lowres.pdf, accessed in February 2017).
- Riasi, A., Raisse, M. and Nourbakhsh, A. (2010). Simulation of transient flow in hydroelectric power plants using unsteady friction, *Journal of Mechanical Engineering*, 56(6): 377-384.
- Rhone, T. and Peterka, A. (1959). Improved tunnel spillway flip buckets, *Journal of the Hydraulics Division*, 85(12): 53-76.
- Robinson, M. (2009). *Turbulence and viscous mixing using smoothed particle hydrodynamics*, Ph.D. Thesis, University of Monash, Melbourne, Australia.
- Robinson, M., Cleary, P. and Monaghan, J. (2008). Analysis of mixing in a twin cam mixer using smoothed particle hydrodynamics, *AIChE Journal*, 54(8): 1987-1998.
- Rogers, B. and Dalrymple, R. (2008). *SPH Modeling of tsunami waves*, Advanced Numerical Models for Simulating Tsunami Waves and Runup, 10: 75-100, World Scientific Publishing Co Pte Ltd.
- Rustico, E., Bilotta, G., Gallo, G., Hérault, A., Del Negro, C. and Dalrymple R. (2012). A journey from single-GPU to optimized multi-GPU SPH with CUDA, *7th International SPHERIC Workshop*, Prato Italy.
- Rutschmann, P. (1988). *Belüftungseinbauten in Schussrinnen [Chute additions for air entrainment]*, Ph.D. Thesis, Eidgenössische Technische Hochschule, Zurich, Switzerland (in German).
- Saunders, K., Prakash, M., Cleary, P. W. and Cordell, M. (2014). Application of Smoothed Particle Hydrodynamics for modelling gated spillway flows, *Applied Mathematical Modelling*, 38(17-18): 4308-4322.
- Savage, B. and Johnson, M. (2001). Flow over Ogee Spillway: Physical and Numerical Model Case Study, *Journal of Hydraulic Engineering*, 127 (8).
- Schmocker, L. (2006). *Belüftungs-Eigenschaften von Skisprüngen [Aeration characteristics of ski jumps]*, MSc Thesis, Eidgenössische Technische Hochschule, Zurich, Switzerland (in German).
- Schmocker, L., Pfister, M., Hager, W. and Minor, H. E. (2008). Aeration characteristics of ski jump jets, *Journal of Hydraulic Engineering*, 134(1): 90-97.
- Scimemi, E. (1930). *Sulla forma delle vene tracimanti* (The form of flow over weir), *L'energia Elettrica: Milano*, 7(4): 293-305 (in Italian).
- Shakibaeinia, A. and Jin, Y. (2011), A mesh-free particle model for simulation of mobile bed dam break, *Advances in Water Resources*, 34(6): 794-807.
- Shao, S. (2006). Incompressible SPH simulation of wave breaking and overtopping with turbulence modeling, *International Journal for Numerical Methods in Fluids*, 50(5): 597-621.
- Shi, H., Yu, X. and Dalrymple, R. (2017). Development of a two-phase SPH model for sediment laden flows, *Computational Physics Communications*, 221, 259-272.
- Souari, L. and Hassairi, M. (2013). Numerical Simulation of the Flow into a Rotating Pelton Bucket, *International Journal of Emerging Technology and Advanced Engineering*, 3(2), 67-74.
- Souto-Iglesias, A., Delorme, L., Pérez-Rojas, L. and Abril-Pérez, S. (2006). Liquid moment amplitude assessment in sloshing type problems with smooth particle hydrodynamics, *Ocean Engineering*, 33, 1462-1484.

REFERENCES

- Speziale, C., So, R. and Younis, B. (1993). On the prediction of turbulent secondary flows, in *Near-Wall Turbulent Flows*, Elsevier, New York, USA.
- Straub, L. and Anderson, A. (1958). Experiments on self-aerated flow in open channels, *Journal of the Hydraulics Division*, 84(7): 1-35.
- Steiner, R., Heller, V., Hager, W. and Minor, H. (2008). Deflector Ski Jump Hydraulics, *Journal of Hydraulic Engineering*, 134(5): 562-571.
- Sun, F., Tan, M. and Xing, J. (2012). Air-water two phase flow simulations using Smoothed Particle Hydrodynamics, *International Conference on Violent Flows*, Nantes, France.
- Sun, P., Colagrossi, A., Marrone, S., Antuono, M. and Zhang, A. (2017). Multi-resolution Delta – plus–SPH with tensile instability control: towards high Reynolds number flows, *Computer Physics Communications*, 224: 63-80.
- Sun, P., Colagrossi, A., Marrone, S., Antuono, M. and Zhang, A. (2019). A consistent approach to particle shifting in the δ -Plus-SPH model, *Computer Methods in Applied Mechanics and Engineering*, 348.
- Swegle, J., Hicks, D. and Attaway S. (1995). Smoothed Particle Hydrodynamics Stability Analysis, *Journal of Computational Physics*, 116: 123-134.
- Tait, P. G. (1888). *Report on some of the physical properties of fresh water and sea water*, Report Scientific Results Voyage H.M.S. Challenger, Physics and Chemistry 2: 1-79.
- Tanchev, L. (2005). *Dam and appurtenant hydraulic structures*, A. A. Balkema Publisher, Leiden, The Netherlands.
- Teixeira, A. S. (2016). *Energia Hidroelétrica em Portugal: passado, presente e futuro. Perspetivas de evolução do sistema electroprodutor, EDP Produção [Hydroelectric Energy in Portugal: past, present and future. Prospects for the evolution of the electricity generation system, EDP Produção]*, HYDRO'storming – Series of lectures, Faculty of Engineering of the University of Porto, (in Portuguese).
- Teklemariam, E., Korbaylo, B., Groeneveld, J. and Fuchs, D. (2002). Computational fluid dynamics: diverse applications in hydropower project's design an analysis, *CWRA 55th Annual Conference*, Vinipegue, Canada.
- Tennekes, H. and Lumley, J.L. (1972). *A first course in turbulence*, MIT Press.
- Terzidis, G., and Strelkoff, T. (1970). Computation of open-channel surges and shocks, *Journal of the Hydraulics Division*, 96(12): 2581–2610.
- Tiwari, H. (2013). Analysis of baffle wall gap in the design of stilling basin model, *International Journal of Civil Engineering and Technology*, 4(4): 66-71.
- Todeschini, S. (2012). Trends in long daily rainfall series of Lombardia (Northern Italy) affecting urban stormwater control, *International Journal of Climatology*, 32(6): 900-919.
- Toral, S. E. (2013). *Comportamiento hidráulico de aliviaderos escalonados en cajeros laterales em presas de HCR [Hydraulic behavior of staggered spillways at RCC dams]*, Ph.D. Thesis, Universitat Politècnica de Catalunya, Spain (in Spanish).
- Toso, J. and Bowers, C. (1988). Extreme Pressures in Hydraulic-Jump Stilling Basins, *Journal of Hydraulic Engineering*, 114(8): 829–843.

REFERENCES

- Ulrich, C. (2013). *Smoothed Particle Hydrodynamics simulation of port hydrodynamic problems*, Ph.D. Thesis, Technische Universität Hamburg, Germany.
- USACE WES. (1952) - revised in subsequent years. *Corps of Engineers Hydraulic Design Criteria*.
- USACE. (1995). *Gravity dam design*, Engineering Manual 1110-2-2200, Washington, USA.
- USBR. (1958). *Hydraulic design of stilling basins and energy dissipators*, Engineering Monograph, N° 25, Denver, USA.
- USCOLD. (1988). *Lessons from dam incidents*, Committee on Dam Safety of the United States Committee on Large Dams (USCOLD), American Society of Civil Engineering, New York, USA.
- Vacondio, R., Rogers, B. and Stansby, P. (2012). Accurate particle splitting for SPH in shallow water with shock capturing, *International Journal for Numerical Methods in Fluids*, 69(8): 1377–1410.
- Vacondio, R., Rogers, B., Stansby, P. and Mignosa, P. (2016). Variable resolution for SPH in three dimensions: towards optimal splitting and coalescing for dynamic adaptivity, *Computer Methods in Applied Mechanics and Engineering*, 300: 442–460.
- Vacondio, R., Rogers, B., Stansby, P., Mignosa, P. and Feldman, J. (2013). Variable resolution for SPH: a dynamic particle coalescing and splitting scheme, *Computer Methods in Applied Mechanics and Engineering*, 256: 132-148.
- Valizadeh, A. and Monaghan, J. (2012). Smoothed particle hydrodynamics simulations of turbulence in fixed and rotating boxes in two dimensions with no-slip boundaries, *Physics of Fluids*, 24(3), 035107.
- Versteeg, H. and Malalasekera, W. (1995). *An introduction to computational fluid dynamics - the finite volume method*, Prentice Hall, Pearson Education Ltd., England.
- Vila, J. (1999). On particle weighted methods and smooth particle hydrodynamics, *Mathematical Models and Methods in Applied Sciences*, 9: 161–209.
- Violeau, D. (2004). One and two-equations turbulent closures for Smoothed Particle Hydrodynamics, *6th International Conference on Hydroinformatics*, Singapore.
- Violeau, D. (2012). *Fluid Mechanics and the SPH Method. Theory and Applications*, Oxford: Oxford University Press.
- Violeau, D., Buvat C., Abed-Meraïm, K. and Nanteuil, E. (2008). Numerical modelling of boom and oil spill with SPH, *Coastal Engineering*, 54: 895–913.
- Violeau, D. and Issa, R. (2007). Numerical modelling of complex turbulent free surface flows with the SPH method: an overview, *International Journal for Numerical Methods in Fluids*, 53(2): 277-304.
- Violeau, D. and Leroy, A., (2014). On the maximum time step in weakly compressible SPH, *Journal of Computational Physics*, 256: 388-415.
- Violeau, D. and Rogers, B. (2016). Smoothed Particle Hydrodynamics (SPH) for free-surface flows: past, present and future, *Journal of Hydraulic Research*, 54(1): 1-26.
- Violeau, D., Piccon, S. and Chabard, J. (2002). *Two attempts of turbulence modelling in Smoothed Particle Hydrodynamics*, in *Advances in Fluid Modelling and Turbulence Measurements*, World Scientific, 339–346.
- Viollet, P., Chabard, J., Esposito, P. and Laurence, D. (2002). *Mécanique des fluides appliquée [Applied fluid mechanics]*, Presses de l’Ecole Nationale des Ponts et Chaussées, 2002. (in French).

REFERENCES

- Visher, D. and Hager, W. (1995). *Energy dissipators*, Balkema, Rotterdam, The Netherlands.
- Vischer, D. and Hager, W. (1998). *Dam hydraulics*, John Wiley & Sons, Chichester, United Kingdom.
- Viseu, T., Carvalho, R., Marques, L. and Silva, J. (2018). Pressure and velocity measurements in prototype. The case of Foz do Tua dam plunge pool, *3rd International Dam World Conference*, Foz Iguacu, Brazil.
- Von Thun, J. (1985) *Application of statistical data from dam failures and accidents to risk based decision analysis on existing dams*, Internal Report, United States Bureau of Reclamation (USBR), Denver, USA.
- Wahl, T., Frizell, K. and Cohen, E. (2008). Computing the trajectories of free jets, *Journal of Hydraulic Engineering*, 134(2): 256–260.
- Wallin, N. and Johansson, A. (2000). An explicit algebraic Reynolds stress model for incompressible and compressible turbulent flows, *Journal of Fluid Mechanics*, 403: 89–132.
- Wendland H. (1995). Piecewise polynomial, positive definite and compactly supported radial functions of minimal degree, *Advances in Computational Mathematics*, 4: 389-396.
- Winkler, D., Rezavand, M. and Rauch, W. (2018). Neighbor lists for Smoothed Particle Hydrodynamics on GPUs, *Computer Physics Communications*, 225: 140-148.
- Wrachien, D. and Mambretti, S. (2006). *Dam-break Problems, Solutions and Case Studies*, WIT Press.
- Wei, W. Deng, J. and Zhang, F. (2016). Development of self-aeration process for supercritical chute flows, *International Journal of Multiphase Flow*, 79:172-180.
- Welton, W. and Pope, S. (1997). PDF model calculations of compressible turbulent flows using smoothed particle hydrodynamics. *Journal of Computational Physics*, 134: 150–168.
- Williamson, T. (2017). *Historic dam failures and recent incidents*, Communication at Engineers Ireland, Dublin, Ireland.
- Wood, I. (1983). Uniform region of self-aerated flow, *Journal of Hydraulic Engineering*, 109(3):447-461.
- Wood, I. (1991). *Air entrainment in free-surface flows*, Hydraulic Design Considerations, Balkema Publisher, Rotterdam, The Netherlands.
- Woolbright, R. (2008). *Hydraulic performance evaluation of RCC stepped spillways with sloped converging training walls*, MSc Thesis, Oklahoma State University, Oklahoma, USA.
- Wu, S. and Rajaratnam, N. (1995). Effect of baffles on submerged flows, *Journal of Hydraulic Engineering*, 121(9): 644–652.
- Yamini, O. and Kavianpour, M. (2011). Experimental study of static and dynamic pressures over simple flip bucket, *5th Symposium on Advances in Science and Technology*, Mashhad, Iran.
- Yuditskii, G. (1963). *Acção hidrodinâmica de uma lâmina descarregada sobre blocos de um leito rochoso e condições de rotura deste*, translated from Izvestiya VNII Gridrotekhniki, Vol. Tradução LNEC No. 442, LNEC, Lisbon, Portugal, (in Portuguese)
- Zubeldia, E., Fourtakas, G., Rogers, B. and Farias, M. (2018). Multi-phase SPH model for simulation of erosion and scouring by means of the shields and Drucker–Prager criteria, *Advances in Water Resources*, 117: 98-114.

REFERENCES

APPENDIX A

OVERGATE DISCHARGE – CASE STUDY I

APPENDIX A

APPENDIX A

Table A.1 - Experimental vs. computed water depths and velocity profiles.

Velocity profile	x	H		U_{max}		U_{mean}		h'	
		Lopes, (2005)	GPUSPH	Lopes, (2005)	GPUSPH	Lopes, (2005)	GPUSPH	Lopes, (2005)	GPUSPH
	[m]	[cm]	[cm]	[m/s]	[m/s]	[m/s]	[m/s]	[cm]	[cm]
P-1	1.06	3.20	3.86	0.434	0.423	0.382	0.356	0.6	0.93
P0	1.09	3.30	3.93	0.415	0.421	0.375	0.358	0.95	1.06
P1	1.12	4.60	5.30	0.367	0.361	0.331	0.285	2.4	2.86
P2	1.17	5.14	5.28	0.345	0.318	0.270	0.272	4.4	5.28
P3	1.22	5.15	5.30	0.349	0.311	0.277	0.267	4.4	5.30
P4	1.27	5.16	5.28	0.326	0.302	0.265	0.268	4.4	5.23
P5	1.32	5.17	5.33	0.322	0.293	0.263	0.263	4.6	5.33
P6	1.37	5.19	5.38	0.332	0.286	0.266	0.258	4.4	5.38
P7	1.42	5.21	5.32	0.319	0.277	0.254	0.253	4.2	5.32
P10	1.57	5.27	5.33	0.307	0.260	0.258	0.240	4.6	2.33
P15	1.82	5.37	5.36	0.300	0.245	0.256	0.227	4.6	5.36

x - distance with respect to the numerical model's coordinate system's origin

APPENDIX A

APPENDIX B

CHUTE FLOW – CASE STUDY I

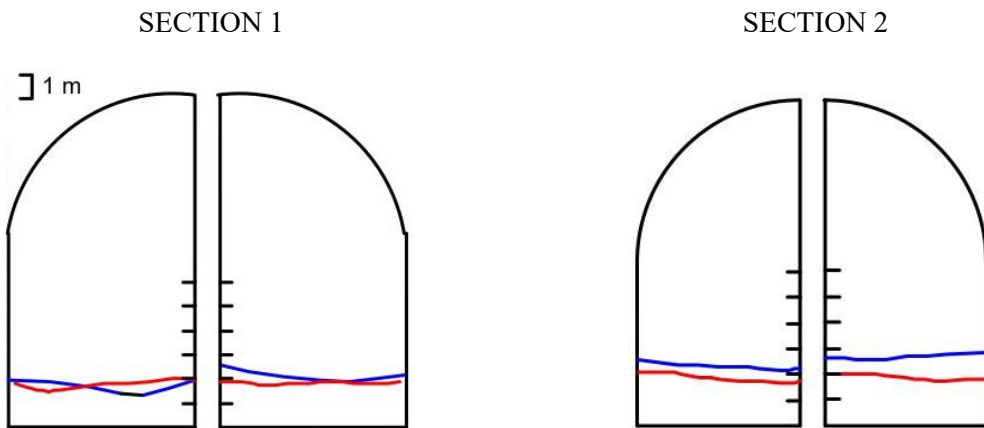


Fig B.1 - Graphic comparison of the free surface for sections 1 and 2 for the flow rate of 690 m³/s: Experimental results - blue line; GPUSPH results - red line.

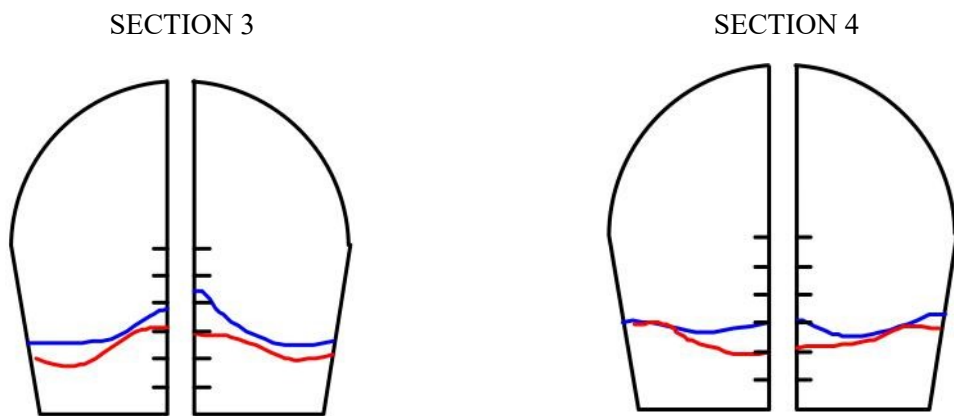


Fig B.2 - Graphic comparison of the free surface for sections 3 and 4 for the flow rate of 690 m³/s: Experimental results - blue line; GPUSPH results - red line.

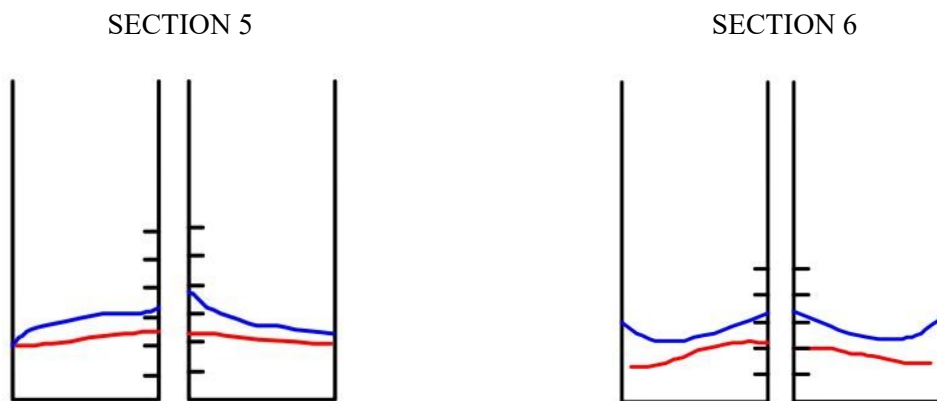


Fig B.3 - Graphic comparison of the free surface for sections 5 and 6 for the flow rate of 690 m³/s: Experimental results - blue line; GPUSPH results - red line.

APPENDIX B

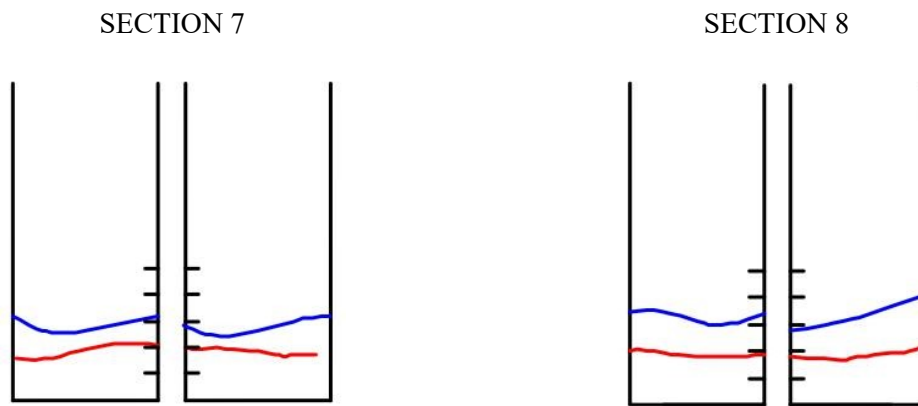


Fig B.4 - Graphic comparison of the free surface for sections 7 and 8 for the flow rate of 690 m³/s: Experimental results - blue line; GPUSPH results - red line.

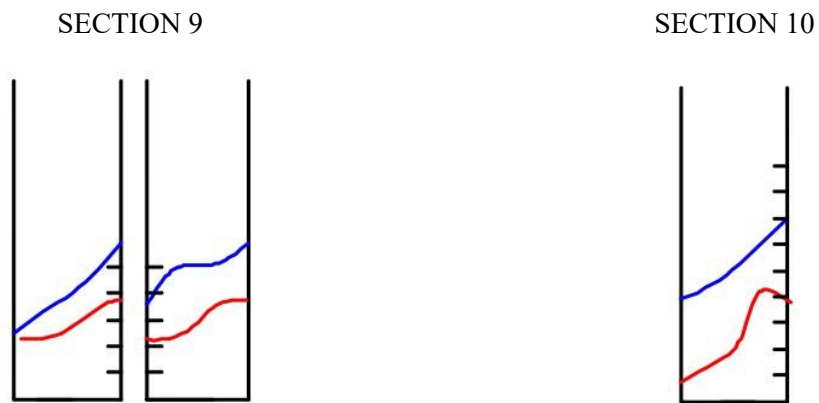


Fig B.5 - Graphic comparison of the free surface for sections 9 and 10 for the flow rate of 690 m³/s: Experimental results - blue line; GPUSPH results - red line.

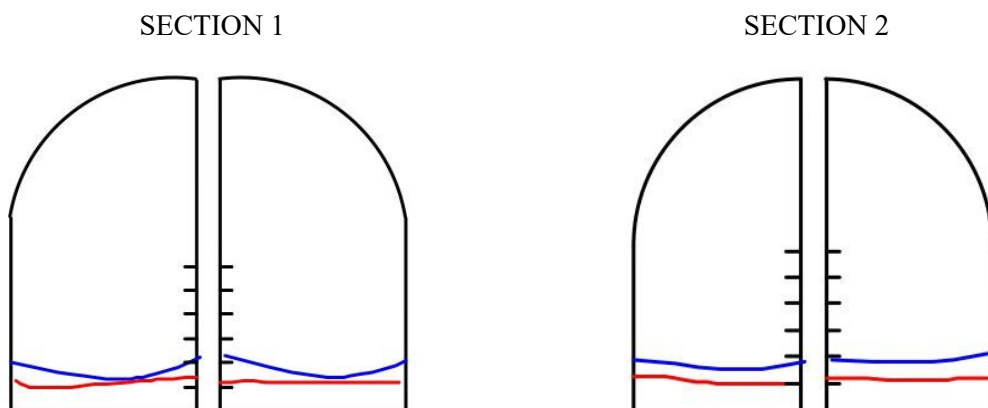


Fig B.6 - Graphic comparison of the free surface for sections 1 and 2 for the flow rate of 527 m³/s: Experimental results - blue line; GPUSPH results - red line.

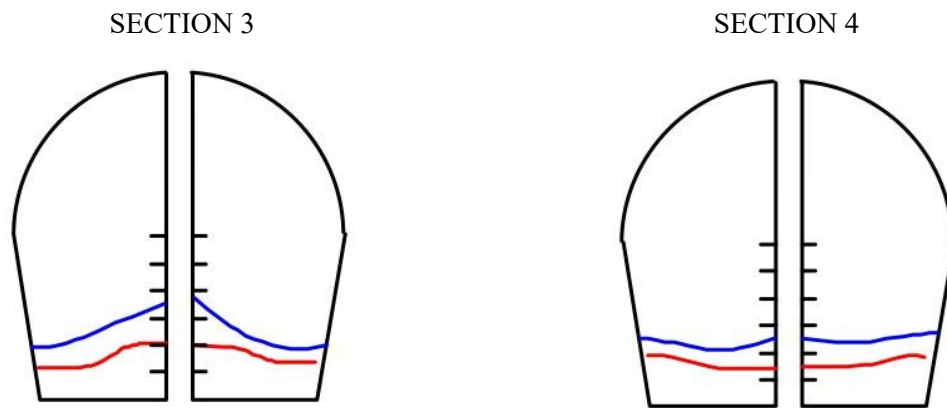


Fig B.7 - Graphic comparison of the free surface for sections 3 and 4 for the flow rate of 527 m³/s: Experimental results - blue line; GPUSPH results - red line.

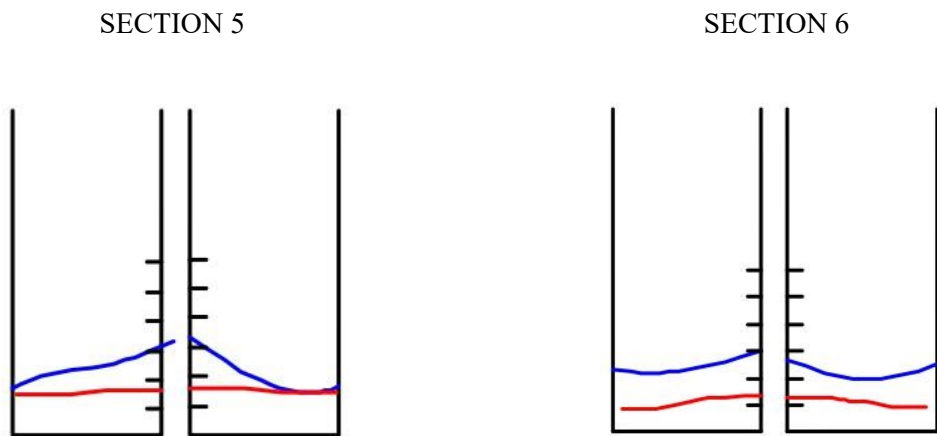


Fig B.8 - Graphic comparison of the free surface for sections 5 and 6 for the flow rate of 527 m³/s: Experimental results - blue line; GPUSPH results - red line.

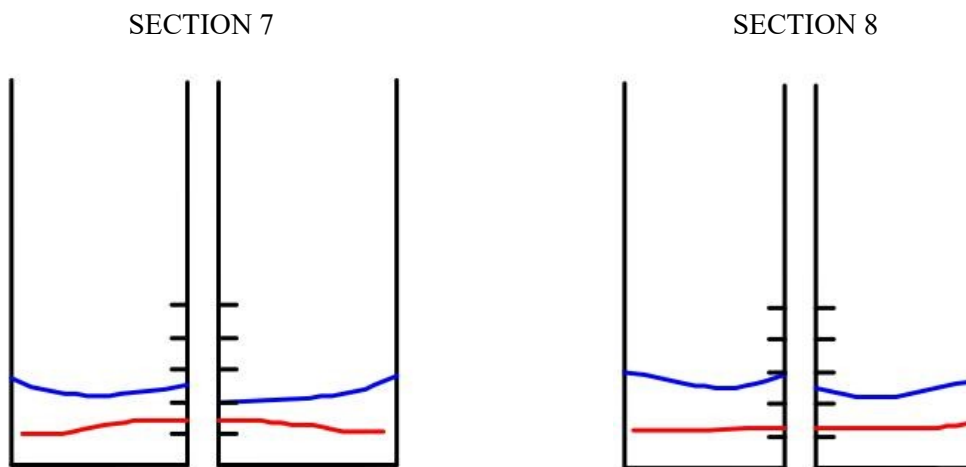


Fig B.9 - Graphic comparison of the free surface for sections 7 and 8 for the flow rate of 527 m³/s: Experimental results - blue line; GPUSPH results - red line.

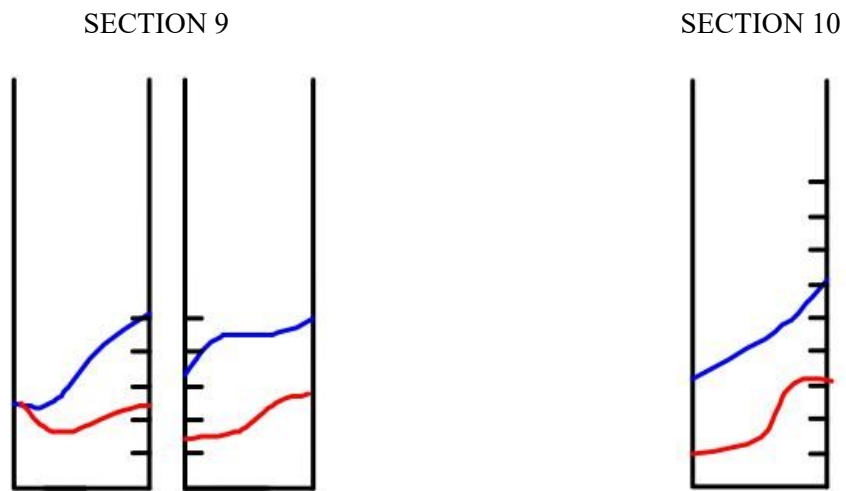


Fig B.10 - Graphic comparison of the free surface for sections 9 and 10 for the flow rate of 527 m³/s: Experimental results - blue line; GPUSPH results - red line.

APPENDIX B

Table B. 1 - Location of test points used for pressure computation.

Piezometer	x	y	z	Piezometer	x	y	z
P1	74.15	45.62	6.66	1D	318.08	40.05	-35.38
P2	76.19	45.43	6.99	1E	318.08	45.49	-35.38
P3	78.74	45.24	6.57	2D	318.08	40.05	-32.18
P4	84.19	44.81	3.96	2E	318.08	45.49	-32.18
P5	89.15	44.5	0.23	3D	325.51	40.73	-35.44
P6	94.17	44.3	-3.63	3E	325.51	45.49	-35.44
P7	105.31	43.84	-11.02	4D	325.51	40.73	-31.97
P8	123.35	43.14	-16.52	4E	325.51	45.49	-31.97
P9	158.45	42.27	-20.13	5D	332.65	41.73	-34.81
P10	184.97	42.27	-22.86	5E	332.65	45.93	-34.81
P11	213.03	42.27	-25.75	6D	332.65	41.73	-31.34
P12	300.1	42.74	-34.72	6E	332.65	45.93	-31.34
P13	318.08	42.77	-36.87	7D	332.65	41.73	-28.3
P14	325.51	43.11	-36.73	7E	332.65	45.93	-28.3
P15	332.65	43.83	-36	8D	338.79	43.02	-32.99
P16	338.79	45.07	-34.48	8E	338.79	47.11	-32.99
				9D	338.79	43.02	-29.52
				9E	338.79	47.11	-29.52
				10D	338.79	43.02	-26.48
				10E	338.79	47.11	-26.48

APPENDIX B

APPENDIX C

SPILLWAY3D CASE EXAMPLE - SOURCE FILE

APPENDIX C

```

/* Copyright 2011-2013 Alexis Herval, Giuseppe Bilotta, Robert
A. Dalrymple, Eugenio Rustico, Ciro Del Negro
  Istituto Nazionale di Geofisica e Vulcanologia
    Sezione di Catania, Catania, Italy
  Università di Catania, Catania, Italy
  Johns Hopkins University, Baltimore, MD

```

This file is part of GPUSPH.

GPUSPH is free software: you can redistribute it and/or modify it under the terms of the GNU General Public License as published by the Free Software Foundation, either version 3 of the License, or (at your option) any later version.

GPUSPH is distributed in the hope that it will be useful, but WITHOUT ANY WARRANTY; without even the implied warranty of MERCHANTABILITY or FITNESS FOR A PARTICULAR PURPOSE. See the GNU General Public License for more details.

You should have received a copy of the GNU General Public License along with GPUSPH. If not, see <http://www.gnu.org/licenses/>.

```

*/

#include <iostream>
#include "Spillway3D.h"
#include "GlobalData.h"
#include "cudasimframework.cu"
Spillway3D::Spillway3D(GlobalData *_gdata) : XProblem(_gdata)
{
  m_name = "Spillway3D";
  m_bndtstart [0]= 0;
  m_bndtend [0]= 0;
  m_bndtstart [1]= 0;
  m_bndtend [1]= 0;

  // Setup the simulation framework
  SETUP_FRAMEWORK(
    kernel<WENDLAND>,
    formulation<SPH_F1>,
    viscosity<KEPSVISC>,
    boundary<SA_BOUNDARY>,
    periodicity<PERIODIC_NONE>,
    flags<ENABLE_FERRARI |
          ENABLE_INLET_OUTLET |
          ENABLE_WATER_DEPTH |
          ENABLE_DENSITY_SUM |
          ENABLE_DTADAPT>
  );

  // Initialization of the physical parameters
  simparams()->sfactor= 1.5f;
  set_deltap(0.0850);
  physparams()->r0 = m_deltap;

  // Gravity
  physparams()->gravity = make_float3(0, 0, -9.81);

```

sfactor represents the smoothing length (h)
 deltap represents the particle's diameter, d_p . For consistency reasons, it should be the same as that adopted for CRIXUS

APPENDIX C

```

// Initialization of the neighbours parameters
simparams()->maxneibsnum = 300;
simparams()->buildneibsfreq = 20;

// Time parameters
simparams()->dt = 1e-05;
simparams()->dtadaptfactor = 0.3;
simparams()->tend= 5;

// Ferrari correction
simparams()->ferrari= 1.0f;

// Writer settings
add_writer(VTKWRITER, 0.5); //writes .vtu files every 0.5s
add_writer(COMMONWRITER, 0.1); //info displayed on
terminal at every 0.1s
addPostProcess(SURFACE_DETECTION);

size_t fluid_0 = add_fluid(1000);
set_kinematic_visc(fluid_0, 1e-06);
setWaterLevel(0.75f);
setMaxParticleSpeed(6.f);
set_equation_of_state(fluid_0, 7, NAN);

// Geometry settings - computational domain dimensions
m_origin = make_double3(0, 0, 0);
m_size = make_double3(2, 0.5, 1.5);

// Fluid definition - call for fluid's .h5sph file
GeometryID fluid = addHDF5File(GT_FLUID, Point(0,0,0),
"./data_files/Spillway3D/0. Spillway3D.fluid.h5sph", NULL);

// Main container - call for geometry's .h5sph file
GeometryID container = addHDF5File(GT_FIXED_BOUNDARY,
Point(0,0,0), "./data_files/ Spillway3D /0.
Spillway3D.boundary.kent0.h5sph", NULL);
disableCollisions(container);

// Special boundaries - call for inlet & outlet's .h5sph
files
GeometryID special_boundary_0 = addHDF5File
(GT_OPENBOUNDARY, Point(0,0,0), "./data_files/ Spillway3D /0.
Spillway3D.boundary.kent1.h5sph", NULL);
disableCollisions(special_boundary_0);
setVelocityDriven(special_boundary_0, 1);
GeometryID special_boundary_1 = addHDF5File
(GT_OPENBOUNDARY, Point(0,0,0), "./data_files/ Spillway3D /0.
Spillway3D.boundary.kent2.h5sph", NULL);
disableCollisions(special_boundary_1);
setVelocityDriven(special_boundary_1, 0);

//Wave gages x,y location
add_gage(0.25, 0.25, 0.0);
//Probes x,y,z location
addPostProcess(TESTPOINTS)
addTestPoint(0.25, 0.25, 0);

disableHydrostaticFilling();
}
uint Spillway3D::max_parts(uint numpart)
{
    return (uint)((float)numpart*1.3f);
}

```

maxneibsnum represents the maximum number of neighbouring particles allowed to perform the SPH interpolation, at each iteration. If this value is surpassed the simulation should crash.

buildneibsfreq represents the frequency at which the neighbours of a certain particle are updated. "20" means they are updated at every twenty iterations. This parameter can be refined during the simulation to speed up convergence.

dtadaptfactor represents the CFL number used to control/adapt the time-step at every iteration.

ferrari represents the Brezzi coefficient

setMaxParticleSpeed represents the magnitude of the maximum flow velocities expected in the numerical model (user for c_0 computation)

the user can have more than one fluid's h5sph file to call (e.g. a fluid volume upstream and another one downstream), by adding similar lines.

setVelocityDriven - 1 - means that the first open boundary (inlet) is velocity driven.

setVelocityDriven - 0 - means that the second open boundary (outlet) is pressure driven.

Max_parts set to 1.3 means that the no. of particles can increase up to 30% during the simulation, thus no more

APPENDIX C

```

namespace cuSpillway3D
{
    using namespace cuforces;
    using namespace cubounds;
    __device__
    void
    Spillway3D_imposeBoundaryCondition(
        const particleinfo info,
        const float3      absPos,
        float             waterdepth,
        float             ustar,
        const float       t,
        float4&          vel,
        float4&          eulerVel,
        float&           tke,
        float&           eps)
    {
        // Default value for eulerVel
        // Note that this default value needs to be
        // physically feasible, as it is used in case of boundary elements
        // without fluid particles in their support.
        // It is also possible to use this default value to impose tangential
        // velocities for pressure outlets.
        eulerVel = make_float4(0.0f, 0.0f, 0.0f,
d_rho0[fluid_num(info)]);
        vel = make_float4(0.0f);
        tke = 1e-5;
        eps = 1e-5;

        // open boundary conditions
        if (IO_BOUNDARY(info)) {
            if (!VEL_IO(info)) {
                // set water depth values
                // Inlet (if we chose a PRESSURE driven boundary)
                if (object(info) == 0) {
                    waterdepth = 0.75;
                }
                // Outlet
                if (object(info) == 1) {
                    waterdepth = 0;
                }
                const float localdepth =
fmaxf(waterdepth - absPos.z, 0.0f);
                const float pressure =
9.81f*localdepth*d_rho0[fluid_num(info)];
                eulerVel.w = RHO(pressure,
fluid_num(info));
            } else {
                // set velocity
                if (object(info) == 0 &&
absPos.z < waterdepth) {
                    eulerVel.x = ustar * ( 1.0f/
KAPPA * log(ustar*max(absPos.z, 0.01f)/d_visccoeff[0]) + 5.2);
                    tke = ustar * ustar /
(sqrtf(CMU)) * (1 - absPos.z/waterdepth);
                    eps = ustar * ustar * ustar /
(KAPPA * max(absPos.z, 0.01f)) * (1 - absPos.z/waterdepth);
                }
            }
        }
    }
}
__global__ void
Spillway3D_imposeBoundaryConditionDevice(

```

memory will be allocated than that needed.

This is not used when inlet boundary is velocity driven

Logarithmic velocity profile imposition at inlet as well as k and ϵ .

APPENDIX C

```

float4*      newVel,
float4*      newEulerVel,
float*       newTke,
float*       newEpsilon,
const float4* oldPos,
const uint*  IOwaterdepth,
const float  t,
const uint   numParticles,
const uint*  particleHash)
{
    const uint index = INTMUL(blockIdx.x,blockDim.x) +
threadIdx.x;

    if (index >= numParticles)
        return;

    float4 vel = make_float4(0.0f);           //imposed
velocity for moving objects
    float4 eulerVel = make_float4(0.0f);     //imposed
velocity/pressure for open boundaries
    float tke = 0.0f;                       //imposed
turbulent kinetic energy for open boundaries
    float eps = 0.0f;                       //imposed
turb. diffusivity for open boundaries

    // Open boundary conditions
    if(index < numParticles) {
        const particleinfo info = tex1Dfetch(infoTex,
index);
        //if (IO_BOUNDARY(info) && (!CORNER(info) ||
!VEL_IO(info))) {
            if (IO_BOUNDARY(info)) {
                // For corners we need to get eulerVel in case of
k-eps and pressure outlet
                if (CORNER(info) && newTke &&
!VEL_IO(info)) {
                    eulerVel = newEulerVel[index];
                }
                const float3 absPos = d_worldOrigin +
as_float3(oldPos[index])+
calcGridPosFromParticleHash(particleHash[index])*d_cellSize +
0.5f*d_cellSize;

                float waterdepth = 0.0f;
                float Channel_Width = 0.5f;
                float ustar = 0.01f;
                float Q = 0.188;
                if (VEL_IO(info)) {
                    waterdepth = ((float)IOwaterdepth
[object(info)]) / ((float)UINT_MAX); // now between 0 and 1
                    waterdepth *= d_cellSize.z *
d_gridSize.z;

                    waterdepth += d_worldOrigin.z;
                    if (waterdepth <= 0.0) {
                        waterdepth = 0.75;
                    }

                    float U = Q / (Channel_Width *
waterdepth);

                    float ustar_error=1.0f;
                    float ustar_prev;
                    uint ustar_iteration = 0;

```

Channel_Width represents the width of the inlet section (if variable a function should be defined)
Q represents the flow rate

APPENDIX C

```

        while (ustar_error > 0.0001f) {
            ustar_prev=ustar;
            ustar = KAPPA*U/log(exp(KAPPA*5.2-
1.0f)*waterdepth*ustar/d_visccoeff[0]);
            ustar_error=abs((ustar-ustar_prev)
/ustar_prev);
            if (ustar_iteration > 50) {
                printf("ustar      iteration
failed");
                break;
            }
            ustar_iteration++;
        }
        //printf("ustar=%f\n", ustar);
    }
    // this now calls the virtual function that is
problem specific
    Spillway3D_imposeBoundaryCondition(info,  absPos,
waterdepth, ustar, t, vel, eulerVel, tke, eps);
    // copy values to arrays
    newVel[index] = vel;
    newEulerVel[index] = eulerVel;
    if(newTke)
        newTke[index] = tke;
    if(newEpsilon)
        newEpsilon[index] = eps;
    }
}
} // end of cuSpillway3D namespace

void
Spillway3D::imposeBoundaryConditionHost(
    MultiBufferList::iterator      bufwrite,
    MultiBufferList::const_iterator  bufread,
    uint*                            IOWaterdepth,
    const float                       t,
    const uint                        numParticles,
    const uint                        numOpenBoundaries,
    const uint                        particleRangeEnd)
{
    float4 *newVel = bufwrite->getData<BUFFER_VEL>();
    float4 *newEulerVel  =  bufwrite->  getData  <
BUFFER_EULERVEL>();
    float *newTke = bufwrite->getData<BUFFER_TKE>();
    float *newEpsilon = bufwrite->getData<BUFFER_EPSILON>();
    const particleinfo *info = bufread->  getData
<BUFFER_INFO>();
    const float4 *oldPos = bufread->getData<BUFFER_POS>();
    const  hashKey  *particleHash  =  bufread-
>getData<BUFFER_HASH>();
    const  uint  numThreads  =  min(BLOCK_SIZE_IOBOUND,
particleRangeEnd);
    const  uint  numBlocks  =  div_up(particleRangeEnd,
numThreads);

    // TODO: Probably this optimization doesn't work with this
function. Need to be tested.
    int dummy_shared = 0;
    #if (__COMPUTE__ == 20)
        dummy_shared = 2560;
    #endif
}

```

APPENDIX C

```

        CUDA_SAFE_CALL(cudaBindTexture(0, infoTex, info,
numParticles*sizeof(particleinfo)));

        cuSpillway3D::Spillway3D_imposeBoundaryConditionDevice<<<
numBlocks, numThreads, dummy_shared >>>
        (newVel, newEulerVel, newTke, newEpsilon, oldPos,
IOWaterdepth, t, numParticles, particleHash);

        CUDA_SAFE_CALL(cudaUnbindTexture(infoTex));

        // reset waterdepth calculation
        if (IOWaterdepth) {
            uint h_IOWaterdepth[numOpenBoundaries];
            for (uint i=0; i<numOpenBoundaries; i
                h_IOWaterdepth[i] = 0;
            CUDA_SAFE_CALL(cudaMemcpy(IOWaterdepth,
h_IOWaterdepth, numOpenBoundaries*sizeof(int),
cudaMemcpyHostToDevice));
        }

        // check if kernel invocation generated an error
        KERNEL_CHECK_ERROR;
    }

```